

# Microstructure Modelling of Additive Manufacturing of Alloy 718

**Chamara Sandun Sarath Kumara**











# **Microstructure Modelling of Additive Manufacturing of Alloy 718**

**Chamara** Sandun Sarath Kumara

University West  
SE-46186 Trollhättan  
Sweden  
+46 520 22 30 00  
[www.hv.se](http://www.hv.se)

© Chamara Kumara 2020

ISBN 978-91-88847-83-6 (Printed)  
ISBN 978-91-88847-82-9 (Electronic)

Dedicated to my  
beloved wife, ***Inoka***  
and  
my son, ***Mineth***



## Acknowledgements

I would like to express my sincere gratitude to the following organizations and personals for their valuable support for this research work.

- *Funding Organisations:* European Regional Development Fund, KK Foundation (Stiftelsen för Kunskaps- och Kompetensutveckling)
  - *Supervisors:* Prof. Per Nylén (University West), Prof. Johan Moverare (Linköping University)
  - *Colleagues from University West:* Prof. Shrikant Joshi, Prof. Robert Pederson, Dr. Sten Wessman, Dr. Fabian Hanning, Mr. Arun Ramanathan Balachandramurthi, Mrs. Paria Karimi, Ms. Sneha Goel, Mr. Jonas Olsson, Mr. Kjell Hurtig, Mr. Mattias Ottosson, Mrs. Eva Bränneby Mrs. Kristina Lindh and Miss. Victoria Sjöstedt.
  - *Colleagues from Linköping University:* Dr. Dunyong Deng
  - *Colleagues from Sandvik Additive:* Mr. Nikhil Dixit
  - *Colleagues from GKN Aerospace, Trollhättan:* Dr. Andreas Segerstark
  - *Support team at MICRESS, ACCESS e.V, Aachen, Germany:* Dr. Bernd Böttger and Dr. Janin Eiken.
- ❖ Special thanks should go to my wife, Inoka, who gave me an enormous support at home. Thank you for your understanding and providing me with the time I needed when I had to work extra hours 😊.

Thank you all...

Chamara Kumara

December 2020



“Scientific research is not about showing results; it’s about understanding reasons for the results by asking right questions”

# Populärvetenskaplig Sammanfattning

*Nyckelord:* Additiv tillverkning; Superlegeringar; Värmebehandling; Fasomvandling; Fasfältmodellering;

Additiv tillverkning (AM) i superlegeringen 718 har under de senaste åren rönt ett ökande intresse eftersom metoden har ett antal fördelar jämfört med konventionella tillverkningsmetoder. Processen innebär dock att byggmaterialet utsätts för komplexa termiska förhållanden som påverkar det byggda materialets mikrostruktur. Ofta utförs dessutom en efterföljande värmebehandling vilket ytterligare förändrar det byggda materialets mikrostruktur. Det är därför en utmanande uppgift att kunna styra mikrostrukturen i processen för att kunna erhålla en önskad slutlig mikrostruktur som ger önskade materialegenskaper. En ökad förståelse för hur mikrostrukturen förändras under additiv tillverkning och efterföljande eftervärmebehandling är värdefull, vilket är syftet med detta arbete. Fasfältmodellering har använts tillsammans med transformationskinetikmodellering för detta syfte. Två olika AM-processer; lasermetaldeponering med pulver som tillsatsmaterial (LMP-DED) och elektronstrålesmältning (EB-PBF) har studerats.

Modelleringsarbetet av LMP-DED processen identifierade att stelningsförhållanden (termiska gradienter och kylhastigheter) som uppstår under processen signifikant påverkar den stelnade mikrostrukturen och dess fassammansättning, exempelvis den resulterande andelen Laves-fas. Ökad kylhastighet visade sig minska volymfraktionen Laves-fas samtidigt som dess fasmorfologi blev mer i form av diskreta partiklar, vilket är önskvärt för att förhindra sprickbildning. Resultaten visade även att de fasförändringar som sker under stelningsprocessen inte genomgår någon signifikant förändring under den termiska cykling som uppstår under processen. Anledningen var att temperaturen i materialet inte överstiger 600 ° C. Om temperaturen skulle höjas över 600 ° C, förväntas dock fasförändringar ske. När det gäller EB-PBF-processen resulterade den höga byggtemperaturen i byggkammaren en "*in situ*" värmebehandling, som i sig hade en homogeniseringseffekt på den stelnade mikrostrukturen. Anledningen till denna homogenisering är ett litet dendritavstånd och relativt låg volymfraktion av Laves fas. Vid LMP-DED observerades en segregering som ändrar jämviktsförhållanden och kinetik. Lokala överskott av  $\gamma' / \gamma$  och  $\delta$  fas predikterades vilket även observerades experimentellt i det interdendritiska området jämfört med dendritkärnan beroende på vilken typ av värmebehandling som använts.

Modelleringsarbete utfördes även för att utvärdera mekaniska egenskaper hos EB-PBF tillverkade objekt. Data avseende kristallografisk orientering samt materialdata från enkristallint material användes som indata i denna modellering.



De anisotropa elastiska egenskaperna predikterades och jämfördes med publicerade experimentella litteraturdata vilket visade en god överensstämmelse. Lokalt påvisade EB-PBF-proverna signifikant anisotropa elastiska egenskaper på grund av den kristallografiska textur som observerats. Längst E-modul observerades längs byggriktningen. Vinkelrätt mot byggriktningen visade sig de elastiska egenskaperna vara isotropa. Globalt visade sig de mekaniska egenskaperna vara jämförbara med ett transversellt isotropt fall.



## Abstract

*Title:* Microstructure Modelling of Additive Manufacturing of Alloy 718

*Keywords:* Phase-Field Modelling; Additive Manufacturing; Phase Transformation; Solidification; Heat Treatment; Superalloy

*ISBN:* 978-91-88847-83-6 (Printed)  
978-91-88847-82-9 (Electronic)

In recent years, additive manufacturing (AM) of Alloy 718 has received increasing interest in the field of manufacturing engineering because of its attractive features compared with those of conventional manufacturing methods. Nevertheless, owing to the inherent nature of the process, the build material is exposed to complex thermal conditions that affect the microstructure. In addition, the post-heat treatments applied to the built component further cause microstructural changes. Thus, obtaining the desired microstructure that gives the desired properties is still a challenging task. Therefore, understanding the microstructure formation during the build and subsequent post-heat treatment is important and is the objective of this thesis work. To this end, a computational modelling approach was used that combines multiphase-field modelling with transformation kinetics modelling. Two different AM processes, laser metal powder directed energy deposition (LM-PDED) and electron beam powder bed fusion (EB-PBF), were considered in this study.

Based on the modelling work, it was observed that solidification conditions (thermal gradients and cooling rates) that occur during the AM process have an impact on the as-solidified microstructure in Alloy 718 and the resultant Laves phase formation. With an increase in cooling rate, the Laves phase volume fraction becomes lower and the morphology tends to become discrete particles, which is important for resisting the formation of liquation cracks in Alloy 718. It was also found that the precipitates formed during the solidification process did not undergo any significant change during subsequent thermal cycles associated with the deposition of subsequent layers, given that the deposition of the subsequent layer does not increase the global temperature of the build to  $> 600\text{ }^{\circ}\text{C}$ . If the global temperature increases above  $600\text{ }^{\circ}\text{C}$ , then phase changes are expected, depending on the temperature value. In the case of the EB-PBF process, the high build temperature maintained in the build chamber resulted in an “*in situ*” heat treatment, which had a homogenisation effect on the as-solidified microstructure because of the smaller dendrite spacing and relatively low Laves phase size. In the case of the LM-PDED, the microsegregation of composition observed in the as-built microstructure was shown to change the equilibrium

conditions and precipitation kinetics of Alloy 718. As a result, excess precipitation of  $\gamma'/\gamma''$  and  $\delta$  was observed in the interdendritic region compared with the dendrite core, depending on the type of heat treatment used.

In addition, modelling was performed to evaluate the elastic properties of EB-PBF Alloy 718. To this end, crystallographic orientation data gathered from EBSD data and single-crystal elastic constants were used. The prediction showed good agreement with published literature data. The hatch (bulk) region of the EB-PBF samples showed significant anisotropic elastic properties because of the strong crystallographic texture observed in the microstructure. The lowest Young's modulus was observed along the build direction. Normal to the build direction, the elastic properties were shown to be isotropic. Overall, the elastic behaviour of the hatch region was similar to that of a transversely isotropic case.

## Appended publications and author's contributions

**Paper A** Toward a better understanding of phase transformations in additive manufacturing of Alloy 718

**Chamara Kumara**, Arun Ramanathan Balachandramurthi, Sneha Goel, Fabian Hanning, and Johan Moverare

Published in *Materialia*, vol. 13, Article No: 100862, Sep. 2020.

DOI: [10.1016/j.mtl.2020.100862](https://doi.org/10.1016/j.mtl.2020.100862)

Author's contributions: Principle author of the paper and the idea originator for the work. Modelling and analysis work was performed by Chamara. Additionally, Chamara generate the idea for the continuous cooling rate study presented in the paper. Chamara set up the experimental plan for continuous cooling study.

**Paper B** Microstructure modelling of laser metal powder directed energy deposition of alloy 718

**Chamara Kumara**, Andreas Segerstark, Fabian Hanning, Nikhil Dixit, Shrikant Joshi, Johan Moverare, Per Nylén

Published in *Additive Manufacturing*, vol. 25, pp. 357–364, 2019.

DOI: [10.1016/j.addma.2018.11.024](https://doi.org/10.1016/j.addma.2018.11.024)

Author's contributions: Principle author of the paper and the idea originator for the modelling work. Modelling and analysis work was performed by Chamara.

**Paper C** Predicting the Microstructural Evolution of Electron Beam Melting of Alloy 718 with Phase-Field Modeling

**Chamara Kumara**, Donyong Deng, Fabian Hanning, Morten Raanes, Johan Moverare, and Per Nylén

Published in *Metallurgical and Materials Transactions A*, vol. 50, no. 5, pp. 2527–2537, 2019

DOI: [10.1007/s11661-019-05163-7](https://doi.org/10.1007/s11661-019-05163-7)

Author's contributions: Principle author of the paper and the idea originator for the modelling work. Modelling and analysis work was performed by Chamara.

**Paper D** Modelling of anisotropic elastic properties in alloy 718 built by electron beam melting.

**Chamara Kumara**, Donyong Deng, Johan Moverare & Per Nylén

Published in *Materials Science and Technology*, 34:5, 529-537.

DOI: [10.1080/02670836.2018.1426258](https://doi.org/10.1080/02670836.2018.1426258)

Author's contributions: Principle author of the paper and the idea originator for the modelling work. Modelling and analysis work was performed by Chamara.



## Related work

The following papers are not appended but are related to the objective of this thesis work.

- **On the Microstructure of Laser Beam Powder Bed Fusion Alloy 718 and Its Influence on the Low Cycle Fatigue Behaviour,**  
Arun Ramanathan Balachandramurthi, Nitesh Raj Jaladurgam, **Chamara Kumara**, Johan Moverare, Thomas Hansson, Johannes Gårdstam, Robert Pederson  
Published in *Materials* 2020, 13, 5198.  
DOI: [10.3390/ma13225198](https://doi.org/10.3390/ma13225198)



# Table of contents

Acknowledgements .....	iii
Populärvetenskaplig Sammanfattning .....	vi
Abstract .....	ix
Appended publications and author's contributions .....	xi
Related work.....	xiv
Table of contents.....	xv
Acronyms.....	xvii
Nomenclature.....	xix
<b>1 Introduction .....</b>	<b>1</b>
1.1 Additive manufacturing.....	1
1.2 Challenges in metal AM .....	2
1.3 Outline of the thesis .....	3
<b>2 Objectives, research questions, scope, and limitations ..</b>	<b>5</b>
2.1 Objectives and research questions .....	5
2.2 Scope and limitations.....	6
<b>Part 1 .....</b>	<b>7</b>
<b>3 Multiphase-field modelling of additive manufacturing of Alloy 718 .....</b>	<b>7</b>
3.1 Microstructure modelling and simulations in additive manufacturing.....	9
3.1.1 Transformation kinetics modelling .....	10
3.1.2 Mean field modelling .....	11
3.1.3 Cellular automata modelling.....	11
3.1.4 Phase-field modelling .....	12
3.2 Processes.....	15
3.2.1 Laser metal directed energy deposition .....	15
3.2.2 Electron beam powder bed fusion .....	16
3.3 Alloy 718.....	20
3.3.1 Background .....	20

3.3.2 Non-equilibrium solidification .....	22
3.4 Microstructure modelling work .....	25
3.4.1 Phase-field model in MICRESS.....	25
3.4.2 Model setup in MICRESS related to LMP-DED .....	31
3.4.3 Model setup in MICRESS related to EB-PBF .....	35
3.4.4 Assumptions, simplifications, and limitations .....	37
3.5 Transformation diagram prediction .....	39
3.6 Experimental work.....	41
3.6.1 Experimental work related to LMP-DED ( <i>Paper B</i> ).....	41
3.6.2 Experimental work related to EB-PBF ( <i>Paper C</i> ).....	42
3.7 Results and discussion.....	45
3.7.1 Laser metal directed energy deposition .....	45
3.7.2 Electron beam powder bed fusion.....	60
3.7.3 Critical discussion of the modelling results.....	65
<b>Part 2 .....</b>	<b>69</b>
<b>4 Elastic property modelling of AM Alloy 718 .....</b>	<b>69</b>
<b>5 Summary and conclusions .....</b>	<b>71</b>
<b>6 Future work .....</b>	<b>73</b>
<b>7 Bibliography .....</b>	<b>75</b>
<b>Appended Papers.....</b>	<b>89</b>

## Acronyms

2D	Two dimensional
3D	Three dimensional
AD	As deposited
AM	Additive manufacturing
APB	Anti-phase boundary
ASTM	American society for testing materials
CAD	Computer aided design
CCT	Continuous-cooling-transformation
CNC	Computer numerical control
CT	Computer tomography
DA	Direct aged
EB-PBF	Electron beam powder bed fusion
HIP	Hot iso-static pressing
HT	Heat treatment
LB-PBF	Laser beam powder bed fusion
LM-DED	Laser metal directed energy deposition
LMP-DED	Laser metal powder directed energy deposition
PDAS	Primary dendrite arm spacing
PF	Phase-field
TTT	Time-temperature-transformation



## Nomenclature

Symbol	Definition	Units
$\phi_\alpha$	Phase-field variable corresponding to phase $\alpha$	-
$\alpha, \beta, ..$	Indices for phases	-
$i, j, ..$	Indices for solutes	-
$v$	Total number of phases	-
$n$	Total number of solutes	-
$\vec{x}$	Position vector	m
$t$	Time	s
$\vec{C}$	Concentration vector	mole/m <sup>3</sup>
$C^i$	Components of the concentration vector that related to the concentration of the solutes	mole/m <sup>3</sup>
$\vec{C}_\alpha$	Concentration vector of phase $\alpha$	mole/m <sup>3</sup>
$C_\alpha^i$	Components of the concentration vector of phase $\alpha$ that related to the concentration of the solutes	mole/m <sup>3</sup>
$F$	Total free energy functional of the multiphase, multicomponent system and	J
$f$	Free energy density function	J/m <sup>3</sup>
$f^{int}$	Interfacial free energy density of $f$	J/m <sup>3</sup>
$f^{th}$	Thermodynamic free energy density of $f$	J/m <sup>3</sup>
$f_\alpha$	Free energy density of phase $\alpha$	J/mol
$\sigma_{\alpha\beta}^0$	Interfacial energy between phase $\alpha$ and $\beta$	J/m <sup>2</sup>
$a_{\alpha\beta}^\sigma$	Anisotropy function for interfacial energy between phase $\alpha$ and $\beta$	-
$\eta$	Numerical interface thickness	m
$\delta_\sigma$	Interfacial stiffness coefficient	-
$\delta_M$	Interfacial mobility coefficient	-
$\theta$	Crystallographic orientation in 2D	rad
$\tilde{\mu}^i$	Diffusion potential of component $i$ in multiphase mixture kinetic	J/m <sup>3</sup>
$\tilde{\mu}_\alpha^i$	Diffusion potential of component $i$ in phase $\alpha$	J/m <sup>3</sup>
$\mu_\alpha^i$	Chemical potential of component $i$ in phase $\alpha$	J/mol
$M_{\alpha\beta}$	Phase-field mobility of the $\alpha$ and $\beta$ interface	m <sup>4</sup> /Js

$a_{\alpha\beta}^M$	Anisotropy function for phase-field mobility of the $\alpha$ and $\beta$ interface	-
$M^{ij}$	Multiphase chemical mobility coefficient	$\text{mol}\cdot\text{m}^2/\text{Js}$
$\mathbf{M}_{\alpha}^{ij}$	Chemical mobilities of solutes in phase $\alpha$	$\text{mol}\cdot\text{m}^2/\text{Js}$

# 1 Introduction

## 1.1 Additive manufacturing

Additive manufacturing (AM) is a manufacturing process in which the component is formed by a layer-by-layer approach based on a 3D model (from a CAD model). AM is also known as 3D printing, rapid manufacturing, rapid prototyping, or freeform fabrication. AM has recently received special interest in the field of manufacturing because of its attractive features compared with conventional manufacturing methods such as casting, shaping, and machining. Examples in this context include the ability to produce near-net-shape complex parts, low cost of retooling, and the possibility of changing the microstructure during processing [1]. The type of energy source that is used to melt the material in AM can be an arc, laser, or electron beam. The material can, for instance, be a metal, ceramic, or polymer, which can be in the form of a powder, wire, or sheet. The interest in producing parts by AM in metallic materials has significantly increased over the previous decade. The technique has attracted both industrial and scientific communities as a result of its broad applications and research potential.

AM is widely used in high-value low-volume manufacturing industries, such as aerospace, biomedical implants, and tool manufacturing. AM is also interesting for sustainability reasons because, in comparison with conventional manufacturing, it reduces material waste. Conventional manufacturing methods such as casting and forging, as well as subtractive manufacturing methods, also impose limitations on design engineers. AM offers designers greater freedom, resulting in the creation of new types of designs with high strength and low weight. One example of a metal product that has utilised this ability is a redesigned fuel nozzle manufactured by GE aviation for the 'LEAP' engine in 2016 [2]. The new nozzle, which is a single part, has several advantages. It provides a better fuel flow geometry, which results in higher combustion efficiency (15%) compared with that of the previous design, which was fabricated by welding and brazing 20 separate parts together. Additionally, the new design is five times stronger and 25% lighter than the previous nozzle. In the aerospace sector, fabrication of components by AM can significantly reduce the buy-to-fly ratio, that is, the weight ratio between the raw material used for a component and the weight of the component itself. In traditional subtractive manufacturing, the buy-to-fly ratio can be as high as 20:1, which results in large material wastage. AM has the ability to produce near-net-shape structures, thus reducing this ratio to nearly 1:1 [3, 4]. AM has also been shown to be a viable method for repairing worn out components in the aerospace industry and to reduce resource usage, costs, and

repair time. In biomedical implant production, AM makes it possible to produce patient-specific implants directly from a CAD model generated from scanned data, thus reducing manufacturing cost, time, and material wastage. Moreover, AM is quite interesting for tool manufacturing. Tools can be generated with custom cooling channels and added functionality; examples include an integrated chip breaker in a machine tool design. To summarise, AM can enable cheaper, more flexible, and more sustainable manufacturing; it is especially interesting for high-value low-volume manufacturing industries.

## **1.2 Challenges in metal AM**

Although AM has gained significant attention, several challenges must be overcome for AM to be used in industrial production more effectively. In particular, the AM of metallic components is a complex process that involves numerous process parameters. During manufacturing, the building material undergoes solidification and thermal cycling because of the layer-upon-layer building process. This causes complex thermal conditions that drive phase transformation from liquid to solid as well as phase transformation in solid-state. In addition, post-treatment, such as hot isostatic pressing (HIP) and heat treatment, causes further changes in the material. These material changes can significantly modify the functional performance of the component. Consequently, obtaining products with the desired quality and performance by AM is not a straightforward task. Thus, it is important to identify the effect of these thermal conditions on the microstructure and how these microstructures affect the functional performance and quality of the printed parts. Understanding these relationships will also make it possible to optimise the AM microstructures for desired applications. However, this is not a simple task. The number of variables (both process- and material-related) that affect the local thermal conditions in an AM build can be very high. Experimental process optimisation will thus be time-consuming and costly. Computational modelling and simulation is an interesting alternative approach that can be of high value for the AM community, as it helps to reduce the number of trial and error style experiments. In addition, modelling and simulation can be a powerful tool to gain a deeper understanding of the process, thus making it possible to provide insight into complex process phenomena that might be impossible to gain experimentally [5]. Furthermore, modelling and simulation can create an accelerated path for process optimisation [6].



## 1.3 Outline of the thesis

The work presented in this thesis is divided into two parts. The first part, which is the main focus of this thesis, is related to the multiphase-field modelling work that was used to understand the relationship between the thermal conditions and microstructure formation during AM and the subsequent heat treatment related to Alloy 718. This is given in *Chapter 3*. The work presented in ***Paper A, B*** and ***C*** is related to this.

The second part is related to the modelling work that reveals the relationships between the AM microstructure and the elastic properties. As the second part is not the core focus of the thesis, only a summary will be given in this thesis in *Chapter 4*. For more details, the reader is referred to the appended ***Paper D***.

Note: This thesis is an extension of the author's Licentiate thesis "*Microstructure Modelling of Additive Manufacturing of Alloy 718*" [7]. However, some contents have been modified and updated in the present thesis. Additionally, some similarities can be found between the text and images in this thesis and the text and images in the appended Papers [8–11].



## **2 Objectives, research questions, scope, and limitations**

### **2.1 Objectives and research questions**

- 1) The main objective of this thesis work was to utilise a modelling approach to gain an understanding of the relationships between thermal conditions and microstructure formation during AM and the subsequent heat treatment related to Alloy 718.

The modelling work was accomplished by trying to answer the following research questions.

**RQ1 How can the microstructure evolution during additive manufacturing and subsequent heat treatments be modelled based on the thermal conditions?**

**RQ2 How do these thermal conditions affect the microstructure formation during the additive manufacturing and subsequent heat treatments?**

**RQ3 How does the segregation of elements that occur during solidification affect the phase transformation kinetics?**

- 2) The second objective of this work was to utilise a modelling approach to understand the relationship between the elastic properties and AM microstructure in Alloy 718.

The modelling work was accomplished by trying to answer the following research questions.

**RQ4 How can the elastic properties be predicted based on the microstructure?**

## 2.2 Scope and limitations

- **Process:** The work was focused on laser metal powder directed energy deposition (LMP-DED) and electron beam powder bed fusion (EB-PBF) AM processes and the following post-heat treatment processes.
- **Material:** The material used in this study was limited to the nickel–iron-based superalloy Alloy 718.
- **Phase:** Only the formation of  $\gamma$  (matrix),  $\gamma'/\gamma''$  (strengthening phases), Laves, and  $\delta$  phases during the solidification and solid-state phase transformation were considered.
- **Elastic property modelling:** Only the crystallographic orientation of the matrix in the hatch (bulk) region was considered.

## **Part 1**

### **3 Multiphase-field modelling of additive manufacturing of Alloy 718**

In this section, the work related to the main objective of this thesis is given, which is the multiphase-field modelling work. This chapter is structured as follows:

- Literature review related to microstructure modelling of AM (*Section 3.1*).
- A short background of the two AM processes used in this thesis (*Section 3.2*).
- A short overview of Alloy 718 and its phases (*Section 3.3*).
- Model implementation in MICRESS (*Section 3.4*).
- Modelling work using JMatPro (*Section 3.5*).
- Experimental work related to MICRESS (*Section 3.6*).
- Results and discussion (*Section 3.7*).

*Papers A, B, and C* are related to the multiphase-field and JMatPro modelling work.



# 3.1 Microstructure modelling and simulations in additive manufacturing

Most of the computational modelling efforts that are currently undertaken in AM are related to process modelling (thermal and/or mechanical). The primary goals of these AM process models are to predict the melt pool shape, spatial time-temperature variation, interface dynamics, and to determine the defect formation and stress build up [1,12]. Because of the difficulties in measuring these quantities experimentally, process models can serve as a powerful tool to obtain these quantities. These parameters can then be used as input conditions to model the microstructure during the process. Compared with the published literature related to process modelling, number of publications related to microstructure modelling in the context of AM are still low.

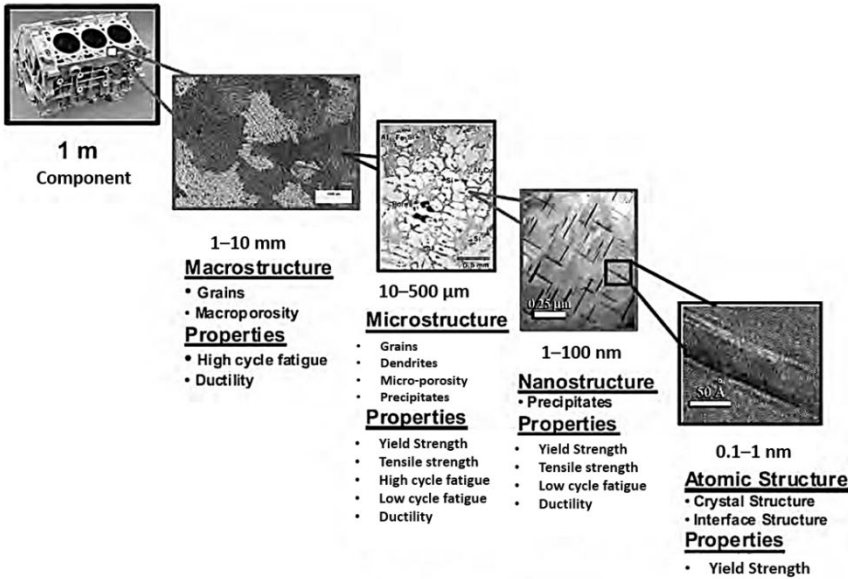


Figure 1: Different metallurgical length scales that dominate properties and behaviours. Adapted from [13]

The field of microstructure modelling itself is a very broad field. The modelling length scale can range from modelling the atomic interaction of a metallic system to modelling at the scale of component-level grain structures [14–16]. The material structures at multiple length scales influence the properties of the material (see **Figure 1**) [13]. The material models thus need to describe phenomena on each of these different length scales. Therefore, different types of models are used by researchers, depending on the length scale of the problem and

the intended outcome. In the following sections, some microstructure models that are widely used in AM are discussed.

### 3.1.1 Transformation kinetics modelling

The Johnson–Mehl–Avrami–Kohnogorov (JMAK) method is a modelling method that attempts to calculate the solid-state phase transformation based on the overall transformation kinetics (nucleation and growth) of phase transformation of a specific alloy at a constant temperature [17]. Using appropriate additive principles [18] and considering time–temperature–transformation diagrams (TTT) as material data inputs, this method has been used to predict the extent of phase formation during the AM process with respect to time and space [19, 20].

Though this modelling method is computationally efficient, it can only be used to model the transformation of one parent phase into one product phase, due to the formulation of the model. This is a limitation when it comes to model phase transformation in Alloy 718, as this alloy tends to have multiple phase transformations simultaneously (see *section 3.3*). To model the decomposition of one parent phase into several product phases at the same time, the simultaneous transformation kinetics (STK) model developed by Jones and Bhadeshia [21] can be used. The authors developed the STK model to describe the decomposition of austenite into several ferrite morphologies in steel using the JMAK model as the basis. Later, this model was applied to Alloy 718 by Makiewicz [22] to predict the  $\gamma'/\gamma''$  phase fraction evolution during the laser metal directed energy deposition process. The remaining phases possible in 718 were disabled for this run due to a lack of quantification and parameters. The actual shape of the phases was not taken into consideration, i.e., they were modelled as spheres. Additionally, the effect of element segregation during solidification and precipitate dissolution caused by diffusion during heating were not considered in this STK model.

In this thesis work, JMatPro [23] software was used to predict the 0.5% transformation TTT diagrams and continuous cooling transformation (CCT) diagrams. In this context, JMatPro uses the JMAK equation as the basis. In JMatPro, this equation has been modified to include the effect of non-spherical particles [24]. Where empirical values are used, for example, shape and nucleation density, particular values have been specified for the various precipitates in each material type [25]. Using additive principles [13], the TTT curves are converted to CCT curves.



### 3.1.2 Mean field modelling

Mean field modelling [26, 27] provides a useful method to reduce a problem with a large number of particles to a one-particle problem. This requires approximating the precipitate morphology by simple geometry and using mean values to describe the chemical concentration within the particle, matrix, and at the particle–matrix interface. The two state variables are particle size and number density; together, they define the particle size distribution. Within this framework, the key models are nucleation (source of new particles), growth (particle size changes) under the mean field, continuity (time evolution of particle size distribution), and mass balance. Therefore, this modelling method allows us to model the nucleation, growth, and coarsening of precipitates in multicomponent systems with the help of thermodynamic databases [27–29]. The commercial software packages TC-PRISMA [30] and MatCalc [31] are based on this mean field approach.

Several authors [27, 29, 32, 33] have used the mean field method to model the precipitation in AM of nickel-based superalloys during the process and/or subsequent heat treatments. However, it should be noted that in their work, the authors have modelled only solid-state precipitation because of the nature of the model implementation. No phase transformation during the solidification of the liquid and element segregation was modelled. Even though the work presented in [29, 33] modelled the effect of element segregation on phase precipitation using the local segregated compositions from the solidification simulation using DICTRA [34], neither simulation accounts for any homogenisation that occurs during post-build heat treatments. This limits the prediction of phase transformation at elevated temperatures, where back diffusion, nucleation, growth, and dissolution can take place simultaneously.

### 3.1.3 Cellular automata modelling

Cellular automata (CA) modelling is another widely used method for simulation of solidification and recrystallisation, as well as grain growth [14, 35]. The CA model requires rules that govern the transition from solid to liquid, from liquid to solid, and setting of crystallographic orientation, speed, and orientation of capturing neighbouring cells for crystal growth. CA follows the rules of solidification theory as well as some probability elements for nucleation. Although the original formulation of CA is to predict grain growth by excluding dendritic structures, advancements have been made by coupling CA with solute diffusion numerically to model dendritic structures [36–38]. In CA, the relationship between the undercooling and growth velocity of the interface is approximated

by a polynomial law. However, recent CA coupled phase-field (PF) models are capable of predicting this growth relationship at the solidification front using the coupled PF method [39]. One common application of CA is related to the prediction of grain structure evolution. Because these predictions provide information about grain size, their distribution, and orientation, one can use these predictions as inputs for crystal plasticity modelling to predict mechanical properties [40].

Several authors have used CA [41–49] to predict the macroscopic grain evolution (from liquid to solid) during AM without considering solute diffusion. The results indicate that the modelling method can be used to qualitatively understand the grain structure evolution during the AM process under various solidification conditions. Works by Koepf et al. [44, 47], show the applicability of CA for predicting grain evolution at the component level (3D). However, their model was not able to capture the nucleation of random grains during the epitaxial growth of the bulk grains in the component. Nie et al. [50] used a 2D CA model coupled with solute diffusion to model the microstructure growth at dendritic scale in Alloy 718 by assuming that Alloy 718 is a Ni–Nb system. Liu and Shin [51] used a 2D CA-PF model to predict the microstructure evolution in AM of Ti–6Al–4V. The 1-D PF component in the model provides the CA component with growth kinetics, including the growth velocity in the solidification front and the equilibrium solute partition at the liquid/solid interface. The 2D CA component in the model calculates the dendrite growth and solute redistribution based on the increment of the solidified fraction in the CA interface cells. Moreover, the PF model is improved by coupling the thermodynamic and solute mobility data of the Ti–Al–V system.

### 3.1.4 Phase-field modelling

Phase-field modelling was utilised in this thesis work to model the evolution of the microstructure. This method has been widely used to simulate microstructure evolution during solidification and solid-state phase transformations [52–57]. There are a wide variety of PF models in the literature; however, they are all based on the diffuse interface description. In the diffusive interface, the PF variable varies smoothly between the two phases. Therefore, in the PF method, the interface will be a part of the solution, i.e., there is no need to track the interface as in the classical sharp interface modelling methods [54, 55, 58]. This permits the handling of complex multi-dimensional patterns such as dendritic morphologies, which are characteristic of solidification processes. The use of a diffuse interface in material science dates back to van der Waals [54], who modelled a liquid–gas system using a density function that varies continuously at the gas/liquid interface more than a century ago. Ginzburg and Landau in 1950 [59] formulated a model

for superconductivity using a complex valued order parameter and its gradients at the diffuse interface. In 1958, Cahn and Hilliard [60] proposed a thermodynamic formulation that considered gradients in thermodynamic quantities in heterogeneous systems with diffuse interfaces. The PF model developed by Ryo Kobayashi [61] in 1993 to model the dendritic growth of a pure substance in an undercooled melt is considered the pioneering work in the context of solidification simulation using a diffuse interface approach.

There are two types of PF variables: conserved and non-conserved [62]. The conserved PF variables (e.g., local composition) must satisfy the local conservation condition. The temporal evolution of the conserved PF variables is obtained using the Cahn–Hilliard [62] equation (*Eq. 3.1*). In this equation,  $\vec{x}$  is the position,  $t$  is time,  $M_{ij}$  is the diffusivities of the species ( $i$  and  $j$ ),  $F$  is the total free energy density of the system, and  $c_i$  are the conserved variables.

$$\frac{\partial c_i(\vec{x}, t)}{\partial t} = \nabla M_{ij} \nabla \frac{\delta F}{\delta c_j(\vec{x}, t)} \quad (3.1)$$

The other type of PF model involves the use of non-conserved PF variables (also known as order parameters). These variables are introduced to distinguish the coexisting phases (with different structure) in the system. The introduction of this order parameter will give an extra degree of freedom, in addition to the alloy composition and temperature. The introduction of the order parameter is an advantage, as it allows for non-equilibrium processes. This is important because most of the technical processes are far from thermodynamic equilibrium, and they involve curvature and kinetic undercooling and supersaturation. The temporal evolution of these non-conserved order parameters is obtained using the Ginzburg and Landau equations (*Eq. 3.2*; also known as Allen–Cahn equation) [62]. In this equation,  $L_{pq}$  is the mobility of the non-conserved variables,  $n_p$ .

$$\frac{\partial n_p(\vec{x}, t)}{\partial t} = -L_{pq} \nabla \frac{\delta F}{\delta n_q(\vec{x}, t)} \quad (3.2)$$

The main differences between the PF models that exist in the literature are primarily results of the treatment of various contributions to the total free energy density,  $F$ .

The PF method was initially developed for pure and binary systems. Later in 1996, this was extended to multicomponent and multiphase systems by I. Steinbach et al. [57]. This model laid the foundation for the multiphase-field model

implemented in the MICRESS software that was used in this thesis work. *Section 3.4.1* will further outline the details of the model implementation in MICRESS.

PF modelling has recently been introduced in the field of AM [56, 63–67]. Sahoo et al. [56] used PF modelling to investigate the effect of thermal gradients and beam scan speed on the microstructure formation during the manufacturing of Ti–6Al–4V in EB-PBF. It was shown that the columnar dendritic spacing and width of the dendrites decrease with an increase in the temperature gradient and beam scan speed. Acharya et al. [63] used the PF modelling approach to model the microstructure evolution during the manufacturing of Alloy 718 using the laser powder bed fusion process. Here, Alloy 718 was modelled as a Ni–Nb binary system. The model was used to predict different features in the microstructure, such as element segregation, dendrite size, dendritic orientation, and dendritic morphology. In [59] and [60], PF modelling was used to investigate the formation of Nb-rich droplets that formed during the laser powder bed fusion process of a Ni–Nb alloy. Kundin et al. [66] investigated the effect of growth velocity during the laser powder bed fusion process on the concentration profile for Alloy 718 using a multiphase-field approach. It was found that the maximum tip velocity during the solidification process became slower than in the steady state. Karayagiz et al. [68] recently adopted the finite interface dissipation PF model proposed by Steinbach et al. [69] to model the Ni–Nb binary alloy under laser beam powder bed fusion process conditions. This model is capable of accounting for the velocity dependent element partitioning. They used the model to simulate the different solidification morphologies observed in the single-track experiments. Such a model (finite interface dissipation PF model) is important if the solidification velocities are in the regime of solute trapping.

## 3.2 Processes

### 3.2.1 Laser metal directed energy deposition

LM-DED is a type of AM process that enables the production of components by melting the material as it is being deposited. This approach can be used for ceramics, polymers, and metal matrix composites [70]. In this process, laser beam energy is directed and focused into a narrow region, melting both the substrate and the feedstock material [70] [71]. The feedstock material can be in either powder or wire form. Each deposition pass of the LM-DED produces a track of solidified material, and depositing multiple tracks together creates a 3D geometry. The deposition is controlled by either moving the heat source and/or moving the substrate. In a three-axis system, the motion is controlled by the movement of the deposition heat source, whereas in a four- or five-axis system, both the deposition heat source and the substrate are moved. Typically, a computer numerical control (CNC) machine or a robot arm is used for this purpose. The most common lasers used in LM-DED are diode lasers (semiconductors), CO<sub>2</sub> lasers (molecules), and Nd: YAG lasers (solid state). In the industry, LM-DED is also referred to as laser engineered net shaping (LENS), directed light fabrication (DLF), direct metal deposition (DMD), 3D laser cladding, laser-based metal deposition (LBMD), laser freeform fabrication (LFF), and others based on the manufacturer of the equipment [70]. Though the approach is almost the same, the differences between these machines generally include changes in laser power, laser spot size, laser type, powder delivery method, inert gas delivery method, feedback control scheme, and/or the type of motion control utilised [70].

This method has become popular as a repair method for corroded and worn gas turbine components because the parts can be repaired with minimal distortion and dilution [72]. The method is also used as a technique to build small components or add features to, for instance, cast components and thus add complexity to products [1]. This makes it possible to reduce the cost of direct-casting components with complex features. The layer-by-layer material deposition results in repeated heating and cooling of the deposited material when subsequent layers are deposited. Depending on the nature of the thermal conditions (such as cooling rate, thermal gradient, maximum temperature, and number of thermal cycles), the material will undergo liquid to solid as well as solid-state phase transformation. Studies have shown that these phenomena will influence the microstructural changes and consequently affect the mechanical properties [72–77]. Unlike in the EB-PBF process, post treatment by hot isostatic pressing (HIP) is not commonly used for LM-DED components. One reason is that this will alter the microstructure of the substrate material, which has already been tailored

for the desired application. The local post-heat treatment, that is, heat treatment of only the geometry that was built, is a solution to this problem.

### 3.2.2 Electron beam powder bed fusion

EB-PBF is a type of powder bed AM technique that was first commercialised in 1997 by Arcam Corporation in Sweden. In the EB-PBF process, an electron beam is used to selectively melt the material using a layer-by-layer approach. EB-PBF has some unique features with respect to the manufacturing of biomedical implants and high-performance components used in aerospace and high-temperature applications. Faster deposition rates resulting from high beam energy and speed, lower residual stresses, the possibility of tailoring the microstructure [78–80], and reduced problems with oxidation are some of the advantages of the EB-PBF process [81]. However, because of the inherent nature of the process, the semi-sintered powder becomes difficult to remove in complex geometries. The components that are manufactured by EB-PBF have higher surface roughness compared with those manufactured by laser beam powder bed fusion (LB-PBF) and thus might require post-treatment.

**Figure 2** shows a schematic representation of the main components of an EB-PBF machine and the building process cycle. The electron beam unit of the machine comprises the electron generating part and the magnetic lenses used to control the beam. The principle of the electron gun is similar to that of the system that can be found in an electron microscope. The heated cathode filament emits electrons in the upper column, as shown in the top image. The potential difference between the cathode and anode is approximately 60 kV. The beam current capacity is usually in the range of 1–50 mA [82]. The shape and deflection of the electron beam are controlled by magnetic lenses in the lower part of the electron gun unit. The astigmatic lenses correct the beam shape, whereas the focus lenses control the size of the beam. The beam position on the build plate is controlled by the deflection lenses. The operation of the EB-PBF process takes place in the so-called ‘controlled vacuum’ environment. In this condition, a small helium pressure of  $10^{-3}$  mbar is applied to prevent the build-up of electrical charges in the powder and to ensure thermal stability [82, 83]. Helium is used because it has less interference with the electron beam as a result of its smaller atom size. The build chamber of the machine consists of a steel build tank, powder feeder hoppers, and a raking system. The build tank contains a build plate on which the component is being printed. This plate can move parallel to the vertical axis of the electron gun unit. This movement depends on the layer thickness of the build geometry. The two powder-feeding hoppers contain the metallic powder that is used as the build material. The rake controls and distributes the powder on the build plane by taking powder from both sides.

## PROCESSES

Based on the CAD data, the component is built through a layer-by-layer approach, as shown schematically in **Figure 2**. The major steps involved in this process are as follows:

1. Build plate heating before applying the first layer. The preheating temperature is slightly above the building temperature.
2. Distribution of powder onto the start plate (raking).
3. Preheating of the powder by an electron beam. This has two main purposes: first, to deliver energy to maintain the temperature within the building volume. Second, to sinter the powder to avoid surface charge accumulation on powder particles and thus the ‘smoking’ effect. During preheating, the build area is scanned several times using a defocused electron beam at high speed. The preheating temperature will depend on the material used for the process. The preheating temperature is approximately 300 °C for pure copper [84], whereas it is approximately 1100 °C for intermetallic species [85]. For Alloy 718, this value is approximately 1025 °C.
4. Melting of the powder layer according to the sectioned CAD geometry data. First, the contour part of the 2D section is melted; then, the interior bulk (called “hatched”) area is melted.
5. Lowering of the build platform by the desired value based on the powder layer thickness.
6. Repetition of step 2 to step 5 until the build is completed.
7. Cooling of the component down to room temperature after the build sequence is complete. The cooling process can be accelerated by injecting helium into the build chamber. As a result of the sintering of the powder during pre-heating, the build component will be embedded inside the sintered powder bed. Therefore, sandblasting using the same powder is used to remove the sintered powder. The recovered powder can be recycled and reused.

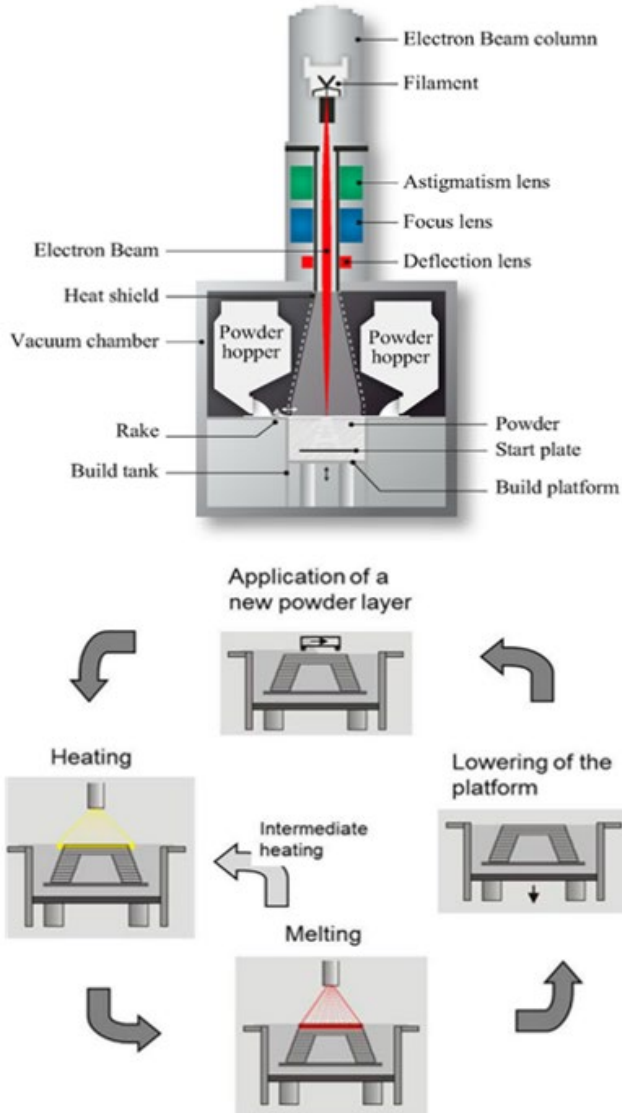


Figure 2: Schematic representation of the Arcam EB-PBF Machine [83] (reprinted with permission) and its building process cycle [82].

Once the build is complete, the component is recovered from the sintered powder bed. Additionally, the support structures that are added to the component must be removed. Furthermore, the EB-PBF build component will be subjected to necessary post-treatments such as surface modification, hot isostatic pressing



## PROCESSES

(HIP), or heat treatment cycles. The as-built surface of the EB-PBF component has a comparatively rough surface because of the sintering of powder particles at the surface of the component. To reduce the surface roughness, machining can be used, but it is limited by the complexity of the geometry. HIP is commonly performed to reduce the porosity inside the microstructure of the as-built component. The temperature condition in the HIP also helps to dissolve the microstructure heterogeneity in the as-built component. To obtain the desired mechanical properties, suitable post-heat treatments are commonly performed.

## 3.3 Alloy 718

### 3.3.1 Background

Alloy 718 is a nickel–iron-based superalloy. It has been extensively used in rocket motors, aircraft engines, nuclear reactors, and pumps [86]. The main reasons for its success are its relatively low cost, good mechanical properties, and corrosion properties at low and intermediate temperatures [87, 88]. However, its use in load-bearing components for elevated-temperature applications is limited to 650 °C because of the strength loss beyond this temperature [89]. The composition of Alloy 718 is complex and involves multiple alloying elements, which are added to obtain the desired microstructure and properties. The nominal composition ranges for the alloy, according to the ASTM standard, and their effect on the microstructure are presented in **Table 1**. The Alloy 718 microstructure is dominated by a face-centred cubic (FCC)  $\gamma$  matrix, wherein precipitates such as  $\gamma'/\gamma''$  (strengthening phases),  $\delta$ , Laves, MC carbides, and nitrides can be found [90]. The crystal structure and representative chemical formula of these commonly observed phases are presented in **Table 2**. In this alloy, the  $\delta$  phase is the equilibrium phase of metastable  $\gamma''$ . When the alloy is subjected to temperatures above 650 °C,  $\gamma''$  will dissolve and  $\delta$  will begin to precipitate. The exact microstructure (phase composition, phase distribution, morphology, and volume fraction) of this alloy is governed by the primary manufacturing technology and successive post heat treatments conditions. **Figure 3** shows the reported phase precipitation windows for Alloy 718. It can be seen that there is an overlap between the  $\delta$  and  $\gamma'/\gamma''$  precipitation windows. Although  $\delta$  is thermodynamically more stable than  $\gamma''$ ,  $\delta$  precipitation up to ~900 °C is always preceded by metastable  $\gamma''$  precipitation [91, 92].

*Table 1: ASTM standard for Alloy 718 composition (wt%) [93] and the effect of the alloying elements [94 , 95]*

Element	Min	Max	Effect
Nickel	50.0	55.0	FCC matrix stabilisation, TCP phase precipitation inhibition
Iron	Bal.		
Chromium	17.0	21.0	Solid-solution strengthening, improved hot-corrosion resistance
Molybdenum	2.80	3.30	Solid-solution strengthening

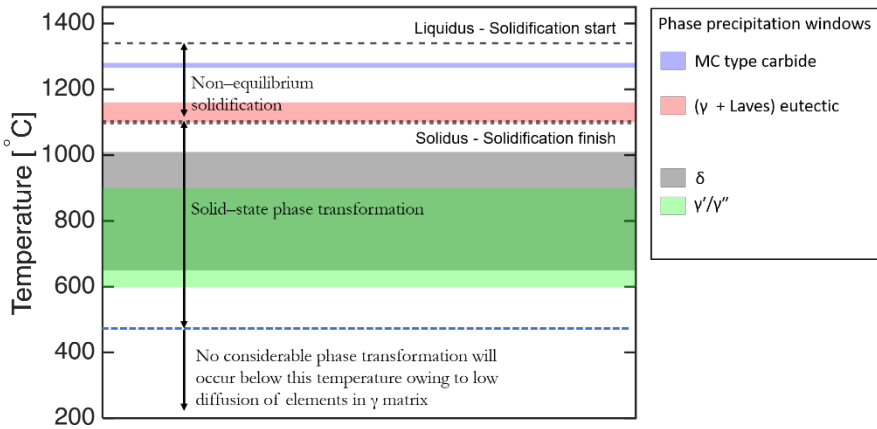
<b>Niobium + Tantalum</b>	4.75	5.50	$\gamma''$ , NbC carbide, $\delta$ -Ni <sub>3</sub> Nb, and TaC carbide precipitation
<b>Titanium</b>	0.65	1.15	$\gamma'$ precipitation
<b>Aluminium</b>	0.20	0.8	$\gamma'$ precipitation, retarded formation of $\eta$ (Ni <sub>3</sub> Ti)
<b>Cobalt</b>	-	1.0	Higher solvus temperature of $\gamma'$
<b>Copper</b>	-	0.3	
<b>Manganese</b>	-	0.35	
<b>Phosphorus</b>	-	0.015	Improved carbide precipitation
<b>Silicon</b>	-	0.35	
<b>Sulphur</b>	-	0.015	
<b>Boron</b>	-	0.006	Improved creep strength and ductility
<b>Carbon</b>	-	0.08	MC formation

Table 2: Commonly observed phases in Alloy 718

Phase	Representative formula	Crystal structure
$\gamma$	N/A	FCC
$\gamma'$	Ni <sub>3</sub> (Al, Ti)	FCC (ordered L1 <sub>2</sub> )
$\gamma''$	Ni <sub>3</sub> Nb	BCT (ordered D0 <sub>22</sub> )
$\delta$	Ni <sub>3</sub> Nb	Orthorhombic (ordered D0 <sub>a</sub> )
<b>Laves</b>	(Ni, Fe,Cr) <sub>2</sub> (Nb,Mo,Ti)	Hexagonal (C <sub>14</sub> )
<b>MC</b>	NbC, TiC	Cubic (B <sub>1</sub> )

### 3.3.2 Non-equilibrium solidification

During solidification processes, such as casting, welding, and AM, Alloy 718 tends to form a dendritic/cellular microstructure [75, 90, 96, 97], the length scale of which varies according to the solidification conditions [75, 98]. Knorovsky et al. [88] and Antonsson et al. [99] experimentally investigated the solidification sequence for Alloy 718. As the temperature drops in the liquid (L) melt, the  $L \rightarrow \text{TiN}$  transformation first occurs above the liquidus temperature. The resulting TiN particles occasionally act as nucleation sites for carbide precipitation at a later stage during solidification [99]. However, in the context of AM, TiN can also be present via the feedstock material and could remain unmelted during the melting process because of its higher melting point (2930 °C) [100].



*Figure 3: Phase precipitation windows ([88, 90, 99]) in Alloy 718 during non-equilibrium solidification and in solid-state phase transformation. It should be noted that even though the liquidus and solidus lines are shown as constant, these could also change depending on the nominal composition of the alloy. (from **Paper A**, reprinted with permission)*

When the temperature drops below the liquidus, solidification of the primary  $\gamma$  phase occurs. Because of their low solubility in the matrix, Nb and C are continuously rejected into the liquid. As the matrix grows, the Nb and C compositions in the liquid reach a level that enables NbC formation. This reaction consumes Nb and the majority of C in the remaining liquid, shifting the remaining liquid composition back to a lower level. As  $\gamma$  phase grows further, the segregation of Nb in the remaining liquid prompts another eutectic reaction,  $L \rightarrow \gamma + \text{Laves}$ , which terminates the solidification process. This is referred to as non-equilibrium solidification (see **Figure 3**).

During the solidification of the  $\gamma$  matrix, microsegregation of alloying elements is typically observed [90]. This is because the solubility of the alloying elements in the matrix phase is different from that in the liquid. Elements such as Nb, Mo, and Ti, which have a low solubility limit in the matrix, tend to segregate to the liquid. Elements such as Cr, Fe, and Al, which have a high solubility limit in the solid, tend to be trapped in the solid (see **Figure 11**). This segregation alters the local thermodynamics of Alloy 718 (see **Figure 12**) and is hence the driving force for phase formation. This is the reason for the formation of Laves and NbC in the interdendritic liquid region during solidification. In the context of AM of Alloy 718, the formed primary carbides and nitrides during non-equilibrium solidification do not change (in terms of size and distribution) noticeably at low temperatures because of their stability at these temperatures.



## 3.4 Microstructure modelling work

This section offers the reader a description of the microstructure modelling work related to the present study. The chapter begins with a brief overview of the multiphase-field model that is implemented in the MICRESS software (the software used in this work) is provided. In addition, this chapter contains more detailed information regarding how the microstructure models were set up to predict the microstructure evolution during the EB-PBF and LMP-DED processes and the subsequent post-heat treatments.

### 3.4.1 Phase-field model in MICRESS

The PF simulations in this work were performed using the commercially available software MICRESS (version 6.4, Access e.V., Aachen, Germany). MICRESS is based on the multiphase-field approach [58, 63]. The multiphase-field theory describes the evolution of the multiple PF parameters  $\phi_{\alpha=1,2,\dots,v}(\vec{x}, t)$  in space,  $\vec{x}$ , and time,  $t$ , with the constraint  $\sum_{\alpha=1}^v \phi_{\alpha}(\vec{x}, t) = 1$ . Here,  $v$  is the total number of local coexisting phases. These multiple PF parameters represent the spatial distribution of multiple phases with different thermodynamic properties and/or multiple grains with different orientations. The PF parameter,  $\phi_{\alpha}$ , will take a value of 1 if phase  $\alpha$  is present locally and a value of 0 if the phase is not locally present. At the interface of phase  $\alpha$ ,  $\phi_{\alpha}$  will vary smoothly from 0 to 1 over an interface thickness of  $\eta$ . Only a summary of the formulation of the time evolution equations that is implemented in MICRESS is presented here. More detailed information about the formulation can be found in [58, 101].

To describe the local composition of the multicomponent alloy, a concentration vector field  $\vec{C}(\vec{x}, t)$  is introduced. The components of this vector,  $C^{i=1,2,\dots,n-1}$ , are the concentrations (mole of solutes per unit volume) of the individual elements. Here,  $n$  is the total number of elements (solutes) in the multicomponent system. By selecting a solvent ( $i = n$ ), the number of independent solute concentrations is reduced to  $n - 1$ . To explicitly partition the solute at the interface, additional individual phase compositions  $\{\vec{C}_{\alpha}(\vec{x}, t)\}$  are introduced.

The time evolution of  $\phi_{\alpha}$  is calculated using the free energy function  $F$ , which integrates the density function  $f$  over the domain  $\Omega$ .

$$F(\{\phi_{\alpha}\}, \vec{C}) = \int_{\Omega} f(\{\phi_{\alpha}\}, \vec{C}), \quad (6.1)$$

where the brackets,  $\{\}$ , represent all phases of  $\alpha$ , and not an individual  $\alpha$ . The density functional,  $f$ , depends on the interface energy density,  $f^{int}$ , and thermodynamic free energy density,  $f^{th}$ ; thus, it can be written as follows:

$$f = f^{int}\{\phi_\alpha\} + f^{th}\{\{\phi_\alpha\}, \vec{C}\} \quad (6.2)$$

The interface energy density is derived as follows:

$$f^{int}\{\phi_\alpha\} = \sum_{\alpha=1}^v \sum_{\beta \neq \alpha}^v \frac{4\sigma_{\alpha\beta}^0 a_{\alpha\beta}^\sigma}{v\eta} \left( -\frac{\eta^2}{\pi^2} \nabla \phi_\alpha \nabla \phi_\beta + \phi_\alpha \phi_\beta \right) \quad (6.3)$$

where  $\sigma_{\alpha\beta}^0$  represents the interfacial energy of the interface between  $\alpha$  and  $\beta$ . The term  $a_{\alpha\beta}^\sigma$  represents the anisotropy function [102]. In 2D, for cubic crystal systems, this function takes the form  $a_{\alpha\beta}^\sigma = 1 - \delta_\sigma \cos(4\theta)$  [101]. Here,  $\delta_\sigma$  is the interface stiffness coefficient and  $\theta$  is the crystallographic orientation in 2D.

The thermodynamic free energy density of the system is derived as follows: it is assumed that in a local unit volume element, there exists a numerical mixture of physical phases with individual phase compositions  $\vec{C}_\alpha$ . Using the phase mixture approach and integrating mass balance with an additional Lagrange term,  $f^{th}$  becomes:

$$f^{th}(\{\phi_\alpha\}, \vec{C}, \vec{C}_\alpha) = \sum_{\alpha=1}^v \phi_\alpha f_\alpha(\vec{C}_\alpha) + (\vec{C} - \sum_{\alpha=1}^v \phi_\alpha \vec{C}_\alpha) \tilde{\mu}^i(\{\phi_\alpha\}, \vec{C}) \quad (6.4)$$

$$\text{Mass balance (mixture approach): } \vec{C} = \sum_{\alpha=1}^v \phi_\alpha \vec{C}_\alpha \quad (6.5)$$

$f_\alpha$  denotes the free energy of the individual phases, which can be obtained from thermodynamic databases as a function of local composition and temperature. In Eq. (6.4), the Lagrange term,  $\tilde{\mu}^i(\{\phi_\alpha\}, \vec{C})$ , is defined as a ‘‘multiphase mixture diffusion potential’’

$$\tilde{\mu}^i(\{\phi_\alpha\}, \vec{C}) = \left( \frac{\partial f^{th}(\{\phi_\alpha\}, \vec{C})}{\partial C^i} \right)_{C^{j \neq i}} = \sum_{\alpha=1}^v \phi_\alpha \sum_{j=1}^k \tilde{\mu}_\alpha^i(\vec{C}_\alpha) \frac{\partial C_\alpha^j}{\partial C^i} \quad (6.6)$$



Here,

$$\tilde{\mu}_\alpha^i(\vec{C}_\alpha) = \left( \frac{f_\alpha(\vec{C}_\alpha)}{\partial C_\alpha^i} \right)_{C_\alpha^{j \neq i}}$$

The term  $\tilde{\mu}_\alpha^i$  determines the chemical driving force for solute diffusion within a phase and is thus called the “phase diffusion potential”. For substitutional elements, the phase diffusion potential is given by the difference in chemical potentials for the elements in the phase. Here,  $n$  is the solvent.

$$\tilde{\mu}_\alpha^i(\vec{C}_\alpha) = \mu_\alpha^i(\vec{C}_\alpha) - \mu_\alpha^n(\vec{C}_\alpha) \quad (6.7)$$

MICRESS assumes that the local diffusional exchange between the phases in an infinitesimally small volume element within the diffuse interface region is instantaneous and that the phases coexist at the same position without any diffusion length between them. Therefore, the individual phase compositions (in each infinitesimally small volume) will adapt instantly to a partial minimum (called the “local quasi-equilibrium”) [58, 101] of the local free energy, given by

$$\left( \frac{\partial f^{th}(\{\phi_\alpha\}, \vec{C}, \vec{C}_\alpha)}{\partial C_\alpha^i} \right)_{\phi, \vec{C}, C_\alpha^{j \neq i}} = \phi_\alpha \left( \frac{f_\alpha(\vec{C}_\alpha)}{\partial C_\alpha^i} \right)_{C_\alpha^{j \neq i}} - \phi_\alpha \tilde{\mu}^i(\{\phi_\alpha\}, \vec{C}) = 0 \quad (6.8)$$

This leads to the condition that all phase diffusion potentials are equal to the mixture diffusion potentials.

$$\tilde{\mu}^i(\{\phi_\alpha\}, \vec{C}) = \tilde{\mu}_\alpha^i(\vec{C}_\alpha) \quad (6.9)$$

Phase transformation is driven by the difference in chemical potential between two (or more) phases. Diffusion is driven by the gradient in the diffusion potential. In total equilibrium, both the chemical and the diffusion potentials are equal in all phases and homogeneous throughout space. In local equilibrium, both the chemical and the diffusion potentials are equal at the interface, but may change with space. In local quasi-equilibrium, the diffusion potentials at the interfaces are locally equal in both phases, but the chemical potentials may differ, predominantly because of curvature and/or kinetic undercooling. (Under the assumption of diffusion control, the kinetic undercooling is negligible, but the curvature undercooling remains.). In contrast with common sharp interface models such as DICTRA, the PF method does not instantaneously adjust the interface position to thermodynamic equilibrium, but instead describes phase transformation based on a relaxation approach with finite kinetics.

Mathematically speaking, local quasi-equilibrium is obtained by minimising Gibbs energy for fixed phase fractions (determined by the local PF parameter), while thermodynamic equilibrium is obtained by minimising Gibbs energy under implicit instantaneous adjustment of phase fractions. Graphically, quasi-equilibrium can be obtained by a parallel tangent [103] construction (see **Figure 4**), with the distance between the tangents determining the driving force (Eq. 6.12) for the phase transition, and the local equilibrium denotes the special case with zero driving force (common tangent construction).

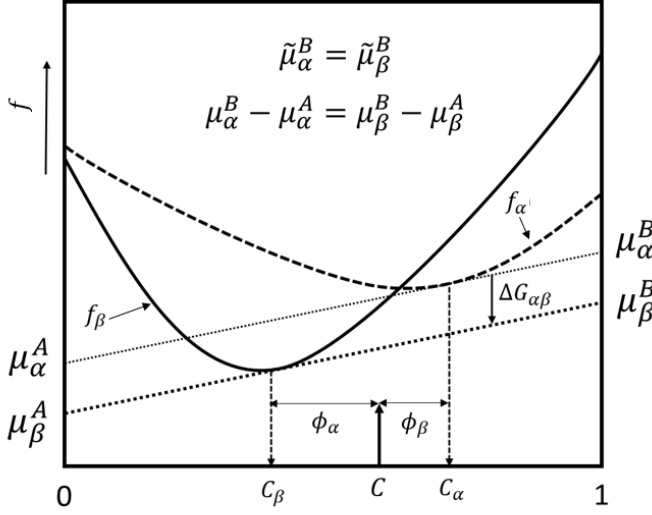


Figure 4: Graphical representation of quasi-equilibrium condition for a binary alloy with two phases. The difference between parallel tangents corresponds to the thermodynamic driving force  $\Delta G_{\alpha\beta}$ .

The multiphase-field equation defining the time evolution of  $\phi_\alpha = (\vec{x}, t)$  in multiple phase transformations is derived by minimising the total free energy  $F$  in Eq. (6.1) by combining Eqs. (6.3) and (6.4), according to the following relaxation principle:

$$\dot{\phi}_\alpha = \sum_{\beta \neq \alpha}^v M_{\alpha\beta} a_{\alpha\beta}^M \left( \frac{\delta F}{\delta \phi_\beta} - \frac{\delta F}{\delta \phi_\alpha} \right) \quad (6.10)$$

Here,  $M_{\alpha\beta}$  is the mobility of the  $\alpha$  and  $\beta$  interfaces. The term  $a_{\alpha\beta}^M$  represents the anisotropy function for interfacial mobility [102]. In 2D, for cubic crystal systems,

this function takes the form  $a_{\alpha\beta}^M = 1 + \delta_M \cos(4\theta)$  [101]. Here,  $\delta_M$  is the interface mobility coefficient.

Then, the general version of the evolution equation including the anisotropy can be written as follows:

$$\dot{\phi}_\alpha = \sum_{\beta \neq \alpha}^v M_{\alpha\beta} a_{\alpha\beta}^M \left[ b_{\alpha\beta} \Delta G_{\alpha\beta} - \sigma_{\alpha\beta}^0 a_{\alpha\beta}^\sigma K_{\alpha\beta}^a + \sum_{\gamma \neq \beta \neq \alpha}^n J_{\alpha\beta\gamma} \right] \quad (6.11)$$

$$\Delta G_{\alpha\beta} = f_\beta(\vec{C}_\beta) - f_\alpha(\vec{C}_\alpha) - \sum_{i=1}^{n-1} \tilde{\mu}^i (C_\beta^i - C_\alpha^i) \quad (6.12)$$

$$b_{\alpha\beta} = \frac{\pi}{\eta} (\phi_\alpha + \phi_\beta) \left( \sqrt{\phi_\alpha \phi_\beta} \right) \quad (6.13)$$

$$\begin{aligned} K_{\alpha\beta}^a = & \frac{2}{v} \left\{ \frac{\pi^2}{2\eta^2} (\phi_\beta - \phi_\alpha) + \frac{1}{2} (\nabla^2 \phi_\beta - \nabla^2 \phi_\alpha) \right. \\ & + \frac{1}{a_{\alpha\beta}^\sigma} \sum_{i=1}^3 \nabla_i \left[ \left( \frac{\partial a_{\alpha\beta}^\sigma}{\partial \nabla_i \phi_\beta} - \frac{\partial a_{\alpha\beta}^\sigma}{\partial \nabla_i \phi_\alpha} \right) \left( \frac{\pi^2}{2\eta^2} (\phi_\alpha \phi_\beta) \right. \right. \\ & \left. \left. - \frac{1}{2} (\nabla \phi_\alpha \nabla \phi_\beta) \right) \right] - \frac{1}{a_{\alpha\beta}^\sigma} \nabla a_{\alpha\beta}^\sigma (\nabla \phi_\beta - \nabla \phi_\alpha) \left. \right\} \end{aligned} \quad (6.14)$$

$$\begin{aligned} J_{\alpha\beta\gamma} = & \frac{2}{v} \left\{ \frac{1}{2} (\sigma_{\beta\gamma}^0 a_{\beta\gamma}^\sigma - \sigma_{\alpha\gamma}^0 a_{\alpha\gamma}^\sigma) \left( \frac{\pi^2}{\eta^2} \phi_\gamma + \nabla^2 \phi_\gamma \right) \right. \\ & + \sigma_{\alpha\gamma}^0 \sum_{i=1}^3 \nabla_i \left[ \left( \frac{\partial a_{\alpha\gamma}^\sigma}{\partial \nabla_i \phi_\alpha} \right) \left( \frac{\pi^2}{2\eta^2} (\phi_\alpha \phi_\gamma) \right. \right. \\ & \left. \left. - \frac{1}{2} (\nabla \phi_\alpha \nabla \phi_\gamma) \right) \right] \\ & - \sigma_{\beta\gamma}^0 \sum_{i=1}^3 \nabla_i \left[ \left( \frac{\partial a_{\beta\gamma}^\sigma}{\partial \nabla_i \phi_\beta} \right) \left( \frac{\pi^2}{2\eta^2} (\phi_\beta \phi_\gamma) \right. \right. \\ & \left. \left. - \frac{1}{2} (\nabla \phi_\beta \nabla \phi_\gamma) \right) \right] + \frac{1}{2} (\sigma_{\beta\gamma}^0 \nabla a_{\beta\gamma}^\sigma - \sigma_{\alpha\gamma}^0 \nabla a_{\alpha\gamma}^\sigma) \nabla \phi_\gamma \left. \right\} \end{aligned} \quad (6.15)$$

where  $K_{\alpha\beta}^a$  is related to the local curvature of the interface and  $J_{\alpha\beta\gamma}$  is related to the third-order junction forces.

However, a more simplified version of the  $J_{\alpha\beta\gamma}$  term is implemented in MICRESS, neglecting the higher-order terms as follows.

$$J_{\alpha\beta\gamma} = \frac{2}{v} \left\{ \frac{1}{2} (\sigma_{\beta\gamma}^0 a_{\beta\gamma}^\sigma - \sigma_{\alpha\gamma}^0 a_{\alpha\gamma}^\sigma) \left( \frac{\pi^2}{\eta^2} \phi_\gamma + \nabla^2 \phi_\gamma \right) \right\} \quad (6.16)$$

The interface motion depends on the curvature contribution ( $\sigma_{\alpha\beta} K_{\alpha\beta}$ ), but also on the thermodynamic driving force,  $\Delta G_{\alpha\beta}(\vec{C}, T)$ . This driving force depends on the temperature,  $T$ , and the local multicomponent composition,  $\vec{C}$ .

The diffusion equation in MICRESS is derived from the free energy functional using the following relaxation approach. In the equation below,  $M^{ij}$  is the multiphase chemical mobility coefficient.

$$\dot{C}^i = \nabla \cdot \sum_{j=1}^{n-1} M^{ij}(\{\phi_\alpha\}, \vec{C}) \nabla \frac{\delta F(\{\phi_\alpha\}, \vec{C})}{\delta C^j} \quad (6.17)$$

After applying the free energy functional given in *Eq. (6.1)* to the above relaxation approach, we obtain

$$\dot{C}^i(\vec{x}, t) = \nabla \cdot \sum_{j=1}^{n-1} M^{ij}(\{\phi_\alpha\}, \vec{C}) \nabla \tilde{\mu}^j \quad (6.18)$$

After applying the mixture approach, it is possible to relate the multiphase chemical mobilities,  $M^{ij}$ , to measurable phase chemical mobilities,  $\mathbf{M}_\alpha^{ij}$ , as follows:

$$M^{ij}(\{\phi_\alpha\}, \vec{C}) = \sum_{\alpha=1}^v \phi_\alpha \mathbf{M}_\alpha^{ij}(\vec{C}_\alpha) \quad (6.19)$$

Replacing the multiphase mobilities and multiphase diffusion potentials in *Eq. (6.18)* with phase-dependent quantities using quasi-equilibrium constraints leads to

$$\dot{C}^i(\vec{x}, t) = \nabla \cdot \sum_{\alpha=1}^v \sum_{j=1}^{n-1} \phi_\alpha \mathbf{M}_\alpha^{ij}(\vec{C}_\alpha) \nabla \tilde{\mu}_\alpha^i(\vec{C}_\alpha) \quad (6.20)$$

$G_{\alpha\beta}(\vec{C}, T)$  and  $M_{\alpha}^{ij}$  (phase chemical mobilities of solutes) are calculated by direct coupling to the thermodynamic (in this thesis-TCNI8) and mobility (in this thesis-MOBN14) databases via the TQ-interface in Thermo-Calc Software [104] at user-specified temperature intervals. Between these temperature intervals, extrapolation is used.

In MICRESS, these coupled sets of equations are solved numerically using the finite difference approach.

### 3.4.2 Model setup in MICRESS related to LMP-DED

The model setup presented in this section is related to the work presented in *Papers A* and *B* appended to this thesis. The objective of this study was to investigate the effect of microstructure formation during the LMP-DED and the manner in which the formed microstructure changes during post heat treatments.

#### 3.4.2.1 Modelling the effect of solidification conditions

The objective of this study was to investigate the effect of varying thermal conditions (thermal gradients and cooling rates) on microstructure formation during the LMP-DED process.

Modelling was performed in 2D. The size of the modelling domain was  $80\ \mu\text{m} \times 80\ \mu\text{m}$ , with  $0.1\ \mu\text{m}$  grid spacing. A constant thermal gradient was applied from the top to the bottom of the domain. A constant cooling rate was applied to the entire domain. This mimics the movement of the liquidus isotherm from bottom to top in the simulation domain. No flux boundary condition was used in all domain boundaries. At the beginning of the simulation, a grain with an almost flat liquid/ $\gamma$  interface with random noise was set at the bottom of the simulation domain. The orientation of this grain was set so that its fast-growth direction,  $\langle 001 \rangle$ , was parallel to the applied thermal gradient direction in the domain. This mimics the growth of epitaxial dendrites from a substrate or remelted layers. During the simulation, the nucleation of new  $\gamma$  grains was set randomly in the liquid using the analytical curvature model implemented in MICRESS [105], and nucleation was set for the new grains with a seed having a 10 nm radius. The nucleation of these new grains was checked at each 0.05 K temperature drop.

During solidification, the Laves phase was allowed for nucleation at the liquid- $\gamma$  interface. To simulate the eutectic formation of Laves+ $\gamma$ , a nucleation site for eutectic  $\gamma$  was allowed to form at the liquid-Laves interface. The ‘seed-undercooling’ model together with the ‘seed stabilisation’ model implemented in the MICRESS software [105] was used for this purpose. For both nucleations, a

critical undercooling value of 2 K was set. At each 5 K temperature drop, the nucleation was checked for the Laves and eutectic  $\gamma$  phases. For simplicity of the simulation, only the liquid/ $\gamma$  interface was modelled as an anisotropic interface having cubic crystal anisotropy [105].

A summary of the modelling parameters can be found in **Table 3**. Thermodynamic and mobility data for the model were dynamically taken from the TCNI8 and MOBNI4 databases of Thermo-Calc. A full multicomponent diffusion matrix based on the local composition values was considered in the solid state. In the liquid state, only the diagonal terms in the diffusion matrix were considered.

*Table 3: Summary of the model parameters used for solidification condition simulations in MICRESS*

<b>Domain size (<math>\mu\text{m} \times \mu\text{m}</math>)</b>	$80 \times 80$
<b>Grid resolution-<math>\Delta x</math> (<math>\mu\text{m}</math>)</b>	0.1
<b>Interface thickness (<math>\eta</math>)</b>	$2.5 \cdot \Delta x$
<b>Interface energy - Liquid/<math>\gamma</math> (<math>\text{J}/\text{cm}^2</math>)</b>	$1.2\text{E}-05$ [66]
<b>Interface energy - Liquid/Laves (<math>\text{J}/\text{cm}^2</math>)</b>	$6\text{E}-06$
<b>Interface energy - <math>\gamma</math>/Laves (<math>\text{J}/\text{cm}^2</math>)</b>	$5\text{E}-06$
<b>Interfacial stiffness coefficient - Liquid/<math>\gamma</math></b>	0.2
<b>Interfacial mobility coefficient - Liquid/<math>\gamma</math></b>	0.2

The MICRESS model setup used here is similar to the model setup reported by Nie et al. [50]. However, Nie et al. used a stochastic modelling approach and modelled the alloy system as a Ni-Nb binary system without explicitly considering the Laves phase formation. In this study, Alloy 718 was modelled as a seven-element system (**Table 4**) and explicitly modelled the formation of the Laves phase in the microstructure. In addition, Nie et al. used a fixed orientation for the new  $\gamma$  grains that form in the liquid.

*Table 4: Nominal chemical composition of the raw powder and the nominal composition used for the PF simulation in LMP-DED*

<b>Element (wt%)</b>	<b>Powder</b>	<b>Simulation</b>
<b>Ni</b>	Bal.	Bal.
<b>Cr</b>	17.5	17.5
<b>Fe</b>	19.4	19.4

<b>Nb</b>	5.0	5.0
<b>Mo</b>	3.17	3.17
<b>Ti</b>	1.07	1.07
<b>Al</b>	0.68	0.68
<b>Co</b>	0.2	-
<b>Mn</b>	0.065	-
<b>Ta</b>	0.003	-
<b>Si</b>	0.088	-
<b>Cu</b>	0.048	-
<b>C</b>	0.031	-
<b>P</b>	0.006	-
<b>B</b>	0.003	-

### **3.4.2.2 Modelling the effect of thermal cycling**

The objective of the modelling work was to investigate the effect of successive thermal cycling in the LMP-DED process on microstructure formation.

A 2D domain was selected normal to the build direction in the 1<sup>st</sup> track of the LMP-DED sample. Therefore, the domain represents an isothermal section. The simulation domain size was taken as  $25\ \mu\text{m} \times 20\ \mu\text{m}$ , with  $0.05\text{-}\mu\text{m}$  grid spacing. This domain size was sufficient to resolve the experimentally observed microstructural features without increasing the computational cost. The simulation began with the complete liquid state with the composition given in **Table 4**. Nine initial  $\gamma$  seeds were randomly positioned in the domain such that the distance between seeds was roughly equal to the experimentally measured primary dendrite arm spacing (PDAS) of  $7.1\ \mu\text{m}$ . The initial temperature of the simulation was set to  $1337\ ^\circ\text{C}$ . This liquidus temperature value was obtained from the Thermo-Calc equilibrium calculations for the current alloy composition. The experimentally measured time-temperature profile in the 1<sup>st</sup> deposited track was input into the model as the thermal condition. The rest of the simulation parameters, including the simplified nominal alloy composition, nucleation of the Laves phase, interfacial energy values, interface thickness, interfacial stiffness/mobility coefficient for anisotropy, diffusion considerations, and domain boundary conditions, were kept identical to the model setup discussed in *Section 3.4.2.1*.

### **3.4.2.3 Modelling the solution heat treatment**

To investigate the effect of solution treatment on the deposited microstructure, a solution heat treatment simulation was performed in MICRESS. The microstructure results from the simulation discussed in *section 3.4.2.2* were used as

the initial microstructure, and the simulation was carried out at 954 °C for 1 h. Only isothermal holding was considered, that is, heating and cooling were not included. During the simulation, orthorhombic  $\delta$ -phase nucleation was allowed within the  $\gamma$  matrix randomly. The ‘seed-undercooling’ model together with ‘seed stabilisation’ model implemented in the MICRESS software [105] was used for this purpose. A minimum undercooling of 1 K was set for the nucleation of the  $\delta$  phase. Because of the limitations of MICRESS, the  $\delta/\gamma$  interface was modelled with tetragonal anisotropy. A full multicomponent diffusion matrix based on the local composition values was considered in the solid state. A summary of the modelling parameters can be found in **Table 5**.

*Table 5: Summary of the model parameters for used solution heat treatment simulation in MICRESS*

<b>Domain size (<math>\mu\text{m} \times \mu\text{m}</math>)</b>	25 × 20
<b>Grid resolution-<math>\Delta x</math> (<math>\mu\text{m}</math>)</b>	0.05
<b>Interface thickness (<math>\eta</math>)</b>	2.5 · $\Delta x$
<b>Interface energy - <math>\gamma/\text{Laves}</math> (<math>\text{J}/\text{cm}^2</math>)</b>	5E-06
<b>Interface energy - <math>\delta/\gamma</math> (<math>\text{J}/\text{cm}^2</math>)</b>	1E-05 [106]
<b>Interface energy - <math>\delta/\text{Laves}</math> (<math>\text{J}/\text{cm}^2</math>)</b>	5E-06
<b>Interfacial stiffness coefficient - Liquid/<math>\gamma</math></b>	0.2
<b>Interfacial mobility coefficient - Liquid/<math>\gamma</math></b>	0.2
<b>Interfacial stiffness coefficient - <math>\delta/\gamma</math></b>	0.05
<b>Interfacial mobility coefficient - <math>\delta/\gamma</math></b>	0.05
<b>Elongation factor for <math>\delta/\gamma</math> interfacial stiffness</b>	2
<b>Elongation factor for <math>\delta/\gamma</math> interface mobility</b>	0.02

#### **3.4.2.4 Modelling the direct aging heat treatment**

To investigate the effect of direct aging (DA) heat treatment on the deposited microstructure, DA simulation (720 °C/8 h, cool furnace to 620 °C at 55 °C/h, hold at 620 °C/8 h) was performed in MICRESS. During the simulation, only the nucleation (randomly) of  $\gamma''$  in the matrix was set for the sake of simplicity.  $\gamma''$  nucleation was checked every 1 s. The grid resolution of the LMP-DED simulation was 50  $\mu\text{m}$ . Therefore, the correct size and morphology of  $\gamma''$  could not be resolved correctly under this grid resolution. To overcome this, an



analytical curvature model [105] implemented in MICRESS was used with a 10 nm critical radius. The anisotropy of  $\gamma' / \gamma''$  was neglected, and an isotropic interaction model was adopted. An interfacial energy of  $1\text{E-}05 \text{ J/cm}^2$  [106] was used. No phase interaction between the Laves phase and  $\gamma''$  was modelled. The rest of the parameters and domain boundary conditions were kept the same as for the model in *section 3.4.2.1*. A full multicomponent diffusion matrix based on the local composition values was considered in the solid state.

### 3.4.3 Model setup in MICRESS related to EB-PBF

The work presented in this section is related to the work presented in *Paper C* appended to this thesis. The objective of this study was to investigate the effect of elevated powder bed temperature in the EB-PBF process on microstructure formation through microstructure modelling.

#### 3.4.3.1 Modelling the as-solidified microstructure

In this work, 2D PF simulations were carried out. The 2D domain was selected normal to the build direction of the EB-PBF sample. Therefore, the domain will be an isothermal cross-section and will be normal to the primary dendrite growth direction. The unit cell approach (representative area) proposed by Warnken et al. [107] was utilised. The edge length of the unit cell is given by the primary dendrite arm spacing (PDAS), and the unit cell contains one representative dendrite. Therefore, a unit cell size of  $6 \mu\text{m} \times 6 \mu\text{m}$  (PDAS was measured experimentally using SEM images) with  $0.025 \mu\text{m}$  grid spacing was taken into account for the EB-PBF solidification simulation. Alloy 718 in the present work was modelled as a seven component system with the composition presented in **Table 6**. This simplification was made to reduce the computational effort required when calculating thermodynamic and mobility data from the databases. The thermodynamic and mobility data for the model were dynamically taken from the TCNI8 and MOBNI4 databases from Thermo-Calc. In addition, the full multi-component diffusion matrix based on the local composition values was taken into account.

*Table 6: Nominal chemical composition of the raw powder and the nominal composition used for the PF simulation in EB-PBF*

Element (wt%)	Powder	Simulation
Ni	Bal.	Bal.
Cr	19.1	19.1
Fe	18.5	18.5
Nb	5.04	5.04
Mo	2.95	2.95

<b>Ti</b>	0.91	0.91
<b>Al</b>	0.58	0.58
<b>Co</b>	0.07	-
<b>Mn</b>	0.05	-
<b>Si</b>	0.13	-
<b>Cu</b>	0.1	-
<b>C</b>	0.035	-
<b>N</b>	0.0128	-

The solidification simulation started with a complete liquid state with the composition given in **Table 6**. The initial  $\gamma$  phase nucleation seed was placed at the centre of the domain. Measuring the cooling rate of the EB-PBF process is difficult because of the inherent nature of the process. Therefore, a value of 2000 K/s was assumed for the simulation. This value is in the range of the reported cooling rate value for EB-PBF Alloy 718 [108]. Periodic boundary conditions were assigned at the boundaries of the simulated domain.

In the present multiphase-field modelling work, only the formation of the Laves phase was modelled to reduce the complexity of the model and thus the computational effort. The rest of the simulation parameters, including the simplified nominal alloy composition, nucleation of the Laves phase, interfacial energy values, interface thickness, and interfacial stiffness/mobility coefficient for anisotropy were kept identical to the model setup discussed in *Section 3.4.2.1*.

### **3.4.3.2 Modelling the effect of elevated powder bed temperature**

To study the effect of an elevated powder bed (called “*in situ* heat treatment”) on the as-solidified microstructure, simulations were performed. For this purpose, an assumption was made that the entire build volume was in thermal equilibrium with the thermocouple at the bottom of the build plate. Hence, the solidification simulation was stopped at 1020 °C. This microstructure resulting from the solidification simulation was used as the input for the *in situ* heat treatment simulations. The model parameters were kept the same as those described in *section 3.4.2.1*.

### **3.4.3.3 Comparing the homogenisation kinetics in EB-PBF and cast Alloy 718**

It was experimentally observed that during this *in situ* heat treatment, the solidified microstructure began to homogenise. The time to achieve homogenisation was approximately 40 min, based on the EB-PBF machine log data file observations.

However, in cast Alloy 718, the homogenisation heat treatments are performed at high temperatures for periods longer than 40 min. Therefore, for comparison purposes, a hypothetical cast microstructure formation and subsequent homogenisation heat treatment were modelled. For the as-cast solidification microstructure simulations, a PDAS of 100  $\mu\text{m}$  was selected, based on published data [98]. Therefore, the unit cell domain size of 100  $\mu\text{m}$   $\times$  100  $\mu\text{m}$  with 0.5  $\mu\text{m}$  grid resolution was selected in accordance with the unit cell model. A cooling rate of 1 K/s was selected based on published data [98]. For the homogenisation heat treatment, a temperature value of 1100  $^{\circ}\text{C}$  was taken into account according to the AMS5383E [109]. A summary of the modelling parameters can be found in Table 7.

*Table 7: Summary of the model parameters for EB-PBF and as-cast microstructure simulations in MICRESS*

	EB-PBF	As-cast*
<b>Domain size (<math>\mu\text{m}</math> X <math>\mu\text{m}</math>)</b>	6 $\times$ 6	100 $\times$ 100
<b>Grid resolution-<math>\Delta x</math> (<math>\mu\text{m}</math>)</b>	0.025	0.5
<b>Interface thickness (<math>\eta</math>)</b>	3 $\cdot \Delta x$	2.5 $\cdot \Delta x$
<b>Cooling rate (K/s)</b>	2000	1
<b>Initial undercooling for <math>\gamma^{\dagger}</math> (K)</b>	11	6
<b>Interface energy - Liquid/<math>\gamma</math> (J/cm<math>^2</math>)</b>	1.2E-05 [66]	
<b>Interfacial stiffness coefficient - Liquid/<math>\gamma</math></b>	0.2	
<b>Interfacial mobility coefficient - Liquid/<math>\gamma</math></b>	0.2	
<b>Interface energy - liquid/Laves (J/cm<math>^2</math>)</b>	6E-06	
<b>Interface energy - <math>\gamma</math>/Laves (J/cm<math>^2</math>)</b>	5E-06	

$^{\dagger}$  The two different initial undercooling values are due to the two different initial nucleation sizes (resulting from the different resolutions of the models) for the  $\gamma$  phase.

\*Simulation was terminated when the material was fully solidified and therefore no further solid-state phase transformation during the cooling was modelled.

### 3.4.4 Assumptions, simplifications, and limitations

- Simulations were performed in 2D on a dendritic scale. This approach was taken considering the available computational resources and calculation times.

- b) Though the MICRESS is capable of handling all the elements in Alloy 718, simplification was made to reduce the computational calculation time associated with thermodynamic and diffusion data calculations. Therefore, the alloy system was modelled as Ni–Cr–Fe–Mo–Nb–Ti–Al. This system contains the major elements that are needed for the formation of the  $\gamma$ ,  $\gamma'$ ,  $\gamma''$ ,  $\delta$ , and Laves phases (refer to **Table 2**). As seen in **Figure 5**, this simplification did not affect the equilibrium significantly, although the solution temperature for  $\gamma'$  had some difference near 19 °C. A similar observation was made on the composition related to **Table 8**.

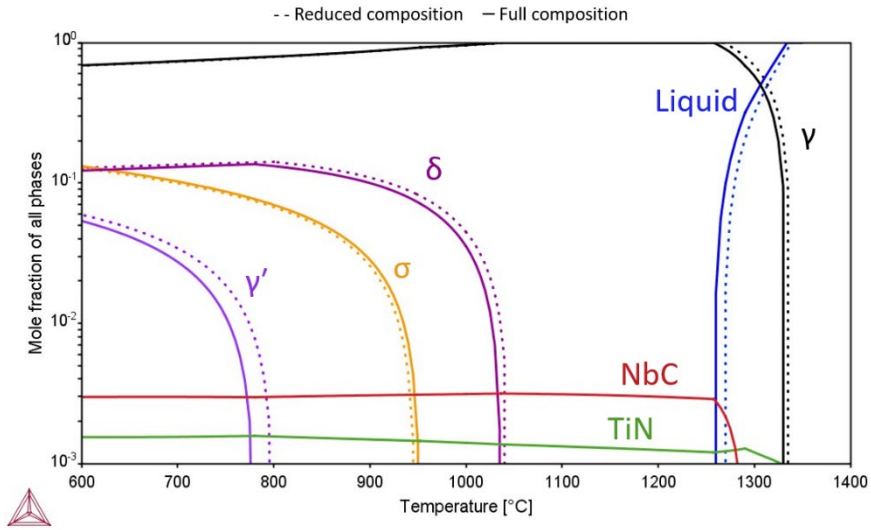


*Figure 5: Equilibrium volume fraction diagram predicted for Alloy 718 considering the full and reduced composition given in Table 6.*

- c) N and C were not considered in this work even though they form TiN and NbC, respectively. The reason behind this is that the N and C proportions (wt%) in the alloy were low compared with those of the other major elements. In addition, the observed volume fractions of nitrides and carbides were very low ( $< 0.3\%$ ) in the microstructure. Therefore, the consumption of Ti and Nb during the formation of nitrides and carbides is considered to be insignificant, and it did not significantly influence the formation of the other phases.
- d) The effect of solid/liquid interface velocity (solidification velocities) dependent element partitioning was not taken into consideration. One reason is that this is still not implemented in MICRESS. However, this criterion is important if the solidification velocities are  $> 1$  m/s, where solute trapping occurs [110]. In all the considered solidification simulations performed in this study, the solidification velocities are  $< 0.1$  m/s.

- e) The effect of latent heat release was ignored.
- f) Interfacial energies were assumed to be constant (i.e., temperature/composition independent).
- g) Interaction between the Laves phase and other phases were assumed to be isotropic.
- h) Effect of fluid flow in the melt on the dendritic growth was ignored.
- i) For all nucleation events in MICRESS, random noise was applied to mimic the stochastic nature of nucleation events. (More details about nucleation models implemented in MICRESS can be found in [105]).
- j) The effect of grain boundaries and dislocations on the phase transformation of the  $\gamma'$ ,  $\gamma''$ ,  $\delta$ , and Laves phases was not considered.
- k) Effect of thermal stresses was ignored.
- l) Misfit strains generate during the phase transformation was not considered.
- m) The thermodynamic and mobility data update via the TQ interface was achieved at every 2 K temperature drop.

### 3.5 Transformation diagram prediction

The time and temperature dependency of the phase transformations during isothermal holding and continuous cooling can be represented by time–temperature–transformation (TTT) diagrams and continuous cooling transformation (CCT) diagrams, respectively. They demonstrate the fraction of the phase transformation as a function of time and temperature. It should be noted that these diagrams have a strong dependency on the alloy composition because the change in the alloy composition will change the equilibrium and driving forces for the phase transformation. To generate the TTT diagram, the desired sample that has been held at a certain temperature is cooled to the chosen test temperature. Thereafter, it was held for a specific time and then quenched to room temperature. The resultant microstructure will be analysed to observe the fraction of phase transformation that occurred during the isothermal holding, and these data will be utilised to generate the TTT diagram. A similar approach was used to generate the CCT diagrams. Instead of using isothermal holding, the sample was cooled to room temperature at a constant cooling rate. The microstructure was analysed in the same way as for the TTT diagram to evaluate the fraction of the transformation.

JMatPro is a multi-platform commercial software that has the capability of predicting the material properties and behaviour of multicomponent alloys. It was used to predict the TTT and CCT diagrams for a given alloy composition. In the present study, JMatPro ver. 10.2 was utilised. The nominal alloy composition and segregated compositions predicted from multiphase-field simulations were utilised to predict the TTT and CCT diagrams.



## 3.6 Experimental work

### 3.6.1 Experimental work related to LMP-DED (Paper B)

Gas-atomised Alloy 718 powder was utilised to generate the LMP-DED built samples in this study. The powder was deposited onto an as-cast Alloy 718 substrate using a coaxial nozzle equipped with a 6-kW ytterbium fibre laser. The nozzle set-up was mounted on an IRB-4400 ABB Robot, which was used to control the motion during deposition of the Alloy 718 samples. Single-wall samples, which comprised a single layer, 2 layers, 3 layers, and 15 layers in the build direction, were deposited. The width of the single wall was equal to the width of a single track, and the lengths of the walls were approximately 35 mm. **Table 4** shows the nominal compositions of the powders. The particle size of the powder was in the range of 20–75  $\mu\text{m}$ . A volumetric powder feeding system was utilised to deliver the powder to the coaxial nozzle with an angular outlet. Argon was used as the carrier gas and as the shielding gas. **Table 8** lists the process parameters used in the present study to generate the deposits. Temperature measurements that served as input for the modelling work in this study were made at the substrate level using type-K thermocouples according to the method previously described by Segerstark et al. [111]. The heat treatment performed in this LMP-DED study was in accordance with the suggestion by Barron [112], and it comprised solutioning the sample using an air furnace at 954 °C/1 h, air-cooling, followed by ageing at 760 °C/5 h-furnace cooled + 650 °C/1 h, and air-cooling. This heat treatment is generally used in the case of Alloy 718 repaired jet engine components to avoid coarsening of  $\gamma''$  precipitates present in the base component [113].

*Table 8: LMP-DED process parameters used in this study*

Parameter	Value
Laser power (W)	1000
Scanning speed (mm/s)	10
Powder feed rate (g/min)	10
Powder standoff distance* (mm)	-1
Shielding gas flow rate (l/min)	11.5
Carrier gas flow rate (l/min)	3.2
Laser spot diameter (mm)	1.6

\* Powder standoff distance is the distance between the powder focus point and the deposition surface.

For microstructure evaluation, samples were sectioned (normal to the longitudinal direction of the deposition) and mounted using non-conductive Bakelite. A Zeiss EVO 50 scanning electron microscope (SEM) was used to analyse the microstructure. To quantify the area fractions of the Nb-rich constituents, SEM images were analysed using the open source software ImageJ. Microhardness measurements were performed using a Vickers micro-hardness testing machine with a load of 0.5 N and a dwell time of 10 s.

### 3.6.2 Experimental work related to EB-PBF (Paper C)

Plasma-atomised powder (nominal size ranging from 25 to 106  $\mu\text{m}$ ) supplied by Arcam AB was used to manufacture Alloy 718 samples in this work. The chemical composition of the powder is listed in **Table 6**. An Arcam A2X EB-PBF machine was used to manufacture the samples, employing Arcam's 'standard' settings (melt parameter version – Inco 4.2.76) for Alloy 718. The manufacturing process started after the powder bed was pre-heated to approximately 1020 °C (measured under the base plate), and this temperature was maintained throughout the process. It should be noted that in this context, the powder bed temperature is the global temperature of the powder bed during the building process. When the material is melted, the temperature increases locally above the melting temperature and then cools down to the global powder bed temperature. Each deposition cycle consisted of 1) pre-heating of the current powder layer, 2) contour melting of the frame of the build, 3) hatch melting of the interior of the build, rotating approximately 65° from the previous scanning vector of the previous layer, 4) post-heating of the current layer, and 5) lowering down the powder bed and raking new powder to form a uniform layer with a thickness of 75  $\mu\text{m}$  for the next cycle.

In this batch, 16 blocks of identical size were fabricated, and the dimension of each block obtained was approximately 35 mm (length)  $\times$  10 mm (width)  $\times$  33 mm (height). The elevated powder bed temperature ( $> 1020$  °C) acts as an '*in situ*' heat treatment for the as-solidified sample. The time at which a specific solidified layer spends at this elevated temperature will vary along the build direction. This will cause the material to have a microstructure gradient along the build direction of the sample. To characterise the microstructural gradient, cross-sections parallel to the build direction were examined at different heights from the top surface. The samples were mounted, mechanically ground successively from 500 grit to 4000 grit, polished with diamond suspension from 3 to  $\frac{1}{4}$   $\mu\text{m}$ , and with OP-U colloidal silica suspension. A Hitachi SU70 FEG scanning electron microscope (SEM), equipped with energy-dispersive X-ray spectroscopy (EDS), was employed to detail the phases ( $\gamma'/\gamma''$ , Laves,  $\delta$ , and MC) in the microstructural



## EXPERIMENTAL WORK

and chemical compositions, operating at an accelerating voltage of 20 kV. To calculate the volume fraction of the Laves phase, SEM images were converted to binary images using the ImageJ program. This was achieved by distinguishing the contrast between the matrix and the Laves phase. Note that, as Laves and NbC cannot be simply distinguished under the SEM because they demonstrate the same contrast, the measured Laves volume fraction actually includes both the Laves phase and NbC. Electron probe microscopic analysis was performed using JEOL JXA-8500F equipment on samples that were cut normal to the build direction.



## 3.7 Results and discussion

### 3.7.1 Laser metal directed energy deposition

The results and discussion given in this section are related to the work presented in **Papers A and B** appended to this thesis.

#### **3.7.1.1 *Effect of solidification conditions on non-equilibrium solidification***

The effect of the thermal gradient and cooling rate on the dendritic structure of Alloy 718 is shown in **Figure 6**. It can be seen that the dendritic structure during solidification changes with the cooling rate and thermal gradient. This ultimately affects the size and morphology of the Laves-phase particles, as shown in **Figure 7**. At low cooling rates, the dendritic structure is coarser. Therefore, the resultant Laves phase precipitates are also coarse, and its morphology tends to have long-chain form, which has been demonstrated to have a negative effect on the microstructure, as it promotes liquation cracking [50]. As Laves form during the final solidification stage, they begin to melt around the eutectic-forming temperature when the temperature of the material is increased. If a Laves phase has a long-chain morphology, liquid can form along with this chain morphology at the reheating stage during thermal cycling above the eutectic-forming temperature. When combined with the tensile stresses generated at the reheating stage, this liquation can easily lead to cracking.

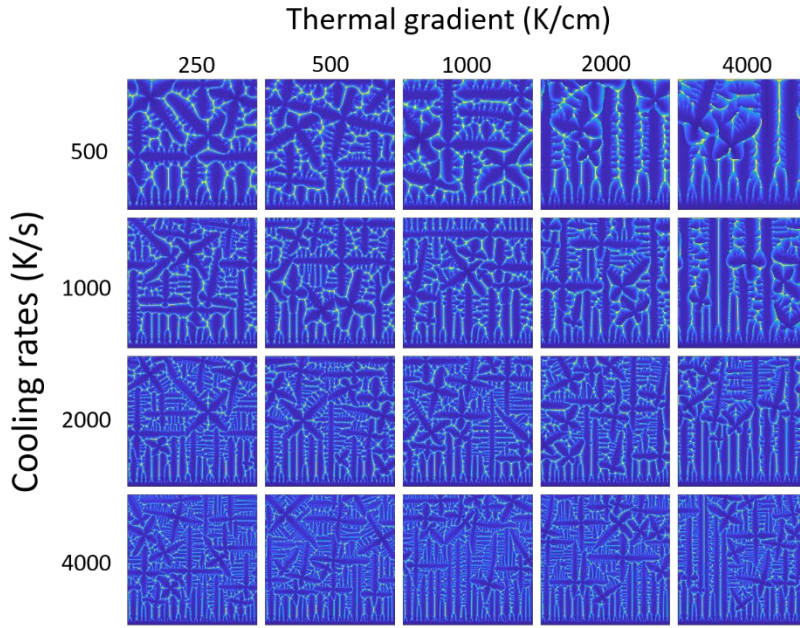


Figure 6: Variation in the dendrite structure under different solidification conditions. (from **Paper A**, reprinted with permission)

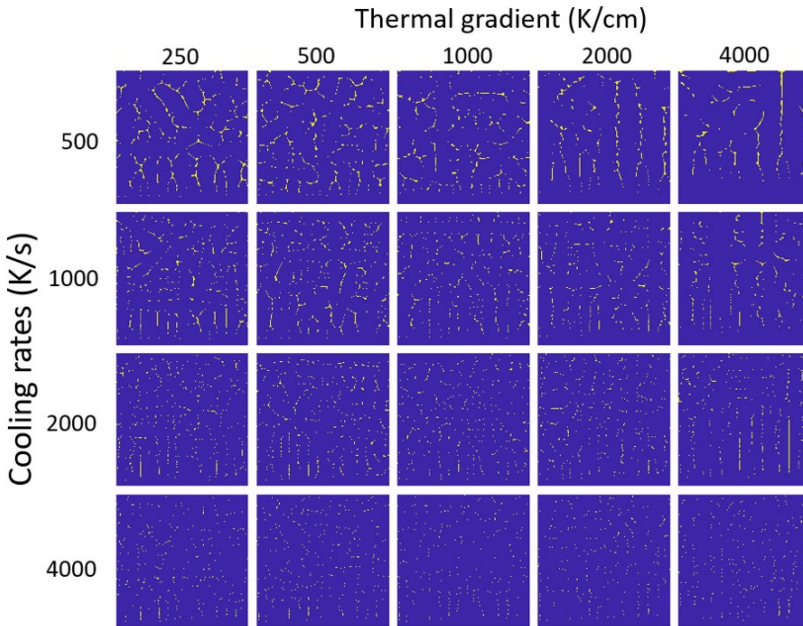


Figure 7: Variation in the Laves-phase morphology under different solidification conditions. (from **Paper A**, reprinted with permission)

## RESULTS AND DISCUSSION

As the cooling rate increases, the amount of undercooling experienced by the liquid increases for a given time. Higher undercooling results in higher excess free energy in the liquid, which is consumed by the liquid–solid interface that is created (though nucleation and/or growth). When the amount of excess free energy becomes large, more liquid–solid interfaces are created per unit area. Consequently, the resultant dendritic structure is finer on the length scale. In fine dendritic microstructures, the thickness and spacing of the primary and secondary dendrite arms become smaller. Therefore, toward the end of solidification, the remaining liquid areas are trapped between these fine dendritic structures. This results in fine and discrete Laves-phase particles at the end of the solidification. When the Laves phase is distributed in the microstructure as discrete and fine particles, the propensity for hot-crack formation is reduced, as a continuous liquid film is difficult to generate. In addition, as the cooling rate increases, the resultant Laves phase area fraction is reduced, as shown in **Figure 8**.

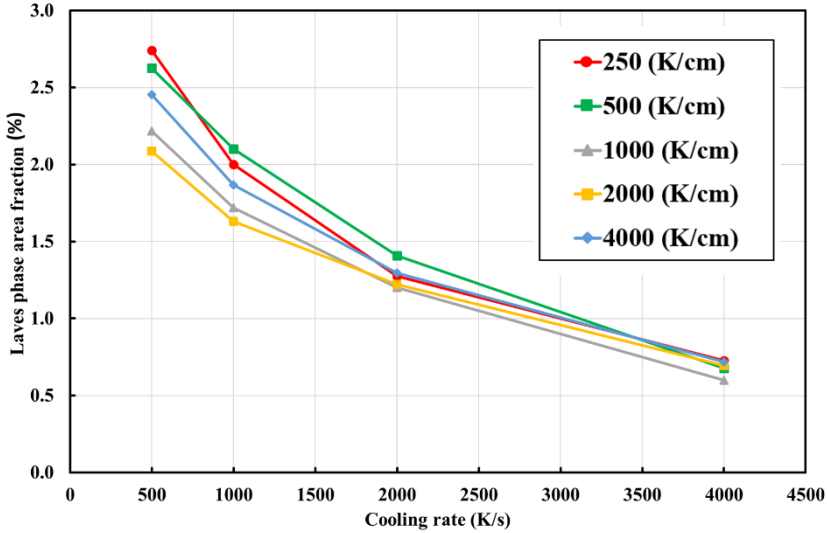
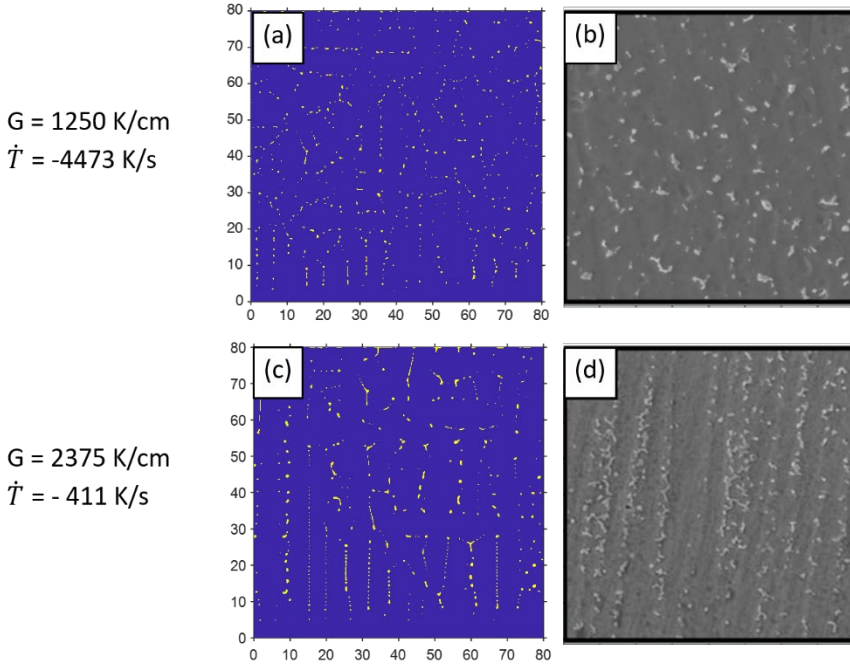


Figure 8: Variation of Laves-phase area fraction under different solidification conditions. (from **Paper A**, reprinted with permission)

The model prediction shows good qualitative agreement with the experimental observations reported by Nie et al. [50] (see **Figure 9**).



*Figure 9: (a), (c) Variation in the Laves-phase morphology under two different solidification conditions and (b), (d) respective experimentally observed Laves phase morphology in the microstructure (size:  $80 \mu\text{m} \times 80 \mu\text{m}$ ). (from **Paper A**, reprinted with permission)*

### 3.7.1.2 Impact of composition segregation

After non-equilibrium solidification (see **Figure 3**), solid-state phase transformations occur as the temperature continues to fall. The main phases that can precipitate in the solid state are  $\gamma'/\gamma''$  and  $\delta$ . Immediately after non-equilibrium solidification, there exists a composition gradient from the dendrite core to the interdendritic region in the  $\gamma$  matrix. Therefore, the local equilibrium conditions and driving forces for solid-state phase transformation change from the dendrite core to the interdendritic region.

**Figure 10** shows a simulated Alloy 718 microstructure at the end of non-equilibrium solidification in the LMP-DED process, and **Figure 11** shows the segregated 1-D composition profiles along a line that goes from the dendrite core to the interdendritic region. The most segregated elements are Nb and Fe,

## RESULTS AND DISCUSSION

whereas the least segregated elements are Ti and Al. The generally accepted chemical composition formula for both  $\gamma''$  and  $\delta$  is  $\text{Ni}_3\text{Nb}$ . Therefore, the distribution of Nb has a profound effect on the distribution of  $\gamma''$  and  $\delta$ . The generally accepted chemical formula for  $\gamma'$  is  $\text{Ni}_3(\text{Al}, \text{Ti})$ . Thus, the distribution of Al and Ti affects the distribution of  $\gamma'$ . From the 1-D segregation profiles shown in **Figure 11**, the Al segregation level is quite low, indicating a relatively homogenous distribution of Al in the microstructure. However, this is not the case for Ti; preferential segregation of Ti is clear, and its distribution could thus affect the distribution of  $\gamma'$ . Nevertheless, as the segregation of Nb is higher than that of Al and Ti, it can be expected that the variation in the distribution of  $\gamma''$  is more pronounced than that of  $\gamma'$  in the matrix.

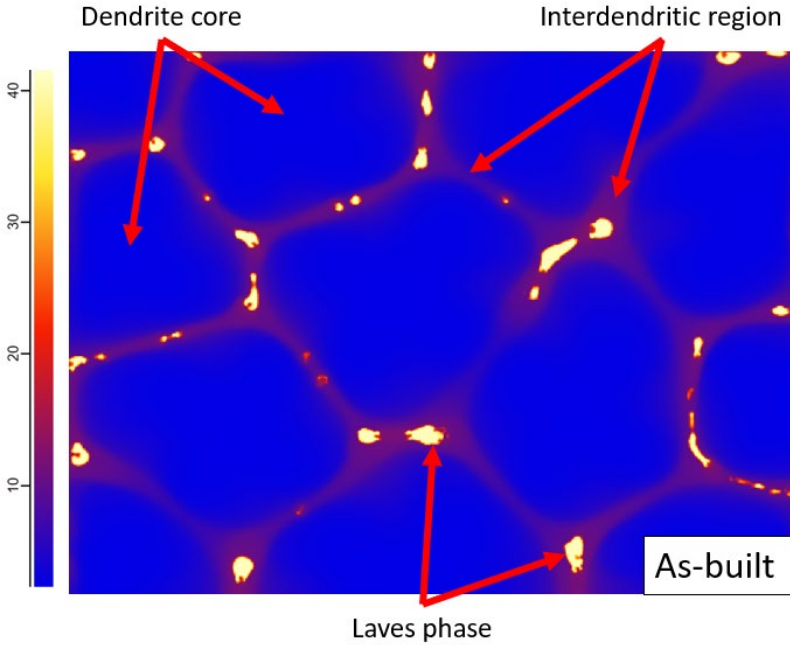


*Figure 10: As-built microstructure at the end of non-equilibrium solidification simulation described in section 3.4.2.2. Scale shows the Nb distribution in wt%. Domain size: 25  $\mu\text{m}$   $\times$  20  $\mu\text{m}$ . (from **Paper A**, reprinted with permission)*

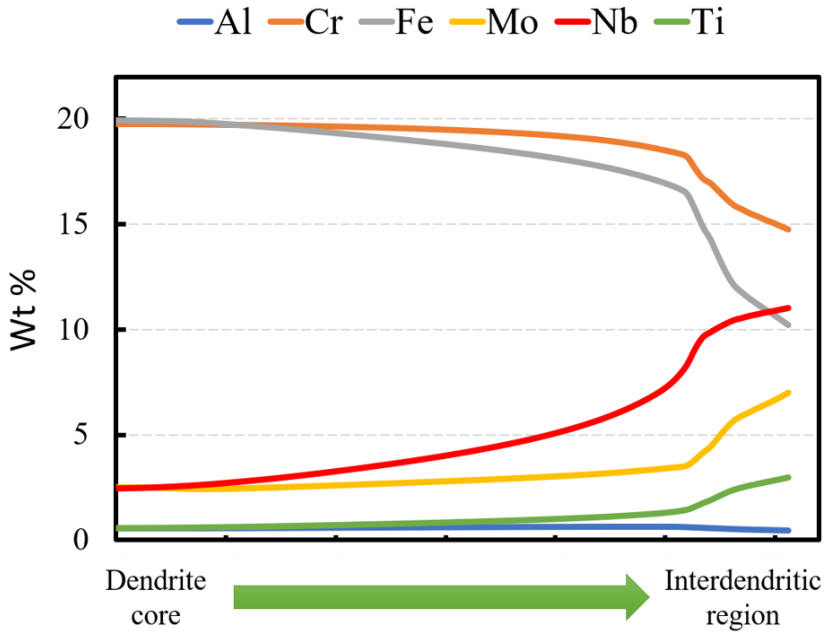


Figure 11: 1-D composition profiles extracted from a line that goes from dendrite core to interdendritic region in Figure 10. (from **Paper A**, reprinted with permission)

To gain insight into the effect of segregation on the local equilibrium conditions of Alloy 718, equilibrium volume fraction diagrams were generated using the JMatPro software package, considering the composition in the dendrite core and the interdendritic region in **Figure 11**. For comparison, the equilibrium volume fraction related to the nominal composition of Alloy 718 was also generated, and the results are shown in **Figure 12**. It can be clearly seen that segregation has a direct effect on the equilibrium conditions for  $\gamma'/\gamma''$  and  $\delta$ . Away from the dendrite core and close to the interdendritic region, there is an increase in the volume fraction of the  $\gamma'/\gamma''$  and  $\delta$  phases; moreover, the equilibrium transformation temperature for the phases changes.



## RESULTS AND DISCUSSION

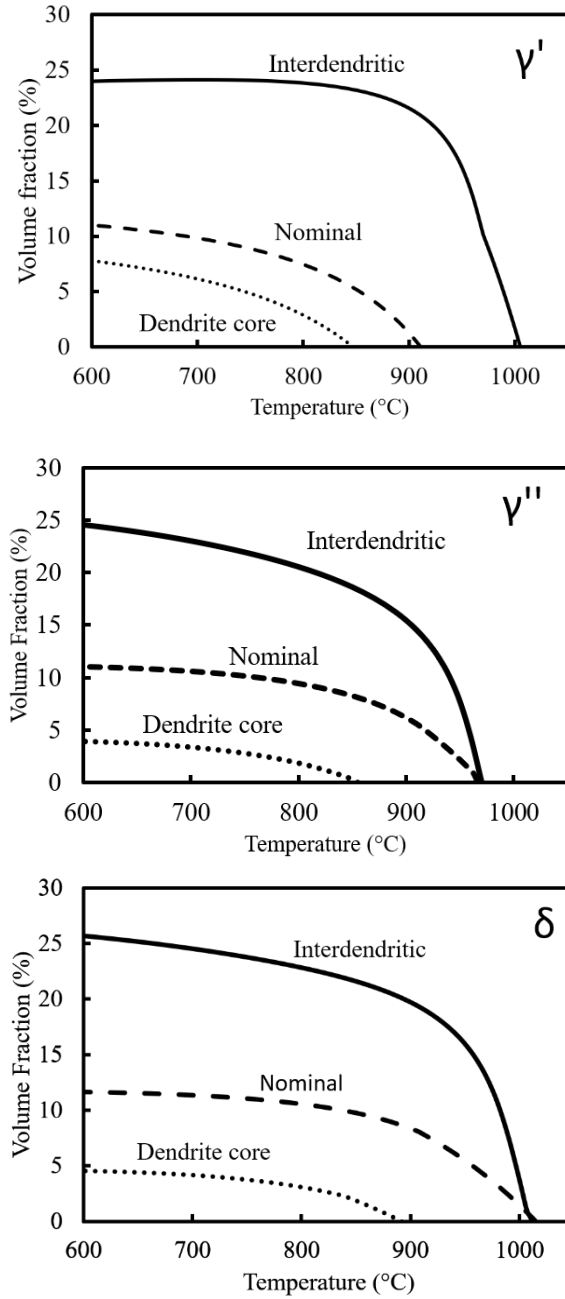
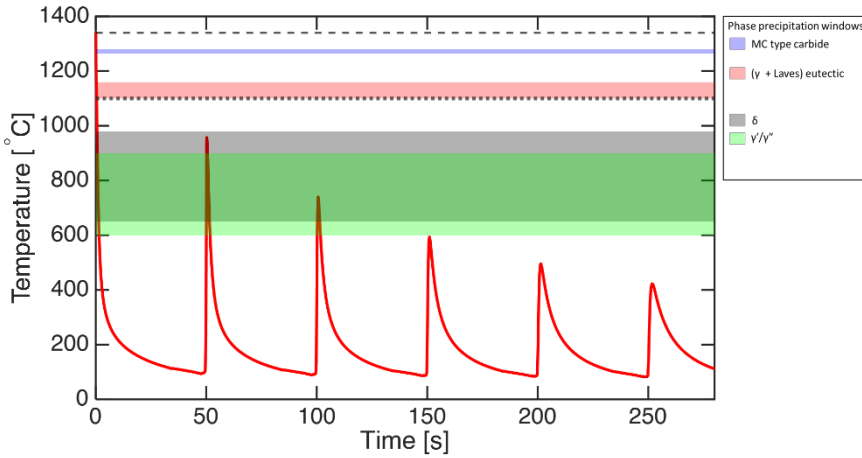


Figure 12: Equilibrium volume fractions of  $\gamma'$ ,  $\gamma''$ , and  $\delta$  predicted using JMatPro for nominal, interdendritic, and dendrite core composition. Composition of the interdendritic and dendrite core taken from Figure 11. In the calculation of  $\gamma''$ ,  $\delta$  was suspended. (from **Paper A**, reprinted with permission)

### 3.7.1.3 Effect of successive thermal cycling

**Figure 13** shows the time–temperature history of the 1<sup>st</sup> layer of a 15-layer single-wall deposited sample. Only measurement data related to the first 6 layers of the 15-layer deposition sample are shown here. As can be seen from the figure, the 1<sup>st</sup> layer is subjected to multiple thermal cycles during the deposition of multiple succeeding layers. **Figure 14** shows the Nb distribution map at the end of the 1<sup>st</sup> and 2<sup>nd</sup> thermal cycles. There is no noticeable difference in the Nb distribution and the formed Laves phase at the end of the 1<sup>st</sup> and 2<sup>nd</sup> thermal cycles. One possible reason for this could be that, in the 2<sup>nd</sup> thermal cycle, the temperature in the 1<sup>st</sup> deposited layer was less than 1000 °C and, therefore, not high enough to have an impact on the elemental diffusion and dissolution of the Laves phase. In addition, the time that the 1<sup>st</sup> deposited layer spent above 600 °C during the 2<sup>nd</sup> thermal cycle was ~2 s, which is too short to have any considerable impact on elemental diffusion in Alloy 718. Based on these observations, it can be expected that there will be a negligible impact on elemental diffusion and the Laves phase upon further thermal cycling (3<sup>rd</sup>, 4<sup>th</sup>, ...). This is also corroborated by the experimentally measured Laves Phase+NbC area fraction measurements in the 1<sup>st</sup> deposited layer, which revealed no noticeable change with further deposition of layers (refer to **Figure 15**).



*Figure 13: Time–temperature history measured at the 1<sup>st</sup> deposited layer of the 15-layer single wall sample. Only measurement data related to the first 6 layers of the 15-layer deposition sample are shown here.*

## RESULTS AND DISCUSSION

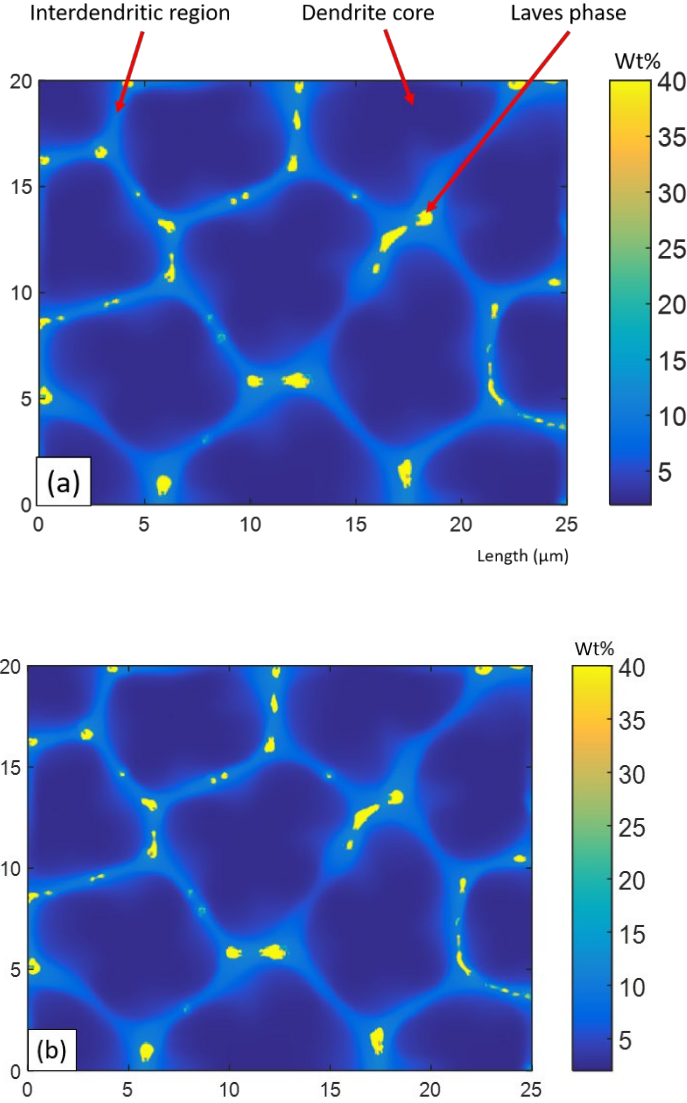


Figure 14: Nb distribution map (a) after the 1<sup>st</sup> thermal cycle and (b) after the 2<sup>nd</sup> thermal cycle from MICRESS simulations. (from **Paper B**, reprinted with permission)

**Figure 16** shows the measured hardness values in the first layer of the LMP-DED deposited samples. From the thermal measurements depicted in **Figure 13**, it can be seen that during the deposition of successive layers, the 1<sup>st</sup> deposited layer temperature goes through the  $\gamma'/\gamma''$  precipitation window for three consecutive thermal cycles. Hence, it is expected that the hardness in the 1<sup>st</sup> layer might

progressively increase following deposition of the 2<sup>nd</sup> and 3<sup>rd</sup> layers. However, this was not clearly evident from the measured hardness values shown in **Figure 16**. It is plausible that, even though the 1<sup>st</sup> deposited layer passes through the  $\gamma'/\gamma''$  precipitation window multiple times, the cumulative time that it spends within the precipitation window is inadequate to have a significant impact on the growth of  $\gamma'/\gamma''$  and, therefore, on the hardness values. However, the situation could be different under the thermal conditions shown in **Figure 17**.

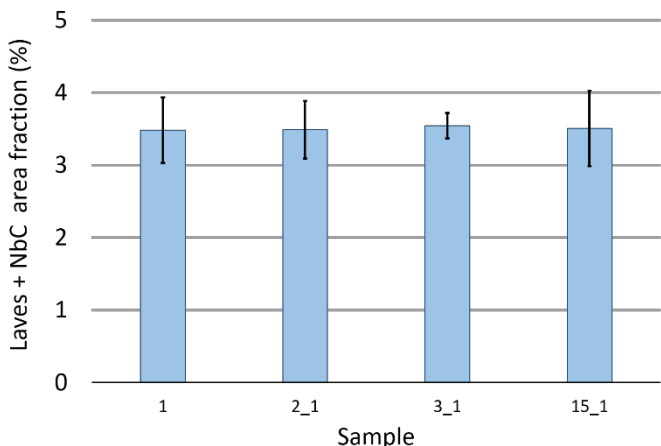


Figure 15: Laves + NbC area fraction in the 1<sup>st</sup> layer of the deposited samples, with varying number of total deposited layers in the single-walled samples. (from **Paper B**, reprinted with permission)

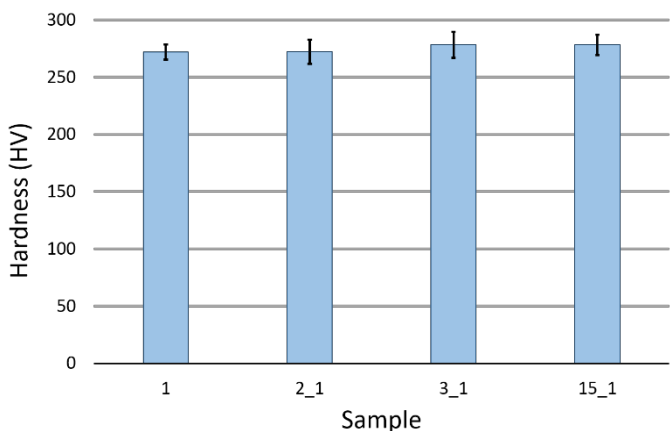
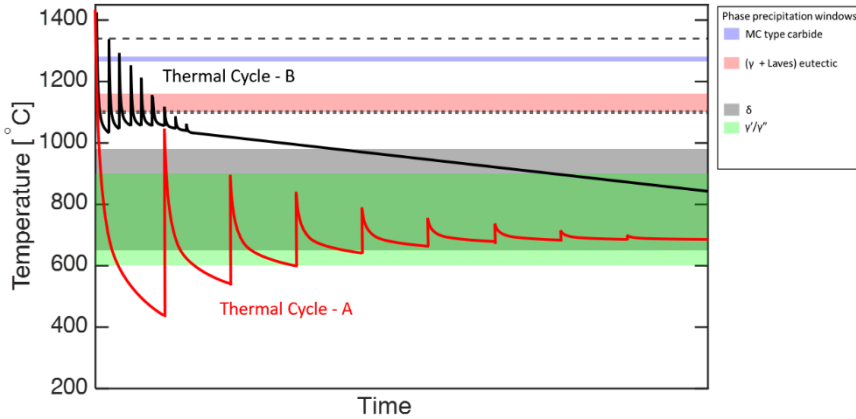


Figure 16: Hardness measurements taken at the 1<sup>st</sup> deposited layer of the samples, with varying number of total deposited layers in the single-walled samples. (from **Paper B**, reprinted with permission)

## RESULTS AND DISCUSSION

Thermal cycle A in **Figure 17** illustrates a case where the deposition of multiple layers is performed without sufficient inter-pass waiting time to cool down the previously deposited material to a temperature close to room temperature. Under these conditions, the global temperature of the deposited material rises because of heat accumulation. The experimentally measured temperature profile in Tian et al. [72] resembles this condition. This rise in the global temperature has an effect similar to that of an heat treatment (HT), both to the deposited and to the base material, if the temperature is above  $\sim 600$  °C. If the thermal conditions during processing resemble those in thermal cycle A, then this may be thought of as *in situ* ageing HT for the previously deposited material. Therefore, with time,  $\gamma'/\gamma''$  begins to precipitate in the material, and this precipitation is influenced by local compositional segregation in the microstructure. It should be noted that the rise in the global temperature ( $> \sim 600$  °C) also affects the substrate material. The amount of  $\gamma'/\gamma''$  precipitates in the interdendritic region is larger than that in the dendrite core as a result of the higher equilibrium volume fraction expected for local variation in the chemical composition. In addition, these precipitates grow in size with the time that the material spends in the *in situ* ageing. This generates a gradient of  $\gamma'/\gamma''$  precipitates from the interdendritic region to the dendrite core, as well as from the bottom to the top of the deposited sample. Therefore, there will be a hardness gradient in the material from top to bottom, which was experimentally confirmed by Tian et al. [72] (Figures 4 and 7 in their paper).



*Figure 17: Schematic representation of different thermal cycles in the LMP-DED process. Note that the start of the thermal cycles shows the final solidification. That means thermal cycles that cause the first melting and further remelting are not shown in this schematic.*

In **Figure 17**, the thermal cycle B is similar to thermal cycle A, but the heat accumulation is greater; therefore, the rise in the global temperature is higher. Such thermal conditions were reported by Li et al. [114] during high-deposition-rate LM-DED of Alloy 718. In this thermal cycle, the global temperature of the material first rises to a higher value ( $> 1000\text{ }^{\circ}\text{C}$ ) and then decreases gradually during the deposition process because of heat conduction. When the temperature decreases, it passes through both the  $\gamma'/\gamma''$  and  $\delta$  precipitation windows. Thus, in this case,  $\gamma'/\gamma''$  and  $\delta$  precipitate in the microstructure. However, their distribution is not uniform because of local compositional segregation. As described previously,  $\gamma'/\gamma''$  and  $\delta$  predominantly precipitate around the Laves phase in the interdendritic region. As the bottom of the sample spends more time at a higher temperature than the top, there will be a difference in the amount of  $\gamma'/\gamma''$  and  $\delta$  between the bottom and top. Such a heterogeneous distribution along the height, as well as from the dendrite core to the interdendritic region, has been reported by Li et al. [114].

It should be noted that for all these thermal cycles, the Laves phase formed during the non-equilibrium solidification of a given layer does not significantly change because of the thermal cycling that occurs during subsequent layer depositions. This is primarily due to the fact that in these thermal cycles, the time-temperature conditions are not sufficient to dissolve the Laves phase significantly. Therefore, to modify the Laves phase, the process parameters of the LM-DED should be changed so that the thermal conditions during non-equilibrium solidification change; otherwise, post-HT is necessary to alter the formed Laves phase. It should also be noted that the non-equilibrium solidification conditions (thermal gradient and cooling rate) can, to a certain degree, change during the deposition of the material as a result of the geometry of the deposited part. This could influence the Laves phase formation locally during the non-equilibrium solidification from the bottom to the top of the build.

#### **3.7.1.4 Effect of post heat treatments**

The phase transformation during solution treatment and DA of LMP-DED Alloy 718 was investigated in this study.

As mentioned in the previous section, the thermal cycle shown in **Figure 13** produces a microstructure with a segregated  $\gamma$  matrix, Laves, and MC phases. The presence of compositional segregation in the matrix has a direct effect on the phase transformation during different post-HTs. To explain this transformation, TTT diagrams, as shown in **Figure 18**, were generated using the JMatPro software package by considering the composition in the dendrite core and the interdendritic region from **Figure 11**.

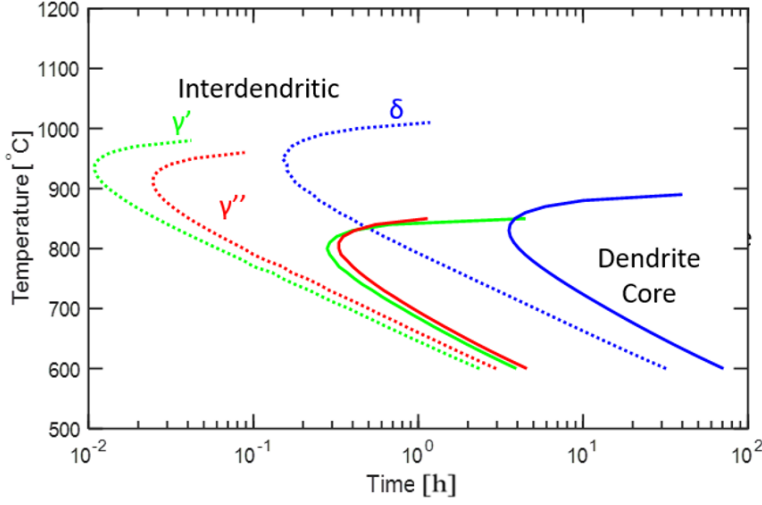
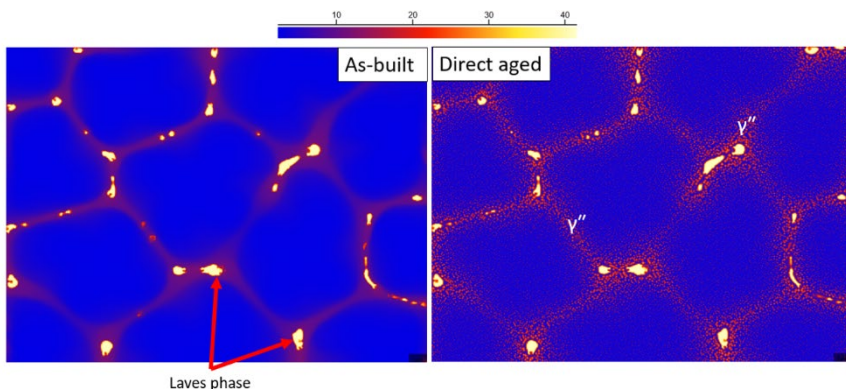


Figure 18: TTT diagram obtained using the JMatPro software package by considering compositions in the dendrite core and the interdendritic region in Figure 11. Dotted lines represent 0.5% precipitation close to the Laves phase, and solid lines represent 0.5% precipitation in the dendrite core. (from **Paper B**, reprinted with permission)

The JMatPro predictions indicate that there is a clear difference (more than an order of magnitude difference in time) in the precipitation kinetics of  $\gamma'/\gamma''$  and  $\delta$  resulting from the compositional segregation. In the interdendritic region, precipitates form more rapidly than in the dendrite core. Moreover, the nose of the TTT curves related to the interdendritic region (dotted lines) corresponds to a higher temperature than that of the curves related to the dendrite core (solid lines). Further, ageing treatment is performed to precipitate the strengthening phases  $\gamma'/\gamma''$ . As shown in **Figure 12**, the equilibrium volume fraction of  $\gamma'/\gamma''$  is higher in the interdendritic region than in the dendrite core. Accordingly, a high volume fraction of  $\gamma'/\gamma''$  forms towards the interdendritic region during DA treatment. The accelerated phase precipitation kinetics causes  $\gamma'/\gamma''$  to precipitate at an earlier stage of HT in the interdendritic region than in the dendrite core. Hence, the  $\gamma'/\gamma''$  precipitates in the interdendritic region experience greater growth than those in the dendrite core. From the segregation level of the elements forming  $\gamma'$  and  $\gamma''$ , as shown in **Figure 11**, it is reasonable to assume that the growth of  $\gamma''$  is supported more than that of  $\gamma'$ . Therefore, even if the equilibrium predictions indicate a high volume fraction for  $\gamma'$  in the interdendritic region, this fraction may not be high compared with that of  $\gamma''$ .



*Figure 19: MICRESS-simulated AD microstructure at the end of thermal cycles similar to thermal cycle-A, and the same microstructure after DA simulation. Domain size: 25  $\mu\text{m}$   $\times$  20  $\mu\text{m}$ . Scale shows the Nb distribution in wt%. (from **Paper A**, reprinted with permission)*

The effect of element segregation on the precipitation of  $\gamma''$  during DA MICRESS simulations is shown in **Figure 19**. The results qualitatively agree with the experimental observations in [72, 86]. In contrast with the dendrite core, towards the interdendritic region, the number density and size of the precipitates increase. It can be assumed that because of the lack of  $\gamma''$  precipitates, the dendrite core is softer than the interdendritic area. Consequently, there is a mechanical property gradient from the dendrite core to the interdendritic region. However, at the macro level, this DA Alloy 718 microstructure possesses relatively higher strength compared with the as-built condition [8]. It should be noted that the temperature in the DA treatment is not sufficiently high to dissolve/change the Laves phase or grain structure. Thus, the increase in strength in this condition compared with the AD condition is due to the precipitation of  $\gamma'/\gamma''$ . This raises the fundamental question of how DA LMP-DED Alloy 718 can result in relatively higher strength (in comparison with AMS5662 wrought standard), even though the distribution of strengthening phases is non-uniform in the microstructure. One possible reason could be that the microstructure has a property gradient from the dendrite core to the interdendritic region. This microstructure can be treated as a composite material with a softer phase (dendrite core area) embedded in a hard phase (interdendritic area). These two (soft and hard) areas mimic the dendritic structure inside the grain. Therefore, the hypothesis is that a hierarchical structure with these two regions and its spatial structure inside the grains give rise to higher strength on the macroscale. This could be verified using crystal plasticity/finite element modelling to study the effect of such a hierarchical microstructure on macroscale properties; this will be addressed in future work.



## RESULTS AND DISCUSSION

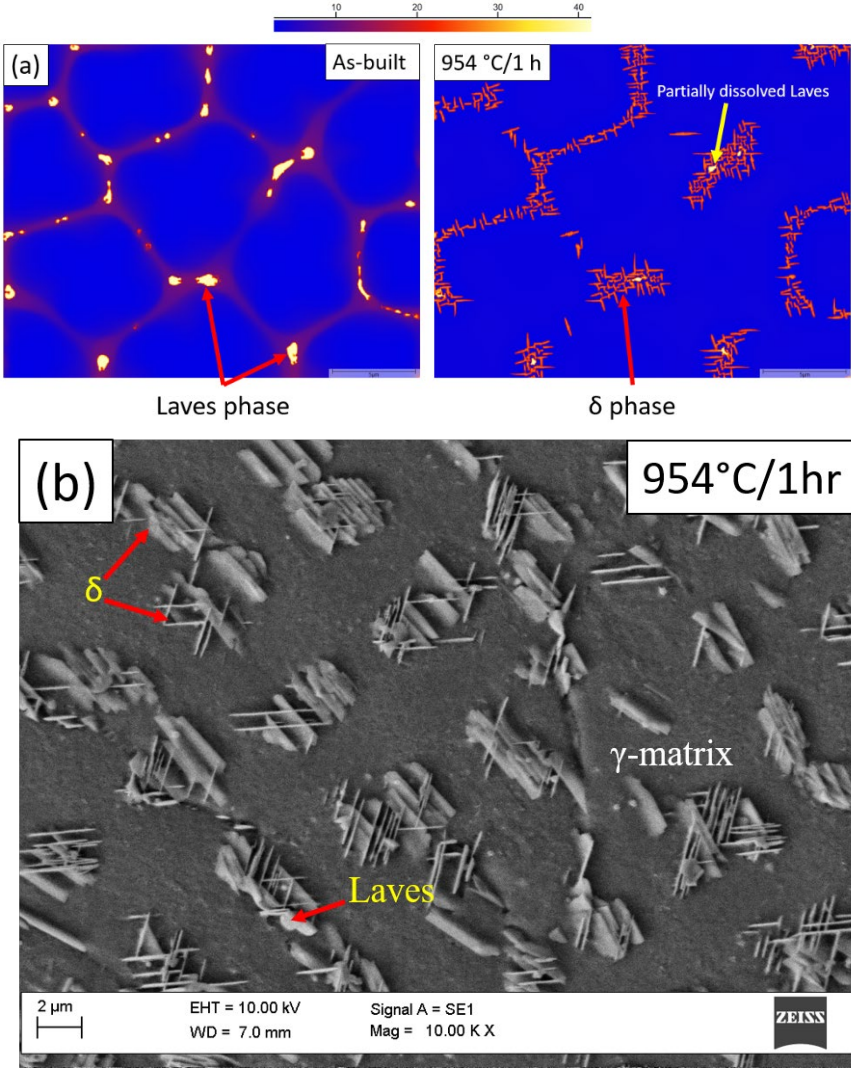


Figure 20: (a) MICRESS simulation showing the microstructure normal to the build direction before and after solution treatment at 954 °C/1 h, domain size: 25 μm × 20 μm; figure shows the Nb distribution in wt%. (b) Experimental microstructure normal to the build direction after 954 °C/1 h. (from **Paper A**, reprinted with permission)

Figure 20(a) shows the Nb distribution map of the microstructure after the solution heat treatment (at 954 °C for 1 h) simulation. The needle-like phases that can be seen in the microstructure represent the δ phase. Some Laves-phase particles can be seen in the microstructure, even though a majority of them have

dissolved. These  $\delta$  needles ( $\delta$  phase will look like needles in a 2D cross-section and have a platelet morphology in 3D) precipitate close to the Laves phase and in the interdendritic region of the microstructure. Nb released during dissolution of the Laves phase also tends to diffuse to the surrounding interdendritic areas and aid the growth of the  $\delta$  phase. This observation is qualitatively in agreement with the experimentally observed microstructure in a heat-treated 15-layer sample, as shown in **Figure 20(b)**, with  $\delta$  needles [113] observed mostly in the interdendritic region, which is predicted by the simulation.

Normally, the solution HT is used to precipitate the  $\delta$  phase at the grain boundaries, as it is performed below the  $\delta$  solvus temperature. The presence of the  $\delta$  phase at the grain boundaries has been demonstrated to have a beneficial effect on stress rupture ductility and to inhibit the growth tendency of the matrix grains during the forging process [115–117]. However, the presence of compositional segregation in the AD LMP-DED microstructure causes  $\delta$  to precipitate inside the grains as well because of the presence of multiple dendrite/cells inside a single grain. In the interdendritic area, the  $\delta$  phase precipitates and grows in large quantities because of the large equilibrium volume fraction (**Figure 12**) and increased precipitation kinetics (**Figure 18**).

### 3.7.2 Electron beam powder bed fusion

The results and discussion given in this section are related to the work presented in **Paper C** appended to this thesis.

#### 3.7.2.1 Effect of elevated powder bed temperature

Because of the inherent nature of this process, the printed material undergoes multiple thermal cycles when successive layers are printed. During this sequential printing, the uppermost layers undergo remelting. Depending on the beam parameters and movement, the number of layers that are remolten varies. When layer melting/remelting occurs, non-equilibrium solidification occurs, as discussed in *Section 3.3.2*. The resulting as-solidified microstructure has a segregated dendritic structure, with interdendritic Laves and NbC phases [97, 108]. Upon building further layers, the microstructure undergoes thermal cycling. However, it does not change significantly with the thermal cycles because of their shorter exposure time. The most significant effect on the microstructure is exerted by the elevated build temperature ( $> 1000\text{ }^{\circ}\text{C}$  for Alloy 718) that occurs during the EB-PBF processing of Alloy 718. This temperature acts as an *in situ* HT and causes microstructural changes. The time that a specific layer undergoes this “*in situ*” heat treatment changes according to the height of the object under construction, which creates a gradient in the microstructure from the top to the bottom of the sample. **Figure 21** shows the measured thermocouple data from

## RESULTS AND DISCUSSION

the bottom of the build plate. According to the temperature measurements shown in **Figure 21**, it is expected that the powder bed temperature remained above 1020 °C throughout the building of the samples. Therefore, this elevated temperature acted as an “*in situ*” heat treatment and changed the “as solidified” microstructure.

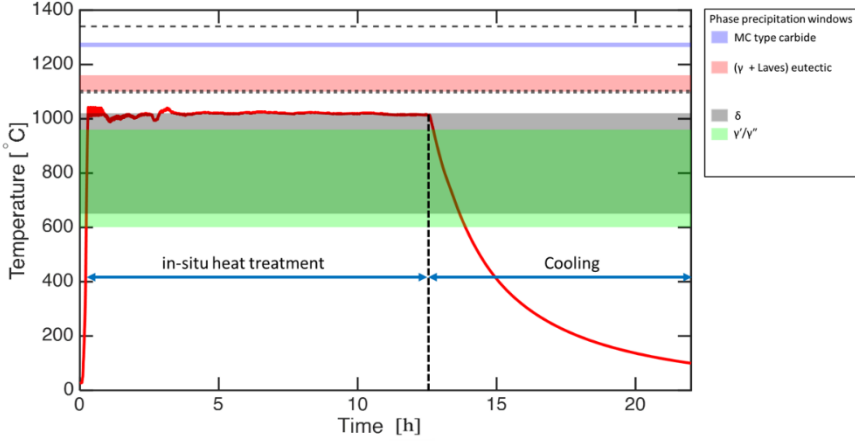


**Figure 21:** Thermocouple measurement from the bottom of the build plate during the EB-PBF process.

Experimental examinations of the microstructure of the sample clearly indicate the presence of a microstructure gradient along the build direction. This gradient along the build direction was visible when observing the bright particles in the interdendritic regions of the microstructure. These particles were confirmed as the Laves phase and NbC/(Nb,Ti)(C,N) according to transmission electron microscopy (TEM) analysis [97]. The area fractions of these phases were measured by image analysis to determine the evolution of the gradients of these phases. The measured Laves + NbC/(Nb,Ti)(C,N) area fractions are shown in **Figure 22**.

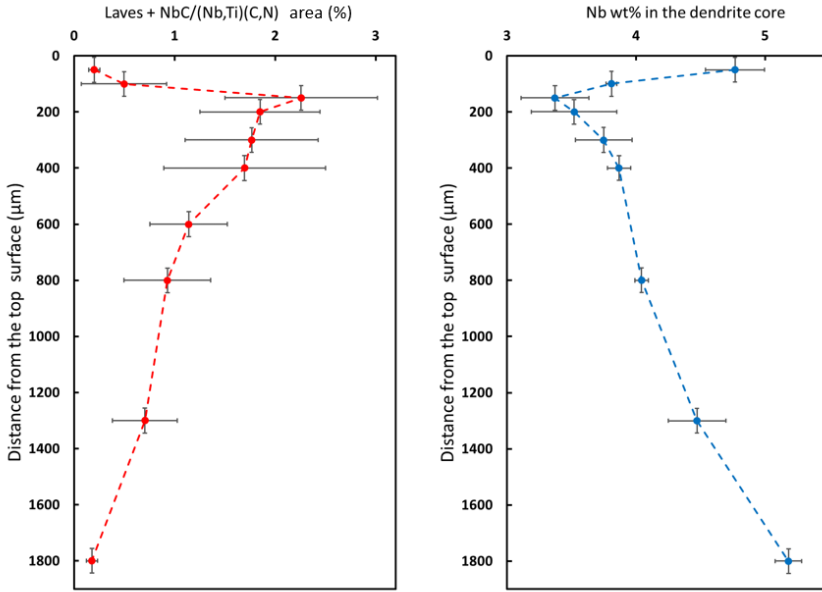


Figure 22: Measured Laves + NbC/(Nb,Ti)(C,N) volume fraction and Nb wt% in the dendrite core from top surface of the sample. Shaded areas represent the possible last-solidified region not subjected to “*in situ*” heat treatment. (from **Paper C**, reprinted with permission)

The area fraction of the Laves + NbC/(Nb,Ti)(C,N) phase began to decrease gradually as the distance increased, which can be attributed directly to the dissolution of the Laves phase during the “*in situ*” heat treatment. Because of their high stability, NbC/(Nb,Ti)(C,N) were not affected by the “*in situ*” heat treatment; thus, their area fractions were expected to remain unchanged with the build height. The Laves phase was no longer visible at a depth of  $\sim 1800$   $\mu\text{m}$  from the top surface and was expected to be fully dissolved. This distance of  $1800$   $\mu\text{m}$  is roughly around the 30<sup>th</sup> layer, counting from the top of the build sample. Considering the total build time and the total number of layers, we estimated that the 30<sup>th</sup> layer was exposed to “*in situ*” heat treatment for roughly 40 min.

As mentioned before, Nb is considered to be one of the most important alloying elements in alloy 718 [90], [50]. The formation of phases such as  $\gamma'/\gamma''$ , Laves, and  $\delta$  is directly related to the level of Nb in the microstructure [90]. Nb is also the most severely segregated element in the microstructure of Alloy 718, so it is relatively easy to measure its segregation. **Figure 22** shows the variation in the proportion of Nb (Nb wt%) at the centre of the dendrite core as a function of the distance from the top surface of the sample. The changes in Nb wt% exhibited

## RESULTS AND DISCUSSION

the opposite relationship to the variations in the Laves + NbC/(Nb,Ti)(C,N) area fractions, thereby indicating that the Nb trapped inside the Laves phase in the “solidified” microstructure was released and diffused back into the dendrite core as a consequence of the “in situ” heat treatment. At a distance of  $\sim 1800\ \mu\text{m}$  from the top surface, the Nb wt% in the dendrite core was similar to the nominal composition of the powder material used in this study, which indicates that the “solidified” microstructure tended to homogenise during the 40-min “in situ” heat treatment.

**Figure 23(a)** shows the elemental distributions of Nb at the end of the solidification simulation. This represents the as-solidified microstructure. The formed Laves phase during solidification is observed in the interdendritic region. **Figure 23(b)** shows the Nb distribution change during the “in situ” heat treatment along line AB. As can be seen from the simulation data, the segregated elements in the as-built condition tended to homogenise after 40 min during the “in situ” heat treatment at  $1020\ ^\circ\text{C}$ . This segregation is expected to be reduced by further “in situ” heat treatment, and the microstructure is expected to reach its nominal composition inside the matrix. However, in the “in situ” simulation, the Laves phase was dissolved after  $\sim 25$  min. The heat treatment simulation of the cast microstructure did not indicate the same homogenisation compared with the EB-PBF microstructure, as shown in **Figure 24(b)**. Some of the Laves phase still remained at the end of the heat treatment simulation for the cast microstructure. In contrast, complete dissolution of the Laves phase was achieved in the heat treatment simulation of the EB-PBF microstructure, which could have been related to the smaller size of the Laves-phase particles in the EB-PBF sample compared with the cast Alloy 718. Smaller particles will dissolve in a shorter time compared with larger particles. Another reason for the relatively rapid homogenisation in the EB-PBF microstructure is the smaller PDAS, as the microstructure obtained in the EB-PBF process will have a relatively smaller ( $\sim$  one order of magnitude) PDAS compared with cast products. This difference will lead to segregation at a finer scale and a smaller diffusion length for the elements. As a consequence, EB-PBF microstructures tend to homogenise more rapidly compared with cast microstructures. It has been shown that other AM processes, such as LM-DED and selective laser melting of Alloy 718, result in PDAS values with a similar order of magnitude to EB-PBF [66, 118], which indicates that the segregated microstructures produced in these processes can be homogenised rather rapidly compared with cast products. This difference could facilitate the design of new heat treatment protocols for AM microstructures.

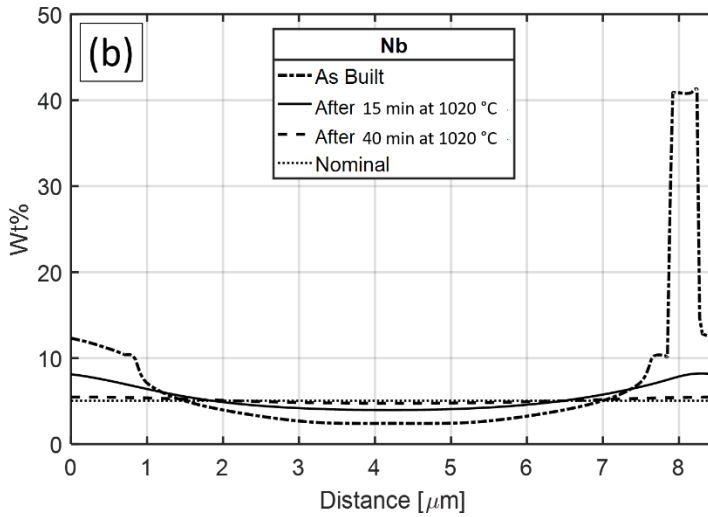
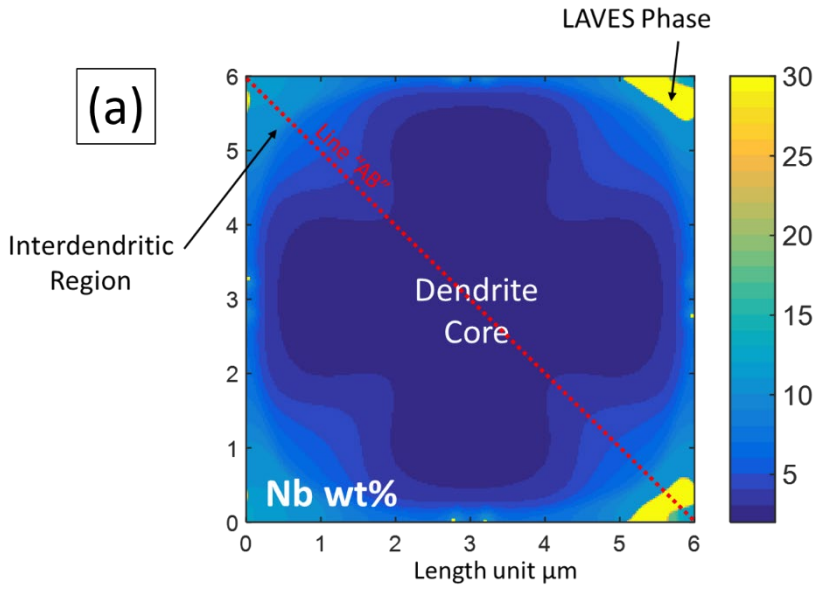


Figure 23: (a) Nb distribution map at the end of non-equilibrium solidification in EB-PBF, (b) Nb distribution map along line AB during “in situ” heat treatment in EB-PBF process. (from **Paper C**, reprinted with permission)

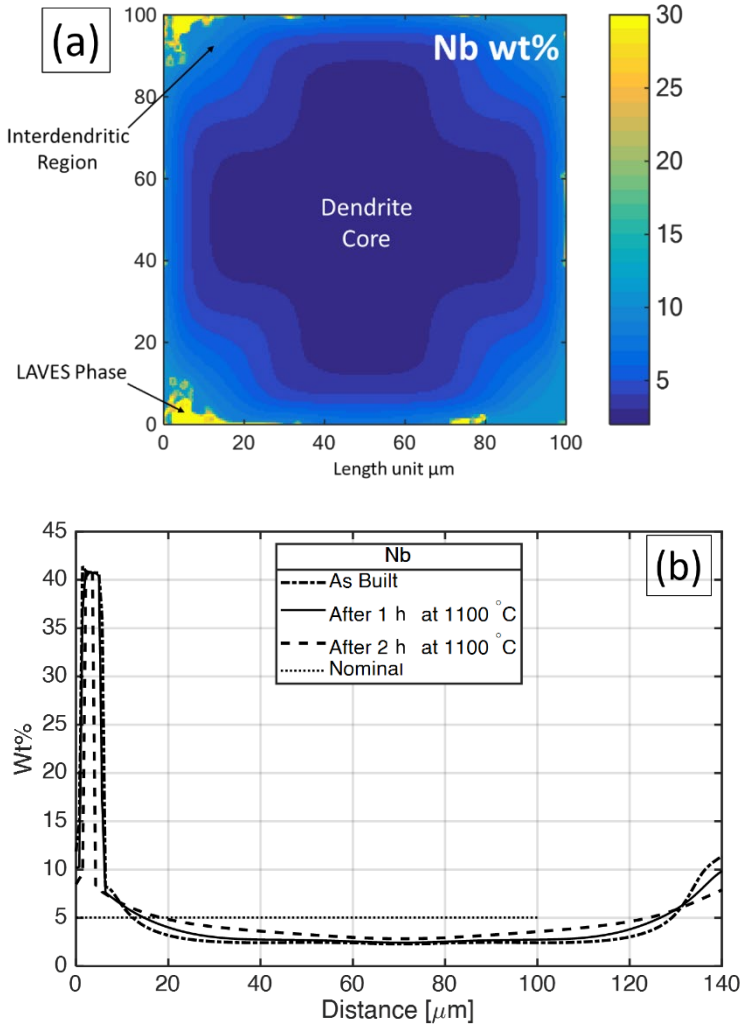


Figure 24: (a) Nb distribution map at the end of solidification in cast Alloy 718, (b) Nb distribution map along line AB during homogenisation heat treatment in cast Alloy 718. (from *Paper C*, reprinted with permission)

### 3.7.3 Critical discussion of the modelling results

The results and discussion presented in *sections 3.7.1* and *3.7.2* provide answers to the research questions stated in *section 2.1*. It has been shown that the multiphase-field modelling approach described in this thesis is capable of modelling the microstructure evolution in AM Alloy 718. This work resulted in a better understanding of how the thermal conditions affect the microstructure formation during the process and subsequent heat treatments. It should be noted that the



modelling approach used in this work can also be used to study the relationships between thermal conditions and microstructure formation in other manufacturing methods with the restriction of diffusion-controlled phase transformations.

The overall results presented in this thesis are qualitative. Predicting quantitative results at the moment is still a challenge. One of the main reasons for this is the errors that were identified in the TCNI8 database, including the fact that the phase diagram description for Alloy 718 in the TCNI8 database contains some errors. As shown in Paper C, there is a major difference between the Nb concentration predicted in the Laves phase and the experimentally observed value. This could influence the equilibrium volume fraction and driving force values for the Laves phase. In addition, the representation of equilibrium volume fractions for  $\gamma'$  and  $\gamma''$  in TCNI8 was identified to be wrong. The database predicts a higher volume fraction for  $\gamma'$  than  $\gamma''$ , whereas experimental data [119, 120] show the opposite trend. Another reason is the uncertainties associated with the mobility database (MOBNI4) used in this work. No experimental validation was performed to this extent in this study.

Another problem that challenges the quantitative prediction of results is the correct representation of the frequency of nucleation (time or temperature intervals for checking nucleation), the number of nucleation sites, and the initial radius of the nucleation seed. In the present work, no calibration was performed from this aspect because of the lack of experimental data. Even if the parameters related to nucleation were calibrated for a given thermal condition (either given constant temperature or given cooling rate), it might be the case that the calibrated parameters may not be adopted in another thermal condition. In general, this is a fundamental challenge that all microstructure models face. Thus, further research is needed to determine the nucleation parameters using detailed experimental data. The nucleation parameters used in the present work are either selected based on trial and error or with an educated guess. Having said this, the simulation work presented in this thesis was able to reveal the important relationships between the process conditions and the underlying microstructure formation during the AM process, as well as in subsequent heat treatments.

The interfacial energy is an important parameter in PF simulations, as it influences the curvature undercooling and morphology of the phase. According to the author's knowledge, there are no experimentally measured values that are available in the literature regarding the interfacial values for the phases considered in this study. Therefore, in the present simulations, the interfacial values reported in other PF studies of Alloy 718 were used. However, interfacial values for the Laves phase were not available in the literature at the time of the modelling work. However, a recent work by H. Jin et al. [121] reported the interfacial energy for the Laves phase ( $\text{Ni}_2\text{Nb}$ ) in a Ni matrix. They showed that the most stable version



## RESULTS AND DISCUSSION

of the Laves phase had an interfacial energy of  $4.32\text{E-}05 \text{ J/cm}^2$ . This value is approximately one order of magnitude larger than the interfacial value used in the modelling work presented in *section 3.4.2.1*. To investigate the impact of this, the simulation that was performed in *Section 3.4.2.2* was run with the above Laves-phase interfacial energy for liquid/Laves and  $\gamma$ /Laves. The results are shown in **Figure 25**. No significant difference was observed regarding either the Laves-phase morphology or volume fraction.

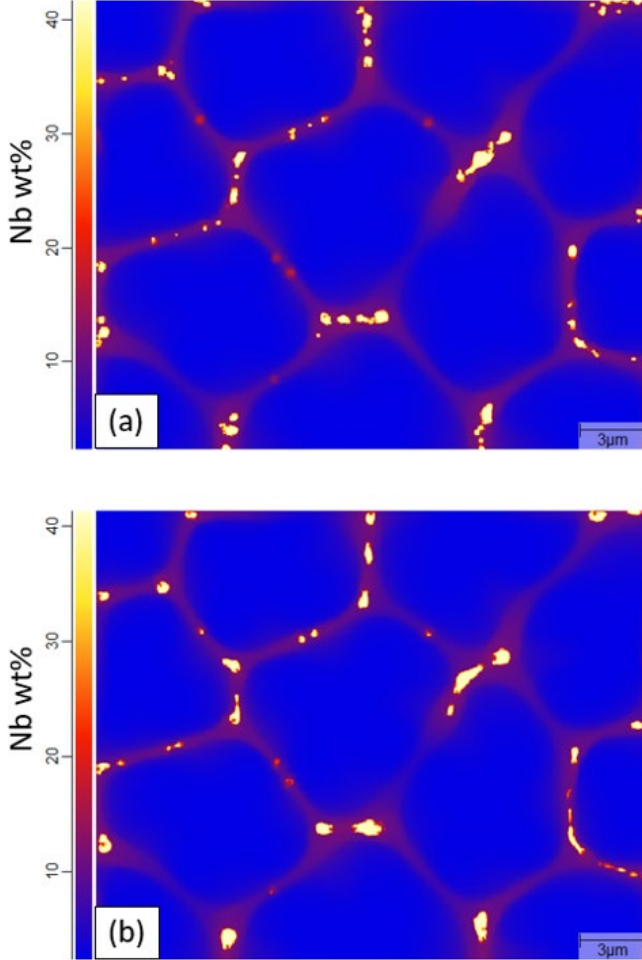


*Figure 25: As-built microstructure at the end of non-equilibrium solidification simulation: (a) with modified Laves phase energy and (b) with Laves phase energy given in Table 3. The domain size is  $25 \mu\text{m} \times 20 \mu\text{m}$ .*

One of the main drawbacks of PF models is that they are computationally demanding; thus, component-scale simulations are still not feasible. However, using techniques such as adaptive grids can reduce the computational time required for PF simulation. In addition, the adaptive grid will also be helpful for resolving the of fine-scale precipitates in a larger grid-size simulation.

When it comes to post heat treatment simulations related to EB-PBF, no simulations were performed in MICRESS. The reason for this is as follows: The EB-PBF-built Alloy 718 is commonly subjected to HIP treatment to remove defects such as pores and lack of fusions that exist in the as-built material. This is usually performed at 1120–1185 °C in an inert atmosphere for 4 h (according to ASTM F3055 standard). This means that after HIP treatment, phases such as  $\gamma'$ ,  $\gamma''$ , and  $\delta$  will completely dissolve and the chemical composition of the matrix will be homogenised. Then, this homogenised matrix will be the starting point for  $\gamma'$ ,  $\gamma''$ , and  $\delta$  phase precipitation. In such a scenario, data related to the phase transformation aspect in Alloy 718 are already available in the literature [115], [117]–[125], and thus modelling was not performed for EB-PBF-built Alloy 718 heat treatments.

## **Part 2**

### **4 Elastic property modelling of AM Alloy 718**

This chapter provides a short summary related to the modelling work that was undertaken to investigate the elastic properties of EB-PBF Alloy 718. For more details, the reader is advised to refer to *Paper D* appended to this thesis.

In this study, the anisotropic elastic properties of EB-PBF Alloy 718 was modelled using experimentally acquired EBSD data. To compare the results with the experimental data, only the EBSD data taken from the hatch region were used. Along the build direction, the samples preferentially showed a strong  $\langle 001 \rangle$  crystallographic orientation. This type of texture in the hatch region is commonly observed in the EB-PBF Alloy 718 when the samples are built using standard Alloy 718 parameters recommended by the equipment manufacturer. Based on the crystallographic orientation data gathered from EBSD data and single crystal elastic constants, the Young's modulus values in the build direction and normal to the build direction were calculated using object-oriented finite element code, OOF2 [131]. The prediction showed good agreement with published data. The hatch region of the EB-PBF samples showed significant anisotropic elastic properties. The lowest Young's modulus was observed along the build direction. Normal to the build direction, the elastic properties were shown to be isotropic. Overall, the elastic behaviour of the hatch region was similar to that of a transversely isotropic case. Using the Hill criteria [132], the full anisotropic elastic stiffness matrix was calculated. This data is important in component-level finite element simulation of EB-PBF build components. It should also be noted that as a result of this anisotropy, the mechanical performance of the component will change depending on how the build part is oriented in the build chamber. It is also worth mentioning that the proposed modelling method can be used to evaluate the elastic properties of functionally graded or tailored microstructures using AM.

One can extend this work to predict the flow curves of a material using the crystal plasticity finite element approach. However, this was not performed in the current study.



## 5 Summary and conclusions

The research work conducted in this thesis demonstrates microstructure modelling work related to AM of Alloy 718. The main objective of this work was to utilise a computational modelling approach to gain an understanding of the relationships between thermal conditions and microstructure formation during AM and the subsequent heat treatment related to Alloy 718. Two different AM processes, namely, LMP-DED and EB-PBF, were considered. In addition to modelling the alloy system with seven elements, the work presented in this thesis is the first modelling (to the best of the authors knowledge) work that involves the modelling of actual Laves phase formation in this alloy. The results obtained from the modelling work have been published in four peer-reviewed journal articles, which are appended to this thesis.

Based on the results presented in *section 3.7*, the following conclusions can be drawn that provide answers to the research questions defined in *section 2.1*.

**RQ1: How can the microstructure evolution during additive manufacturing and subsequent heat treatments be modelled based on the thermal conditions?**

- The combined approach involving multiphase multicomponent PF modelling and transformation kinetic modelling can be used to model the microstructure formation during AM of Alloy 718 and subsequent heat treatments. This approach was able to reveal the important relationships between the thermal conditions and microstructure formation. Details regarding the modelling approach can be found in *Section 3.4* and *3.5*.

**RQ2: How do these thermal conditions affect the microstructure formation during the additive manufacturing and subsequent heat treatments?**

- Solidification conditions (thermal gradient and cooling rate) that occur during the AM process do have an impact on the microstructure evolution and the resultant Laves phase formation. With an increase in cooling rate, the Laves phase volume fraction becomes lower and the morphology tends to become discrete particles. The impact of the cooling rate is more pronounced than the impact of the thermal gradients (for more details, refer to *section 3.7.1.1*).
- Precipitates that formed during deposition do not undergo any significant change during subsequent thermal cycles associated with the deposition of

subsequent layers, given that the deposition of the subsequent layer does not increase the global temperature  $> 600\text{ }^{\circ}\text{C}$ . If the global temperature were to increase above  $600\text{ }^{\circ}\text{C}$ , then phase changes would be expected, depending on the temperature value (for more details, refer to *section 3.7.1.3*).

- In the case of the EB-PBF process, the high build temperature during production resulted in an “*in situ*” heat treatment, which had a homogenisation effect on the as-solidified microstructure (for more details, refer to *section 3.7.2*).
- Because of the smaller dendrite spacing and relatively small Laves phase size, AM Alloy 718 exhibited more rapid homogenisation compared with the cast material (for more details, refer to *section 3.7.2*).

**RQ3: How does the segregation of elements that occur during solidification affect phase transformation kinetics?**

- Microsegregation of the composition observed in the as-built microstructure was shown to change the equilibrium conditions and precipitation kinetics of Alloy 718. As a result, excess precipitation of  $\gamma'/\gamma''$  and  $\delta$  is observed in the interdendritic region compared with the dendrite core depending on the type of heat treatment that is used (for more details, refer to *section 3.7.1.2*).

**RQ4: How can the elastic properties be predicted based on the microstructure?**

- Using the crystallographic orientation data and single crystal elastic constants, the elastic properties can be modelled using the finite element method. In addition, the Hill criteria could also be used to calculate the full stiffness matrix. (for more details, refer to *chapter 4*)

## 6 Future work

When looking at the recent developments in metal AM, it is evident that metal AM has begun to revolutionise the manufacturing industry. It has opened up new possibilities for engineers that did not exist with traditional manufacturing techniques. Nevertheless, to be able to fully employ its potential, further research is needed that provides a solid understanding of the process–microstructure–property relationships with metal AM. To this end, the main research work presented in this thesis utilised a modelling approach to reveal the relationship between the thermal condition and microstructure formation in AM of Alloy 718. The approach provided in this thesis can also be extended to other alloy systems. While providing answers to the research questions defined in this thesis, it was identified that further work is needed to fully capitalise on the capability of the microstructure modelling framework. It is therefore suggested that future research should be aimed at the following areas.

As mentioned in *section 3.7.3*, further work is required to determine the nucleation parameters of the phases. Detailed experimental work should be performed to obtain these nucleation parameters for a variety of alloys. In addition, further work is also needed to determine the interfacial energy of the phase boundaries as a function of temperature. First-principles calculations using density functional theory could shed light on this aspect. The outcome of this research work will improve the accuracy and predictability of the microstructure models. Thermodynamic databases provided from Thermo-Calc databases also provide the values for interfacial energies for the phase boundaries. However, at present, the accuracy of these values is questionable. The accuracy of the thermodynamic and mobility databases should also be improved. This will not only help to improve the microstructure prediction, but will also help to design new alloy systems for AM-specific applications.

In the present study, the elastic interactions were neglected because of the lack of elastic data available for each phase. Therefore, future research could aim to obtain these values for individual phases. Experimental techniques such as nanoindentation can shed light on this aspect. This will help predict the overall elastic properties of the predicted microstructure. In addition, the PF models provide information related to phase volume fractions and their growth and morphology. This information could be used as inputs to constitutive models that predict the mechanical properties.

Additive manufacturing allows the production of a wide range of grain microstructures, from columnar to equiaxed grains, in a single part. Consequently, designing HIP and HTs applicable to all these different grain structures will definitely be a challenging task, as these structures tend to behave differently under post-HIP and HT conditions. Therefore, microstructure models at the grain scale could be used to gain an understanding of how temperature and phases affect grain growth. To this end, PF models could also be used. However, challenges remain when determining parameters related to grain boundary energies and mobilities.

When it comes to mechanical property modelling (eg: tensile stress–strain response, fatigue), future research could focus on the crystal plasticity modelling approach. This approach can be used to model the tensile behaviour of different grain structures and their combinations, as AM has been proven to be a manufacturing method that enables local grain structure control. Another advantage of AM is that it enables designers to incorporate lattice structures into the component to reduce the weight. However, finite element modelling of a full-scale component with all the actual lattice structures will require a huge amount of computational resources and, in some cases, it might not even be practical. Hence, homogenisation approaches should be developed to correctly model and transfer the mechanical response of the unit cell of a lattice structure to an equivalent continuum unit cell model, which can be efficiently used to reduce the computational cost.



## 7 Bibliography

- [1] T. DebRoy, H. L. Wei, J. S. Zuback, T. Mukherjee, J. W. Elmer, J. O. Milewski, A. M. Beese, A. Wilson-Heid, A. De, and W. Zhang, “Additive manufacturing of metallic components – Process, structure and properties,” *Progress in Materials Science*, vol. 92, pp. 112–224, Mar. 2018, doi: 10.1016/j.pmatsci.2017.10.001.
- [2] T. Rockstroh, D. Abbott, K. Hix, and J. Mook, “Additive manufacturing at GE Aviation,” *Industrial Laser Solutions*, 2013. <https://www.industrial-lasers.com/articles/print/volume-28/issue-6/features/additive-manufacturing-at-ge-aviation.html> (accessed Jul. 12, 2018).
- [3] S. Ford and M. Despeisse, “Additive manufacturing and sustainability: An exploratory study of the advantages and challenges,” *Journal of Cleaner Production*, vol. 137, pp. 1573–1587, 2016, doi: 10.1016/j.jclepro.2016.04.150.
- [4] M. K. Hod Lipson, *Fabricated The New World of 3D Printing*, no. 1. John Wiley and Sons, 2013.
- [5] M. Markl and C. Körner, “Multiscale Modeling of Powder Bed–Based Additive Manufacturing,” *Annual Review of Materials Research*, vol. 46, pp. 93–123, Mar. 2016, doi: 10.1146/annurev-matsci-070115-032158710.
- [6] M. M. Francois, A. Sun, W. E. King, N. J. Henson, D. Tournet, C. A. Bronkhorst, N. N. Carlson, C. K. Newman, T. Haut, J. Bakosi, J. W. Gibbs, V. Livescu, S. A. Vander Wiel, A. J. Clarke, M. W. Schraad, T. Blacker, H. Lim, T. Rodgers, S. Owen, F. Abdeljawad, J. Madison, A. T. Anderson, J.-L. Fattebert, R. M. Ferencz, N. E. Hodge, S. A. Khairallah, and O. Walton, “Modeling of additive manufacturing processes for metals: Challenges and opportunities,” *Current Opinion in Solid State and Materials Science*, vol. 21, no. 4, pp. 198–206, Aug. 2017, doi: 10.1016/j.cossms.2016.12.001.
- [7] C. Kumara, “Microstructure Modelling of Additive Manufacturing of Alloy 718,” Licentiate Thesis: University West, 2018.
- [8] C. Kumara, A. R. Balachandramurthi, S. Goel, F. Hanning, and J. Moverare, “Toward a better understanding of phase transformations in additive manufacturing of Alloy 718,” *Materialia*, vol. 13, no. June, p. 100862, Sep. 2020, doi: 10.1016/j.mtla.2020.100862.

- [9] C. Kumara, A. Segerstark, F. Hanning, N. Dixit, S. Joshi, J. Moverare, and P. Nylén, “Microstructure modelling of laser metal powder directed energy deposition of alloy 718,” *Additive Manufacturing*, vol. 25, pp. 357–364, Jan. 2019, doi: 10.1016/j.addma.2018.11.024.
- [10] C. Kumara, D. Deng, F. Hanning, M. Raanes, J. Moverare, and P. Nylén, “Predicting the Microstructural Evolution of Electron Beam Melting of Alloy 718 with Phase-Field Modeling,” *Metallurgical and Materials Transactions A: Physical Metallurgy and Materials Science*, vol. 50, no. 5, pp. 2527–2537, 2019, doi: 10.1007/s11661-019-05163-7.
- [11] C. Kumara, D. Deng, J. Moverare, and P. Nylén, “Modelling of anisotropic elastic properties in alloy 718 built by electron beam melting,” *Materials Science and Technology*, vol. 34, no. 5, pp. 529–537, Mar. 2018, doi: 10.1080/02670836.2018.1426258.
- [12] H. L. Wei, T. Mukherjee, W. Zhang, J. S. Zuback, G. L. Knapp, A. De, and T. DebRoy, “Mechanistic models for additive manufacturing of metallic components,” *Progress in Materials Science*, p. 100703, Jun. 2020, doi: 10.1016/j.pmatsci.2020.100703.
- [13] D. U. Furrer and S. L. Semiatin, *ASM Handbook Volume 22A Fundamentals of Modeling for Metals Processing*, vol. 22A. ASM International ASM, 2009.
- [14] K. Janssens, D. Raabe, E. Kozeschnik, M. A. Miodownik, and B. Nestler, *Computational materials engineering: an introduction to microstructure evolution*. Academic Press, 2010.
- [15] A. . Fallis, *Computational Methods for Microstructure-Property Relationships*, vol. 53, no. 9. 2013.
- [16] D. U. Furrer, *ASM Handbook Volume 22B Metals Process Simulation*, vol. 22B. ASM International, 2010.
- [17] Porter D A; E. K. E, and M. Y. SHERIF, *Phase Transformations in metals and alloys*. CRC Press, 2009.
- [18] J. W. Christian, “The Theory of Transformations in Metals and Alloys,” *Materials Today*, vol. 6, no. 3, p. 53, Mar. 2003, doi: 10.1016/S1369-7021(03)00335-3.
- [19] L.-E. Lindgren, A. Lundbäck, M. Fisk, R. Pederson, and J. Andersson, “Simulation of additive manufacturing using coupled constitutive and microstructure models,” *Additive Manufacturing*, vol. 12, pp. 144–158, Oct. 2016, doi: 10.1016/j.addma.2016.05.005.

## BIBLIOGRAPHY

- [20] S. M. Kelly, “Thermal and Microstructure Modeling of Metal Deposition Processes with Application to Ti-6Al-4V,” 2004.
- [21] S. J. JONES and H. K. D. H. BHADESHIA, “KINETICS OF THE SIMULTANEOUS DECOMPOSITION OF AUSTENITE INTO SEVERAL TRANSFORMATION PRODUCTS,” *Acta Materialia*, vol. 45, no. 7, pp. 2911–2920, Jul. 1997, doi: 10.1016/S1359-6454(96)00392-8.
- [22] K. T. Makiewicz, “Development of simultaneous transformation kinetics microstructure model with application to laser metal deposited Ti-6Al-4V and alloy 718,” The Ohio State University, 2013.
- [23] “Sente Software - JMatPro®.”  
<https://www.sentesoftware.co.uk/jmatpro> (accessed Oct. 08, 2020).
- [24] X. Li, A. P. Miodownik, and N. Saunders, “Modelling of materials properties in duplex stainless steels,” *Materials Science and Technology*, vol. 18, no. 8, pp. 861–868, 2002, doi: 10.1179/026708302225004694.
- [25] N. Saunders, Z. Guo, X. Li, A. P. Miodownik, and J. P. Schillé, “Using JMatPro to model materials properties and behavior,” *Jom*, vol. 55, no. 12, pp. 60–65, 2003, doi: 10.1007/s11837-003-0013-2.
- [26] H. J. Jou, P. Voorhees, and G. B. Olson, “Computer simulations for the prediction of microstructure/property variation in aeroturbine disks,” *Proceedings of the International Symposium on Superalloys*, pp. 877–886, 2004, doi: 10.7449/2004/superalloys\_2004\_877\_886.
- [27] M. J. Anderson, C. Panwisawas, Y. Sovani, R. P. Turner, J. W. Brooks, and H. C. Basoalto, “Mean-field modelling of the intermetallic precipitate phases during heat treatment and additive manufacture of Inconel 718,” *Acta Materialia*, vol. 156, pp. 432–445, 2018, doi: 10.1016/j.actamat.2018.07.002.
- [28] J. Svoboda, F. D. Fischer, P. Fratzl, and E. Kozeschnik, “Modelling of kinetics in multi-component multi-phase systems with spherical precipitates I: Theory,” *Materials Science and Engineering A*, vol. 385, no. 1–2, pp. 166–174, 2004, doi: 10.1016/j.msea.2004.06.018.
- [29] G. Lindwall, C. E. Campbell, E. A. Lass, F. Zhang, M. R. Stoudt, A. J. Allen, and L. E. Levine, “Simulation of TTT Curves for Additively Manufactured Inconel 625,” *Metallurgical and Materials Transactions A*, vol. 50, no. 1, pp. 457–467, Jan. 2019, doi: 10.1007/s11661-018-4959-7.
- [30] Thermo-Calc Software, “Precipitation module (TC-PRISMA),” 2017.

[https://www.thermocalc.com/products-services/software/precipitation-module-\(tc-prisma\)/](https://www.thermocalc.com/products-services/software/precipitation-module-(tc-prisma)/) (accessed Jul. 24, 2020).

- [31] E. Kozeschnik, “Matcalc - Solid State and Kinetics Precipitation.” <https://www.matcalc.at/> (accessed Oct. 06, 2020).
- [32] H. C. Basoalto, C. Panwisawas, Y. Sovani, M. J. Anderson, R. P. Turner, B. Saunders, and J. W. Brooks, “A computational study on the three-dimensional printability of precipitate-strengthened nickel-based superalloys,” *Proceedings of the Royal Society A: Mathematical, Physical and Engineering Sciences*, vol. 474, no. 2220, 2018, doi: 10.1098/rspa.2018.0295.
- [33] M. J. Anderson, J. Benson, J. W. Brooks, B. Saunders, and H. C. Basoalto, “Predicting Precipitation Kinetics During the Annealing of Additive Manufactured Inconel 625 Components,” *Integrating Materials and Manufacturing Innovation*, vol. 8, no. 2, pp. 154–166, 2019, doi: 10.1007/s40192-019-00134-7.
- [34] Thermocalc, “Diffusion Module (DICTRA),” *Thermo-Calc Software*, 2019. [https://www.thermocalc.com/products-services/software/diffusion-module-\(dictra\)/](https://www.thermocalc.com/products-services/software/diffusion-module-(dictra)/) (accessed Jul. 24, 2020).
- [35] D. Raabe, “Cellular Automata in Materials Science with Particular Reference to Recrystallization Simulation,” *Annual Review of Materials Research*, vol. 32, no. 1, pp. 53–76, 2002, doi: 10.1146/annurev.matsci.32.090601.152855.
- [36] H. B. Dong and P. D. Lee, “Simulation of the columnar-to-equiaxed transition in directionally solidified Al-Cu alloys,” *Acta Materialia*, vol. 53, no. 3, pp. 659–668, 2005, doi: 10.1016/j.actamat.2004.10.019.
- [37] R. C. Atwood and P. D. Lee, “Simulation of the three-dimensional morphology of solidification porosity in an aluminium-silicon alloy,” *Acta Materialia*, vol. 51, no. 18, pp. 5447–5466, 2003, doi: 10.1016/S1359-6454(03)00411-7.
- [38] Y. Zhao, R. S. Qin, and D. F. Chen, “A three-dimensional cellular automata model coupled with finite element method and thermodynamic database for alloy solidification,” *Journal of Crystal Growth*, vol. 377, pp. 72–77, 2013, doi: 10.1016/j.jcrysgro.2013.05.006.
- [39] W. Tan, N. S. Bailey, and Y. C. Shin, “A novel integrated model combining Cellular Automata and Phase Field methods for microstructure evolution during solidification of multi-component and multi-phase alloys,” *Computational Materials Science*, vol. 50, no. 9, pp. 2573–2585, 2011, doi:

## BIBLIOGRAPHY

10.1016/j.commatsci.2011.03.044.

- [40] F. Roters, P. Eisenlohr, T. R. Bieler, and D. Raabe, *Crystal Plasticity Finite Element Methods*, 1st ed. Weinheim, Germany: Wiley-VCH Verlag GmbH & Co. KGaA, 2010.
- [41] F. Liu, F. Lyu, F. Liu, X. Lin, and C. Huang, “Laves phase control of inconel 718 superalloy fabricated by laser direct energy deposition via  $\delta$  aging and solution treatment,” *Journal of Materials Research and Technology*, vol. 9, no. 5, pp. 9753–9765, Sep. 2020, doi: 10.1016/j.jmrt.2020.06.061.
- [42] Y. Lian, Z. Gan, C. Yu, D. Kats, W. K. Liu, and G. J. Wagner, “A cellular automaton finite volume method for microstructure evolution during additive manufacturing,” *Materials and Design*, vol. 169, p. 107672, 2019, doi: 10.1016/j.matdes.2019.107672.
- [43] X. P. Tan, S. Chandra, Y. Kok, S. B. Tor, G. Seet, N. H. Loh, and E. Liu, “Revealing competitive columnar grain growth behavior and periodic microstructural banding in additively manufactured Ti-6Al-4 V parts by selective electron beam melting,” *Materialia*, vol. 7, no. May, p. 100365, 2019, doi: 10.1016/j.mtla.2019.100365.
- [44] J. A. Koepf, D. Soldner, M. Ramsperger, J. Mergheim, M. Markl, and C. Körner, “Numerical microstructure prediction by a coupled finite element cellular automaton model for selective electron beam melting,” *Computational Materials Science*, vol. 162, no. March, pp. 148–155, 2019, doi: 10.1016/j.commatsci.2019.03.004.
- [45] J. Akram, P. Chalavadi, D. Pal, and B. Stucker, “Understanding grain evolution in additive manufacturing through modeling,” *Additive Manufacturing*, vol. 21, no. February, pp. 255–268, 2018, doi: 10.1016/j.addma.2018.03.021.
- [46] J. Yang, H. Yu, H. Yang, F. Li, Z. Wang, and X. Zeng, “Prediction of microstructure in selective laser melted Ti-6Al-4V alloy by cellular automaton,” *Journal of Alloys and Compounds*, vol. 748, pp. 281–290, 2018, doi: 10.1016/j.jallcom.2018.03.116.
- [47] J. A. Koepf, M. R. Gotterbarm, M. Markl, and C. Körner, “3D multi-layer grain structure simulation of powder bed fusion additive manufacturing,” *Acta Materialia*, vol. 152, pp. 119–126, Jun. 2018, doi: 10.1016/j.actamat.2018.04.030.
- [48] A. Zinoviev, O. Zinovieva, V. Ploshikhin, V. Romanova, and R. Balokhonov, “Evolution of grain structure during laser additive manufacturing. Simulation by a cellular automata method,” *Materials &*

*Design*, vol. 106, pp. 321–329, 2016, doi: 10.1016/j.matdes.2016.05.125.

- [49] A. Rai, M. Markl, and C. Körner, “A coupled Cellular Automaton–Lattice Boltzmann model for grain structure simulation during additive manufacturing,” *Computational Materials Science*, vol. 124, pp. 37–48, 2016, doi: 10.1016/j.commatsci.2016.07.005.
- [50] P. Nie, O. A. Ojo, and Z. Li, “Numerical modeling of microstructure evolution during laser additive manufacturing of a nickel-based superalloy,” *Acta Materialia*, vol. 77, pp. 85–95, Sep. 2014, doi: 10.1016/j.actamat.2014.05.039.
- [51] S. Liu and Y. C. Shin, “Integrated 2D cellular automata-phase field modeling of solidification and microstructure evolution during additive manufacturing of Ti6Al4V,” *Computational Materials Science*, vol. 183, no. May, p. 109889, 2020, doi: 10.1016/j.commatsci.2020.109889.
- [52] S. G. Kim and W. Tae Kim, “Phase-field modeling of rapid solidification,” *Materials Science and Engineering: A*, vol. 304–306, pp. 281–286, May 2001, doi: 10.1016/S0921-5093(00)01453-2.
- [53] B. Echebarria, R. Folch, A. Karma, and M. Plapp, “Quantitative Phase Field Model of Alloy Solidification,” *Review E - Statistical, Nonlinear, and Soft Matter Physics*, vol. 70, no. 6, pp. 1–51, 2004, doi: 10.1103/PhysRevE.70.061604.
- [54] N. Moelans, B. Blanpain, and P. Wollants, “An introduction to phase-field modeling of microstructure evolution,” *Calphad*, vol. 32, no. 2, pp. 268–294, Jun. 2008, doi: 10.1016/j.calphad.2007.11.003.
- [55] I. Steinbach, “Phase-field models in materials science,” *Modelling and Simulation in Materials Science and Engineering*, vol. 17, no. 7, pp. 73001–31, 2009, doi: 10.1088/0965-0393/17/7/073001.
- [56] S. Sahoo and K. Chou, “Phase-field simulation of microstructure evolution of Ti–6Al–4V in electron beam additive manufacturing process,” *Additive Manufacturing*, vol. 9, pp. 14–24, Jan. 2016, doi: 10.1016/j.addma.2015.12.005.
- [57] I. Steinbach, F. Pezzolla, B. Nestler, M. Seeßelberg, R. Prieler, G. J. Schmitz, and J. L. L. Rezende, “A phase field concept for multiphase systems,” *Physica D: Nonlinear Phenomena*, vol. 94, no. 3, pp. 135–147, Jul. 1996, doi: 10.1016/0167-2789(95)00298-7.
- [58] J. Eiken, B. Böttger, and I. Steinbach, “Multiphase-field approach for multicomponent alloys with extrapolation scheme for numerical

## BIBLIOGRAPHY

- application,” *Physical Review E*, vol. 73, no. 6, p. 066122, Jun. 2006, doi: 10.1103/PhysRevE.73.066122.
- [59] V. L. Ginzburg and L. D. Landau, “On the Theory of Superconductivity,” in *On Superconductivity and Superfluidity*, Berlin, Heidelberg: Springer Berlin Heidelberg, 2008, pp. 113–137.
- [60] J. W. Cahn and J. E. Hilliard, “Free energy of a nonuniform system. I. Interfacial free energy,” *The Journal of Chemical Physics*, vol. 28, no. 2, pp. 258–267, Feb. 1958, doi: 10.1063/1.1744102.
- [61] R. Kobayashi, “Modeling and numerical simulations of dendritic crystal growth,” *Physica D: Nonlinear Phenomena*, vol. 63, no. 3–4, pp. 410–423, Mar. 1993, doi: 10.1016/0167-2789(93)90120-P.
- [62] L. Q. Chen, “Phase-field models for microstructure evolution,” *Annual Review of Materials Science*, vol. 32, pp. 113–140, 2002, doi: 10.1146/annurev.matsci.32.112001.132041.
- [63] R. Acharya, J. A. Sharon, and A. Staroselsky, “Prediction of microstructure in laser powder bed fusion process,” *Acta Materialia*, vol. 124, pp. 360–371, Feb. 2017, doi: 10.1016/j.actamat.2016.11.018.
- [64] S. Ghosh, L. Ma, and N. Ofori-Opoku, “On the primary spacing and microsegregation of cellular dendrites in laser deposited Ni-Nb alloys,” *Modelling Simul. Mater. Sci. Eng.*, vol. 25, pp. 1–22, 2017, doi: 10.1088/1361-651X/aa7369.
- [65] S. Ghosh, M. R. Stoudt, L. E. Levine, and J. E. Guyer, “Formation of Nb-rich droplets in laser deposited Ni-matrix microstructures,” *Scripta Materialia*, vol. 146, pp. 36–40, 2017, doi: 10.1016/j.scriptamat.2017.10.034.
- [66] J. Kundin, L. Mushongera, and H. Emmerich, “Phase-field modeling of microstructure formation during rapid solidification in Inconel 718 superalloy,” *Acta Materialia*, vol. 95, pp. 343–356, Aug. 2015, doi: 10.1016/j.actamat.2015.05.052.
- [67] X. Gong and K. Chou, “Phase-Field Modeling of Microstructure Evolution in Electron Beam Additive Manufacturing,” *Jom*, vol. 67, no. 5, pp. 1176–1182, 2015, doi: 10.1007/s11837-015-1352-5.
- [68] K. Karayagiz, L. Johnson, R. Seede, V. Attari, B. Zhang, X. Huang, S. Ghosh, T. Duong, I. Karaman, A. Elwany, and R. Arróyave, “Finite interface dissipation phase field modeling of Ni–Nb under additive manufacturing conditions,” *Acta Materialia*, vol. 185, pp. 320–339, 2020,

doi: 10.1016/j.actamat.2019.11.057.

- [69] I. Steinbach, L. Zhang, and M. Plapp, “Phase-field model with finite interface dissipation,” *Acta Materialia*, vol. 60, no. 6–7, pp. 2689–2701, 2012, doi: 10.1016/j.actamat.2012.01.035.
- [70] Ian Gibson, D. Rosen, and B. Stucker, *Additive Manufacturing Technologies 3D Printing, Rapid Prototyping, and Direct Digital Manufacturing*, 2nd ed. Springer US, 2014.
- [71] “Laser Metal Deposition LMD Feed Nozzle.” <http://www.twi-global.com/capabilities/joining-technologies/additive-manufacturing/laser-metal-deposition/> (accessed May 31, 2017).
- [72] Y. Tian, D. McAllister, H. Colijn, M. Mills, D. Farson, M. Nordin, and S. Babu, “Rationalization of Microstructure Heterogeneity in INCONEL 718 Builds Made by the Direct Laser Additive Manufacturing Process,” *Metallurgical and Materials Transactions A*, vol. 45, no. 10, pp. 4470–4483, Sep. 2014, doi: 10.1007/s11661-014-2370-6.
- [73] F. Liu, X. Lin, C. Huang, M. Song, G. Yang, J. Chen, and W. Huang, “The effect of laser scanning path on microstructures and mechanical properties of laser solid formed nickel-base superalloy Inconel 718,” *Journal of Alloys and Compounds*, vol. 509, no. 13, pp. 4505–4509, Mar. 2011, doi: 10.1016/j.jallcom.2010.11.176.
- [74] H. Qi, M. Azer, and A. Ritter, “Studies of Standard Heat Treatment Effects on Microstructure and Mechanical Properties of Laser Net Shape Manufactured INCONEL 718,” *Metallurgical and Materials Transactions A*, vol. 40, no. 10, pp. 2410–2422, Oct. 2009, doi: 10.1007/s11661-009-9949-3.
- [75] Y. Zhang, Z. Li, P. Nie, and Y. Wu, “Effect of Cooling Rate on the Microstructure of Laser-Remelted INCONEL 718 Coating,” *Metallurgical and Materials Transactions A*, vol. 44, no. 12, pp. 5513–5521, Dec. 2013, doi: 10.1007/s11661-013-1903-8.
- [76] Y. Zhang, Z. Li, P. Nie, and Y. Wu, “Effect of Precipitation on the Microhardness Distribution of Diode Laser Epitaxially Deposited IN718 Alloy Coating,” *Journal of Materials Science and Technology*, vol. 29, no. 4, pp. 349–352, 2013, doi: 10.1016/j.jmst.2013.01.002.
- [77] X. Zhao, J. Chen, X. Lin, and W. Huang, “Study on microstructure and mechanical properties of laser rapid forming Inconel 718,” *Materials Science and Engineering: A*, vol. 478, no. 1–2, pp. 119–124, Apr. 2008, doi: 10.1016/j.msea.2007.05.079.



## BIBLIOGRAPHY

- [78] R. R. Dehoff, M. M. Kirka, W. J. Sames, H. Bilheux, A. S. Tremsin, L. E. Lowe, and S. S. Babu, "Site specific control of crystallographic grain orientation through electron beam additive manufacturing," *Materials Science and Technology*, vol. 31, no. 8, pp. 931–938, 2015, doi: 10.1179/1743284714Y.0000000734.
- [79] M. M. Kirka, Y. Lee, D. A. Greeley, A. Okello, M. J. Goin, M. T. Pearce, and R. R. Dehoff, "Strategy for Texture Management in Metals Additive Manufacturing," *JOM*, vol. 69, no. 3, pp. 523–531, Mar. 2017, doi: 10.1007/s11837-017-2264-3.
- [80] N. Raghavan, R. Dehoff, S. Pannala, S. Simunovic, M. Kirka, J. Turner, N. Carlson, and S. S. Babu, "Numerical modeling of heat-transfer and the influence of process parameters on tailoring the grain morphology of IN718 in electron beam additive manufacturing," *Acta Materialia*, vol. 112, pp. 303–314, 2016, doi: 10.1016/j.actamat.2016.03.063.
- [81] W. J. SAMES, "Additive manufacturing of inconel 718 using electron beam melting: processing, post-processing, & mechanical properties," Texas A&M University, 2015.
- [82] C. Körner, "Additive manufacturing of metallic components by selective electron beam melting — a review," *International Materials Reviews*, vol. 61, no. 5, pp. 361–377, Jul. 2016, doi: 10.1080/09506608.2016.1176289.
- [83] M. Galati and L. Iuliano, "A literature review of powder-based electron beam melting focusing on numerical simulations," *Additive Manufacturing*, vol. 19, pp. 1–20, 2018, doi: 10.1016/j.addma.2017.11.001.
- [84] M. A. Lodes, R. Guschlbauer, and C. Körner, "Process development for the manufacturing of 99.94% pure copper via selective electron beam melting," *Materials Letters*, vol. 143, pp. 298–301, 2015, doi: 10.1016/j.matlet.2014.12.105.
- [85] J. Schwerdtfeger and C. Körner, "Selective electron beam melting of Ti-48Al-2Nb-2Cr: Microstructure and aluminium loss," *Intermetallics*, vol. 49, pp. 29–35, 2014, doi: 10.1016/j.intermet.2014.01.004.
- [86] S. Sui, H. Tan, J. Chen, C. Zhong, Z. Li, W. Fan, A. Gasser, and W. Huang, "The influence of Laves phases on the room temperature tensile properties of Inconel 718 fabricated by powder feeding laser additive manufacturing," *Acta Materialia*, vol. 164, no. February, pp. 413–427, 2019, doi: 10.1016/j.actamat.2018.10.032.
- [87] M. Anderson, A.-L. Thielin, F. Bridier, P. Bocher, and J. Savoie, "δ Phase precipitation in Inconel 718 and associated mechanical properties,"

- Materials Science and Engineering: A*, vol. 679, pp. 48–55, Jan. 2017, doi: 10.1016/j.msea.2016.09.114.
- [88] G. A. Knorovsky, M. J. Cieslak, T. J. Headley, A. D. Romig, and W. F. Hammetter, “INCONEL 718: A solidification diagram,” *Metallurgical Transactions A*, vol. 20, no. 10, pp. 2149–2158, Oct. 1989, doi: 10.1007/BF02650300.
  - [89] R. W. Hayes, “Creep Deformation of Inconel Alloy 718 in the 650°C To 760°C,” in *Superalloys 718, 625 and Various Derivatives (1991)*, 1991, pp. 549–562, doi: 10.7449/1991/Superalloys\_1991\_549\_562.
  - [90] J. F. Radavich, “The Physical Metallurgy of Cast and Wrought Alloy 718,” in *Superalloys 718 Metallurgy and Applications*, 1989, pp. 229–240, doi: 10.7449/1989/Superalloys\_1989\_229\_240.
  - [91] M. Sundararaman, P. Mukhopadhyay, and S. Banerjee, “Precipitation of the Delta-Ni<sub>3</sub>Nb phase in two nickel base superalloys,” *Metallurgical Transactions A*, vol. 19, no. 3, pp. 453–465, 1988, doi: 10.1007/BF02649259.
  - [92] S. Azadian, L. Y. Wei, and R. Warren, “Delta phase precipitation in inconel 718,” *Materials Characterization*, vol. 53, no. 1, pp. 7–16, 2004, doi: 10.1016/j.matchar.2004.07.004.
  - [93] ASTM F3055-14a, *Standard Specification for Additive Manufacturing Nickel Alloy ( UNS N07718 ) with Powder Bed Fusion*. ASTM International, West Conshohocken, PA, 2014, www.astm.org.
  - [94] J. K. Wessel, *Handbook of Advanced Materials*. Hoboken, NJ, USA: John Wiley & Sons, Inc., 2004.
  - [95] B. Geddes, H. Leon, and X. Huang, *Superalloys - Alloying and Performance*. ASM International, 2010.
  - [96] J. T. Tharappel and J. Babu, “Welding processes for Inconel 718- A brief review Welding processes for Inconel 718- A brief review,” 2018, doi: 10.1088/1757-899X/330/1/012082.
  - [97] D. Deng, R. L. Peng, H. Söderberg, and J. Moverare, “On the formation of microstructural gradients in a nickel-base superalloy during electron beam melting,” *Materials & Design*, vol. 160, pp. 251–261, 2018, doi: 10.1016/J.MATDES.2018.09.006.
  - [98] J. K. Tien and T. Caulfield, *Superalloys, supercomposites and superceramics*. Academic Press, 1989.

## BIBLIOGRAPHY

- [99] T. Antonsson and H. Fredriksson, “The effect of cooling rate on the solidification of INCONEL 718,” *Metallurgical and Materials Transactions B*, vol. 36, no. 1, pp. 85–96, Feb. 2005, doi: 10.1007/s11663-005-0009-0.
- [100] W. M. Haynes, *CRC Handbook of Chemistry and Physics - Google Books*, 97th ed. CRC Press, 2016.
- [101] B. Böttger, J. Eiken, and M. Apel, “Multi-ternary extrapolation scheme for efficient coupling of thermodynamic data to a multi-phase-field model,” *Computational Materials Science*, vol. 108, pp. 283–292, Oct. 2015, doi: 10.1016/j.commatsci.2015.03.003.
- [102] J. Eiken, “A phase-field model for technical alloy solidification,” Shaker Verlag GmbH, Germany, 2010.
- [103] M. Hillert, *Phase Equilibria, Phase Diagrams and Phase Transformations*. Cambridge: Cambridge University Press, 2007.
- [104] “Thermo-Calc Software.” <http://www.thermocalc.com/> (accessed May 25, 2018).
- [105] Micress Group, “MICRESS 6.4 - User Guide Volume II: Running MICRES.” [Online]. Available: [http://web.micress.de/MICRESS\\_Documentation/Vol2\\_Running\\_MICRESS.pdf](http://web.micress.de/MICRESS_Documentation/Vol2_Running_MICRESS.pdf).
- [106] N. Zhou, D. C. Lv, H. L. Zhang, D. McAllister, F. Zhang, M. J. Mills, and Y. Wang, “Computer simulation of phase transformation and plastic deformation in IN718 superalloy: Microstructural evolution during precipitation,” *Acta Materialia*, vol. 65, pp. 270–286, Feb. 2014, doi: 10.1016/j.actamat.2013.10.069.
- [107] N. Warnken, D. Ma, A. Drevermann, R. C. Reed, S. G. Fries, and I. Steinbach, “Phase-field modelling of as-cast microstructure evolution in nickel-based superalloys,” *Acta Materialia*, vol. 57, no. 19, pp. 5862–5875, 2009, doi: 10.1016/j.actamat.2009.08.013.
- [108] M. M. Kirka, K. A. Unocic, N. Raghavan, F. Medina, R. R. Dehoff, and S. S. Babu, “Microstructure Development in Electron Beam-Melted Inconel 718 and Associated Tensile Properties,” *JOM*, vol. 68, no. 3, pp. 1012–1020, Mar. 2016, doi: 10.1007/s11837-016-1812-6.
- [109] SAE, *AMS5383E-Nickel Alloy, Corrosion and Heat-Resistant, Investment Castings*. 2012.
- [110] M. J. Aziz, “Model for solute redistribution during rapid solidification,”

*Journal of Applied Physics*, vol. 53, no. 2, pp. 1158–1168, Feb. 1982, doi: 10.1063/1.329867.

- [111] A. Segerstark, J. Andersson, and L. Svensson, “Evaluation of a temperature measurement method developed for laser metal deposition,” *Science and Technology of Welding and Joining*, vol. 22, no. 1, pp. 1–6, Jan. 2017, doi: 10.1080/13621718.2016.1169363.
- [112] M. L. Barron, “Crack Growth-Based Predictive Methodology for the Maintenance of the Structural Integrity of Repaired and Nonrepaired Aging Engine Stationary Components,” 1999.
- [113] A. Segerstark, J. Andersson, L. Svensson, and O. Ojo, “Microstructural characterization of laser metal powder deposited Alloy 718,” *Materials Characterization*, vol. 142, no. June, pp. 550–559, Aug. 2018, doi: 10.1016/j.matchar.2018.06.020.
- [114] Z. Li, J. Chen, S. Sui, C. Zhong, X. Lu, and X. Lin, “The microstructure evolution and tensile properties of Inconel 718 fabricated by high-deposition-rate laser directed energy deposition,” *Additive Manufacturing*, vol. 31, no. November 2019, p. 100941, 2020, doi: 10.1016/j.addma.2019.100941.
- [115] J. F. Muller and M. J. Donachie, “The effects of solution and intermediate heat treatments on the notch-rupture behavior of Inconel 718,” *Metallurgical and Materials Transactions A*, vol. 6, no. 12, pp. 2221–2227, 1975, doi: 10.1007/BF02818647.
- [116] G. Sjöberg, N. G. Ingesten, and R. G. Carlson, “Grain Boundary  $\delta$ -phase Morphologies, Carbides and Notch Rupture Sensitivity of Cast Alloy 718,” in *Superalloys 718, 625, 706 and Derivatives 1991*, 1991, pp. 603–620, doi: 10.7449/1991/Superalloys\_1991\_603\_620.
- [117] D. Cai, W. Zhang, P. Nie, W. Liu, and M. Yao, “Dissolution kinetics of  $\delta$  phase and its influence on the notch sensitivity of Inconel 718,” *Materials Characterization*, vol. 58, no. 3, pp. 220–225, 2007, doi: 10.1016/j.matchar.2006.04.020.
- [118] Y. S. Lee and W. Zhang, “Modeling of heat transfer, fluid flow and solidification microstructure of nickel-base superalloy fabricated by laser powder bed fusion,” *Additive Manufacturing*, 2016, doi: 10.1016/j.addma.2016.05.003.
- [119] M. C. Chaturvedi and Y. Han, “Strengthening mechanisms in Inconel 718 superalloy,” *Metal Science*, vol. 17, no. 3, pp. 145–149, 1983, doi: 10.1179/030634583790421032.

## BIBLIOGRAPHY

- [120] F. Theska, K. Nomoto, F. Godor, B. Oberwinkler, A. Stanojevic, S. P. Ringer, and S. Primig, "On the early stages of precipitation during direct ageing of Alloy 718," *Acta Materialia*, vol. 188, pp. 492–503, 2020, doi: 10.1016/j.actamat.2020.02.034.
- [121] H. Jin, J. Zhang, Y. Zhang, W. Zhang, and P. Li, "First-principles investigations of effects of solute elements on stability and electronic structure of laves phase/matrix interface in Ni-based superalloys," *Journal of Physics and Chemistry of Solids*, vol. 136, no. September 2019, p. 109166, 2020, doi: 10.1016/j.jpcs.2019.109166.
- [122] M. C. Chaturvedi and Y. Han, "Strengthening mechanisms in Inconel 718 superalloy," *Metal Science*, vol. 17, no. 3, pp. 145–149, Mar. 1983, doi: 10.1179/030634583790421032.
- [123] Y. Han, P. Deb, and M. C. Chaturvedi, "Coarsening behaviour of  $\gamma$ '- and  $\gamma$ '-particles in Inconel alloy 718," *Metal Science*, vol. 16, no. 12, pp. 555–562, Dec. 1982, doi: 10.1179/030634582790427118.
- [124] C. Slama, C. Servant, and G. Cizeron, "Aging of the Inconel 718 alloy between 500 and 750 °C," *Journal of Materials Research*, vol. 12, no. 9, pp. 2298–2316, 1997, doi: 10.1557/JMR.1997.0306.
- [125] M. Sundararaman, N. Sachin, B. S. Jung, V. Amit, P. Bhaskar, and R. Kishore, "Evolution of  $\delta$  Phase Microstructure in Alloy 718," *7th International Symposium on Superalloys 718 and Derivatives*, pp. 737–750, 2010, doi: 10.1002/9781118495223.ch57.
- [126] S. Mahadevan, S. Nalawade, J. B. Singh, A. Verma, B. Paul, and K. Ramaswamy, "Evolution of Delta Phase Microstructure in Alloy 718," in *7th International Symposium on Superalloy 718 and Derivatives*, 2010, pp. 737–750.
- [127] T. Alam, M. Chaturvedi, S. P. Ringer, and J. M. Cairney, "Precipitation and clustering in the early stages of ageing in Inconel 718," *Materials Science and Engineering A*, vol. 527, no. 29–30, pp. 7770–7774, 2010, doi: 10.1016/j.msea.2010.08.053.
- [128] Y. Ji, Y. Lou, M. Qu, J. D. Rowatt, F. Zhang, T. W. Simpson, and L. Q. Chen, "Predicting Coherency Loss of  $\gamma$ ' Precipitates in IN718 Superalloy," *Metallurgical and Materials Transactions A: Physical Metallurgy and Materials Science*, vol. 47, no. 6, pp. 3235–3247, 2016, doi: 10.1007/s11661-016-3480-0.
- [129] A. Drexler, B. Oberwinkler, S. Primig, C. Turk, E. Povoden-Karadeniz, A. Heinemann, W. Ecker, and M. Stockinger, "Experimental and

numerical investigations of the  $\gamma''$  and  $\gamma'$  precipitation kinetics in Alloy 718,” *Materials Science and Engineering A*, vol. 723, no. December 2017, pp. 314–323, 2018, doi: 10.1016/j.msea.2018.03.013.

- [130] R. Shi, D. P. McAllister, N. Zhou, A. J. Detor, R. DiDomizio, M. J. Mills, and Y. Wang, “Growth behavior of  $\gamma'/\gamma$ ” coprecipitates in Ni-Base superalloys,” *Acta Materialia*, vol. 164, pp. 220–236, 2019, doi: 10.1016/j.actamat.2018.10.028.
- [131] “OOF2.” <https://www.ctcms.nist.gov/oof/oof2/> (accessed May 13, 2017).
- [132] R. Hill, “The Elastic Behaviour of a Crystalline Aggregate,” *Proceedings of the Physical Society. Section A*, vol. 65, no. 5, pp. 349–354, May 1952, doi: 10.1088/0370-1298/65/5/307.

## **Appended Papers**





## Paper A

# Toward a better understanding of phase transformations in additive manufacturing of Alloy 718

Chamara Kumara

Arun Ramanathan Balachandramurthi

Sneha Goel

Fabian Hanning

Johan Moverare

Published in *Materialia*

vol. 13, Article No: 100862, Sep. 2020.

DOI: 10.1016/j.mtla.2020.100862

Reprinted with CC BY-NC-ND 4.0





## Full Length Article

## Toward a better understanding of phase transformations in additive manufacturing of Alloy 718

Chamara Kumara<sup>a</sup>, Arun Ramanathan Balachandramurthi<sup>a</sup>, Sneha Goel<sup>a</sup>, Fabian Hanning<sup>a</sup>, Johan Moverare<sup>a,b</sup><sup>a</sup> Division of Subtractive and Additive Manufacturing Processes, Department of Engineering Science, University West, 461 86 Trollhättan, Sweden<sup>b</sup> Division of Engineering Materials, Department of Management and Engineering, Linköping University, SE-58183 Linköping, Sweden

## ARTICLE INFO

**Keywords:**  
Additive Manufacturing  
Alloy 718  
Phase transformation  
Modelling

## ABSTRACT

This paper presents a discussion on the phase-transformation aspects of additively manufactured Alloy 718 during the additive manufacturing (AM) process and subsequent commonly used post-heat treatments. To this end, fundamental theoretical principles, thermodynamic and kinetics modeling, and existing literature data are employed. Two different AM processes, namely, laser-directed energy deposition and electron-beam powder-bed fusion are considered. The general aspects of phase formation during solidification and solid state in Alloy 718 are first examined, followed by a detailed discussion on phase transformations during the two processes and subsequent standard post heat-treatments. The effect of cooling rates, thermal gradients, and thermal cycling on the phase transformation in Alloy 718 during the AM processes are considered. Special attention is given to illustrate how the segregated composition during the solidification could affect the phase transformations in the Alloy 718. The information provided in this study will contribute to a better understanding of the overall process–structure–property relationship in the AM of Alloy 718 718.

## 1. Introduction

In recent years, compared with conventional manufacturing methods, additive manufacturing (AM) of nickel-based super Alloy 718 s has attracted considerable attention in aerospace and power generation applications [1]. In AM, a certain part is manufactured using a layer-by-layer approach using a 3D-digital model of the part. An important feature of this process is that it allows the production of complex, near-net-shape objects (even through generative design), with minimal material waste. Furthermore, it enables part integration, thus reducing the number of assemblies and sub-assemblies required in the fabrication process. In addition, it allows manufacturing on demand, thereby reducing the need for a large inventory of spare parts. For these reasons, AM is considered a suitable manufacturing method for nickel-based super Alloy 718 components for aerospace and power-generation applications [2,3].

However, certain challenges should be overcome before AM could be used more effectively in aerospace and power-generation applications. One such challenge is to obtain the appropriate microstructure that provides the desired mechanical performance to the AM component. During the layer-by-layer deposition process, the material undergoes melting, solidification, and thermal cycling. This induces a liquid-to-solid phase transformation, as well as solid-state transformations. Therefore, the as-built microstructure of the component often leads to a heterogeneous microstructure with heterogeneous mechanical properties on a macroscopic length scale [1]. To overcome this, the common practice is to use suitable post-heat treatment (HT) protocols, with or without hot iso-

static pressing (HIP), for the as-built part. These HTs further change the microstructure according to its composition segregation level, phases, and grain structure (morphology and texture). Therefore, to achieve the desired properties, it is necessary to understand the phase transformations during the formation of the as-built microstructure and under different HTs before the appropriate optimization is performed.

This study focuses on understanding the phase transformation of additively manufactured Alloy 718. Specifically, we use fundamental theoretical principles, thermodynamic and kinetics modeling, and existing literature data to explain the observed phase changes during the AM and post-HT of Alloy 718. Two different AM processes, namely, laser-directed energy deposition (L-DED) and electron-beam powder-bed fusion (EB-PBF) are considered. General aspects of the phase formation in Alloy 718 are first examined, followed by a discussion on the phase transformations during the two processes and subsequent HTs.

## 2. Alloy 718

Alloy 718 is a nickel–iron-based super Alloy 718. It has been extensively used in rocket motors, aircraft engines, nuclear reactors, and pumps [4]. The main reasons for its success are its relatively low cost and good mechanical as well as corrosion properties at low and intermediate temperatures [5,6]. However, its use in load-bearing components for elevated-temperature applications is limited to 650 °C owing to the strength loss beyond this temperature [7]. The composition of Alloy 718 is complex and involves several Alloy 718 ing elements,

<https://doi.org/10.1016/j.mtl.2020.100862>

Received 8 June 2020; Accepted 8 August 2020

Available online 11 August 2020

2589-1529/© 2020 Acta Materialia Inc. Published by Elsevier B.V. This is an open access article under the CC BY-NC-ND license.

(<http://creativecommons.org/licenses/by-nc-nd/4.0/>)

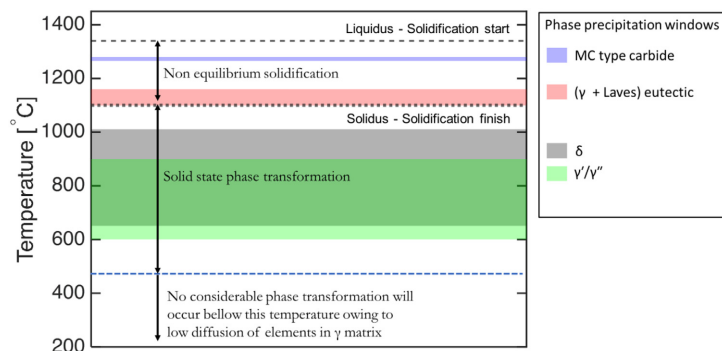


Fig. 1. Phase precipitation windows ([6,9,12]) in Alloy 718 during non-equilibrium solidification and in solid-state transformation.

which are added to obtain the desired microstructure and properties. The nominal composition ranges for the Alloy 718 (according to the ASTM standard), their effect on the microstructure and crystal structure information of the commonly observed phases in Alloy 718 can be found in reference [8]. The Alloy 718 microstructure is primarily dominated by a face-centered cubic (FCC)  $\gamma$  matrix, wherein precipitates such as  $\gamma'/\gamma''$  (strengthening phases),  $\delta$ , Laves, MC carbides, and nitrides can be found [9]. The  $\delta$  phase is the equilibrium phase of the metastable  $\gamma''$ . The exact microstructure (phase composition, phase distribution, morphology, and volume fraction) of this Alloy 718 is mainly governed by the primary manufacturing technology and successive post-HT conditions. Fig. 1 shows the reported phase precipitation windows for Alloy 718. It can be seen that there is an overlap between the  $\delta$  and  $\gamma'/\gamma''$  precipitation windows. Although  $\delta$  is thermodynamically more stable than  $\gamma''$ ,  $\delta$  precipitation up to  $\sim 900^\circ\text{C}$  is always preceded by  $\gamma''$  precipitation [10,11].

## 2.1. Non-equilibrium solidification

During solidification processes, such as casting, welding, and AM, Alloy 718 tends to form a dendritic/cellular microstructure [9,13–15], the length scale of which varies according to the solidification conditions [15,16]. Khorovskiy et al. [6] and Antonsson et al. [12] experimentally investigated the solidification sequence for Alloy 718. As temperature drops in the liquid (L) melt, the  $L \rightarrow \text{TiN}$  transformation first occurs above the liquidus temperature. The resulting TiN particles occasionally act as nucleation sites for carbide precipitation at a later stage in the solidification [12]. However in the context of AM, TiN can also come via the feedstock material and could remain unmelted due to their higher melting point ( $2930^\circ\text{C}$ ) [17].

When the temperature drops below liquidus, the solidification of the primary  $\gamma$  phase takes place. During the solidification of the  $\gamma$  matrix, segregation of Alloy 718 ing elements is typically observed [9]. This is because the solubility of the Alloy 718 ing elements in the matrix phase is different from that in the liquid. Elements such as Nb, Mo, and Ti, which have a low solubility limit in the matrix, tend to segregate to the liquid. Elements such as Cr, Fe, and Al, which have a high solubility limit in the solid, tend to be trapped in the solid. This segregation alters the local thermodynamics of Alloy 718 and, hence, the driving force for phase formation. Therefore, phases such as Laves and NbC begin to form in the interdendritic liquid region during solidification. Owing to their low solubility in the matrix, Nb and C are continuously rejected into the liquid. As the matrix grows, the Nb and C compositions in the liquid reach a level that enables NbC formation. This reaction consumes Nb and the majority of C in the remaining liquid, shifting the remaining liquid composition back to a lower level. As  $\gamma$  grows further, the segregation of Nb in the remaining liquid prompts another eutectic reaction  $L \rightarrow$

$\gamma + \text{Laves}$ , which terminates the solidification process. This is referred to as non-equilibrium solidification (Fig. 1). In the context of AM of Alloy 718, the formed primary carbides and nitrides during non-equilibrium solidification do not change (in terms of size and distribution) noticeably at low temperatures owing to their stability at these temperatures. Therefore, in this study, the focus is on understanding the transformation of the  $\gamma'/\gamma''$ ,  $\delta$ , and Laves phases.

## 2.2. Effect of solidification conditions on non-equilibrium solidification

The partitioning of the elements and the level of segregation depend on the solidification conditions of the process, and it affects the formation of the secondary phases [12] during non-equilibrium solidification.

Antonsson et al. [12] studied the effect of the cooling rate (from  $2.5 \times 10^{-1}$  to  $2 \times 10^4$   $^\circ\text{C/s}$ ) on the solidification of Alloy 718. During the rapid solidification that occurs at higher cooling rates ( $>10^4$   $^\circ\text{C/s}$ ), it was observed that the interdendritic region contains less Nb, and Laves phases are not present. Owing to the rapid solidification, the solutes become trapped in the moving solid/liquid interface because of the incomplete solute partitioning [18]. This results in less Nb segregation to the interdendritic liquid and hence insufficient concentration for Laves-phase formation. In contrast, during slower solidification (similar to the conditions in traditional casting), the interdendritic region was observed to have more dominant Nb and Laves phases.

However, in laser-beam powder-bed fusion (LB-PBF) of Alloy 718, Laves-phase formation is observed under non-equilibrium solidification conditions [19,20], even though the reported cooling rates during the solidification of the melt pool are in the order of  $10^5$   $^\circ\text{C/s}$  [21,22]. This contradicts the observation made by Antonsson et al., highlighting the fact that one cannot simply use the cooling rate alone as a criterion to describe whether the solidification process would result in Laves-phase formation; rather, one should also consider the solid–liquid interface velocity, thermal gradients, and undercooling conditions [18]. In the literature on the microstructure of additively manufactured Alloy 718, it has been demonstrated that Laves phases are present, implying that non-equilibrium solidification conditions occur [23–26]. This indicates that the solidification conditions during these processes do not trap a significant fraction of Alloy 718 ing elements in the moving solid/liquid interface, allowing the occurrence of element partition and hence Laves-phase formation (see Fig. 2).

The presence of Laves phases in the microstructure has a negative effect on the mechanical properties of Alloy 718 (tensile strength, ductility, fatigue life, and fracture toughness) [29,30], owing to its brittle nature. Usually, liquation cracking is often observed in the microstructure when Laves phases are present in a long-chain morphology [30]. The low melting point of the Laves phase and the long-chain morphology will promote liquation cracking. As the Laves phase forms toward the

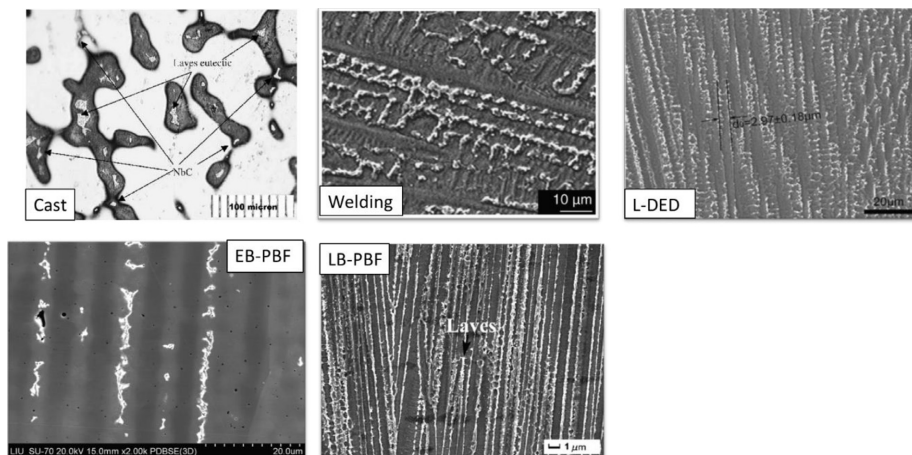


**Fig. 2.** Microstructures obtained from different process, exhibiting the formed Laves + NbC (white precipitates) at the end of non-equilibrium solidification. In L-DED, EB-PBF, and LB-PBF, the build direction is from bottom to top.

Source: Sources: cast [12], welding [27], L-DED [15], EB-PBF [14] and LB-PBF [28].

end of non-equilibrium solidification, its morphology is directly related to the morphology of the dendritic structure at that time. Therefore, by changing the solidification conditions, that is, thermal gradient ( $G$ ), cooling rate ( $T$ ), and liquid-solid interface velocity ( $R = \frac{T}{G}$ ) [31,32]. This is true in the case of AM of Alloy 718 as well, where it can be achieved by changing the process parameters that directly affect the thermal conditions in the melt pool. Depending on these conditions, the resulting dendritic structure could have a columnar, equiaxed, or mixed morphology [33,34].

It is well known in the casting and welding community that the dendritic structure during the solidification process can be altered by changing the solidification conditions, that is, thermal gradient ( $G$ ), cooling rate ( $T$ ), and liquid-solid interface velocity ( $R = \frac{T}{G}$ ) [31,32]. This is true in the case of AM of Alloy 718 as well, where it can be achieved by changing the process parameters that directly affect the thermal conditions in the melt pool. Depending on these conditions, the resulting dendritic structure could have a columnar, equiaxed, or mixed morphology [33,34].

The effect of the thermal gradient (from bottom to top in the domain) and cooling rate on the dendritic structure of Alloy 718 is shown in Fig. 3. These results were obtained from multiphase-field simulations of Alloy 718 under different thermal conditions. Information about this modelling is presented in Appendix A.

It can be seen in Fig. 3 (a) that the dendritic structure during solidification changes with the cooling rate and thermal gradient. This ultimately affects the size and morphology of the Laves-phase particles, as shown in Fig. 3 (b). At low cooling rates, the dendritic structure is coarser. Therefore, the resultant Laves-phase structure is also coarse, and its morphology tends to the long-chain form, which has been demonstrated to have a negative effect on the microstructure, as it promotes liquation cracking [30]. As Laves phases form during the final solidification stage, they begin to melt around the eutectic-forming temperature when the temperature of the material is raised. If a Laves phase has a long-chain morphology, liquid can form along with this chain morphology at the reheating stage during thermal cycling above the eutectic-forming temperature. When combined with the tensile stresses generated at the reheating stage, this liquation can easily lead to cracking.

As the cooling rate increases, the amount of undercooling experienced by the liquid becomes higher for a given time. Higher undercooling results in higher excess free energy in the liquid, which is consumed by the liquid-solid interface that is created (though nucleation and/or

growth). When the amount of excess free energy becomes large, more and more liquid-solid interfaces are created per unit area. Consequently, the resultant dendritic structure is finer on the length scale. In fine dendritic microstructures, the thickness and spacing of the primary and secondary dendrite arms become smaller. Therefore, toward the end of the solidification, the remaining liquid areas are trapped between these fine dendritic structures. This results in fine and discrete Laves-phase particles at the end of the solidification. When the Laves phase distributes in the microstructure as discrete and fine particles, the propensity for hot-crack formation is reduced, as a continuous liquid film is difficult to generate. In addition, as the cooling rate increases, the resultant Laves-phase area fraction is reduced, as shown in Fig. 3 (c).

### 2.3. Solid-state phase transformation after non-equilibrium solidification

After non-equilibrium solidification, solid-state phase transformations take place as the temperature continues to fall. The main phases that can precipitate in the solid state are  $\gamma'/\gamma''$  and  $\delta$ . Immediately after non-equilibrium solidification, there exists a composition gradient from the dendrite core to the interdendritic region in the  $\gamma$  matrix. Therefore, the local equilibrium conditions and driving forces for solid-state phase transformation change from the dendrite core to the interdendritic region [24,35,36].

Fig. 4 shows a simulated Alloy 718 microstructure at the end of a non-equilibrium solidification [23] in the L-DED process and the segregated 1-D composition profiles along a line from the dendrite core to the interdendritic region. Reader is referred to [23] for details about the modelling work. In this simulation, Alloy 718 is modeled as a seven-element system with Ni-Fe-Cr-Mo-Nb-Ti-Al. The most segregated elements are Nb and Fe, whereas the least segregated are Ti and Al. The generally accepted chemical composition formula for both  $\gamma'$  and  $\delta$  is  $\text{Ni}_3\text{Nb}$  [4]. Therefore, the distribution of Nb has a profound effect on the distribution of  $\gamma'$  and  $\delta$ . The generally accepted chemical formula for  $\gamma'$  is  $\text{Ni}_3(\text{Al}, \text{Ti})$  [4]. Thus, the distribution of Al and Ti affects the distribution of  $\gamma'$ . These modeling results agree well with the experimental observations made by Sui et al. [4]. From the 1-D segregation profiles, the Al segregation level is quite low, indicating a relatively homogenous distribution of Al in the microstructure. However, this is not the case for

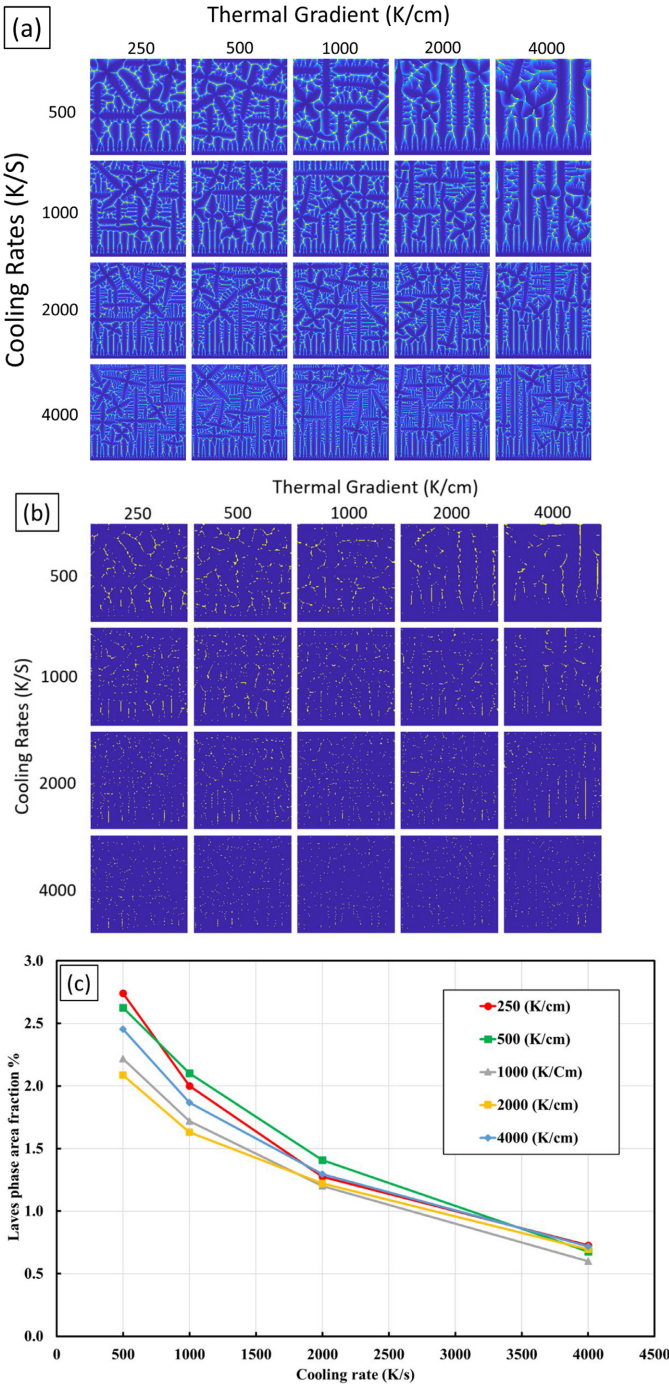


Fig. 3. (a) Variation in the dendrite structure under different solidification conditions. (b) Variation in the Laves-phase morphology under different solidification conditions. (c) Variation of Laves-phase area fraction under different solidification conditions. Both (a) and (b) were taken at the end of non-equilibrium solidification simulation described in Appendix A. Domain size is  $80 \mu\text{m} \times 80 \mu\text{m}$ .

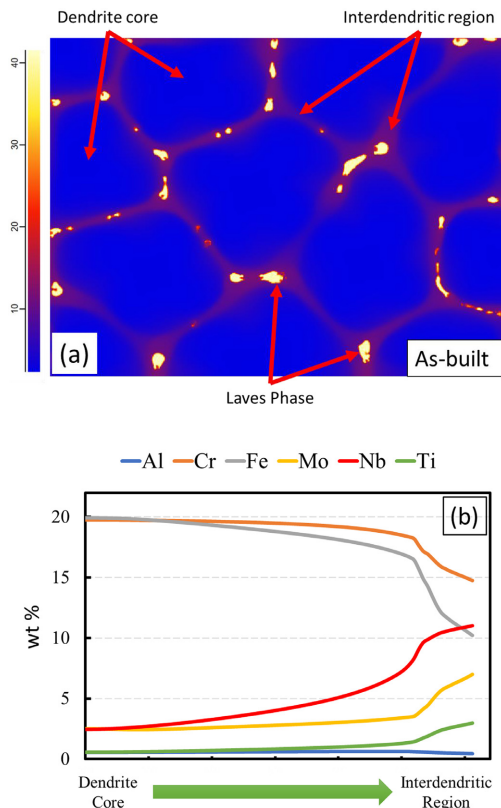


Fig. 4. (a) As-built microstructure at the end of non-equilibrium solidification simulation performed using MICRESS, domain size  $25 \mu\text{m} \times 20 \mu\text{m}$ . Scale shows the Nb distribution in wt%.

(b) 1D composition profiles extracted from a multiphase field simulation at the end of the non-equilibrium simulation.

Note: Simulation results were taken from a previous simulation work published in [23].

Ti; preferential segregation of Ti is clear, and thus its distribution could affect the distribution of  $\gamma'$ . Nevertheless, as the segregation of Nb is higher than that of Al and Ti, it can be expected that the variation in the distribution of  $\gamma''$  is more pronounced than that of  $\gamma'$  in the matrix.

To gain insight into the effect of segregation on the local equilibrium conditions of Alloy 718, equilibrium volume fraction diagrams were generated using the JMatPro (JMatPro is a trademark of Sun Microsystems, Inc - ver10.2) software package considering the composition in the dendrite core and the interdendritic region in Fig. 4. For comparison, the equilibrium volume fraction related to the nominal composition of Alloy 718 was also generated, and the results are shown in Fig. 5. It can be clearly seen that segregation has a direct effect on the equilibrium conditions for  $\gamma'/\gamma''$  and  $\delta$ . Away from the dendrite core and close to the interdendritic region, there is an increase in the volume fraction for the  $\gamma'/\gamma''$  and  $\delta$  phases; moreover, the equilibrium transformation temperature for the phases changes.

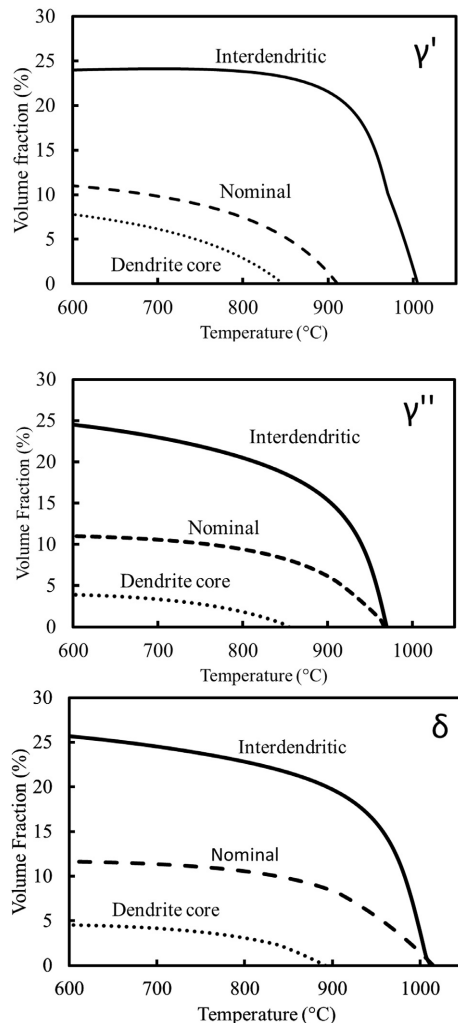


Fig. 5. Equilibrium volume fractions of  $\gamma'$ ,  $\gamma''$ , and  $\delta$  predicted using JMatPro for nominal, interdendritic, and dendrite core composition. Composition for the interdendritic and dendrite core was taken from Fig. 4(b). In the calculation of  $\gamma''$ ,  $\delta$  was suspended.

#### 2.4. Effect of cooling rate on solid-state phase transformation after non-equilibrium solidification

The solid-state phase transformation in Alloy 718 is a diffusion-controlled process. That is, the phase transformation is affected by element diffusion. As the element diffusion coefficient in the  $\gamma$  phase is lower than that in the liquid phase, the extent of solid-state phase transformation is influenced by the cooling rate of the process. In the case of slow cooling (as in traditional casting) shown in Fig. 6, the as-solidified material spends a relatively longer time in the precipitation windows of the  $\gamma'/\gamma''$  and  $\delta$  phases. Therefore, there is sufficient time for phase nu-



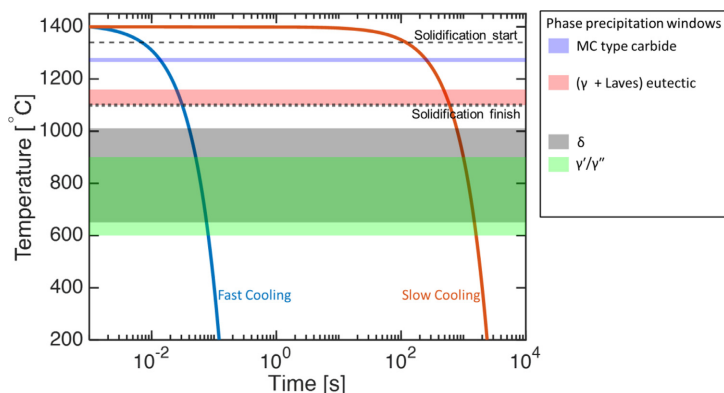


Fig. 6. Schematic representation of slow and fast cooling.

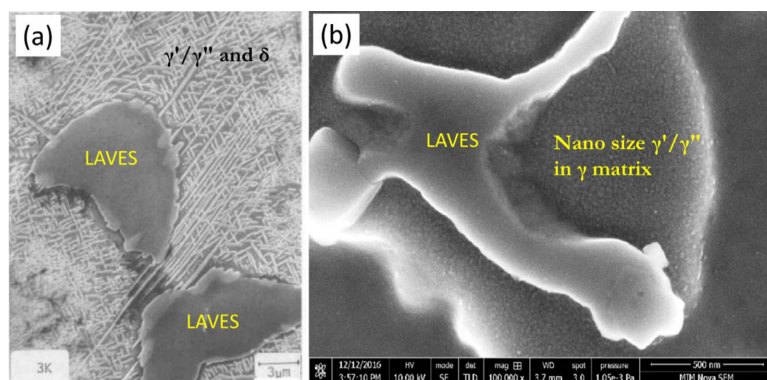


Fig. 7. (a) SEM image of the interdendritic area of an as-cast Alloy 718.  $\gamma'/\gamma''$  and  $\delta$  phases have precipitated around the Laves. Taken from [9]. (b) Nano-SEM image of the interdendritic region of LMDED Alloy 718.  $\gamma'/\gamma''$  has precipitated around the Laves phase. Taken from [38].

cleation and growth. At the end of the slow cooling process,  $\gamma'/\gamma''$  and  $\delta$  phases can be observed in the microstructure. These tend to nucleate and grow in size primarily in the segregated interdendritic regions (close to Laves phases that are also present), as in the case of cast Alloy 718 (Fig. 7 (a)) [37]. The reason for this is similar to the explanation of the segregation affecting the equilibrium conditions and inducing phase transformation in Alloy 718. The size growth of these phases is also supported by the high element concentration in the interdendritic region. However, as the segregation of Nb is comparatively higher than that of Al and Ti, the growth of the  $\gamma''$  and  $\delta$  phases in the interdendritic region is expected to be higher compared to that of the  $\gamma'$  phase.

In the case of rapid cooling (as in AM), as shown in Fig. 6, the as-solidified material spends a small amount time in the precipitations windows of  $\gamma'/\gamma''$  and  $\delta$ . Therefore, these phases only have a short period time for nucleation and growth in the microstructure. The precipitation, in this case, is likely to occur in interdendritic regions owing to the compositional segregation. However, the size of the  $\gamma'/\gamma''$  and  $\delta$  phases is quite small compared with that of the cast material upon initial cooling to temperatures below 500 °C. In an experimental study by Segerstark et al. [38], where transmission electron microscopy was used, nano-size precipitation of  $\gamma'/\gamma''$  was observed in the interdendritic region of the final layer of material that had been deposited through laser metal powder directed energy deposition. However, no  $\delta$  phase was observed in

the as-built microstructure. It is interesting to note that the  $\delta$  phase precipitates in the interdendritic region when the process has slow cooling (as in casting), but not when the process has faster cooling (as in AM). The time that the microstructure spent in the  $\delta$  precipitation window in AM is shorter than that during casting (Fig. 5). Thus, there is more time for the  $\delta$  phase to grow in casting.

This implies that the final microstructure of Alloy 718 is influenced by the cooling rate of the process, and therefore different microstructures resulting from different process conditions will respond differently when subjected to further HTs.

### 3. Laser-directed energy deposition

Laser-directed energy deposition is a directed energy deposition AM process, where laser energy is directed and focused into a narrow region in the substrate/previously deposited layer, melting both the substrate/previously deposited layer and the feedstock material that is being deposited. The latter can be in the form of either powder or wire. This method is widely used to repair corroded and worn gas-turbine components because it involves minimal distortion and dilution [36]. Moreover, it is used to construct small components or add features to, for instance, cast components, thus adding complexity to products [2]. Thereby, the cost of components with complex features can be reduced.



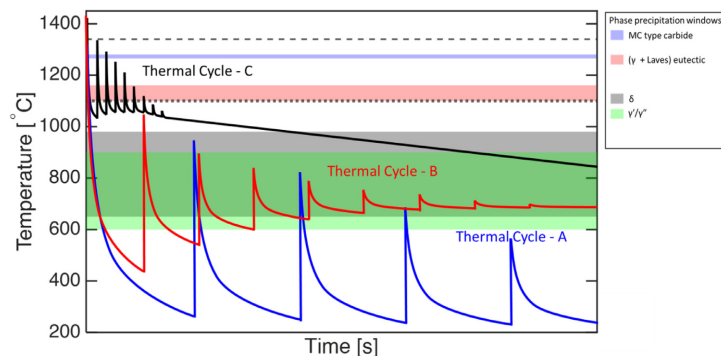


Fig. 8. Schematic representation of different thermal cycles in L-DED process.

Note that the start of the thermal cycles shows the final solidification. That means thermal cycles that cause the first melting and further remelting are not shown in this schematic.

### 3.1. Phase formation during L-DED of Alloy 718

Owing to the inherent nature of L-DED, the material undergoes multiple thermal cycles when adjacent tracks/beads are deposited. Depending on the nature of these thermal cycles, phase transformations occur, resulting in different microstructures that contain different phases and phase fractions.

In L-DED, during the solidification of Alloy 718, phase transformations occur as described in Section 2. After the solidification of the material, the underlying microstructure has a segregated dendritic microstructure with interdendritic Laves and NbC phases [23]. Thereafter, this microstructure undergoes changes during the ensuing thermal cycles owing to the subsequent material deposition. For a better understanding of the solid-state phase transformation during this thermal cycling, we consider the thermal cycles shown in Fig. 8. These thermal cycles resemble the thermal conditions that are typically encountered during material deposition.

In thermal cycle A, there is sufficient time between the deposition of successive layers so that the material addition does not cause a rise in the global temperature of the deposited material. This type of thermal cycling resembles the thermal cycles reported in [23,38,39]. In this case, even though the temperature goes through the precipitation windows of  $\gamma'/\gamma''$  and  $\delta$  during the thermal cycling, no significant phase transformation is observed. This is because the time that the material spends in these precipitation windows is quite short. Thus, diffusion and hence phase growth cannot occur. In addition, this type of thermal cycling does not significantly affect the Laves phases formed during the first cycle. This has been experimentally demonstrated in [23]. However, the situation may be different under such thermal conditions as those in thermal cycle B.

Thermal cycle B illustrates a case where the deposition of multiple layers is performed without sufficient inter-pass waiting time to cool down the previously deposited material to a temperature close to room temperature. In these conditions, the global temperature of the deposited material rises owing to heat accumulation. The experimentally measured temperature profile in Tian et al. [36] resembles such a condition. This rise in the global temperature has an effect similar to that of an HT, both to the deposited and to the base material, if the temperature is above  $\sim 600^\circ\text{C}$ . If the thermal conditions during processing resemble those in thermal cycle B, then this may be thought of as *in situ* ageing HT for the previously deposited material. Therefore, with time,  $\gamma'/\gamma''$  begins to precipitate in the material, and this precipitation is influenced by the local compositional segregation in the microstructure. It should be noted that the rise in the global temperature ( $> \sim 600^\circ\text{C}$ ) also affects the substrate material. The amount of the  $\gamma'/\gamma''$  precipitate in the interdendritic region is larger compared with that in the dendrite

core owing to the higher equilibrium volume fraction expected for local variation in the chemical composition. In addition, these precipitates grow in size with the time that the material spends in the *in situ* ageing. This generates a gradient of  $\gamma'/\gamma''$  precipitates from the interdendritic region to the dendrite core, as well as from the bottom to the top of the deposited sample. Therefore, there will be a hardness gradient in the material from top to bottom, which was experimentally confirmed by Tian et al. [36] (Figs. 4 and 7 in their paper).

Thermal cycle C is similar to thermal cycle B, but the heat accumulation is greater; therefore, the rise in the global temperature is higher than that in thermal cycle B. Such a thermal condition was reported by Z. Li et al. [40] during high-deposition-rate L-DED of Alloy 718. In this thermal cycle, the global temperature of the material first rises to a higher value ( $> 1000^\circ\text{C}$ ) and then drops gradually during the deposition process owing to heat conduction. When the temperature drops, it passes both the  $\gamma'/\gamma''$  and  $\delta$  precipitation windows. Thus, in this case,  $\gamma'/\gamma''$  and  $\delta$  precipitate in the microstructure. However, their distribution is not uniform owing to the local compositional segregation. As described previously,  $\gamma'/\gamma''$  and  $\delta$  predominantly precipitate around the Laves phase in the interdendritic region. As the bottom of the sample spends more time at a higher temperature than the top, there will be a difference in the amount of  $\gamma'/\gamma''$  and  $\delta$  between the bottom and top. Such a heterogeneous distribution along the height as well as from the dendrite core to the interdendritic region has been reported by Z. Li et al. [34].

It should be noted that for all these thermal cycles, the Laves phase formed during the non-equilibrium solidification of a given layer does not significantly change owing to the thermal cycling that occurs during subsequent layer depositions. This is primarily due to the fact that in these thermal cycles, the time-temperature conditions are not sufficient to dissolve the Laves phase significantly. Therefore, to modify the Laves phase, the process parameters of the L-DED should be changed so that the thermal conditions during non-equilibrium solidification change; otherwise, post-HT is necessary to alter the formed Laves phase. It should also be noted that the non-equilibrium solidification conditions (thermal gradients and cooling rates) can, to a certain degree, change during the deposition of the material owing to the geometry of the deposited part. This could influence the Laves phase formation locally during the non-equilibrium solidification from bottom to top of the build.

### 3.2. Phase transformation during heat treatment of L-DEDed Alloy 718

Heat treatments (homogenization, solution treatment, and ageing) are often used for Alloy 718 to remove compositional segregation and obtain the appropriate phase distribution so that desired mechanical properties for the required application may be obtained. Depending on

**Table 1**  
Standard heat treatment as per AMS5383 for cast Alloy 718

Homogenization	Solution treatment	Ageing
1093 ± 14°C for 1–2 h, followed by air cooling or faster cooling	(954–982) ± 14°C for more than 1 h, followed by air cooling or faster cooling	718 ± 8°C for 8 h, furnace cool to 621 ± 8°C at 55 ± 8°C/h, hold at 621 ± 8°C for 8 h, followed by air cooling

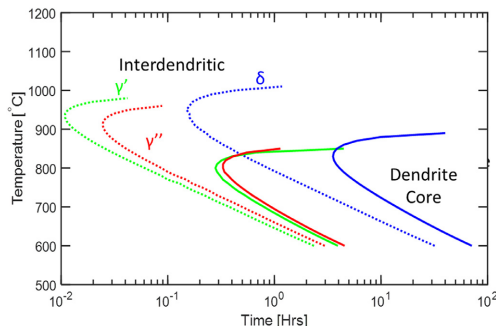


**Fig. 9.** TTT diagram obtained using the JMatPro software package by considering compositions in the dendrite core and the interdendritic region in Fig. 4(b). Dotted lines represent 0.5% precipitation close to Laves phase, and solid lines represent 0.5% precipitation in the dendrite core.

the initial microstructure and the final application, different HT combinations can be used.

In L-DED Alloy 718, the as-deposited (AD) microstructure varies according to the thermal conditions of the process, as described previously. Therefore, the HTs could be prepared according to the AD microstructure. In addition, the selection of HT is influenced by the final application. For example, if L-DED was used to repair damaged or worn-out components, then the HT should be selected so that the base material of the component that is in fully heat-treated condition is not affected.

In the literature on post-HT for L-DED Alloy 718, the commonly used HTs are as per the AMS 5383 standard, which was originally developed for cast Alloy 718 [4,27,41–47]. The details of this standard are shown in Table 1. Direct ageing (DA), solution treatment and ageing (STA), homogenization and STA (HSTA), and homogenization and ageing (HA) are the common HTs used for L-DED Alloy 718.

**3.2.1. Phase transformation during heat treatment of a microstructure resulting from thermal cycle A**

As mentioned in the previous section, thermal cycle A produces a microstructure with segregated  $\gamma$  matrix, Laves, and MC phases. The presence of the compositional segregation in the matrix has a direct effect on the phase transformation during different post-HTs. To explain this transformation, time-temperature transformation (TTT) diagrams, as shown in Fig. 9, were generated using the JMatPro software package by considering the composition in the dendrite core and the interdendritic region from Fig. 4(b).

The JMatPro predictions indicate that there is a clear difference (more than an order of magnitude difference in time) in the precipitation kinetics of  $\gamma'/\gamma''$  and  $\delta$  owing to the compositional segregation. In the interdendritic region, precipitates form more rapidly than in the dendrite core. Moreover, the nose of the TTT curves related to the interdendritic region (dotted lines) corresponds to a higher temperature than that of the curves related to the dendrite core (solid lines). Further, ageing treatment is performed to precipitate the strengthening phases  $\gamma'/\gamma''$ . As shown in Fig. 5, the equilibrium volume fraction of  $\gamma'/\gamma''$  is higher in the interdendritic region than in the dendrite core. Accord-

ingly, a high volume fraction of  $\gamma'/\gamma''$  forms toward the interdendritic region during DA treatment. The accelerated phase precipitation kinetics causes  $\gamma'/\gamma''$  to precipitate at an earlier stage of the HT in the interdendritic region than in the dendrite core. Hence, the  $\gamma'/\gamma''$  precipitates in the interdendritic region experience greater size growth than those in the dendrite core. From the segregation level of the elements forming  $\gamma'$  and  $\gamma''$ , as shown in Fig. 5, it is reasonable to assume that the growth of  $\gamma''$  is supported more than that of  $\gamma'$ . Therefore, even if the equilibrium predictions indicate a high volume fraction for  $\gamma'$  in the interdendritic region, this fraction may not be high compared with that of  $\gamma''$ .

The effect of element segregation on the precipitation of  $\gamma''$  during DA MICRESS simulations performed using the AD microstructure related to thermal cycle A is shown in Fig. 10 (see Appendix B for modeling details). The results qualitatively agree with the experimental observations [36,38]. In contrast with the dendrite core, toward the interdendritic region, the number density and size of the precipitates increase. It can be assumed that owing to the lack of  $\gamma''$  precipitates, the dendrite core is softer than the interdendritic area. Consequently, there is a mechanical property gradient from the dendrite core to the interdendritic region. However, at the macro level, this DA Alloy 718 microstructure possesses a relatively higher strength than in the as-built condition, as shown in Fig. 11. It should be noted that the temperature in DA treatment is not sufficiently high to dissolve/change a Laves phase or grain structure. Thus, the increase in strength in this condition compared with the AD condition is due to the precipitation of  $\gamma'/\gamma''$ . This raises the fundamental question of explaining how DA L-DED Alloy 718 can result in relatively higher strength (in comparison with AMS5662 wrought standard) even though the distribution of strengthening phases is non-uniform in the microstructure. A possible reason could be that the microstructure has a property gradient from the dendrite core to the interdendritic region. This microstructure could be treated as a composite material having a softer phase (dendrite core area) embedded in a hard phase (interdendritic area). These two (soft and hard) areas mimic the dendritic structure inside the grain. Therefore, our hypothesis is that a hierarchical structure with these two phases and its spatial structure inside the grains give rise to the higher strength on the macro scale. This could be verified by using crystal plasticity/finite element modeling to study the effect of such a composite microstructure on macroscale properties; this is left for future work.

Solution treatment and ageing is another type of HT that is used in L-DED Alloy 718. Here, the AD microstructure is first subjected to solution treatment followed by ageing. The solution treatment according to AMS5383 is used to precipitate the  $\delta$  phase at the grain boundaries, as it is performed below the  $\delta$  solvus temperature. The presence of the  $\delta$  phase at the grain boundaries has been demonstrated to have a beneficial effect on stress rupture ductility, and to inhibit the growth tendency of the matrix grains during the forging process [48–50]. However, the presence of a compositional segregation in AD L-DED microstructure causes  $\delta$  to precipitate inside the grains as well, owing to the presence of multiple dendrite/cells inside a single grain. In the interdendritic area, the  $\delta$  phase precipitates and grows in large quantities owing to the large equilibrium volume fraction (Fig. 5) and increased precipitation kinetics (Fig. 9). In addition, the Laves phase in the AD structure is also dissolved to some extent. However, the amount of dissolution depends on the solution treatment temperature. At low temperatures, the dissolution of the Laves phase is slower. This is evident from the simulations performed by C. Kumara et al. [23] and the experimental observations [38,42,51] (Fig. 12). Similar observations have been made for laser-

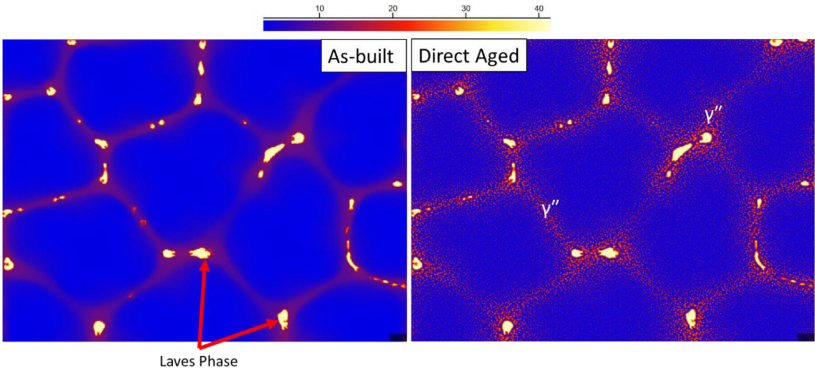


Fig. 10. MICRESS simulated AD microstructure at the end of thermal cycles similar to thermal cycle-A, and the same microstructure after DA simulation. Domain size  $25\ \mu\text{m} \times 20\ \mu\text{m}$ . Scale shows the Nb distribution in wt%. Note: See Appendix B for details about the modelling work.

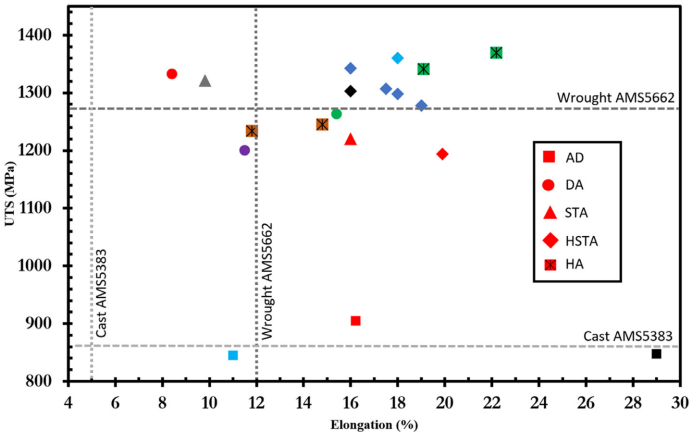
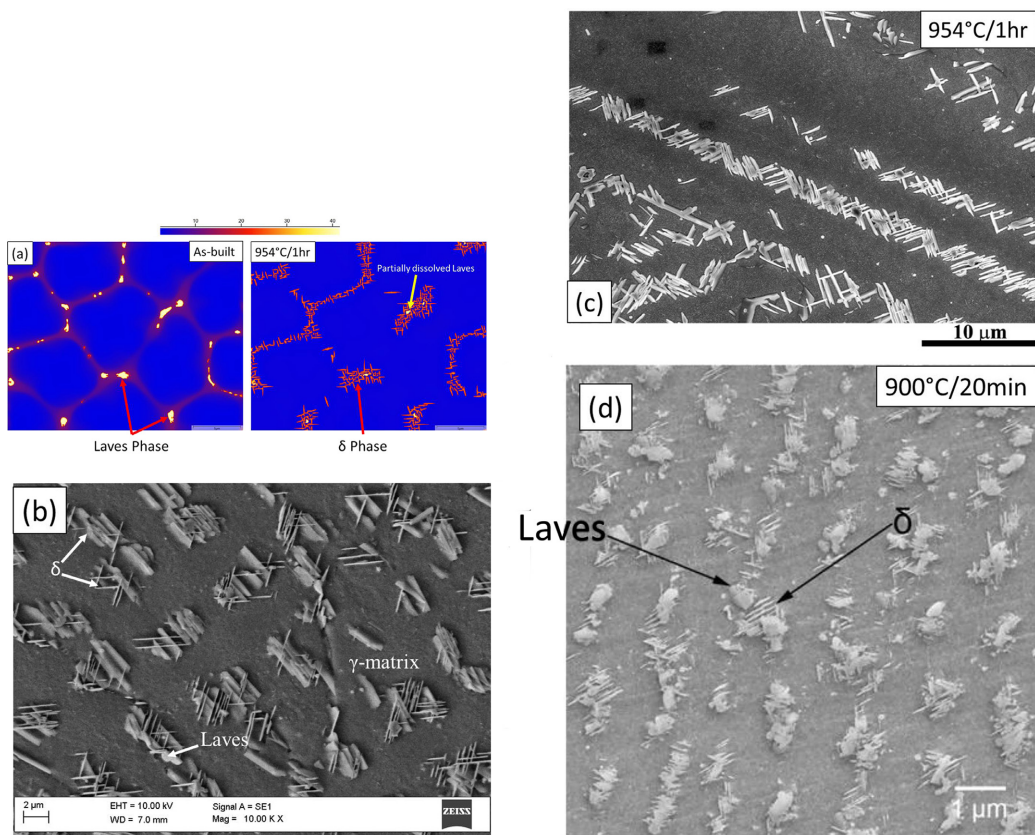


Fig. 11. Ultimate tensile strength vs elongation of L-DED Alloy 718. Data taken from [4,27,41–47].

- AD
- ◆ Hom (1080 °C/1.5 h/AC) + STA (980 °C/1 h/AC + 720 °C/8 h/FC/620 °C/8 h/AC)
- ◆ Hom (1080 °C/1.5 h/AC) + STA (980 °C/1 h/AC + 720 °C/8 h/FC/620 °C/8 h/AC)
- DA (718 °C/8 h/FC/621 °C/8 h/AC)
- ▲ STA (980 °C/1 h/AC + 718 °C/8 h/FC/621 °C/8 h/AC)
- ◆ Hom (1093 °C/1-2 h/AC) + STA (980 °C/1 h/AC + 718 °C/8 h/FC/621 °C/8 h/AC)
- DA (720 °C/8 h/FC/620 °C/8 h/AC)
- Hom (1100 °C/0.5 h/WQ) + DA (720 °C/8 h/FC/620 °C/8 h/AC)
- Hom (1100 °C/1 h/WQ) + DA (720 °C/8 h/FC/620 °C/8 h/AC)
- AD
- ◆ Hom (1093 ± 14 °C/2 h/AC) + STA (954-980 °C/>1 h/AC + 718 ± 8 °C/8 h/FC/621 ± 8 °C/8 h/AC)
- DA (720 °C/8 h/FC/620 °C/8 h/AC)
- Hom (1050 °C/15min/WQ) + DA (720 °C/8 h/FC/620 °C/8 h/AC)
- Hom (1050 °C/45min/WQ) + DA (720 °C/8 h/FC/620 °C/8 h/AC)
- ▲ STA (954 °C/1h/AC + 732C/8h/FC/599C/8h/AC)
- ◆ Hom (1100 °C/1.5 h/AC) + STA (980 °C/1 h/AC + 720 °C/8 h/FC/620 °C/8 h/AC)



**Fig. 12.** Precipitation of  $\delta$  phase in the interdendritic region in L-DED microstructures subjected to solution treatment.

(a) MICRESS simulation showing the microstructure normal to the build direction before and after solution treatment at 954°C/1 h, domain size 25  $\mu\text{m}$   $\times$  20  $\mu\text{m}$ : Fig. shows the Nb distribution in wt%.

Note: MICRESS simulation results were taken from a previous simulation work published in [23].

(b) Microstructure normal to the build direction after 954°C/1 h [23].

(c) Microstructure parallel to the build direction after 954°C/1 h [38].

(d) Microstructure parallel to the build direction after 900°C/20 min [51].

welded Alloy 718 subjected to solution treatment [27]. The amount of  $\delta$  that precipitates in the interdendritic region is also affected by the solution treatment temperature. The volume fraction of  $\delta$  is higher for a solution treatment at 954 °C than at 980 °C (see Fig. 5). No evidence of precipitation of  $\gamma'/\gamma''$  has been reported in the literature at the solution treatment temperatures even though the JMatPro predictions indicate that there could be a possibility of  $\gamma'/\gamma''$  precipitation (see Fig. 9). As  $\delta$  is rich in Nb, its precipitation consumes a certain level of Nb from the matrix phase. Therefore, during ageing HT (after the solution treatment), a lower volume fraction of  $\gamma''$  could be expected than during DA. As the  $\delta$  phase is incoherent with the  $\gamma$  matrix, it does not contribute to the strength of the Alloy 718 as much as the coherent and semicoherent  $\gamma'$  and  $\gamma''$  phases, respectively.

Homogenization HT is performed to dissolve the non-equilibrium Laves phase and homogenize the compositional segregation resulting from the non-equilibrium solidification. L-DED Alloy 718 produces a microstructure with a finer length scale than that in cast Alloy

718. Therefore, the Laves phase in L-DED Alloy 718 has a smaller size. In addition, L-DED produces a smaller dendritic structure than in the cast material. Thus, its compositional segregation length scale is smaller. Consequently, the homogenization kinetics of L-DED Alloy 718 is faster than that of cast Alloy 718; this is evident in the study by Shang Sui et al. [52]. As the homogenization temperature increases, the dissolution of the Laves phase is faster, and eventually homogenization of the composition will occur. However, whether this treatment results in a fully homogenized matrix without any Laves phases depends on the Laves particle size, dendrite arm spacing, HT temperature, and time. During the treatment,  $\gamma'/\gamma''$  and  $\delta$  do not form in the material, as the temperature is above their precipitation temperature window. In addition, MC present in the microstructure is not affected significantly, and grain growth is commonly observed [4,25,43,45]. Similar observations can be made regarding the homogenization of microstructures formed by thermal cycles B and C.

If STA or DA were to be performed after homogenization HT, the phase transformation kinetics would be different, as the chemical composition in the  $\gamma$  matrix is different from that in the AD condition. Owing to the relatively homogenized composition in the  $\gamma$  matrix after homogenization HT, the  $\delta$  phase tends to precipitate mainly at grain boundaries during the 1 h solution treatment of STA [25,43,53]. At a grain boundary, the nucleation energy barrier for solid-state precipitation of a phase is less than that of the defect-free matrix [54]. In addition,  $\delta$  could also precipitate at twin boundaries within the grains because a twin boundary also has a lower energy barrier for nucleation [55]. The amount of  $\delta$  that precipitates during the 1 h solution treatment is below the equilibrium volume fraction of  $\delta$  at that temperature; this is evident from the study by S. Azadian et al. [11]. Therefore, the precipitated  $\delta$  during the solution treatment does not consume the Nb entirely, and there remains a sufficient amount of Nb to precipitate  $\gamma''$  during ageing HT. However, the Nb depletion at the vicinity of the  $\delta$  precipitate hinders the  $\gamma''$  precipitation, resulting in a  $\gamma''$ -free zone around the  $\delta$  phase [10].

During ageing HT, the strengthening phases mainly start to precipitate uniformly owing to the homogenized elemental distribution [4]. However, during the precipitation and growth of  $\gamma'$  and  $\gamma''$ , the local chemical composition near the vicinity of the precipitate could change due to difference in solubility of elements in these phases. This could affect the nucleation and growth of secondary precipitates of  $\gamma'$  and  $\gamma''$  [56]. As seen in Fig. 11, these  $\gamma'/\gamma''$  that precipitate and grow during ageing HT will increase the strength of the material

### 3.2.2. Phase transformation during heat treatment of a microstructure resulting from thermal cycle B

As mentioned above, thermal cycle B results in a microstructure that contains Laves, MC, and  $\gamma'/\gamma''$  phases. Therefore, the phase transformation during the HT is rather complex. Performing STA may not be suitable for this microstructure, as the existing  $\gamma''$  can act as nucleation sites (stacking faults in the  $\gamma''$  particles) that precipitate and grow  $\delta$  phases at the solution treatment temperatures [10,11]. Laves-phase dissolution can be expected to a certain degree, as mentioned in Section 3.2.1.

During DA,  $\gamma'/\gamma''$  phases in the AD condition can be expected to grow, as the temperature conditions favor their growth. In addition, the precipitation gradient observed in the build direction of the microstructure is reduced. No changes to the Laves phase can be expected, as the temperature is so low that cannot dissolve them.

### 3.2.3. Phase transformation during heat treatment of a microstructure resulting from thermal cycle C

Thermal cycle C results in a microstructure that contains Laves,  $\delta$ , MC, and  $\gamma'/\gamma''$ . Performing STA may not be suitable for this microstructure, as the existing  $\gamma''$  can act as nucleation site for the precipitation and growth of  $\delta$ . In addition, the existing  $\delta$  can also grow larger in size. The Laves phase will dissolve only to a certain degree in this case as well.

During DA,  $\gamma'/\gamma''$  phases in the AD condition can be expected to grow, as the temperature conditions favor their growth. The existing  $\delta$  phase is expected to be unaffected during ageing HT [55]. No changes to the Laves phase can be expected.

It should be noted that no data are available in literature relating to Sections 3.2.2 and 3.2.3. Thus, the discussion provided is based on the understanding of phase transformations presented in previous sections and references therein.

## 4. Electron-beam powder-bed fusion

Electron-beam melting is a type of powder-bed AM technique that was first commercialized in 1997 by Arcam Corporation in Sweden. In the EB-PBF process, an electron beam is used to selectively melt the material in a layer-by-layer manner. This process has unique advantages in relation to the manufacturing of biomedical implants and high-performance components used in aerospace and high-temperature appli-

cations: higher build rates owing to high beam energy and speed, lower residual stresses (due to elevated powder bed temperature), the possibility of tailoring the microstructure [34,57,58], and reduced oxidation issues [59]. However, owing to the inherent nature of this process, the semi-sintered powder is difficult to remove from complex geometries. Components manufactured by EB-PBF have higher surface roughness than those manufactured by LB-PBF and may thus require post-treatment.

### 4.1. Phase transformation during the EB-PBF processing of Alloy 718

Owing to the inherent nature of this process, the printed material undergoes multiple thermal cycles when successive layers are printed. During this sequential printing, the uppermost layers undergo remelting. Depending on the beam parameters and movement, the number of layers that are remelted varies. When layer melting/remelting occurs, non-equilibrium solidification takes place, as discussed in Section 2. The resulting as-solidified microstructure has a segregated dendritic structure with interdendritic Laves and NbC phases [14,60]. Upon building further layers, the microstructure experiences thermal cycling. However, it does not change significantly by the thermal cycles owing to their shorter exposure time. The most significant effect on the microstructure is exerted by the elevated build temperature that occurs during the EB-PBF processing of Alloy 718. This temperature acts as an *in situ* HT and causes microstructural changes. As each layer that is built is exposed to the elevated temperature for a different amount of time, there exists a microstructure gradient from the top to the bottom layer. Once the printing is completed, the obtained part is cooled down by injecting helium into the build chamber. During this cooling, further phase transformations take place.

D. Deng et al. [14] and Kumara et al. [24] investigated the effect of the elevated build temperature on the as-solidified microstructure through experiments and modeling. The thermocouple data from the bottom of the build plate from these studies are shown in Fig. 13. It is evident that throughout the building process, the global temperature of the powder bed was greater than 1020 °C. It was demonstrated that this temperature caused the material to homogenize, gradually toward the bottom, by dissolving the Laves phase and homogenizing the element distribution in the matrix. Furthermore, this diffuse region extended between 150  $\mu\text{m}$  to 1800  $\mu\text{m}$  from the top layer. Beyond 1800  $\mu\text{m}$ , a fully homogenized region was observed. This homogenization process was accelerated by the smaller dendrite spacing and hence smaller segregation length scale and smaller Laves-phase particle size. The MC phase was not affected by this *in situ* treatment, as it was more stable. No precipitation of  $\delta$  and  $\gamma'/\gamma''$  was expected during printing, as the temperature was above the precipitation windows of these phases. Precipitation of  $\delta$  and  $\gamma'/\gamma''$  took place during the cooling stage of the process, as the temperature dropped through the precipitation windows of these phases. In the as-solidified region,  $\delta$  and  $\gamma'/\gamma''$  precipitated primarily in the interdendritic region owing to the high Nb segregation. In the transition region (150–1800  $\mu\text{m}$ ) the precipitation level was influenced by the change in the local chemical composition. In the homogenized region, few  $\delta$  particles were observed at high-angle grain boundaries. This can be attributed to the cooling stage, as the microstructure spent ~15 min in the  $\delta$  precipitation window. The  $\gamma'/\gamma''$  phase also precipitated uniformly owing to the relatively homogenized composition in this region, resulting in a hardness of ~420 HV. This value indicates that a significant volume fraction of  $\gamma'/\gamma''$  precipitated during the cooling. The time that the microstructure spent in the  $\gamma'/\gamma''$  precipitation window was ~60 min. This indicates that the average cooling rate that the material experienced in the  $\gamma'/\gamma''$  process window was approximately 5 °C/min. Similar hardness observations have been reported in the as-built condition of EB-PBF Alloy 718 [61,62]. These observations agree well with continuous cooling experiments conducted by L. Geng et al. for wrought Alloy 718 [63]. In the following section, it has been demonstrated that this cooling down



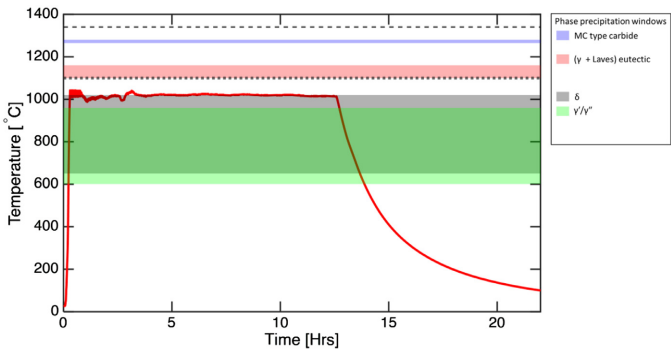


Fig. 13. Thermocouple measurement from the bottom of the build plate of the EB-PBF process. Raw data taken from D. Deng et al. [14] and Kumara et al. [24].

**Table 2**  
Standard heat treatment as per ASTM F3055 for cast Alloy 718

HIP	Solution treatment	Ageing
1120 to 1185 ± 15°C in an inert atmosphere for 240 ± 60 min at ≥ 100 MPa, followed by furnace cooling to < 425°C	1066 ± 14°C (except not below 1038°C) for 1–2 h, followed by air cooling or faster cooling	760 ± 8°C for 10 ± 0.5 h, furnace cool to 649 ± 8°C, hold at 649 ± 8°C for total precipitation time of 20 h, followed by air cooling or faster cooling
	927–1010 ± 14°C for 1 h (except not exceeding 1016°C), followed by air cooling or faster cooling	718–760 ± 8°C for 8 h, furnace cool to 621 ± 8°C, hold at 621 ± 8°C for total precipitation time of 18 h, followed by air cooling or faster cooling

stage can be used as an alternative method for ageing HT in some applications.

Kirka et al. [60] have also investigated the microstructure development in EB-PBF Alloy 718. However, unlike in D. Deng et al. [12] and Kumara et al. [21], the powder-bed elevated temperature was maintained at ~975°C. As this is within the  $\delta$  precipitation window, the  $\delta$  phase precipitated at grain boundaries as well as within the matrix during the building process. The transition region, in this case, was longer, as the bed temperature was lower. The amount of  $\delta$  phase increased toward the bottom of the sample, as the bottom layers of the sample remained for a longer time at ~975°C than the top layers. Therefore, the volume fraction  $\gamma''$  that precipitated during the cooling stage of the process was higher toward the top of the sample than the bottom. The consequence of such heterogeneity with height is evident in the reported room-temperature mechanical properties. As the distance from the bottom of the build increased, the yield and tensile strength as well as elongation gradually increased [60].

4.2. Phase transformation during heat treatment of EB-PBF Alloy 718

For EB-PBF Alloy 718, post-HTs are typically used to remove the heterogeneous phase distribution and reduce defects (porosity and lack of fusion) so that the required mechanical performance may be achieved [64]. The HIP and post-HT protocols for EB-PBF Alloy 718, as recommended in the ASTM F3055 standard [65], are shown in Table 2.

HIP is mainly carried out to heal defects (porosity and lack of fusion) in the as built material. However, Oxides present at the defect surface prevent complete healing of defects after HIP [66]. As this is performed at high temperature (> 1100 °C) for a longer period (~4 h), different phases (Laves,  $\delta$ , and  $\gamma'/\gamma''$ ) in the as-built condition completely dissolve back into the matrix phase [67,68]. However, owing to the high-temperature stability, carbides do not dissolve during this process [67]. At the end of the HIP cycle, the chemical composition of the matrix can be considered homogenized. However, to prevent phase transformation during the cooling-down part of the HIP cycle, a rapid cooling (quenching) must be performed, at the end of which, the microstructure is re-

ported to have a  $\gamma$  matrix that has homogenized chemical composition and is precipitation free, except for carbides [69].

After the HIP cycle, the EB-PBF Alloy 718 is subjected to STA or DA, depending on the requirements and application. If rapid quenching can be performed, then the solution treatment at 1066°C is redundant, as this does not cause any phase precipitation; otherwise, solution treatment at 1066°C is necessary to dissolve the undesired phase distribution. However, compared with HIP, solution treatment involves relatively low temperature and holding time, and therefore complete phase dissolution may or may not be achieved. Balachandramurthi et al. [61] reported that after 1066 °C/1 h, a certain  $\delta$ -phase level was observed at some grain boundaries. However, their size was reduced compared with that in the as-built condition owing to the dissolution process during the solution treatment. D. Deng et al. [70] reported complete dissolution of the  $\delta$  phase after treating EBM Alloy 718 at 1080°C/1h. It is worth mentioning that the size of the  $\delta$  phase in the as-built condition observed by D. Deng et al. [70] was smaller than that observed by Balachandramurthi et al. [61].

After the HIP cycle with rapid quenching, to control the precipitation of the  $\delta$  phase in the material, solution HT should be performed within the  $\delta$  precipitation window. In such solution treatments, grain-boundary  $\delta$  precipitation is primarily observed [70]. As discussed in Section 3.2.1, solution treatment at the lower end of the  $\delta$  window will result in a higher volume fraction owing to the higher equilibrium volume fraction. In EB-PBF Alloy 718, S. Goel [71] observed greater precipitation of the  $\delta$  phase after solution treatment at 954 °C than at 980 °C, both performed for 1 h. Furthermore, as discussed in Section 3.2.1, the amount of  $\delta$  that precipitates during the 1 h solution treatment does not give rise to the equilibrium volume fraction of  $\delta$  at the solution HT temperature.

S. Goel [71] demonstrated the possibility of performing STA inside the HIP vessel combined with the HIP cycle, thereby retaining a high pressure during STA. In this combined cycle, the argon gas pressure inside the HIP vessel was retained above 100 MPa. However, the solution treatment performed at 980 °C with pressure (~160 MPa) did not yield any  $\delta$  precipitation in the microstructure, compared with the same solution treatment performed without pressure. This could be explained by the Clausius–Clapeyron relation [54] (Equation (1)), which describes

**Table 3**  
Theoretical calculations of Clausius-Clapeyron relation values using values from TTNi8 database

Phase	$\Delta H_f \rightarrow \text{precipitate}$ (kJ/mol)	$T_{eq}$ (K)	$\Delta V^* = V_f - V_{\text{precipitate}}$ ( $10^{-6}$ m <sup>3</sup> /mol)	$\frac{dT_{eq}}{dP}$ (K/100MPa)
$\delta$	27.8	1283	$7.3 - 7.9 = -0.6$	-2.8
$\gamma''$	27.2	1203	$7.3 - 7.8 = -0.5$	-2.8
$\gamma'$	34.9	1140	$7.3 - 7.6 = -0.3$	-0.98

\* calculated using the data from TCNi8 database since volume data is not available in TTNi8

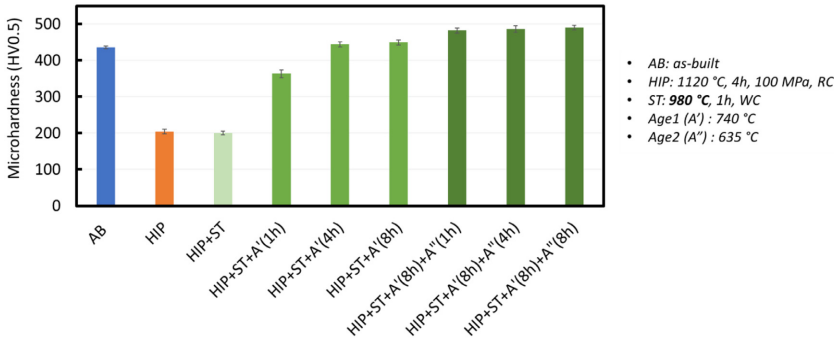


**Fig. 14.** Microhardness of the as-built and post-treated specimens of EB-PBF Alloy 718[71].

the effect of pressure on the phase-transformation equilibrium temperature in a given system.

$$\frac{dT_{eq}}{dP} = \frac{T_{eq} \Delta V}{\Delta H} \quad (1)$$

Here,  $P$  is the pressure,  $T_{eq}$  is the equilibrium phase-transformation temperature,  $\Delta H$  is the enthalpy change, and  $\Delta V$  is the molar volume difference between the two phases during phase transformation. If  $\frac{dT_{eq}}{dP} < 0$ , then an increase in pressure will suppress the phase equilibrium temperature, which is the case for the  $\delta$  phase, as seen from the theoretical calculation of the Clausius-Clapeyron relation (Table 3). One can argue that the values shown in Table 3 may have a negligible effect in reality. However, the purpose of this theoretical calculation is to demonstrate that an increase in pressure will lower the equilibrium temperature of the  $\gamma'/\gamma''$  and  $\delta$  phases. Experiments are required to confirm the exact level of drop in the equilibrium temperature owing to the elevated pressure on Alloy 718.

Finally, ageing HT is performed to increase the material strength by precipitating the strengthening phases. Owing to the homogenized composition distribution state of the  $\gamma$  matrix after the previous HTs, strengthening precipitation occurs uniformly in the matrix, thereby resulting in increased hardness of the material [71]. S. Goel et al. [67] demonstrated that regardless of the initial variation in the hardness of EB-PBF Alloy 718, after HIP and HT involving ageing, higher and uniform hardness can be obtained. It is worth mentioning that HT operations used for conventional cast and wrought Alloy 718 are typically employed for EB-PBF Alloy 718[58,72,73]. This is also reflected in the ASTM F3055 standard for PBF Alloy 718, where the HT parameters appear to be taken from the existing AMS 5363 standard for cast [74], and the AMS 2774 standard for wrought Alloy 718[75]. However, as stated previously, it is evident from the literature that the microstructure of conventional cast-wrought Alloy 718 is highly different from that of EB-PBF or other AM Alloy 718[20,76,77]. Thus, using standard cast-wrought Alloy 718 HT procedures may not be the ideal solution for EB-PBF materials. Therefore, there is a need for exploring HT protocols tailored to such materials. Previous work by the authors' research group has demonstrated that, for precipitation of strengthening phases in EB-PBF Alloy 718, the HT time (particularly for ageing) can be significantly

reduced compared with the schedule recommended in the ASTM F3055 standard (see Fig. 14) [71,78].

In Fig. 14, it is seen that the hardness of the Alloy 718 material was significantly reduced after the HIP treatment (1120°C, 4 h, 100 MPa). This is expected, as HIP dissolves the strengthening phases completely, and the application of fast cooling after the holding time inhibits any significant re-precipitation [63]. In addition, as explained earlier, HIP treatment results in a matrix that has a homogenized composition distribution, with compositional values close to those of the nominal composition of the Alloy 718. It was observed that in the first ageing step (Age 1), hardness increased as the ageing time increased from 1 h to 4 h, and with prolonged holding at the Age 1 temperature for 4 h, no further hardness change was noticed. Similarly, during the second ageing step (Age 2), following an 8 h treatment in the first step, hardness increased after 1 h of holding time. However, no further effect on hardness was observed for longer holding time. Therefore, hardness appeared to flatten after 4 h for Age 1, and after 1 h for Age 2. These results are indicative of the possibility to reduce the duration of traditional double ageing treatment. Detailed microstructure characterization related to evaluating the shortening of the ageing time and the correlation with hardness is part of another ongoing study in the authors' research group. A similar hardness increase within 5 h during the first step of aging at 760 °C is also reported (see Fig. 15) in Fisk et al. [79] for Alloy 718 that was hot-rolled and solution-treated at 954 °C for 1 h prior to ageing.

An alternative approach to precipitating strengthening phases in HIPed EB-PBF Alloy 718 could be continuous cooling, as mentioned in Section 4.1. Experiments were conducted to evaluate the feasibility of this approach for performing STA through controlled cooling after holding at HIP temperature (see Appendix C for details). Fig. 16 shows the hardness results from the continuous cooling experiments, with pressure (STA was performed inside the HIP vessel directly after the HIP treatment) and without pressure (STA in a heat treatment furnace). The results are in good agreement with those by L. Geng et al. [63]. A detailed microstructure characterization related to the continuous cooling experiments and the correlation with hardness is part of another ongoing study.

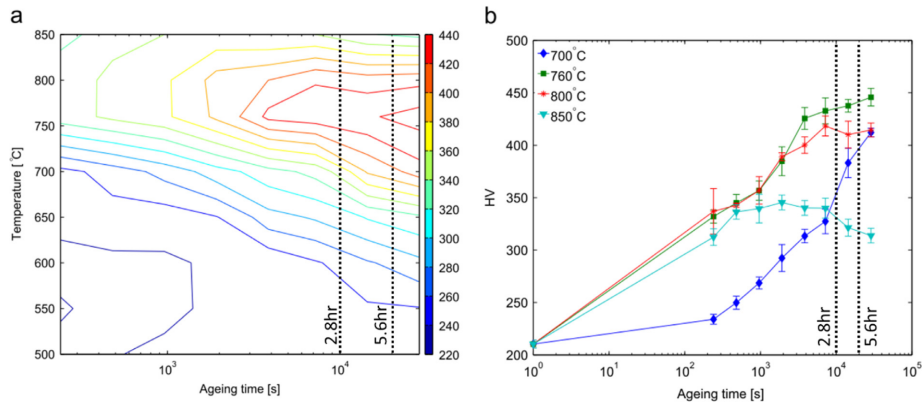


Fig. 15. (a) Contour plot of ageing time, temperature, and microhardness; (b) variation in microhardness with ageing time at four different temperatures for Alloy 718. Taken from [79].

Table 4  
Time that Alloy 718 microstructure spent in  $\delta$  and  $\gamma'/\gamma''$  precipitation window.

Cooling rate (°C/min)	0.5	2	5	20
Time (min) spent in direct $\delta$ precipitation window (1020–900°C)	240	60	24	6
Time (min) spent in $\gamma'/\gamma''$ precipitation window (900–600°C)	600	150	60	15
Time (min) required to cool down to 500°C from 1120°C	1240	310	124	31

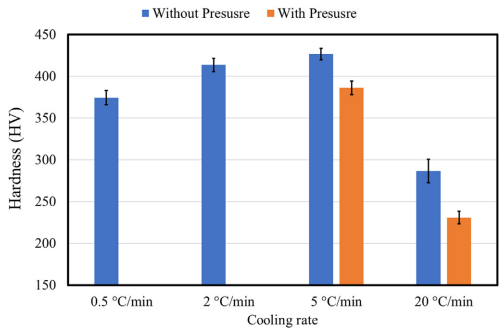


Fig. 16. Effect of cooling rate on hardness of EB-PBF Alloy 718 after holding at 1120°C.

In the continuous cooling experiments by L. Geng et al. [63], the hardness variation was explained by the variation of  $\delta$  and  $\gamma''$  observed in the microstructure under different cooling rates. At 5 °C/min, a peak in hardness was observed. Below 5 °C/min, as the cooling rate decreased, hardness dropped gradually. This can be explained by the increase in the  $\delta$  phase volume fraction that precipitates with the decrease in the cooling rate. No  $\delta$  was observed for cooling rates above 5 °C/min [63]. As seen in Table 4, at 0.5 °C/min, the microstructure had spent approximately 4 h in the direct  $\delta$  precipitation window; this allows the  $\delta$  phase to nucleate and grow, thus reaching a higher volume fraction and consuming more Nb from the matrix. This lowers the equilibrium volume fraction for  $\gamma''$  that can precipitate and thereby results in lower hardness. The higher hardness at 5 °C/min corresponds to a structure with a high density of fine and discrete  $\gamma''$  precipitates formed during the time

(~1 h) that the microstructure spent in the  $\gamma'/\gamma''$  precipitation window at a cooling rate of 5 °C/min. In S. Goel's study [71], it was reported that HIPed Alloy 718 without any other subsequent HT (therefore no  $\gamma'/\gamma''$ ) had a hardness of ~200 HV. Comparing this with the hardness resulting from a 20 °C/min cooling implies that during the 15 min strengthening-phase precipitation window, precipitation did occur.

As seen in Fig. 16, the continuous cooling experiments conducted inside the HIP vessel under pressure resulted in lower hardness. This could also be related to the effect of pressure on the phase transformation, as discussed above.

## 5. Summary and conclusions

In this paper, we presented and discussed aspects of phase transformation in Alloy 718 during the L-DED and EB-PBF AM processes and the commonly used subsequent post HIP and HTs. Data gathered from the literature, theoretical principles, and additional modeling results were used in this study. The present discussion demonstrated that the phase transformation in Alloy 718 is complex and influenced by factors such as solidification thermal conditions, the thermal history as well as the composition segregation observed during the process. Therefore, controlling the thermal condition during the AM process is of the utmost importance. In addition to that, the change in local thermodynamics and kinetics of the Alloy 718 due to the local change in composition influence the phase transformation during the standard post HT for the Alloy 718.

Discussion presented in this article reveal that the common HTs originally designed for cast-and-wrought Alloy 718 may not be the optimal solution for additively manufactured Alloy 718 parts. Therefore, focus should be placed on designing new HTs specifically for additively manufactured Alloy 718. In this study, the grain structure changes during HIP and HTs were not discussed in detail. However, in the design of new HTs for AM Alloy 718, the effect of grain structure (morphology, distribution, and texture) changes should also be considered, particularly if



the HT temperatures are high ( $> 1000$  °C), where grain growth can occur. Additive manufacturing allows the production of a wide range of grain microstructures, from columnar to equiaxed grains, in a single part [1,2,33]. Consequently, designing HIP and HTs applicable to all these different grain structures will definitely be a challenging task, as these structures tend to behave differently under post-HIP and HT conditions.

Even though LB-PBF was not considered, it is conceivable that the information and discussion provided herein could be used to understand the phase transformation during LB-PBF and the subsequent HIP and HTs. As LB-PBF is a colder process, the discussion given in Section 3 may be a starting point to understand the phase transformation for this process as well. However, owing to the increased cooling rate, the length scale of LB-PBF will be smaller than that of the L-DED process.

In conclusion, we believe that the information and discussion presented in this paper will promote the understanding of the overall process–structure–property relationship in AM of Alloy 718.

### Acknowledgements

The funding from the European Regional Development Fund for project 3Dprint, and from KK Foundation (Stiftelsen för Kunskaps- och Kompetensutveckling) for project SUMAN-Next is also acknowledged. The authors are very grateful to Mr Mats Högström, University West and Mr Johannes Gårdstam, Quintus Technologies AB, Västerås, Sweden for carrying out the continuous cooling experiments.

### Declaration of Competing Interest

None.

### Appendix: A

#### Modeling the effect of solidification on Alloy 718 conditions using MICRESS

Herein, the MICRESS software package, which is based on the multiphase-field method [80–83], is used to investigate the effect of solidification condition of Laves-phase formation in Alloy 718. The models were set up as follows.

Modeling was performed in 2D. The size of the modelling domain was  $80\ \mu\text{m} \times 80\ \mu\text{m}$  with  $0.1\ \mu\text{m}$  grid spacing. A constant thermal gradient was applied from top to bottom of the domain. A constant cooling rate was applied to the whole domain. This mimics the moving of the liquidus isotherm from bottom to top in the simulation domain. At the beginning of the simulation, a grain which has almost flat liquid/ $\gamma$  interface with random noise was set at the bottom of the simulation domain. The orientation of this grain was set so that its fast-growth direction is parallel to the applied thermal gradient direction in the domain. This mimics the growth of epitaxial dendrites from a substrate or the re-melted layers. During the simulation, the nucleation of new  $\gamma$  grains were set randomly in the liquid. For simplicity, only the liquid/ $\gamma$  interface was modeled as an anisotropic interface having cubic crystal anisotropy. The rest of the simulation parameters, including simplified nominal Alloy 718 composition, nucleation of Laves phase, interfacial energy values, interface thickness, and interfacial stiffness/mobility coefficient for anisotropy were taken from [23]. Thermodynamic and mobility data were taken from the TCNI8 and MOBNI4 databases from Thermo-Calc [84].

The MICRESS model setup we used here is similar to the model setup reported in Nie et al. [30]. However, in Nie et al has used a stochastic modelling approach and modelled the Alloy 718 system as Ni-Nb bi-

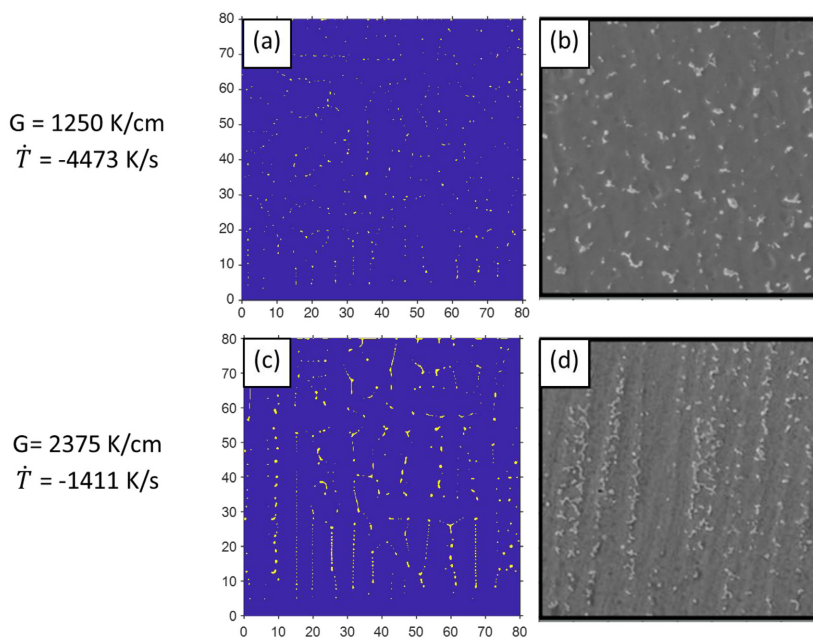


**Fig. A1.** (a), (c) Predicted morphology of the Laves phase at two different thermal conditions and (b), (d) respective experimentally observed Laves phase morphology in the microstructure (size  $80\ \mu\text{m} \times 80\ \mu\text{m}$ ). Thermal conditions and the experimentally observed microstructures were taken from Nie et al. [30].

nary system without considering the Laves phase formation explicitly. Whereas in our case we have modelled the Alloy 718 as 6 element system (Ni-Cr-Fe-Mo-Nb-Ti) and explicitly modelled the formation of Laves phase in the microstructure. In addition to that, Nie et al. have used fixed orientation for the new  $\gamma$  grains that form in the liquid. The model predictions in our current study were also in a better agreement with the experimental observations (see Fig. A1) reported in Nie et al. [30].

## Appendix: B

### Direct ageing heat-treatment simulations using MICRESS

Herein, DA, as per AMS5383, was simulated using MICRESS. The microstructure resulted from the L-DED thermal cycle simulation in [23] was used as the initial starting microstructure. During the simulation, only the nucleation (randomly) of  $\gamma''$  in the matrix was set for simplicity. The grid resolution of the L-DED simulation was 50  $\mu\text{m}$ . Therefore, the correct size and morphology of  $\gamma''$  could not be resolved correctly under this grid resolution. To overcome this, the analytical curvature model [82,85,86] implemented in MICRESS was used. The anisotropy of  $\gamma/\gamma''$  was neglected, and an isotropic interaction model was adopted. An interfacial energy of  $1 \times 10^{-5} \text{ J/cm}^2$  [87] was used. No phase interaction between the Laves phase and  $\gamma''$  was modeled. The rest of the parameters, including simplified Alloy 718 composition, were taken from [23].

## Appendix: C

### Continuous cooling experiments without pressure

HIPed EB-PBF Alloy 718 samples were used for the continuous cooling experiments. Samples (17 mm  $\times$  15 mm  $\times$  55 mm) were printed with an Arcam A2X machine using Arcam Standard parameters. Before the continuous cooling, the samples were again homogenized at 1120 °C for 1 h. The experiments related to 0.5 °C/min and 2 °C/min cooling rates were conducted using an alumina tube furnace (model R120/500/13, Nabetherm GmbH, Germany) in an inert argon atmosphere. The rest of the cooling rate experiments were conducted using a Gleeble 3800D system (Dynamic Systems Inc, Poestenkill, NY, USA). All the cooling rates were maintained up to 500 °C, and thereafter the samples were quenched to room temperature. The samples were metallographically prepared for hardness evaluation. Hardness measurements were performed using a Shimadzu HMV-2 microhardness tester with 1 kg load and 15 s dwell time.

### Continuous cooling experiments with pressure

The continuous cooling rate studies inside the HIP furnace (Model QIH21, Quintus Technologies, Sweden) were performed under pressure. EB-PBF Alloy 718 samples were first HIPed at 1120 °C/100 MPa for 4 h before being continuously cooled at 5 °C/min and 20 °C/min. However, during cooling, the pressure gradually dropped with temperature to a value of 40 MPa. The samples were metallographically prepared for hardness evaluation. Hardness measurements were performed using a Shimadzu HMV-2 microhardness tester with 1 kg load applied for 15 s.

## References

- [1] S.S. Babu, et al., Additive Manufacturing of Nickel SuperAlloy 718 s: Opportunities for Innovation and Challenges Related to Qualification, *Metall. Mater. Trans. A* 49 (9) (Sep. 2018) 3764–3780.
- [2] T. DebRoy, et al., Additive manufacturing of metallic components – Process, structure and properties, *Prog. Mater. Sci.* 92 (Mar. 2018) 112–224.
- [3] M.M. Attallah, R. Jennings, X. Wang, L.N. Carter, Additive manufacturing of Ni-based superAlloy 718 s: The outstanding issues, *MRS Bull* 41 (10) (2016) 758–764.
- [4] S. Sui, et al., The influence of Laves phases on the room temperature tensile properties of Inconel 718 fabricated by powder feeding laser additive manufacturing, *Acta Mater* 164 (2019) 413–427 February.
- [5] M. Anderson, A.-L. Thielin, F. Bridier, P. Bocher, J. Savoie,  $\delta$  Phase precipitation in Inconel 718 and associated mechanical properties, *Mater. Sci. Eng. A* 679 (Jan. 2017) 48–55.
- [6] G.A. Khorovskiy, M.J. Cieslak, T.J. Headley, A.D. Romig, W.F. Hammett, INCONEL 718: a solidification diagram, *Metall. Trans. A* 20 (10) (Oct. 1989) 2149–2158.
- [7] R.W. Hayes, Creep Deformation of Inconel Alloy 718 in the 650 °C To 760 °C, in: *SuperAlloy 718 s 718, 625 and Various Derivatives*, 1991, 1991, pp. 549–562.
- [8] C. Kumara, Microstructure Modelling of Additive Manufacturing of Alloy 718, 2018.
- [9] J.F. Radavich, The physical metallurgy of cast and wrought alloy 718, *SuperAlloy 718 s 718 Metall. Appl.* (1989) 229–240.
- [10] M. Sundaraman, P. Mukhopadhyay, S. Banerjee, Precipitation of the Delta-Ni3Nb phase in two nickel base superAlloy 718s, *Metall. Trans. A* 19 (3) (1988) 453–465.
- [11] S. Azadian, L.Y. Wei, R. Warren, Delta phase precipitation in inconel 718, *Mater. Charact.* 53 (1) (2004) 7–16.
- [12] T. Antonsson, H. Fredriksson, The effect of cooling rate on the solidification of INCONEL 718, *Metall. Mater. Trans. B* 36 (1) (Feb. 2005) 85–96.
- [13] J.T. Tharappel, J. Babu, Welding processes for Inconel 718: A brief review welding processes for Inconel 718- a brief review, *IOP Conf. Series: Materials Science and Engineering*, 330, 2018.
- [14] D. Deng, R.L. Peng, H. Söderberg, J. Moverare, On the formation of microstructural gradients in a nickel-base superAlloy 718 during electron beam melting, *Mater. Des.* 160 (2018) 251–261.
- [15] Y. Zhang, Z. Li, P. Nie, Y. Wu, Effect of cooling rate on the microstructure of laser-remelted INCONEL 718 coating, *Metall. Mater. Trans. A* 44 (12) (Dec. 2013) 5513–5521.
- [16] J.K. Tien, T. Caulfield, SuperAlloy 718s, supercomposites and superceramics, Academic Press, 1989.
- [17] W.M. Haynes, CRC Handbook of Chemistry and Physics - Google Books, 97th ed., CRC Press, 2016.
- [18] R. Trivedi, W. Kurz, Solidification microstructures: a conceptual approach, *Acta Metall. Mater.* 42 (1) (1994) 15–23.
- [19] Z. Wang, K. Guan, M. Gao, X. Li, X. Chen, X. Zeng, The microstructure and mechanical properties of deposited-IN718 by selective laser melting, *J. Alloy 718s Compd.* 513 (2012) 518–523.
- [20] D. Deng, R.L. Peng, H. Brodin, J. Moverare, Microstructure and mechanical properties of Inconel 718 produced by selective laser melting: sample orientation dependence and effects of post heat treatments, *Mater. Sci. Eng. A* 713 (October 2017) 294–306 2018.
- [21] S. Ghosh, et al., Single-track melt-pool measurements and microstructures in Inconel 625, *Jom* (2018) February.
- [22] S. Ghosh, M.R. Stoudt, L.E. Levine, J.E. Guyer, Formation of Nb-rich droplets in laser deposited Ni-matrix microstructures, *Scr. Mater.* 146 (2017) 36–40.
- [23] C. Kumara, et al., Microstructure modelling of laser metal powder directed energy deposition of Alloy 718, *Addit. Manuf.* 25 (2019) 357–364.
- [24] C. Kumara, D. Deng, F. Hanning, M. Raanes, J. Moverare, P. Nylén, Predicting the Microstructural Evolution of Electron Beam Melting of Alloy 718 with Phase-Field Modeling, *Metall. Mater. Trans. A Phys. Metall. Mater. Sci.* 50 (5) (2019) 2527–2537.
- [25] H. Qi, M. Azer, A. Ritter, Studies of standard heat treatment effects on microstructure and mechanical properties of laser net shape manufactured INCONEL 718, *Metall. Mater. Trans. A* 40 (10) (Oct. 2009) 2410–2422.
- [26] W. Huang, J. Yang, H. Yang, G. Jing, Z. Wang, X. Zeng, Heat treatment of Inconel 718 produced by selective laser melting: Microstructure and mechanical properties, *Mater. Sci. Eng. A* 750 (2019) 98–107 February.
- [27] G.D. Janaki Ram, A. Venugopal Reddy, K. Prasad Rao, G.M. Reddy, J.K. Sarin Sundar, Microstructure and tensile properties of Inconel 718 pulsed Nd-YAG laser welds, *J. Mater. Process. Technol.* 167 (1) (Aug. 2005) 73–82.
- [28] X. Li, et al., Effect of heat treatment on microstructure evolution of Inconel 718 Alloy 718 fabricated by selective laser melting, *J. Alloy 718s Compd.* 764 (2018) 639–649.
- [29] J.J. Schirra, R.H. Cales, R.W. Hatala, The effect of laves phase on the mechanical properties of wrought and cast + HIP Inconel 718, in: *SuperAlloy 718 s 718, 625 and Various Derivatives*, 1991, 1991, pp. 375–388.
- [30] P. Nie, O.A. Ojo, Z. Li, Numerical modeling of microstructure evolution during laser additive manufacturing of a nickel-based superAlloy 718, *Acta Mater* 77 (Sep. 2014) 85–95.
- [31] F.D.J. Kurz W., Fundamentals of solidification, 1988, CRC Press, 1998 June 1.
- [32] Ø. Grong, Metallurgical modelling of welding, Institute of Materials, 1997.
- [33] A.R. Balachandramurthi, J. Olsson, J. Ålgårdh, A. Snis, J. Moverare, R. Pederson, Microstructure tailoring in Electron Beam Powder Bed Fusion additive manufacturing and its potential consequences, *Results Mater* 1 (2019) 100017 August.
- [34] N. Raghavan, et al., Numerical modeling of heat-transfer and the influence of process parameters on tailoring the grain morphology of IN718 in electron beam additive manufacturing, *Acta Mater* 112 (2016) 303–314.
- [35] G. Lindwall, et al., Simulation of TTT curves for additively manufactured Inconel 625, *Metall. Mater. Trans. A* 50 (1) (Jan. 2019) 457–467.
- [36] Y. Tian, et al., Rationalization of microstructure heterogeneity in INCONEL 718 builds made by the direct laser additive manufacturing process, *Metall. Mater. Trans. A* 45 (10) (Sep. 2014) 4470–4483.
- [37] R.G. Carlson, J.F. Radavich, Microstructural characterization of cast 718, *SuperAlloy 718 s 718 Metall. Appl.* (1989) 79–95.
- [38] A. Segerstark, J. Andersson, L. Svensson, O. Ojo, Microstructural characterization of laser metal powder deposited Alloy 718, *Mater. Charact.* 142 (Aug. 2018) 550–559 June.

- [39] A. Segerstark, J. Andersson, L. Svensson, Evaluation of a temperature measurement method developed for laser metal deposition, *Sci. Technol. Weld. Join.* 22 (1) (Jan. 2017) 1–6.
- [40] Z. Li, J. Chen, S. Sui, C. Zhong, X. Lu, X. Lin, The microstructure evolution and tensile properties of Inconel 718 fabricated by high-deposition-rate laser directed energy deposition, *Addit. Manuf.* 31 (2020) 100941 November 2019.
- [41] X. Zhao, J. Chen, X. Lin, W. Huang, Study on microstructure and mechanical properties of laser rapid forming Inconel 718, *Mater. Sci. Eng. A* 478 (1–2) (Apr. 2008) 119–124.
- [42] Y.-N. Zhang, X. Cao, P. Wanjara, M. Medraj, Tensile properties of laser additive manufactured Inconel 718 using filler wire, *J. Mater. Res.* 29 (17) (Sep. 2014) 2006–2020.
- [43] C. Zhong, A. Gasser, J. Kittel, J. Fu, Y. Ding, R. Poprawe, Microstructures and tensile properties of Inconel 718 formed by high deposition-rate laser metal deposition, *J. Laser Appl.* 28 (2) (2016) 022010.
- [44] Y. Zhang, L. Yang, T. Chen, W. Zhang, X. Huang, J. Dai, Investigation on the optimized heat treatment procedure for laser fabricated IN718 Alloy 718, *Opt. Laser Technol.* 97 (2017) 172–179 October.
- [45] L. Zhu, Z. Xu, Y. Gu, Effect of laser power on the microstructure and mechanical properties of heat treated Inconel 718 superAlloy 718 by laser solid forming, *J. Alloy 718s Compd.* 746 (2018) 159–167.
- [46] S. Sui, C. Zhong, J. Chen, A. Gasser, W. Huang, J.H. Schleifenbaum, Influence of solution heat treatment on microstructure and tensile properties of Inconel 718 formed by high-deposition-rate laser metal deposition, *J. Alloy 718s Compd.* 740 (2018) 389–399.
- [47] S. Sui, et al., Microstructures and stress rupture properties of pulse laser repaired Inconel 718 superAlloy 718 after different heat treatments, *J. Alloy 718s Compd.* 770 (2019) 125–135.
- [48] J.F. Muller, M.J. Donachie, The effects of solution and intermediate heat treatments on the notch-rupture behavior of Inconel 718, *Mater. Trans. A* 6 (12) (1975) 2221–2227.
- [49] G. Sjoberg, N.G. Ingesten, R.G. Carlson, Grain boundary  $\delta$ -phase morphologies, carbides and notch rupture sensitivity of cast alloy 718, in: *SuperAlloy 718s* 718, 625, 706 and Derivatives, 1991, 1991, pp. 603–620.
- [50] D. Cai, W. Zhang, P. Nie, W. Liu, M. Yao, Dissolution kinetics of  $\delta$  phase and its influence on the notch sensitivity of Inconel 718, *Mater. Charact.* 58 (3) (2007) 220–225.
- [51] S. Sui, et al., Microstructures and stress rupture properties of pulse laser repaired Inconel 718 superAlloy 718 after different heat treatments, *J. Alloy 718s Compd.* 770 (2019) 125–135.
- [52] S. Sui, J. Chen, Z. Li, H. Li, X. Zhao, H. Tan, Investigation of dissolution behavior of Laves phase in Inconel 718 fabricated by laser directed energy deposition, *Addit. Manuf.* (2020) 101055 January.
- [53] L. Zhu, Z. Xu, Y. Gu, Effect of laser power on the microstructure and mechanical properties of heat treated Inconel 718 superAlloy 718 by laser solid forming, *J. Alloy 718s Compd.* 746 (2018) 159–167.
- [54] Porter D A, E.K. E, M.Y. SHERIF, *Phase Transformations in metals and Alloy 718s*, CRC Press, 2009.
- [55] M. Sundararaman, N. Sachin, B.S. Jung, V. Amit, P. Bhaskar, R. Kishore, Evolution of  $\delta$  phase microstructure in Alloy 718, 7th Int. Symp. SuperAlloy 718s 718 Deriv. (2010) 737–750.
- [56] F. Theska, et al., On the early stages of precipitation during direct ageing of Alloy 718, *Acta Mater* 188 (2020) 492–503.
- [57] R.R. Dehoff, et al., Site specific control of crystallographic grain orientation through electron beam additive manufacturing, *Mater. Sci. Technol.* 31 (8) (2015) 931–938.
- [58] M.M. Kirka, et al., Strategy for Texture Management in Metals Additive Manufacturing, *JOM* 69 (3) (2017) 523–531.
- [59] W.J. SAMES, Additive manufacturing of Inconel 718 using electron beam melting: processing, post-processing, & mechanical properties, A&M University, Texas, 2015.
- [60] M.M. Kirka, K.A. Unocic, N. Raghavan, F. Medina, R.R. Dehoff, S.S. Babu, Microstructure development in electron beam-melted Inconel 718 and associated tensile properties, *JOM* 68 (3) (2016) 1012–1020.
- [61] A.R. Balachandramurthi, J. Moverare, S. Mahade, R. Pederson, Additive manufacturing of Alloy 718 via electron beam melting: Effect of post-treatment on the microstructure and the mechanical properties, *Materials (Basel)* 12 (1) (2018).
- [62] S. Goel, M. Ahlfor, F. Babhou, S. Joshi, Effect of different post-treatments on the microstructure of EBM-built Alloy 718, *J. Mater. Eng. Perform.* 28 (2) (2019) 673–680.
- [63] L. Geng, Y. Na, N.-K. Park, Continuous cooling transformation behavior of Alloy 718, *Mater. Lett.* 30 (5–6) (1997) 401–405.
- [64] W.J. Sames, F.A. List, S. Pannala, R.R. Dehoff, S.S. Babu, The metallurgy and processing science of metal additive manufacturing, *Int. Mater. Rev.* 6608 (2016) 1–46 March.
- [65] ASTM, Standard Specification for Additive Manufacturing Nickel Alloy 718 (UNS N07718) with Powder Bed Fusion F3055-14a, ASTM International, West Conshohocken, PA, 2014 [www.astm.org](http://www.astm.org).
- [66] A.R. Balachandramurthi, J. Moverare, N. Dixit, R. Pederson, Influence of defects and as-built surface roughness on fatigue properties of additively manufactured Alloy 718, *Mater. Sci. Eng. A* 735 (2018) 463–474 August.
- [67] S. Goel, J. Olsson, M. Ahlfor, U. Klement, S. Joshi, The effect of location and post-treatment on the microstructure of EBM-built Alloy 718, in: *Proceedings of the 9th International Symposium on SuperAlloy 718& Derivatives: Energy, Aerospace, and Industrial Applications*, 2018, 2018, pp. 115–129. June.
- [68] M.M. Kirka, F. Medina, R. Dehoff, A. Okello, Mechanical behavior of post-processed Inconel 718 manufactured through the electron beam melting process, *Mater. Sci. Eng. A* (2016) 1–9.
- [69] S. Goel, A. Sittithi, I. Charit, U. Klement, S. Joshi, Effect of post-treatments under hot isostatic pressure on microstructural characteristics of EBM-built Alloy 718, *Addit. Manuf.* 28 (2019) 727–737 June.
- [70] D. Deng, J. Moverare, R.L. Peng, H. Söderberg, Microstructure and anisotropic mechanical properties of EBM manufactured Inconel 718 and effects of post heat treatments, *Mater. Sci. Eng. A* 693 (2017) 151–163 December 2016.
- [71] S. Goel, Post-treatment of Alloy 718 produced by electron beam melting Licentiate Thesis, University West, 2019.
- [72] P. Nandwana, M. Kirka, A. Okello, R. Dehoff, Electron beam melting of Inconel 718: effects of processing and post-processing, *Mater. Sci. Technol. (United Kingdom)* 34 (5) (2018) 612–619.
- [73] K.A. Unocic, L.M. Kolbus, R.R. Dehoff, S.N. Dryepondt, B.A. Pint, High-Temperature performance of UNS N07718 processed by additive manufacturing, corrosion, 2014, 2014 November 2015.
- [74] SAE, AMS5383E-Nickel Alloy 718, Corrosion and Heat-Resistant, Investment Castings, 2012.
- [75] ASTM, ASTM 2774A - Heat Treatment Wrought Nickel Alloy 718 and Cobalt Alloy 718 Parts AMS, 2011.
- [76] A. Strödel et al., "Microstructure and mechanical properties of nickel based super-Alloy 718 IN718 produced by rapid prototyping with electron beam melting (EBM) Microstructure and mechanical properties of nickel based superAlloy 718 IN718 produced by rapid prototyping with electro," vol. 0836, 2013.
- [77] A. Chamanfar, L. Sarraf, M. Jahazi, M. Asadi, A. Weck, A.K. Koul, Microstructural characteristics of forged and heat treated Inconel-718 disks, *Mater. Des.* 52 (2013) 791–800.
- [78] E. Zaninelli, Effects of post-processing on EBM fabricated Inconel 718 Master Thesis, Università degli studi di Modena e Reggio Emilia, 2018.
- [79] M. Fisk, J. Andersson, R. du Riet, S. Haas, S. Hall, Precipitate evolution in the early stages of ageing in Inconel 718 investigated using small-angle x-ray scattering, *Mater. Sci. Eng. A* 612 (2014) 202–207.
- [80] I. Steinbach, et al., A phase field concept for multiphase systems, *Phys. D Nonlinear Phenom.* 94 (3) (Jul. 1996) 135–147.
- [81] J. Eiken, B. Böttger, I. Steinbach, Multiphase-field approach for multicomponent Alloy 718s with extrapolation scheme for numerical application, *Phys. Rev. E* 73 (6) (Jun. 2006) 066122.
- [82] B. Böttger, J. Eiken, I. Steinbach, Phase field simulation of equiaxed solidification in technical Alloy 718s, *Acta Mater* 54 (10) (2006) 2697–2704.
- [83] J. Eiken, A phase-field model for technical Alloy 718 solidification, Shaker Verlag GmbH, Germany, 2010.
- [84] "Thermo-Calc Software." [Online]. Available: <http://www.thermocalc.com/>. [Accessed: 25-May-2018].
- [85] B. Böttger, M. Apel, B. Laux, S. Pieger, Detached melt nucleation during diffusion brazing of a technical Ni-based superAlloy 718: A phase-field study, *IOP Conf. Ser. Mater. Sci. Eng.* 84 (1) (2015).
- [86] B. Böttger, M. Apel, B. Daniels, L. Dankl, T. Göhler, T. Jokisch, Systematic Phase-field study on microstructure formation during brazing of Mar-M247 with a Si-Based AMS4782 Filler, *Metall. Mater. Trans. A* (2019).
- [87] N. Zhou, et al., Computer simulation of phase transformation and plastic deformation in IN718 superAlloy 718: Microstructural evolution during precipitation, *Acta Mater* 65 (Feb. 2014) 270–286.



## Paper B

# Microstructure modelling of laser metal powder directed energy deposition of alloy 718

Chamara Kumara

Andreas Segerstark

Fabian Hanning

Nikhil Dixit

Shrikant Joshi

Johan Moverare

Per Nylén

Published in *Additive Manufacturing*

vol. 25, pp. 357–364, 2019.

DOI: 10.1016/j.addma.2018.11.024

Reprinted with CC BY-NC-ND 4.0





## Full Length Article

## Microstructure modelling of laser metal powder directed energy deposition of alloy 718



Chamara Kumara<sup>a,\*</sup>, Andreas Segerstark<sup>b</sup>, Fabian Hanning<sup>c</sup>, Nikhil Dixit<sup>a</sup>, Shrikant Joshi<sup>a</sup>, Johan Moverare<sup>a,d</sup>, Per Nylén<sup>a</sup>

<sup>a</sup> Division of Subtractive and Additive Manufacturing Processes, Department of Engineering Science, University West, 461 86 Trollhättan, Sweden

<sup>b</sup> GKN Aerospace Engine Systems AB, Trollhättan, SE-461 81, Sweden

<sup>c</sup> Department of Industrial and Materials Science, Chalmers University of Technology, 412 96 Gothenburg, Sweden

<sup>d</sup> Division of Engineering Materials, Department of Management and Engineering, Linköping University, SE-58183 Linköping, Sweden

## ARTICLE INFO

**Keywords:**  
Phase-field  
DED  
Heat treatment  
Thermal cycle  
Modelling

## ABSTRACT

A multi-component and multi-phase-field modelling approach, combined with transformation kinetics modelling, was used to model microstructure evolution during laser metal powder directed energy deposition of Alloy 718 and subsequent heat treatments. Experimental temperature measurements were utilised to predict microstructural evolution during successive addition of layers. Segregation of alloying elements as well as formation of Laves and  $\delta$  phase was specifically modelled. The predicted elemental concentrations were then used in transformation kinetics to estimate changes in Continuous Cooling Transformation (CCT) and Time Temperature Transformation (TTT) diagrams for Alloy 718. Modelling results showed good agreement with experimentally observed phase evolution within the microstructure. The results indicate that the approach can be a valuable tool, both for improving process understanding and for process development including subsequent heat treatment.

## 1. Introduction

Nickel-based superalloys represent one of the most important categories of alloys used in aerospace and gas turbine engines due to the desirable combination of good high-temperature strength, high resistance to creep deformation and corrosion resistance [1,2] that they offer. Among these superalloys, Alloy 718 is one of the most commonly employed nickel-iron based superalloys. This alloy has good weldability due to the sluggish precipitation of strengthening phases present in it [3]. Alloy 718 has a microstructure that is dominated by a  $\gamma$  Face Centred Cubic (FCC) matrix. Within the matrix, precipitates such as Laves,  $\gamma'/\gamma''$  (strengthening phases),  $\delta$  and various metallic carbides and nitrides can be found [4]. The specific microstructure (phase constitution, phase distribution and morphology) of the alloy is mainly governed by the primary manufacturing technology and succeeding post-processing conditions. Suitable heat treatments are commonly employed to tailor the microstructure of Alloy 718 to achieve the properties required for any targeted application.

According to the ASTM standard [5] directed energy deposition (DED) process is an additive manufacturing process in which a focused energy source (eg: laser, electron beam, plasma arc) is used to fuse

materials by melting as they are being deposited. The deposition material can be in the form of powder or wire [6]. In the present study, a laser source was used as the focused energy source and deposition material was in the form of powder. Thus in this article, this process is being referred to as laser metal powder directed energy deposition (LMPDED). Among the repair methods for worn and corroded gas turbine components, this LMPDED method has become popular due to that fact that the parts can be repaired with minimal dilution and distortion [7]. In addition, this method is also used to add features to cast and forged components [8]. In layer-by-layer material deposition that LMPDED involves, the deposited material undergoes repeated heating and cooling when successive layers are being deposited. This causes the solidified material to experience remelting, resolidification and solid-state phase transformation, depending on the nature of the local thermal conditions (such as heating rates, cooling rates, thermal gradients, maximum temperature and number of thermal cycles). Prior published literature reveals that each of the above ultimately influence the underlying microstructure and the resulting mechanical properties [7,9–13].

Tian et al [7] reported a higher hardness in the bottom region than in the top region of Alloy 718 builds deposited by LMPDED. This was

\* Corresponding author.

E-mail address: [chamara.kumara@hv.se](mailto:chamara.kumara@hv.se) (C. Kumara).

<https://doi.org/10.1016/j.addma.2018.11.024>

Received 29 August 2018; Received in revised form 20 November 2018; Accepted 20 November 2018

Available online 22 November 2018

2214-8604/ © 2018 The Authors. Published by Elsevier B.V. This is an open access article under the CC BY-NC-ND license (<http://creativecommons.org/licenses/by-nc-nd/4.0/>).

rationalised based on the measured thermal profiles at the bottom of the sample and the niobium (Nb) segregation during thermal cycles. The above finding is consistent with the observations made by Zhang et al. [12] and Tabernero et al. [14] in as-built Alloy 718 samples fabricated using a similar process. Qi et al [10] studied the tensile properties of LMPDED Alloy 718 samples in the as-deposited condition and after standard heat treatments (direct age, solution treatment and age i.e., STA, and homogenization followed by STA). The observed differences in mechanical properties in as-built and post-treated conditions were correlated to the corresponding changes observed in microstructure. Liu et al [9] investigated the influence of two different laser scanning paths, namely single direction raster scanning (SDRS) and cross direction raster scanning (CDRS), on the microstructure and mechanical properties. The growth of columnar dendrites was observed to occur along the deposition direction in SDRS samples compared to CDRS samples. However, the CDRS samples showed better ductility compared to the SDRS samples. Apart from experimental studies, modelling studies have also been performed on LMPDED, with the primary focus being on predicting melt pool characteristics, thermal conditions, grain structure and residual stresses [8]. However, relatively less attention has been paid to developing models to predict microconstituent phase formation during the LMPDED process. Nie et al [15] showed the presence of relationships between cooling rates as well as thermal gradients and Laves phase formation during LMPDED of Alloy 718 through stochastic modelling work using a simplified nickel (Ni)-niobium (Nb) Alloy system. Their observations indicated that low thermal gradients and high cooling rates can lead to a distribution of Laves phase as discrete particles rather than in the form of a continuous network and, thus, reduce the risk of cracking.

Based on the above, it is apparent that an improved understanding of microstructure formation during the LMPDED process is important in order to achieve the desired build performance and quality. However, experimental observation of microstructure formation during the build process and subsequent post heat treatments is a difficult and time-consuming task. Therefore, reliable computational modelling methods are highly desirable for this purpose. In the present study, phase-field modelling, combined with transformation kinetics calculations, have been utilised to investigate microstructure formation (growth of dendrites, element segregation and phase formation) during LMPDED of Alloy 718 and subsequent heat treatment.

## 2. Experimental work

Gas atomized Alloy 718 powder was utilised to generate the LMPDED built samples in this study. The powder was deposited onto an as-cast Alloy 718 substrate using a coaxial nozzle equipped with a 6 kW Ytterbium fibre laser. The nozzle set-up was mounted on an IRB-4400 ABB Robot, which was used to control the motion during deposition of the Alloy 718 samples. Single-wall samples comprised of a single layer, 2-layers, 3-layers and 15-layers in the build direction were deposited. The width of the single wall was equal to a width of a single-track (~1.89 mm) and the length of the walls were roughly 35 mm. Table 1 shows the nominal compositions of both powder and substrate. The particle size of the powder was in the range of 20–75  $\mu\text{m}$ . A volumetric powder feeding system was utilised to deliver the powder to the coaxial nozzle with an angular outlet. Argon was used as the carrier gas as well as the shielding gas. Table 2 shows the process parameters used in the present study to generate the deposits. Temperature measurements that served as input for the modelling work in this study were made at the first deposited track level, using type-K thermocouples according to the method previously described by Segerstark et al. [16].

The heat treatment performed in this study was according to the suggestion by Barron [17] and comprised solutionizing the sample using an air furnace at 954 °C/1 h - air-cooled followed by ageing at 760 °C/5 h-furnace cooled + 650 °C/1 h - air-cooled. This heat treatment is generally used in case of Alloy 718 repaired jet engine

**Table 1**

Nominal chemical composition of the raw powder and the nominal chemical composition used for the phase-field simulation. Substrate chemical composition is also given for the reference.

Element	Substrate (wt%)	Powder (wt%)	Simulation (wt%)
Fe	Bal.	Bal.	Bal.
Ni	53.4	52.7	52.7
Cr	18.35	17.5	17.5
Nb	5.24	5.0	5.0
Mo	3.02	3.17	3.17
Ti	0.92	1.07	1.07
Al	0.48	0.68	0.68
Co	0.08	0.2	–
Mn	0.04	0.065	–
Ta	–	0.003	–
Si	0.08	0.088	–
Cu	0.02	0.048	–
C	0.046	0.031	–
P	0.009	0.006	–
B	–	0.003	–

**Table 2**

LMPDED Process parameters used in this study.

Parameter	Value
Laser Power (W)	1000
Scanning Speed (mm/s)	10
Powder Feed rate (g/min)	10
Powder standoff distance (mm)	–1
Shielding gas flow rate (l/min)	11.5
Carrier gas flow rate (l/min)	3.2
Lase spot diameter (mm)	1.6

**Table 3**

Summary of the model parameters used in the multiphase-field simulations in MICRESS.

Parameter	Value
Domain size	25 $\mu\text{m}$ $\times$ 20 $\mu\text{m}$
Grid resolution ( $\Delta x$ )	0.05 $\mu\text{m}$
Interface thickness ( $\eta$ )	2.5 $\Delta x$
Thermal Gradient	0
Interface Energy - Liquid/ $\gamma$ (J/cm <sup>2</sup> )	1.2E-05 [33]
Interface Energy Liquid/Laves (J/cm <sup>2</sup> )	6E-06
Interface Energy $\gamma$ /Laves (J/cm <sup>2</sup> )	5E-06
Interface Energy $\delta$ / $\gamma$ (J/cm <sup>2</sup> )	1E-05 [34]
Interface Energy $\delta$ /Laves (J/cm <sup>2</sup> )	5E-06
Interfacial stiffness Coefficient - Liquid/ $\gamma$	0.2
Interfacial mobility Coefficient - Liquid/ $\gamma$	0.2
Interfacial stiffness Coefficient - $\delta$ / $\gamma$	0.05
Interfacial mobility Coefficient - $\delta$ / $\gamma$	0.05
Elongation factor for $\delta$ / $\gamma$ Interfacial stiffness	2
Elongation factor for $\delta$ / $\gamma$ interface mobility	0.02

components to avoid coarsening of  $\gamma''$  precipitates present in the base component.

For microstructure evaluation, samples were sectioned and mounted using non-conductive Bakelite. Zeiss EVO 50 Scanning Electron Microscope (SEM) was utilised to analyse the microstructure. In order to quantify the area fractions of Nb-rich constituents, SEM images were analysed using the open source software ImageJ. Microhardness measurements were performed using a Vickers micro-hardness testing machine with a load of 0.5 N and a dwell time of 10 s.

## 3. Modelling work

### 3.1. About MICRESS and the governing equations

The phase-field method has been utilized in the current work to



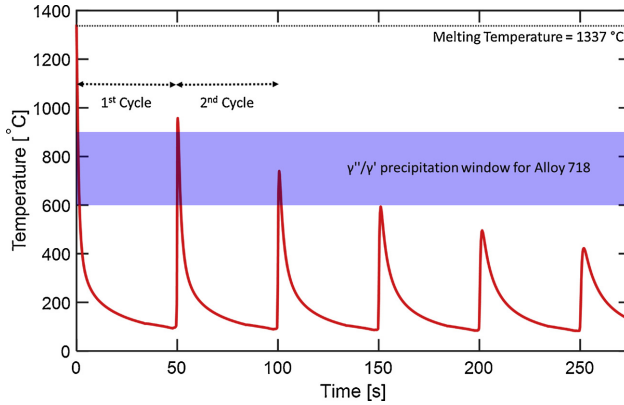


Fig. 1. Time-Temperature history measured at the 1<sup>st</sup> deposited layer. Indicated precipitation windows for  $\gamma'/\gamma''$  for Alloy 718 was taken from [4] and the melting temperature was taken from Thermo-Calc calculation for reduced composition used in the MICRESS simulations.

model the evolution of microstructure during LMPDED and subsequent heat treatment. This method has been widely used to simulate microstructure evolution in materials in the past two decades [18,19]. The advantage of the phase-field method is that there is no need to track the interface, as in classical sharp interface modelling methods. This is achieved by introducing a phase-field parameter (also known as order parameter) that varies smoothly between two phases. Therefore, in the phase-field method, the interface will be a part of the solution.

The simulations in the current work have been performed using the commercially available phase-field software MICRESS (version 6.400, Access e.V., Aachen, Germany) based on the multi-phase-field approach [20,21]. The multi-phase-field theory describes the evolution of multiple phase-field parameters,  $\phi_{\alpha=1,2,\dots,v}(\vec{x}, t)$ , in space and time. These represent the spatial distribution of multiple phases with different thermodynamic properties and/or multiple grains with different orientations. The phase-field parameter,  $\phi_{\alpha}$ , assumes a value of 1 if the phase  $\alpha$  is present locally and a value of 0 if the phase is not present locally. At the interface of the phase  $\alpha$ ,  $\phi_{\alpha}$  varies smoothly between 0–1 over the interface thickness of  $\eta$ . Only a summary of the formulation of the time evolution equations implemented in MICRESS software are presented here. A more detailed formulation is further described in [21,22].

The time evolution of the phase-field variable,  $\phi_{\alpha}$ , is calculated from the free energy functional  $F$ , which integrates the density functional  $f$  over the domain  $\Omega$ .

$$F(\{\phi_{\alpha}\}, \{\vec{C}_{\alpha}\}) = \int_{\Omega} f(\{\phi_{\alpha}\}, \{\vec{C}_{\alpha}\}) \quad (1)$$

Here, the brackets  $\{\}$  contains all phases of  $\alpha$  present in the domain, and should not be considered as a locally present  $\alpha$ .  $\vec{C}_{\alpha}$  represents the composition of the phase  $\alpha$ . The density functional  $f$  depends on the interface energy density  $f^{int}$  and chemical free energy  $f^{chem}$  and can, therefore, be written as follows:

$$f = f^{int}(\{\phi_{\alpha}\}) + f^{chem}(\{\phi_{\alpha}\}, \{\vec{C}_{\alpha}\}) \quad (2)$$

$$f = \sum_{\alpha=1}^v \sum_{\beta \neq \alpha} \frac{4\sigma_{\alpha\beta}}{v\eta} \left( -\frac{\eta^2}{\pi^2} \nabla \phi_{\alpha} \nabla \phi_{\beta} + \phi_{\alpha} \phi_{\beta} \right) + \sum_{\alpha=1}^v \phi_{\alpha} f_{\alpha}(\vec{C}_{\alpha}) \quad (3)$$

In the Eq. (3) above,  $\sigma_{\alpha\beta}$  represents the anisotropic interface energy of the interface between  $\alpha$  and  $\beta$ . The variable  $v$  represents the total number of local co-existing phases. The multiphase-field equation, which defines the time evolution of  $\phi_{\alpha} = (\vec{x}, t)$  in multiple phase

transformations, is derived by minimization of the total free energy  $F$  following a relaxation principle.

$$\dot{\phi}_{\alpha} = - \sum_{\beta=1}^v M_{\alpha\beta} \frac{\pi^2}{8\eta} \left( \frac{\delta F}{\delta \phi_{\alpha}} - \frac{\delta F}{\delta \phi_{\beta}} \right) \quad (4)$$

A generic version of the multiphase-field equation can be written as [22]:

$$\dot{\phi}_{\alpha} = \sum_{\beta \neq \alpha} M_{\alpha\beta} \left[ \frac{\sigma_{\alpha\beta}}{v} K_{\alpha\beta} + \sum_{\gamma \neq \beta \neq \alpha} J_{\alpha\beta\gamma} + |\nabla \phi| \Delta G_{\alpha\beta} \right] \quad (5)$$

$$K_{\alpha\beta} = \frac{1}{2} (\nabla^2 \phi_{\alpha} - \nabla^2 \phi_{\beta}) + \frac{\pi^2}{2\eta_{\alpha\beta}^2} (\phi_{\alpha} - \phi_{\beta}) \quad (6)$$

$$J_{\alpha\beta\gamma} = \frac{1}{2} (\sigma_{\beta\gamma} - \sigma_{\alpha\gamma}) \left( \frac{\pi^2}{\eta^2} \phi_{\gamma} + \nabla^2 \phi_{\gamma} \right) \quad (7)$$

Here,  $M_{\alpha\beta}$  is the mobility of the  $\alpha$ - $\beta$  interface. The parameter  $K_{\alpha\beta}$  is related to the local curvature of the interface. The interface motion depends on the curvature contribution ( $\sigma_{\alpha\beta} K_{\alpha\beta}$ ) as well as on the thermodynamic driving force  $\Delta G_{\alpha\beta}(\vec{C}, T)$ . This driving force, in turn, depends on the temperature  $T$  and the local multi-component composition  $\vec{C}$ . The multi component composition couples the phase-field equation to the multi-phase diffusion equations given below.

$$\dot{\vec{C}} = \nabla \sum_{\alpha=1}^v \phi_{\alpha} \vec{D}_{\alpha} \nabla \vec{C}_{\alpha} \quad (8)$$

$$\vec{C} = \sum_{\alpha=1}^v \phi_{\alpha} \vec{C}_{\alpha} \quad (9)$$

The parameter  $\vec{D}_{\alpha}$  in Eq. (7) represents the multi-component diffusion coefficient matrix for phase  $\alpha$ . Here  $\vec{D}_{\alpha}$  and  $\Delta G_{\alpha\beta}(\vec{C}, T)$  are calculated through direct coupling to mobility and thermodynamic databases, respectively, via the TQ-interface of Thermo-Calc Software [23].

### 3.2. Model setup in MICRESS

In the present work, 2D simulations were carried out. The 2D domain was selected normal to the build direction in the 1<sup>st</sup> track of the LMPDED sample. Therefore, the domain is an isothermal section without any thermal gradients. In such a domain, the solidification simulations can be carried out by giving only a time-temperature history

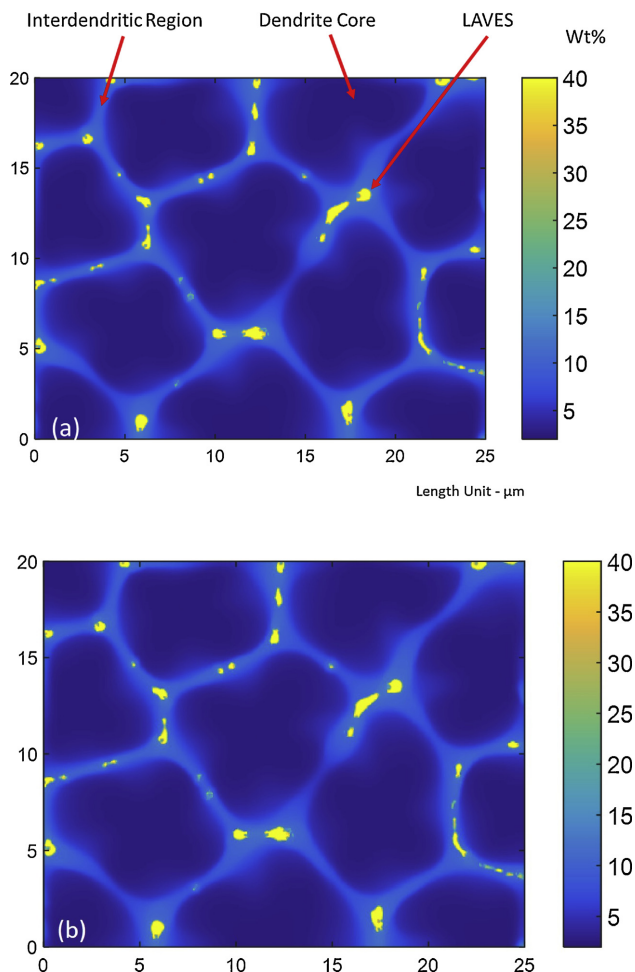


Fig. 2. Nb (wt%) distribution map (a) after the 1<sup>st</sup> thermal cycle and (b) after the 2<sup>nd</sup> thermal cycle of the MICRESS simulations of the LMPDED process.

for the thermal conditions. A simulation domain size of 25  $\mu\text{m}$  X 20  $\mu\text{m}$  with 0.05  $\mu\text{m}$  grid spacing was considered. Alloy 718 was modelled as a 7-component system having the composition shown in Table 4. This simplification was made to reduce the computational effort that is needed when calculating the thermodynamic and mobility data needed for the simulation. The thermodynamic and mobility data for the model was dynamically taken from TCNI8 and MOBNI4 databases from Thermo-Calc. In addition, a complete multicomponent diffusion matrix based on the local composition values was taken into account.

The simulations started from a complete liquid state, with the composition given in Table 4. 9 initial  $\gamma$  seeds were positioned in the domain such that the distance between seeds was roughly equal to the experimentally measured Primary Dendrite Arm Spacing (PDAS) of 7.1  $\mu\text{m}$ . The initial temperature of the simulation was set to 1337  $^{\circ}\text{C}$ . This liquidus temperature value is taken from Thermo-Calc equilibrium calculations for the current alloy composition. The experimentally measured temperature profile in the 1<sup>st</sup> track served as input for the

model as the thermal condition.

During solidification, phases such as titanium nitride (TiN), MC and Laves are known to form from the liquid [24]. However, TiN formation is not plausible in case of the nominal alloy composition considered in this study since it does not contain any nitrogen (N). In addition, MC too could not be modelled since the simplified alloy system does not contain carbon (C).  $\gamma'/\gamma''$  formation was also not modelled in the present work as, in order to capture the formation of these nano-scale precipitates, a very small grid spacing (typically in the range of 1 nm) is required demanding greater computational effort. Hence, in the current phase-field modelling work, only formation of the Laves phase and  $\delta$  phase were modelled to reduce the complexity of the model and associated computational effort.

During the simulation of microstructure evolution in LMPDED process, the Laves phase was allowed to nucleate at the liquid- $\gamma$  interface. To simulate the eutectic formation of Laves +  $\gamma$ , nucleation site for eutectic  $\gamma$  was allowed to form at the liquid-Laves interface. For both

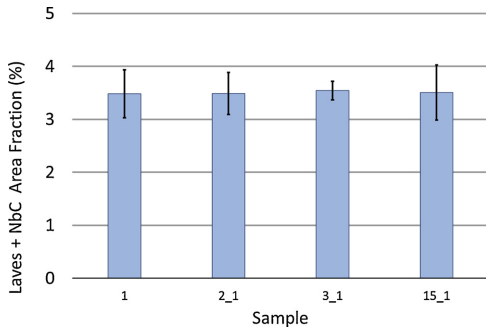


Fig. 3. Laves + NbC area fraction in the 1<sup>st</sup> layer of the deposited samples, with varying number of total deposited layers in the single wall samples.

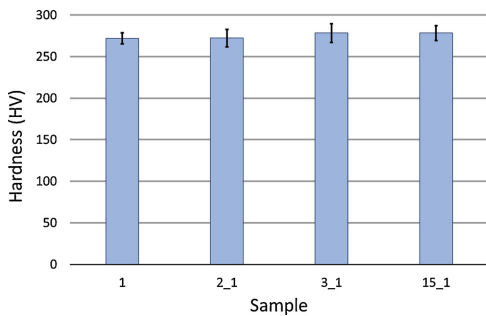


Fig. 4. Hardness measurements taken at the 1<sup>st</sup> deposited layer of the samples, with varying number of total deposited layers in the single wall samples.

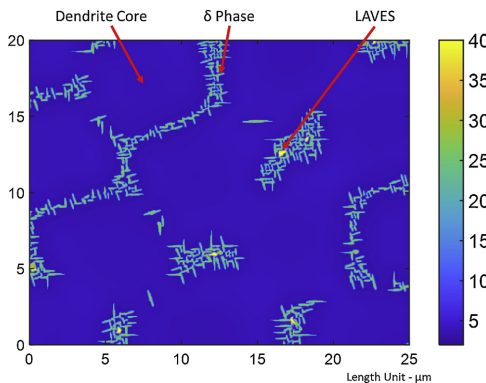


Fig. 5. Nb (wt%) distribution map after the solution heat-treatment simulation at 954 °C for 1 h using MICRESS.

Laves and eutectic  $\gamma$  nucleations, a critical undercooling value of 2 K was set. For simplicity of the simulation, only the liquid/ $\gamma$  interface was modelled as an anisotropic interface having cubic crystal anisotropy [25].

To investigate the effect of solution heat treatment on the microstructure of the LMPDED build, solution heat treatment simulation was performed. The microstructure predicted from the preceding thermal

cycle simulation was used as the initial microstructure and the solution heat treatment simulation was carried out at 954 °C for 1 h (similar to the experimental solution heat treatment). During simulation, orthorhombic  $\delta$  phase nucleation was allowed within the  $\gamma$  matrix. A critical undercooling of 1 K was set for the nucleation of the  $\delta$  phase. The  $\delta$  phase observed to have,  $(010)_{\delta} \parallel \{111\}_{\gamma}$ ;  $[100]_{\delta} \parallel \langle 1 \bar{1} 0 \rangle_{\gamma}$ , relationship with  $\gamma$  matrix [26,27]. This relationship was used to set two different orientations for the  $\delta$  phase in the simulation. Due to limitations in the anisotropic interface models in MICRESS,  $\delta/\gamma$  interface was modelled with a tetragonal anisotropy. Ageing heat treatment was not simulated since the current model resolution was not sufficient to model the precipitation of  $\gamma'/\gamma''$ . A summary of the model parameters used is given in Table 3. Numerical parameters related to interfacial stiffness and mobility were chosen based on a trial-and-error approach, in order to get the correct morphology for the phases as observed in experimentally.

MICRESS simulations were performed on a Linux server equipped with AMD Opteron(tm) Processor 6386 SE - 2.8 GHz (16 cores, only 8 cores was used for the simulations) and 128 GB of RAM. Total simulation time took around 29 h.

### 3.3. CCT and TTT diagram calculation using JMatPro/Thermo-Calc

The time and temperature dependency of phase transformations during isothermal holding and continuous cooling can be represented by Time-Temperature-Transformation (TTT) diagrams and Continuous Cooling Transformation (CCT) diagrams respectively. They show the fraction of the phase transformation as a function of time and temperature. In order to investigate the effect of local elemental segregated on the precipitation of  $\gamma'/\gamma''$  and  $\delta$  phases, TTT and CCT diagrams were generated using JMatPro (JMatPro is a trademark of Sun Microsystems, Inc - ver10.2) software. The local segregated elemental compositions predicted from the phase-field simulations were utilized for this purpose.

## 4. Results and discussion

In this section, most important experimental results from the microstructural observations relevant for the current modelling effort and their subsequent qualitative validation are discussed. More detailed information about the microstructural characterization of LMPDED Alloy 718 and the ensuing results are published elsewhere [28].

### 4.1. Effect of thermal cycling on the as-solidified microstructure

Fig. 1 shows the time-temperature history of the 1<sup>st</sup> layer of a 15-layer single wall deposited sample. Only measurement data related to the first 6-layers of the 15-layer deposition sample is being shown here. As can be seen from the figure, the 1<sup>st</sup> layer is subjected to multiple thermal cycles during deposition of multiple succeeding layers.

During solidification of Alloy 718, elements such as Nb, molybdenum (Mo) and Ti segregate into interdendritic region due to low solubility of these elements in the  $\gamma$ -matrix [4]. Such segregation of elements alters the local thermodynamics of Alloy 718 as well as the driving force for formation of various phases. Therefore, phases such as Laves,  $\delta$ , NbC and TiN begin to form in the interdendritic region during solidification. In addition, segregation of these elements changes the precipitation kinetics of strengthening phases ( $\gamma'/\gamma''$ ) in the  $\gamma$ -matrix.

Fig. 2 shows the Nb distribution map after the 1<sup>st</sup> and 2<sup>nd</sup> cycles. During the 1<sup>st</sup> thermal cycle, the deposited melt material solidifies. As mentioned earlier, during solidification, Nb segregates into the interdendritic region. Nb is one of the elements that segregates most in Alloy 718. Therefore, its segregation can have a strong impact on the build microstructure [4,15,29]. The Nb distribution map reveals that the lowest concentration of Nb is found at the dendrite core, which represents the initial solidified part of the primary dendrite. When

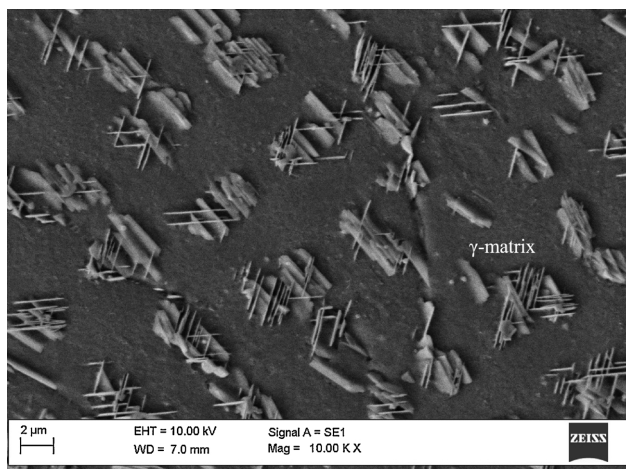


Fig. 6. Microstructure of the heat-treated 15-layer sample. Needle like precipitate in the  $\gamma$ -matrix are the  $\delta$  precipitates. (SEM image was taken normal to the build direction at the 1<sup>st</sup> deposited track of the 15-layer sample).

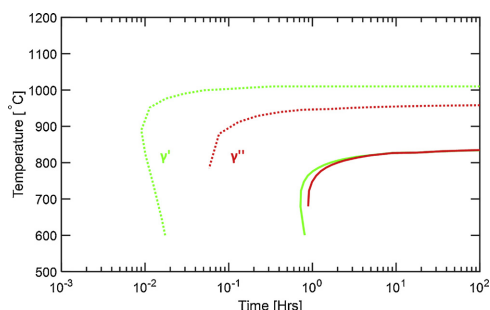


Fig. 7. Continuous cooling transformation (CCT) diagram created using segregated compositions predicted from MICRESS. Dotted line represent the 0.5% precipitation close to Laves phase and solid line represent 0.5% precipitation in the dendrite core.

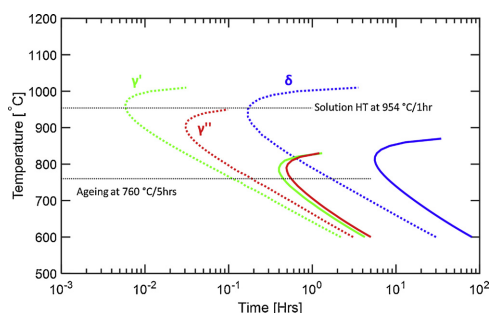


Fig. 8. Time temperature transformation (TTT) diagram created using segregated compositions predicted from MICRESS. Dotted line represent the 0.5% precipitation close to Laves phase and solid line represent 0.5% precipitation in the dendrite core.

moving away from the dendrite core to the interdendritic region, Nb concentration tends to increase. During the growth of the  $\gamma$  dendrite, Nb is continually rejected from the solid to the liquid. Hence, the Nb concentration in the liquid continues to increase. As a result, the liquid-solid interface advances into the liquid region with high Nb content, thereby resulting in an increase in Nb content from the dendrite core to the interdendritic region.

From the experimental work reported by Antonsson et.al. [29], it can be noted that the Nb content in the interdendritic liquid has to be above 20 wt% in order to form the Laves phase. During simulation, it was observed that the Laves phase starts to nucleate in regions where Nb content is greater than 17 wt%. This difference could be attributed to errors in the TCNI8 database or due to simplification of the alloy system. Formed Laves phase can be seen in Fig. 2 as bright yellow particles. The predicted Laves phase in the simulation contained ~40 wt% of Nb and ~0.9 wt% of Mo. These predicted values were higher and lower, respectively, compared to the values reported for Nb and Mo in the Laves phase [30–32]. One reason for higher Nb and lower Mo values in the predictions could be errors in the TCNI8 database. A simple Scheil simulation was performed using Thermo-Calc to check the Nb and Mo contents in Laves phase when it starts to form, and these were found to be around 41 wt% Nb and 0.7 wt% Mo. It was confirmed with the Thermo-Calc company that no parameter has been assessed for chromium (Cr)-Nb-Mo system in the TCNI8 database and this could have led to solubilities of Nb and Mo in Laves phase deviating from the expected values.

Fig. 2(b) shows the Nb distribution map at the end of the 2<sup>nd</sup> thermal cycle. It can be noted that there is almost no difference in the Nb distribution and the formed Laves phase at the end of the 1<sup>st</sup> and 2<sup>nd</sup> thermal cycles. One possible reason for this could be that, in the 2<sup>nd</sup> thermal cycle, the temperature in the 1<sup>st</sup> deposited layer was less than 1000 °C and, therefore, not high enough to have an impact on elemental diffusion and dissolution of the Laves phase. In addition, the time that the 1<sup>st</sup> deposited layer spent above 600 °C during the 2<sup>nd</sup> thermal cycle is ~2 s, which is too short to have any considerable impact on elemental diffusion in Alloy 718. Based on these observations, it can be expected that there will be negligible impact on elemental diffusion and Laves phase upon further thermal cycling (3<sup>rd</sup>, 4<sup>th</sup>, ...). This is also corroborated by the experimentally measured Laves Phase + NbC area fraction measurements in the 1<sup>st</sup> deposited layer which revealed no

visible change with further deposition of layers (refer Fig. 3).

Fig. 4 shows the measured hardness values in the first layer in the LMPDED deposited samples. From the thermal measurements depicted in Fig. 1, it can be seen that during deposition of successive layers, the 1<sup>st</sup> deposited layer temperature goes through the  $\gamma'/\gamma$  precipitation window for three consecutive thermal cycles. Hence, one can expect that the hardness in the 1<sup>st</sup> layer might progressively increase following deposition of the 2<sup>nd</sup> and 3<sup>rd</sup> layers. However, this was not clearly evident from the measured hardness values shown in Fig. 4. It is plausible that, even though the 1<sup>st</sup> deposited layer passes through the  $\gamma'/\gamma$  precipitation window multiple times, the cumulative time that it spends within the precipitation window is inadequate to have a significant impact on the growth of  $\gamma'/\gamma$  and, therefore, on the hardness values.

#### 4.2. Effect of heat treatment on the as-built microstructure

Fig. 5 shows the Nb distribution map of the predicted microstructure after solution heat treatment (at 954 °C for 1 h) simulation. The needle-like phases that can be seen in the microstructure represent the  $\delta$  phase. Some Laves phase particles can be seen in the microstructure even though a majority of them have dissolved. These  $\delta$  needles ( $\delta$  phase will look like needles in a 2D cross-section and have a platelet morphology in 3D) precipitate close to the Laves phase and in the interdendritic region of the as-built microstructure. One possible reason for this could be the change in the local driving force for precipitation of the  $\delta$  phase in the above regions due to local segregated composition. Nb released during dissolution of the Laves phase also tends to diffuse to the surrounding interdendritic areas and aid growth of the  $\delta$  phase. This observation is qualitatively in good agreement with the experimentally observed microstructure in a heat-treated 15-layer sample as shown in Fig. 6, with  $\delta$  needles [28] observed mainly in the interdendritic region as predicted by the simulation. Rest of the samples (single layer, two layer and three layer) were also observed to have similar microstructures after the heat treatment.

#### 4.3. Effect of element segregation on the precipitation kinetics

To ascertain the effect of elemental segregation on precipitation during the LMPDED process, CCT diagrams were created using JMatPro, taking the composition close to the Laves phase and in the dendritic core from phase-field simulations. As can be seen from Fig. 7, the kinetics of precipitation change due to changes in local composition. Close to the Laves phase,  $\gamma'/\gamma$  precipitate earlier (more than an order of magnitude in time) compared to the core of the dendrite. Such accelerated kinetics could result in a higher number density of  $\gamma'/\gamma$  close to Laves phase than in the core of the dendrite. This prediction is consistent with the experimental work performed by Segerstark et al. [28]. In the as-built microstructure, a higher number density of  $\gamma'/\gamma$  was observed close to the Laves phase compared to the core of the dendrite.

Fig. 8 shows the TTT diagram generated based on the segregated element compositions at dendrite core and interdendritic regions. It can be clearly seen that there is a difference between the precipitation kinetics due to element segregation. Close to Laves phase, the precipitation kinetics of  $\gamma'/\gamma$  and  $\delta$  are more than an order of magnitude faster compared to the dendrite core during the isothermal holding. In addition, as mentioned earlier, the Laves phase begins to dissolve during solution treatment at 954 °C, as seen from the heat treatment simulations. Hence, the Nb trapped in the Laves phase is released and diffuses to its surrounding. This favours growth of  $\gamma'/\gamma$  and  $\delta$  phases even further during solution heat treatment. During ageing heat treatment,  $\gamma'/\gamma$  precipitates in the core of the dendrites also. However, the amount of these strengthening phases will be lower in the dendrite core as compared to the interdendritic region. In addition, growth of previously precipitated phases can also be expected.

## 5. Conclusions

In this study, microstructure evolution during laser metal powder directed energy deposition Alloy 718 and subsequent heat treatment have been investigated. For this purpose, phase-field modelling as well as precipitation kinetic modelling using JMatPro were utilised. The following conclusions were drawn based on the observed results:

- Phases such as Laves and  $\gamma'/\gamma$  formed during deposition did not undergo any significant change during subsequent thermal cycles associated with deposition of subsequent layers
- Segregation of alloying elements in the interdendritic region was shown to change the precipitation kinetics of Alloy 718 and caused formation of high amounts of  $\gamma'/\gamma$  compared to the dendritic core in the as-built condition
- The  $\delta$  phase observed in the interdendritic region in heat-treated samples was precipitated during solution heat treatment at 954 °C for 1 h. This was predicted during the heat treatment simulation of the as-built microstructure. Elemental segregation was found to be responsible for this  $\delta$  precipitation.
- A combined approach involving phase-field modelling and transformation kinetic modelling seems promising to provide better insight into microstructure formation during AM of Ni-based superalloys and subsequent heat treatments.

## Acknowledgements

The authors would like to thank Dr. Bernd Böttger at Access e.V., Aachen, Germany for his valuable discussions and inputs regarding the modelling work in MICRESS. The funding from the European Regional Development Fund for project

3Dprint, and from KK Foundation (Stiftelsen för Kunnskaps- och Kompetensutveckling) for project SUMAN-Next is also acknowledged.

## References

- [1] M.M. Attallah, R. Jennings, X. Wang, L.N. Carter, Additive manufacturing of Ni-based superalloys: the outstanding issues, *MRS Bull.* 41 (10) (2016) 758–764.
- [2] C. Körner, Additive manufacturing of metallic components by selective electron beam melting—a review, *Int. Mater. Rev.* 61 (July (5)) (2016) 361–377.
- [3] J.C. Lippold, S.D. Kiser, J.N. DuPont, *Welding Metallurgy and Weldability of Nickel-Base Alloys*, John Wiley & Sons, 2009.
- [4] J.F. Radavich, The physical metallurgy of cast and wrought alloy 718, *Superalloys 718 Metallurgy and Applications*, (1989), pp. 229–240.
- [5] ASTM F2792-12a, *Standard Terminology for Additive Manufacturing Technologies* (Withdrawn 2015), (2018).
- [6] Ian Gibson, D. Rosen, B. Stucker, *Additive Manufacturing Technologies 3D Printing, Rapid Prototyping, and Direct Digital Manufacturing*, 2nd ed., Springer, US, 2014.
- [7] Y. Tian, et al., Rationalization of microstructure heterogeneity in INCONEL 718 builds made by the direct laser additive manufacturing process, *Metall. Mater. Trans. A* 45 (September (10)) (2014) 4470–4483.
- [8] T. DebRoy, et al., Additive manufacturing of metallic components – process, structure and properties, *Prog. Mater. Sci.* 92 (March) (2018) 112–224.
- [9] F. Liu, et al., The effect of laser scanning path on microstructures and mechanical properties of laser solid formed nickel-based superalloy Inconel 718, *J. Alloys Compd.* 509 (March (13)) (2011) 4505–4509.
- [10] H. Qi, M. Azer, A. Ritter, Studies of standard heat treatment effects on microstructure and mechanical properties of laser net shape manufactured INCONEL 718, *Metall. Mater. Trans. A* 40 (Oct ober (10)) (2009) 2410–2422.
- [11] Y. Zhang, Z. Li, P. Nie, Y. Wu, Effect of cooling rate on the microstructure of laser-remelted INCONEL 718 coating, *Metall. Mater. Trans. A* 44 (December (12)) (2013) 5513–5521.
- [12] Y. Zhang, Z. Li, P. Nie, Y. Wu, Effect of precipitation on the microhardness distribution of diode laser epitaxially deposited IN718 alloy coating, *J. Mater. Sci. Technol.* 29 (4) (2013) 349–352.
- [13] X. Zhao, J. Chen, X. Lin, W. Huang, Study on microstructure and mechanical properties of laser rapid forming Inconel 718, *Mater. Sci. Eng. A* 478 (April (1–2)) (2008) 119–124.
- [14] I. Tabernero, A. Lamikiz, S. Martínez, E. Ukar, J. Figueras, Evaluation of the mechanical properties of Inconel 718 components built by laser cladding, *Int. J. Mach. Tools Manuf.* 51 (June (6)) (2011) 465–470.
- [15] P. Nie, O.A. Ojo, Z. Li, Numerical modelling of microstructure evolution during laser additive manufacturing of a nickel-based superalloy, *Acta Mater.* 77 (September) (2014) 85–95.
- [16] A. Segerstark, J. Andersson, L. Svensson, Evaluation of a temperature measurement

- method developed for laser metal deposition, *Sci. Technol. Weld. Join.* 22 (January (1)) (2017) 1–6.
- [17] M.L. Barron, Crack Growth-Based Predictive Methodology for the Maintenance of the Structural Integrity of Repaired and Nonrepaired Aging Engine Stationary Components, (1999).
- [18] N. Moelans, B. Blanpain, P. Wollants, An introduction to phase-field modeling of microstructure evolution, *Calphad Comput. Coupling Phase Diagrams Thermochem.* 32 (2) (2008) 268–294.
- [19] I. Steinbach, Phase-field models in materials science, *Model. Simul. Mater. Sci. Eng.* 17 (no. 7) (2009) 73001–73031.
- [20] R. Acharya, J.A. Sharon, A. Staroselsky, Prediction of microstructure in laser powder bed fusion process, *Acta Mater.* 124 (February) (2017) 360–371.
- [21] J. Eiken, B. Böttger, I. Steinbach, Multiphase-field approach for multicomponent alloys with extrapolation scheme for numerical application, *Phys. Rev. E* 73 (June (6)) (2006) p. 066122.
- [22] B. Böttger, J. Eiken, M. Apel, Multi-ternary extrapolation scheme for efficient coupling of thermodynamic data to a multi-phase-field model, *Comput. Mater. Sci.* 108 (October) (2015) 283–292.
- [23] Thermo-Calc Software, (2018) [Online]. Available: <http://www.thermocalc.com/>. [Accessed: 25-May-2018].
- [24] G.A. Khorovskiy, M.J. Cieslak, T.J. Headley, A.D. Romig, W.F. Hammett, INCONEL 718: a solidification diagram, *Metall. Trans. A* 20 (October (10)) (1989) 2149–2158.
- [25] Micress Group, MICRESS 6.4 - User Guide Volume II: Running MICRES, (2018).
- [26] M. Sundararaman, N. Sachin, B.S. Jung, V. Amit, P. Bhaskar, R. Kishore, Evolution of  $\delta$  phase microstructure in alloy 718, 7th Int. Symp. Superalloys 718 Deriv. (2010), pp. 737–750.
- [27] M. Sundararaman, P. Mukhopadhyay, S. Banerjee, Precipitation of the delta-Ni<sub>3</sub>Nb phase in two nickel base superalloys, *Metall. Trans. A* 19 (3) (1988) 453–465.
- [28] A. Segerstark, J. Andersson, L. Svensson, O. Ojo, Microstructural characterization of laser metal powder deposited alloy 718, *Mater. Charact.* 142 (June) (2018) 550–559.
- [29] T. Antonsson, H. Fredriksson, The effect of cooling rate on the solidification of INCONEL 718, *Metall. Mater. Trans. B* 36 (February (1)) (2005) 85–96.
- [30] M.M. Kirka, K.A. Unocic, N. Raghavan, F. Medina, R.R. Dehoff, S.S. Babu, Microstructure development in electron beam-melted inconel 718 and associated tensile properties, *JOM* 68 (March (3)) (2016) 1012–1020.
- [31] K. Sivaprasad, S. Ganesh Sundara Raman, Influence of weld cooling rate on microstructure and mechanical properties of alloy 718 weldments, *Metall. Mater. Trans. A* 39 (September (9)) (2008) 2115–2127.
- [32] J.J. Schirra, R.H. Caless, R.W. Hatala, The effect of laves phase on the mechanical properties of wrought and cast + HIP inconel 718, Superalloys 718, 625 and Various Derivatives (1991), (1991), pp. 375–388.
- [33] J. Kundin, L. Mushongera, H. Emmerich, Phase-field modeling of microstructure formation during rapid solidification in inconel 718 superalloy, *Acta Mater.* 95 (August) (2015) 343–356.
- [34] N. Zhou, et al., Computer simulation of phase transformation and plastic deformation in IN718 superalloy: microstructural evolution during precipitation, *Acta Mater.* 65 (February) (2014) 270–286.

## Paper C

# Predicting the Microstructural Evolution of Electron Beam Melting of Alloy 718 with Phase-Field Modeling

C

Chamara Kumara

Dunyong Deng

Fabian Hanning

Morten Raanes

Johan Moverare

Per Nylén

Published in *Metallurgical and Materials Transactions A*

vol. 50, no. 5, pp. 2527–2537, 2019

DOI: 10.1007/s11661-019-05163-7

Reprinted with CC BY 4.0





# Predicting the Microstructural Evolution of Electron Beam Melting of Alloy 718 with Phase-Field Modeling



CrossMark

CHAMARA KUMARA, DUNYONG DENG, FABIAN HANNING,  
MORTEN RAANES, JOHAN MOVERARE, and PER NYLÉN

Electron beam melting (EBM) is a powder bed additive manufacturing process where a powder material is melted selectively in a layer-by-layer approach using an electron beam. EBM has some unique features during the manufacture of components with high-performance superalloys that are commonly used in gas turbines such as Alloy 718. EBM has a high deposition rate due to its high beam energy and speed, comparatively low residual stresses, and limited problems with oxidation. However, due to the layer-by-layer melting approach and high powder bed temperature, the as-built EBM Alloy 718 exhibits a microstructural gradient starting from the top of the sample. In this study, we conducted modeling to obtain a deeper understanding of microstructural development during EBM and the homogenization that occurs during manufacturing with Alloy 718. A multicomponent phase-field modeling approach was combined with transformation kinetic modeling to predict the microstructural gradient and the results were compared with experimental observations. In particular, we investigated the segregation of elements during solidification and the subsequent “*in situ*” homogenization heat treatment at the elevated powder bed temperature. The predicted elemental composition was then used for thermodynamic modeling to predict the changes in the continuous cooling transformation and time–temperature transformation diagrams for Alloy 718, which helped to explain the observed phase evolution within the microstructure. The results indicate that the proposed approach can be employed as a valuable tool for understanding processes and for process development, including post-heat treatments.

<https://doi.org/10.1007/s11661-019-05163-7>  
© The Author(s) 2019

## I. INTRODUCTION

RECENTLY, powder bed additive manufacturing (AM) has attracted great interest from the manufacturing industries and research community because of its capacity to produce near net shape structures with complex geometries, which cannot be manufactured

with traditional methods. Among the powder bed manufacturing processes, electron beam melting (EBM) process has attracted more attention because of its relatively higher productivity due to the high beam speed and high beam power density. In addition, the EBM operation occurs at a high temperature in a vacuum environment, which creates less residual stress and less oxidation in the component obtained.<sup>[1]</sup> These features are beneficial for the manufacture of the critical components used in aerospace applications and gas turbine engines.

Nickel-based superalloys are among the most important alloys used in aerospace applications and gas turbine engines because of their high-temperature strength, high resistance to creep deformation, and corrosion resistance.<sup>[2,3]</sup> Among these superalloys, Alloy 718 is one of the most widely used nickel-iron-based superalloys and it is suitable for AM processes because of its good weldability due to the sluggish precipitation of the main strengthening phase  $\gamma''$ .<sup>[4]</sup> The microstructure of Alloy 718 is dominated by an austenitic  $\gamma$  fcc matrix. Precipitates such as Laves,  $\gamma'/\gamma''$ , and  $\delta$  phases, and various metallic carbides and nitrides can be found within the matrix. The formation of the Laves phase is

---

CHAMARA KUMARA and PER NYLÉN are with the Division of Subtractive and Additive Manufacturing Processes, Department of Engineering Science, University West, 461 86 Trollhättan, Sweden. Contact e-mail: [chamara.kumara@hv.se](mailto:chamara.kumara@hv.se) DUNYONG DENG is with the Division of Engineering Materials, Department of Management and Engineering, Linköping University, 58183 Linköping, Sweden. FABIAN HANNING is with the Department of Industrial and Materials Science, Chalmers University of Technology, 412 96 Göteborg, Sweden. MORTEN RAANES is with the Department of Materials Science and Engineering, IMA, NTNU, Alfred Getz vei 2, 7491 Trondheim, Norway. JOHAN MOVERARE is with the Division of Subtractive and Additive Manufacturing Processes, Department of Engineering Science, University West and also with the Division of Engineering Materials, Department of Management and Engineering, Linköping University.

Manuscript submitted November 21, 2018.

usually observed in the interdendritic region due to the segregation of the elements. The complete microstructure, including the phases present as well as their distribution, morphology, and orientation, is mainly related to the primary manufacturing technology employed and the subsequent post-processing conditions. Heat treatments are commonly used to tailor the microstructure of Alloy 718 to obtain the desired properties required for the application.

Due to the inherent features of the layer-by-layer manufacturing approach, the microstructure of Alloy 718 after the EBM process exhibits a gradient along the build direction.<sup>[5,6]</sup> During the melting process, the powder material is melted and it then solidifies, thereby leading to the formation of different phases, as mentioned earlier. As the subsequent layers are built, the solidified structure gradually undergoes “*in situ*” heat treatment due to the elevated powder bed temperature (> 1000 °C for Alloy 718) in the EBM process. The time that a specific layer undergoes this “*in situ*” heat treatment changes according to the height of the object under construction, which creates a gradient in the microstructure from the top to the bottom of the sample.

In this study, we modeled the microstructure using the multiphase-field method and the transformation kinetics were determined to understand the formation of the microstructural gradient in Alloy 718 samples produced using EBM. First, the solidified microstructure was modeled and the model was then used to simulate the “*in situ*” heat treatment in order to observe the changes in the alloy composition and any subsequent phase changes. The results were compared with experimental observations.

II. EXPERIMENTAL

A plasma atomized powder (nominal size ranges from 25 to 106 μm) supplied by Arcam AB was used to manufacture the Alloy 718 samples in this study. The chemical composition of the powder is shown in Table I.

Table I. Nominal Chemical Composition of the Raw Powder and the Nominal Composition Used for the Phase-Field Simulation

Element (Weight Percent)	Measured	Simulation
Ni	bal.	bal.
Cr	19.1	19.1
Fe	18.5	18.5
Nb	5.04	5.04
Mo	2.95	2.95
Co	0.07	—
Ti	0.91	0.91
Al	0.58	0.58
Mn	0.05	—
Si	0.13	—
Cu	0.1	—
C	0.035	—
N	0.0128	—

An Arcam A2X EBM system was used to manufacture the samples with the standard settings for Alloy 718 (listed in Table II). The manufacturing process started after the powder bed was pre-heated to about 1020 °C (measured under the base plate) and this temperature was maintained throughout the whole process. Each deposition cycle comprised (1) pre-heating the current powder layer, (2) contour melting the frame for the build, (3) hatch melting the interior of the build and rotating about 65° from the previous scanning vector, (4) post-heating the current layer, and (5) lowering down the powder bed and raking new powder to form a uniform layer measuring 75 μm for the next cycle. In each batch, 16 identical-sized blocks were fabricated and the dimension of each block was approximately 35 mm (length) × 10 mm (width) × 33 mm (height).

Cross-sections parallel to the build direction were examined at different heights from the top surface in order to characterize the microstructural gradient. Samples were mounted, mechanically ground successively from 500 grit to 4000 grit, and polished with a diamond suspension from 3 to 1/4 μm, and then finally with OP-U colloidal silica suspension. A Hitachi SU70 FEG scanning electron microscope (SEM) that operated at an accelerating voltage of 20 kV, which was equipped with an energy dispersive X-ray spectroscopy system, was employed to determine the microstructural features and chemical compositions. In order to calculate the volume fraction of the Laves phase, SEM images were converted into binary images using the ImageJ program, before distinguishing the contrast between the matrix and Laves + NbC phases. Electron probe microscopic analysis was performed using a JEOL JXA-8500F system with samples that were cut normal to the build direction.

III. MODELING

A. MICRESS and the Governing Equation

The phase-field method was employed to model the evolution of the microstructure. This method has been used widely during the last two decades to simulate the microstructural evolution of materials.<sup>[7,8]</sup> The advantage of the phase-field method is that there is no need to track the interface, unlike the classical sharp interface modeling methods. An order parameter is introduced that varies smoothly between two phases, and thus the

Table II. Main Parameters of the Arcam Standard Parameters for Alloy 718 (Theam Name-“Inconel 718 Melt 75 μm V3”)

Parameter	Value
Hatch-current max (mA)	18
Hatch-scan speed (m/s)	automatic (scan function 63)
Hatch-line offset (mm)	0.125
Pre-heating temperature (°C)	1025
Layer thickness (μm)	75
Electron beam power (W)	3000

interface is part of the solution in the phase-field method.

Our simulations were performed using the commercially available phase-field modeling software MICRESS (version 6.400, Access e.V., Aachen, Germany). MICRESS is based on the multiphase-field approach.<sup>[9,10]</sup> The multiphase-field theory describes the evolution of multiple phase-field parameters  $\phi_{\alpha=1,2,\dots,v} = (\vec{x}, t)$  (with the constraint  $\sum_{\alpha=1}^v \phi_{\alpha} = 1$ ) in space and time, which represent the spatial distribution of multiple phases with different thermodynamic properties and/or multiple grains with different orientations. The phase-field parameter,  $\phi_{\alpha}$  takes a value of 1 if phase  $\alpha$  is present locally and a value of 0 if the phase is not present locally. At the interface of the phase  $\alpha$ ,  $\phi_{\alpha}$  will vary smoothly from 0 to 1 over the interface thickness ( $\eta$ ). The time evolution of  $\phi_{\alpha}$  is calculated using the free energy functional,  $F$ , which integrates the density functional,  $f$ , over the domain  $\Omega$ .

$$F(\{\phi_{\alpha}\}, \{\vec{C}_{\alpha}\}) = \int_{\Omega} f(\{\phi_{\alpha}\}, \{\vec{C}_{\alpha}\}), \quad [1]$$

where the brackets,  $\{\}$ , represent all phases of  $\alpha$ , and not an individual  $\alpha$ . The density functional,  $f$ , depends on the interface energy density,  $f^{\text{int}}$ , and chemical free energy,  $f^{\text{chem}}$ , and thus it can be written as follows:

$$f = f^{\text{int}}\{\{\phi_{\alpha}\} + f^{\text{chem}}\{\{\phi_{\alpha}\}, \{\vec{C}_{\alpha}\}\}, \quad [2]$$

$$f = \sum_{\alpha=1}^v \sum_{\beta \neq \alpha}^v \frac{4\sigma_{\alpha\beta}^0 a_{\alpha\beta}^{\sigma}}{v\eta} \left( -\frac{\eta^2}{\pi^2} \nabla \phi_{\alpha} \nabla \phi_{\beta} + \phi_{\alpha} \phi_{\beta} \right) + \sum_{\alpha=1}^v \phi_{\alpha} f_{\alpha}(\vec{C}_{\alpha}), \quad [3]$$

where  $\sigma_{\alpha\beta}^0$  represents the interfacial energy of the interface between  $\alpha$  and  $\beta$ .  $v$  is the total number of local coexisting phases. The term  $a_{\alpha\beta}^{\sigma}$  represents the anisotropy function for the interfacial stiffness.<sup>[11]</sup> In 2D, for cubic crystal systems, this function takes the form  $a_{\alpha\beta}^{\sigma} = 1 - \delta_{\sigma} \cos(4\theta)$ .<sup>[12]</sup>

The multiphase-field equation defining the time evolution of  $\phi_{\alpha} = (\vec{x}, t)$  in multiple phase transformations is derived by minimizing the total free energy,  $F$ , according to a relaxation principle.

$$\dot{\phi}_{\alpha} = \sum_{\beta \neq \alpha}^v M_{\alpha\beta} a_{\alpha\beta}^M \left( \frac{\delta F}{\delta \phi_{\beta}} - \frac{\delta F}{\delta \phi_{\alpha}} \right) \quad [4]$$

Here  $M_{\alpha\beta}$  is the mobility of the  $\alpha$  and  $\beta$  interface. The term  $a_{\alpha\beta}^M$  represents the anisotropy function for the interfacial mobility.<sup>[11]</sup> In 2D, for cubic crystal systems, this function takes the form  $a_{\alpha\beta}^M = 1 + \delta_M \cos(4\theta)$ .<sup>[12]</sup>

The general version of the evolution equation including the anisotropy can be written as follows.

$$\dot{\phi}_{\alpha} = \sum_{\beta \neq \alpha}^v M_{\alpha\beta} a_{\alpha\beta}^M \left[ b_{\alpha\beta} \Delta G_{\alpha\beta} - \sigma_{\alpha\beta}^0 a_{\alpha\beta}^{\sigma} K_{\alpha\beta}^{\alpha} + \sum_{\gamma \neq \beta \neq \alpha}^n J_{\alpha\beta\gamma} \right] \quad [5]$$

$$b_{\alpha\beta} = \frac{\pi}{\eta} (\phi_{\alpha} + \phi_{\beta}) \left( \sqrt{\phi_{\alpha} \phi_{\beta}} \right) \quad [6]$$

$$K_{\alpha\beta}^{\alpha} = \frac{2}{v} \left\{ \frac{\pi^2}{2\eta^2} (\phi_{\beta} - \phi_{\alpha}) + \frac{1}{2} (\nabla^2 \phi_{\beta} - \nabla^2 \phi_{\alpha}) + \frac{1}{a_{\alpha\beta}^{\sigma}} \sum_{i=1}^3 \nabla_i \times \left[ \left( \frac{\partial a_{\alpha\beta}^{\sigma}}{\partial \nabla_i \phi_{\beta}} - \frac{\partial a_{\alpha\beta}^{\sigma}}{\partial \nabla_i \phi_{\alpha}} \right) \left( \frac{\pi^2}{2\eta^2} (\phi_{\alpha} \phi_{\beta}) - \frac{1}{2} (\nabla \phi_{\alpha} \nabla \phi_{\beta}) \right) \right] - \frac{1}{a_{\alpha\beta}^{\sigma}} \nabla a_{\alpha\beta}^{\sigma} (\nabla \phi_{\beta} - \nabla \phi_{\alpha}) \right\} \quad [7]$$

$$J_{\alpha\beta\gamma} = \frac{2}{v} \left\{ \frac{1}{2} \left( \sigma_{\beta\gamma}^0 a_{\beta\gamma}^{\sigma} - \sigma_{\alpha\gamma}^0 a_{\alpha\gamma}^{\sigma} \right) \left( \frac{\pi^2}{\eta^2} \phi_{\gamma} + \nabla^2 \phi_{\gamma} \right) + \sigma_{\alpha\gamma}^0 \sum_{i=1}^3 \nabla_i \left[ \left( \frac{\partial a_{\alpha\gamma}^{\sigma}}{\partial \nabla_i \phi_{\alpha}} \right) \left( \frac{\pi^2}{2\eta^2} (\phi_{\alpha} \phi_{\gamma}) - \frac{1}{2} (\nabla \phi_{\alpha} \nabla \phi_{\gamma}) \right) \right] - \sigma_{\beta\gamma}^0 \sum_{i=1}^3 \nabla_i \left[ \left( \frac{\partial a_{\beta\gamma}^{\sigma}}{\partial \nabla_i \phi_{\beta}} \right) \left( \frac{\pi^2}{2\eta^2} (\phi_{\beta} \phi_{\gamma}) - \frac{1}{2} (\nabla \phi_{\beta} \nabla \phi_{\gamma}) \right) \right] + \frac{1}{2} \left( \sigma_{\beta\gamma}^0 \nabla a_{\beta\gamma}^{\sigma} - \sigma_{\alpha\gamma}^0 \nabla a_{\alpha\gamma}^{\sigma} \right) \nabla \phi_{\gamma} \right\}, \quad [8]$$

where  $K_{\alpha\beta}^{\alpha}$  is related to the local curvature of the interface and  $J_{\alpha\beta\gamma}$  relates to the third-order junction forces.

However, more simplified version of the  $J_{\alpha\beta\gamma}$  term is implemented in MCRESS neglecting the higher order terms as follows.

$$J_{\alpha\beta\gamma} = \frac{2}{v} \left\{ \frac{1}{2} \left( \sigma_{\beta\gamma}^0 a_{\beta\gamma}^{\sigma} - \sigma_{\alpha\gamma}^0 a_{\alpha\gamma}^{\sigma} \right) \left( \frac{\pi^2}{\eta^2} \phi_{\gamma} + \nabla^2 \phi_{\gamma} \right) \right\}. \quad [9]$$

The interface motion depends on the curvature contribution,  $(\sigma_{\alpha\beta} K_{\alpha\beta})$ , but also on the thermodynamic driving force,  $\Delta G_{\alpha\beta}(\vec{C}, T)$ . This driving force depends on the temperature,  $T$ , and the local multicomponent composition,  $\vec{C}$ , which couples the phase-field equation to the multiphase diffusion equations:

$$\dot{\vec{C}} = \nabla \sum_{\alpha=1}^v \phi_{\alpha} \vec{D}_{\alpha} \nabla \vec{C}_{\alpha} \quad [10]$$

$$\vec{C} = \sum_{\alpha=1}^v \phi_{\alpha} \vec{C}_{\alpha}, \quad [11]$$

where  $\bar{D}_\alpha$  represents the multicomponent diffusion coefficient matrix for the phase  $\alpha$ .  $\Delta G_{\alpha\beta}(\vec{C}, T)$  and  $\bar{D}_\alpha$  are calculated by direct coupling to the thermodynamic (TCN18) and mobility (MOBNI4) databases via the TQ-interface in Thermo-Calc Software.<sup>[13]</sup> The driving force,  $\Delta G_{\alpha\beta}(\vec{C}, T)$ , is calculated based on the quasi-equilibrium approach with the combination of mass balance condition. For detail information, reader is advised to refer.<sup>[10,11]</sup>

### B. Model Setup in MICRESS and Assumptions

Two-dimensional (2D) multiphase-field simulations were conducted in the present study. The 2D domain selected was normal to the build direction of the EBM sample. Therefore, the domain had an isothermal cross section and it was normal to the primary dendrite growth direction. The unit cell approach proposed by Warnken *et al.*<sup>[14]</sup> was employed, where the edge length of the unit cell was given by primary dendrite arm spacing (PDAS) and the unit cell contained one representative dendrite. Therefore, we considered a unit cell size of  $6\ \mu\text{m} \times 6\ \mu\text{m}$  (the PDAS was measured experimentally based on SEM images) with a grid spacing of  $0.025\ \mu\text{m}$  for the EBM solidification simulation. Alloy 718 was modeled as a seven-component system with the composition shown in Table I. This simplifying assumption reduced the computational effort required to calculate the thermodynamic and mobility data. Both of these types of data were dynamically extracted from the TCN18 and MOBNI4 databases by Thermo-Calc. In addition, we considered the full multicomponent diffusion matrix based on the local composition values.

The simulation started from a complete liquid state with the composition in Table I. The  $\gamma$  phase nucleation seed was placed at the center of the domain. Measuring the cooling rate of the EBM process is rather difficult due to the inherent nature of the process. Therefore, a value of  $2000\ \text{K/s}$  was assumed for the simulation, which is in the range of the cooling rate values reported for EBM Alloy 718.<sup>[6]</sup> Periodic boundary conditions were assigned at the boundaries of the simulated domain.

During the solidification process, various phases such as TiN, MC, and Laves phases begin to precipitate from the liquid.<sup>[4]</sup> However, in the present study, we only considered the formation of the Laves phase. This simplifying assumption reduced the complexity of the model and the computational effort required. However, TiN and MC could not be modeled because the simplified alloy system did not contain N and C. This simplification can be justified as follows.

- I. The N and C proportions (wt pct) in the alloy were comparatively low compared with those of the other major elements.
- II. The observed volume fractions of nitrides and carbides were very low in the microstructure. Therefore, the consumption of Ti and Nb during the formation of nitrides and carbides was not

significant and it did not significantly influence the formation of the other phases.

- III. The abundances of carbides and nitrides did not vary significantly throughout the build height of the sample.

In addition, the formation of the strengthening phases,  $\gamma'/\gamma''$ , was not modeled. A very small grid resolution (typically in the range of  $1\ \text{nm}$ ) is required in order to capture the formation of these nano-scale precipitates, thereby demanding greater computational effort.

The modeled Laves phase was allowed to nucleate at the liquid- $\gamma$  interface. In order to simulate the eutectic formation of Laves +  $\gamma$ , the nucleation site for eutectic  $\gamma$  was allowed to form at the liquid-Laves interface. For both types of nucleation, a critical undercooling value of  $2\ \text{K}$  was set. To simplify the simulation, only the liquid/ $\gamma$  interface was modeled as an anisotropic interface with cubic crystal anisotropy.<sup>[15]</sup> The parameters used in the simulations are summarized in Table III.

According to the thermocouple measurements (see Figure 1) obtained from the bottom of the base plate in the EBM system, the temperature of the base plate was around  $1020\ ^\circ\text{C}$  throughout the build time. We assumed that the entire build volume was in isothermal equilibrium with the thermocouple at this temperature during the process. This “*in situ*” heat treatment changed the solidified microstructure. Therefore, the heat treatment simulation was performed at  $1020\ ^\circ\text{C}$  in order to observe its effects on the solidified microstructure. The microstructure obtained from the solidification simulation (solidified microstructure) was used as the initial microstructure for the *in situ* heat treatment simulation.

The homogenization behavior observed in the EBM solidified microstructure in the simulations and experiments was more rapid than the homogenization behavior observed in the cast Alloy 718. Therefore, for comparative purposes, the hypothetical cast microstructure formation and subsequent homogenization heat treatment were modeled in a similar manner. A PDAS of  $100\ \mu\text{m}$  was selected for the cast solidification microstructure simulations.<sup>[16]</sup> Therefore, the domain size was  $100\ \mu\text{m} \times 100\ \mu\text{m}$  with a grid resolution of  $0.5\ \mu\text{m}$ . A cooling rate of  $1\ \text{K/s}$  was employed.<sup>[16]</sup> For the homogenization heat treatment, a temperature value of  $1100\ ^\circ\text{C}$  was used according to AMS5383E.<sup>[17]</sup>

### C. Calculation of Continuous Cooling Transformation (CCT) and Time-Temperature Transformation (TTT) Diagrams Using JMatPro

The  $\gamma'/\gamma''$  and  $\delta$  phase precipitation processes were not modeled in the multiphase-field simulations. However, in order to observe their kinetic behavior during precipitation due to element segregation, CCT diagrams were generated using the JMatPro (ver10.2) material modeling software package.<sup>[18]</sup> The nominal alloy composition and the segregated compositions predicted by the multiphase-field simulations were utilized in these simulations.

Table III. Summary of the Model Parameters

	EBM	As cast
Domain size	$6\ \mu\text{m} \times 6\ \mu\text{m}$	$100\ \mu\text{m} \times 100\ \mu\text{m}$
Grid resolution ( $\Delta x$ )	$0.025\ \mu\text{m}$	$0.5\ \mu\text{m}$
Interface thickness ( $\eta$ )	$3\Delta x$	$2.5\Delta x$
Cooling Rate (K/s)	2000	1
Initial undercooling for $\gamma^{**}$ (K)	11	6
Interface energy liquid/ $\gamma$ (J/cm <sup>2</sup> )	$1.2\text{E}-05^{[8]}$	
Anisotropic interfacial stiffness coefficient ( $\delta\sigma$ )*-liquid/ $\gamma$	0.2	
Anisotropic interfacial mobility coefficient ( $\delta M$ )*-liquid/ $\gamma$	0.2	
Assumed interface energy liquid/laves (J/cm <sup>2</sup> )	$6\text{E}-06$	
Assumed interface energy $\gamma$ /laves (J/cm <sup>2</sup> )	$5\text{E}-06$	

\*Values were selected based on trial and error approach to get the desired dendrite morphology.

†The two different initial undercooling values are due to the two different initial nucleation size (due to the different resolution of the models) for the  $\gamma$  phase.

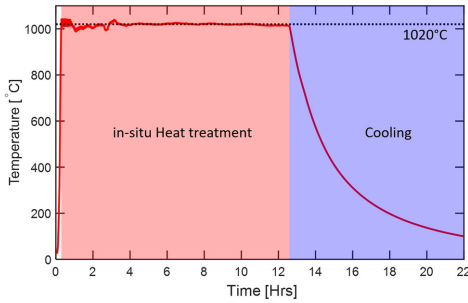


Fig. 1—Thermocouple measurement from the bottom of the build plate.

#### IV. RESULTS AND DISCUSSION

##### A. Experimental Results: “In Situ” Homogenization and Phase Formation

In the following, we present the experimental results obtained from the microstructural observations that were most relevant for the modeling and validation studies. Detailed information regarding the microstructural characterization process and the results obtained were published previously.<sup>[19]</sup>

Experimental examinations of the microstructure of the sample clearly indicated the presence of a microstructure gradient along the build direction as well as from the dendrite core to the interdendritic region. This gradient along the build direction was visible when observing the bright particles in the interdendritic regions of the microstructure, as shown in Figure 2. These particles were confirmed as the Laves phase and NbC/(Nb,Ti)(C,N) according to transmission electron microscopy (TEM) analysis. The area fractions of these phases were measured by image analysis in order to determine the evolution of the gradients of these phases. The measured Laves + NbC/(Nb,Ti)(C,N) volume fractions are shown in Figure 3. In the area close to the top surface of the sample, a low volume fraction of Laves + NbC/(Nb,Ti)(C,N) was observed.

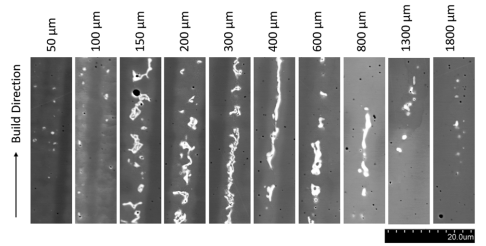


Fig. 2—Laves + NbC/(Nb,Ti)(C,N) phases morphology at different distance from the top surface.

However, the peak volume fraction was found at a depth of around  $150\ \mu\text{m}$ . Kirka *et al.*<sup>[6]</sup> showed that melting current layer of the powder material in the EBM process will lead to re-melting of the top two layers below the current layer that is added. Therefore, the  $225\ \mu\text{m}$  layer from the top of the sample can be considered as the “solidified” region without further re-melting. In the “solidified” region, the amount of Laves + NbC/(Nb,Ti)(C,N) phases decreased when moving closer to the top surface, which could be attributed to the change in the solidification velocity of the melt pool. Raghavan *et al.*<sup>[20]</sup> showed that the initial solidification velocity is relatively lower during the solidification of the melt pool in the EBM process. When the solidification velocity is low and it is lower than the element diffusion velocity, the elements will have sufficient time to partition and segregate into the interdendritic region. However, the solidification velocity was shown to increase towards the end of the solidification of the melt pool. As the solidification velocity increases, more elements are increasingly trapped inside the dendrite,<sup>[21]</sup> which results in less element segregation in the interdendritic region, thereby reducing the formation of Laves + NbC/(Nb,Ti)(C,N). It should be noted that this phenomenon was not modeled in the present study.

According to the temperature measurements shown in Figure 1, we expected that the powder bed temperature remained above  $1020\ ^\circ\text{C}$  throughout the building of the

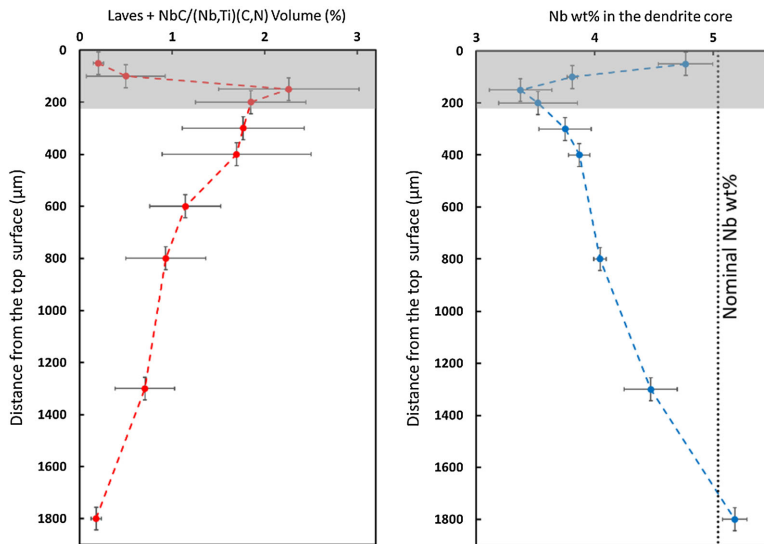


Fig. 3—Measured Laves + NbC/(Nb,Ti)(C,N) volume fraction and Nb wt pct in the dendrite core from top surface of the sample. Shaded areas represent the possible last-solidified region without subjecting to “*in situ*” heat treatment.

samples. Therefore, this elevated temperature acted as an “*in situ*” heat treatment and changed the “solidified” microstructure. The effect of this “*in situ*” heat treatment on the “solidified” microstructure was evident when moving away from the peak location for the Laves + NbC/(Nb,Ti)(C,N) phase, as shown in Figure 3. The volume fraction of the Laves + NbC/(Nb,Ti)(C,N) phase started to decrease gradually as the distance increased, which can be attributed directly to the dissolution of the Laves phase during the “*in situ*” heat treatment. Due to their high stability, NbC/(Nb,Ti)(C,N) were not affected by the “*in situ*” heat treatment, and thus their volume fractions were expected to remain unchanged with the build height. The Laves phase was no longer visible at a depth of ~1800 μm from the top surface and it was expected to be fully dissolved. This distance of 1800 μm is roughly around the 30th layer counting from the top of the build sample. Considering the total build time and the total number of layers, we estimated that the 30th layer was exposed to “*in situ*” heat treatment at a time of roughly 40 minutes.

Nb is considered to be one of the most important alloying elements in Alloy 718.<sup>[22,23]</sup> The formation of phases such as  $\gamma'/\gamma''$ , Laves, and  $\delta$  is directly related to the level of Nb in the microstructure.<sup>[22]</sup> Nb is also the most severely segregated element in the microstructure of Alloy 718, and thus it is relatively easy to measure its segregation. Figure 3 shows the variation in the proportion of Nb (Nb wt pct) at the center of the dendrite core as a function of the distance from the top surface of the sample. The changes in Nb wt pct exhibited the

opposite relationship to the variations in the Laves + NbC/(Nb,Ti)(C,N) volume fractions, thereby indicating that the Nb trapped inside the Laves phase in the “solidified” microstructure was released and it diffused back into the dendrite core as a consequence of the “*in situ*” heat treatment. At a distance of ~1800 μm from the top surface, the Nb wt pct in the dendrite core was similar to the nominal composition of the powder material used in this study, which indicates that the “solidified” microstructure tended to homogenize during the 40-min “*in situ*” heat treatment.

#### B. Phase-Field Solidification Simulation Results of EBM alloy 718 and Cast Alloy 718

During the solidification of Alloy 718, elements such as Nb, Mo, and Ti will segregate into the interdendritic region due to the low solubility of these elements in the  $\gamma$ -matrix.<sup>[22]</sup> This elemental segregation leads to the formation of phases such as Laves,  $\delta$ , NbC, and TiN. In addition, the depletion of these elements in the  $\gamma$ -matrix will affect the precipitation kinetics for the strengthening phases (which we illustrate later using CCT diagrams generated by JMatPro). Figure 4 shows the distribution maps obtained for Nb, Fe, and Ti based on the solidification simulation for EBM Alloy 718, which demonstrates that Nb and Ti were depleted inside the dendrite but enriched in the interdendritic region, whereas Fe exhibited the opposite variation. This discrepancy was due to the different partition coefficients of Nb, Ti, and Fe in the alloy system. The segregation of elements during solidification modified



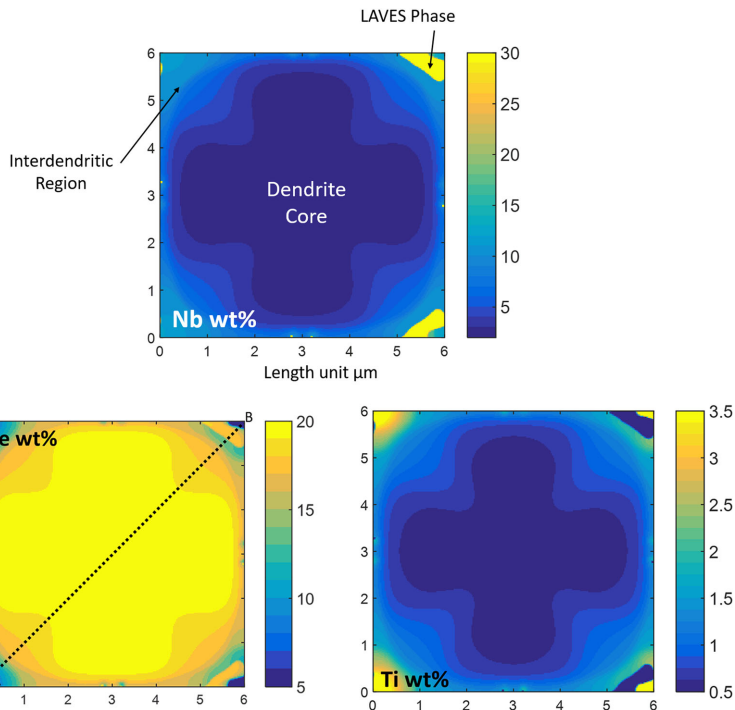


Fig. 4—Nb, Fe, and Ti, distribution maps at the end of the solidification of EBM Alloy 718.

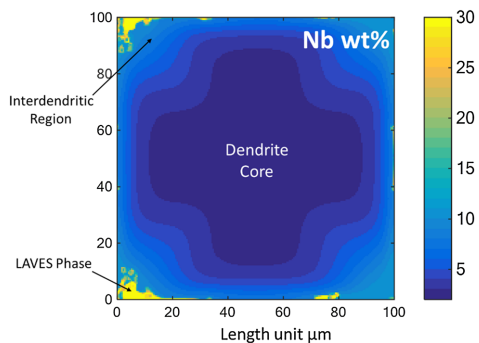


Fig. 5—Nb distribution maps at the end of the solidification of cast Alloy 718 simulation. Line AB was used to do the virtual EDX on the modeled microstructure.

the local thermodynamics and created the necessary driving force to form the Laves phase in the interdendritic region. Figure 5 shows the distribution map

obtained for Nb at the end of the cast simulation, where the observed segregation behavior of the elements was similar to the EBM microstructure. The size of the Laves phase particles in the cast microstructure was larger than that in the EBM microstructure, which was related to the larger length solidification scale in the cast microstructure.

Table IV shows the compositions measured at the dendrite core and the Laves phase in both the phase-field model and the actual sample's microstructure. In the Laves phase, the amounts of Nb and Mo obtained by phase-field modeling differed considerably compared with the values measured in the composition of the EBM sample. These high Nb and low Mo values could be explained by errors in the TCNI8 database. A simple Scheil simulation was performed using Thermo-Calc (using TCNI8 and MOBNI4 databases) to check the Nb and Mo contents of the Laves phase from the start of its formation. In Scheil simulation, it also predicted around 41 wt pct Nb and 0.7 wt pct Mo. According to the Thermo-Calc company, no parameters in the TCNI8 database have been assessed for the Cr-Nb-Mo system, which could have led to the high and low solubilities for Nb and Mo in the Laves phase, respectively.

Table IV. Composition Measured in the Dendrite Core and Laves Phase Both from Phase-Field Model and Real Sample

			Al	Ti	Cr	Nb	Fe	Mo
Laves	Model		0.16	0.32	15.32	40.85	17.72	0.88
	EPMA	Average	0.20	0.86	14.33	28.52	13.36	6.87
		Standard deviation	0.06	0.05	0.92	1.37	0.24	0.35
Dendrite core	Model		0.56	0.57	19.71	2.41	19.91	2.49
	EPMA	Average	0.57	0.77	20.03	3.38	19.97	2.57
		Standard deviation	0.04	0.07	0.19	0.13	0.18	0.12

### C. Homogenization Behavior of EBM Alloy 718 and Cast Alloy 718

The homogenization heat treatments for Alloy 718 cast products are usually performed at a high temperature ( $> 1090$  °C) for a sufficient time ( $> 1$  hours) until the Laves phase dissolve.<sup>[22]</sup> The Laves phase contains a high amount of Nb, so dissolution of the Laves phase is important for redistributing the trapped Nb, which is needed to form the strengthening phases. Nonetheless, even if the Laves dissolves, obtaining a homogeneous distribution of elements in the microstructure is not economically viable.<sup>[22]</sup> However, as mentioned above, the observed homogenization of the elements in the microstructure of the EBM Alloy 718 samples occurred rather quickly ( $\sim 40$  minutes) during the “*in situ*” heat treatment in the build process.

Figure 6 shows the elemental distributions of Nb, Fe, and Ti along the line AB (the line AB is shown in Figure 4) in the EBM Alloy 718 at the end of the solidification simulation (“as built”) and during the “*in situ*” heat treatment simulation. The segregated elements in the as-built condition tended to homogenize after 40 minutes during the “*in situ*” heat treatment at around 1020 °C. Both Nb and Ti exhibited very low segregation after 40 minutes, whereas some segregation of Fe was still observed. This segregation is expected to be reduced by further “*in situ*” heat treatment and the microstructure is expected to reach its nominal composition.

However, the heat treatment simulation of the cast microstructure did not indicate the same homogenization compared with the EBM microstructure, as shown in Figure 7. Some of the Laves phase still remained at the end of the heat treatment simulation for the cast microstructure. By contrast, complete dissolution of the Laves phase was achieved in the heat treatment simulation of the EBM microstructure, which could have been related to the smaller size of the Laves phase particles in the EBM sample compared with the cast Alloy 718. Smaller particles will dissolve in a shorter time than larger particles. Another reason for the relatively rapid homogenization in the EBM microstructure is the smaller PDAS because the microstructure obtained in the EBM process will have a relatively smaller ( $\sim$ one order of magnitude smaller) PDAS compared with cast products. This difference will lead to segregation at a finer scale and a smaller diffusion length for the elements. As a consequence, EBM microstructures will tend to homogenize more rapidly compared with cast microstructures. It has been has

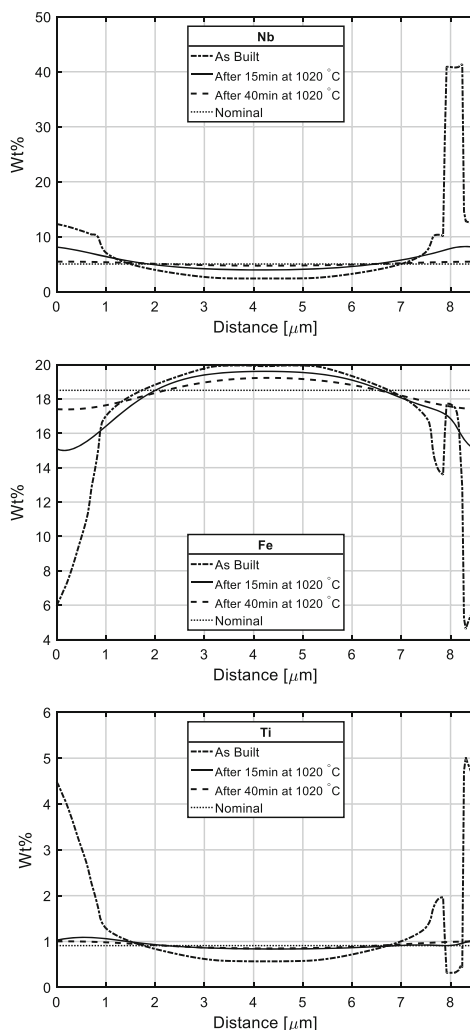


Fig. 6—Nb, Fe, and Ti variation along the “AB” virtual EDX line in the EBM microstructure-simulated domain.



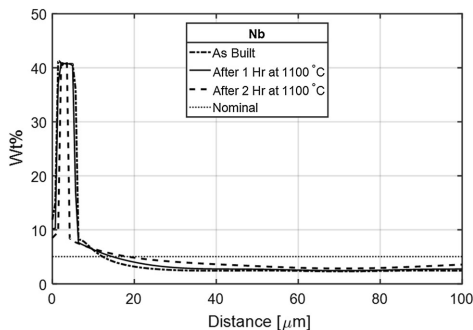


Fig. 7—Nb variation along the “AB” virtual EDX line in the cast microstructure-simulated domain.

shown that other AM processes such as laser metal directed energy deposition and selective laser melting of Alloy 718 resulted PDAS values with a similar order of magnitude to EBM,<sup>[8,24]</sup> which indicates that the segregated microstructures produced in these processes can be homogenized rather rapidly compared with cast products. This difference could facilitate the design of new heat treatment protocols for AM microstructures.

#### D. Change in Precipitation Kinetics of Phases in the Microstructure

The precipitation kinetics of an alloy depend on the local composition levels. The local composition of the microstructure in Alloy 718 differs from its nominal composition value because of the segregation of the elements during solidification. A segregated microstructure behaves in a different manner compared with a microstructure in the nominal composition of the same alloy,<sup>[25]</sup> which is illustrated based on the CCT diagrams obtained (as explained in Section III-C) for Alloy 718 in the following.

As mentioned above, during the building of the sample, the temperature of the build volume was around 1020 °C or above. This temperature is greater than the solvus temperature for  $\gamma'/\gamma''$  and around the solvus temperature for  $\delta$ ,<sup>[26,27]</sup> which implies that the formation of these phases could have occurred during the cooling stage of the build process. After the last layer was built, helium gas was blown in to cool the build chamber, as shown by the thermocouple measurements in Figure 1. During the cooling process, the temperature dropped through the precipitation temperature ranges for  $\gamma'/\gamma''$  and  $\delta$ .

In the “solidified” microstructure of the EBM sample, relatively higher amounts of  $\gamma'/\gamma''$  and  $\delta$  were observed close to the Laves phase. The density of these precipitates decayed when moving away from the Laves phase, as shown in Figure 8. Similar observations were reported previously for Alloy 718 built by direct laser additive manufacturing.<sup>[28]</sup> We produced CCT diagrams using JMatPro for compositions close to the Laves phase and in the dendrite core based on phase-field

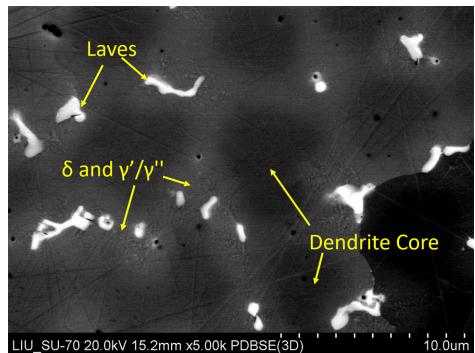


Fig. 8—SEM that shows the Laves phase and precipitation around it. (Image has been taken from a section Normal to the Build direction). It should be noted that  $\gamma'/\gamma''$  precipitates close to the Laves phase have been mainly observed through TEM analysis work. Ref. [19] for more information about the TEM work.

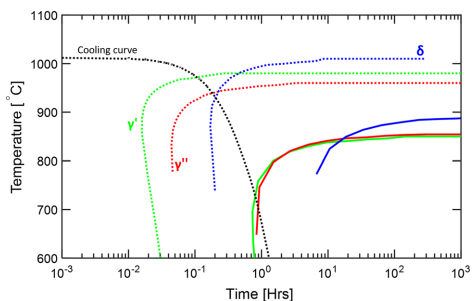


Fig. 9—CCT diagram created using JMatPro. Dotted line represents the 0.5 pct transformation close to Laves phase and solid line represent 0.5 pct transformation in the dendrite core. The cooling curve has been created from the thermocouple measurement in the cooling stage in Fig. 1.

simulations in order to explain the observed gradient in the precipitates. As shown in Figure 9, the precipitation kinetics were altered due to the change in the local composition, where  $\gamma'/\gamma''$  and  $\delta$  precipitated much earlier close to the Laves phase (more than an order of magnitude in time) compared with the core of the dendrite. The accelerated kinetics with the combination of change in local equilibrium conditions due to the local change in the composition, led to a higher density of the  $\gamma'/\gamma''$  and  $\delta$  phases close to the Laves phase. Due to the lower density of  $\gamma'/\gamma''$  in the dendrite core of the “solidified” microstructure, the hardness measured in the dendrite core was expected to be low compared with that in the interdendritic region.

Figure 10 shows the CCT curves obtained based on the nominal composition of the alloy and the dendrite core composition of the “solidified” microstructure. As the “*in situ*” heat treatment progressed, the elemental segregation in the “solidified” microstructure became

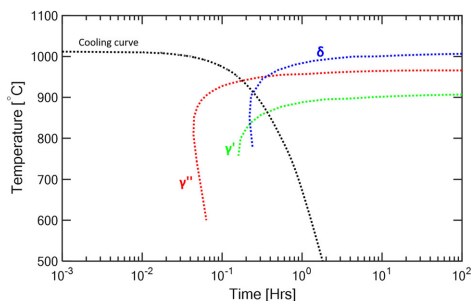


Fig. 10—CCT diagram created using JMatPro that relates to the homogenized part of the microstructure. The dotted line represents the 0.5 pct transformation related to the nominal composition of the Alloy. The cooling curve has been created from the thermocouple measurement in the cooling stage in Fig. 1.

more homogeneous and reached the nominal values. Therefore, the CCT curves generated based on the nominal composition can be used to describe the homogenized part of the microstructure of the sample (below 1800  $\mu\text{m}$  from the top of the surface). According to Figure 10, the  $\gamma'/\gamma''$  particles precipitated earlier and increased in size more rapidly in the homogenized part of the sample compared with the dendrite core of the “solidified” microstructure. Therefore, the hardness was higher in the homogenized part of the microstructure compared with the dendrite core of the “solidified” microstructure. This prediction was confirmed by previously reported hardness observations.<sup>[19]</sup>

According to the CCT curves obtained for  $\gamma'$  and  $\gamma''$ , as shown in Figure 9,  $\gamma'$  started to precipitate earlier than  $\gamma''$ . However, the CCT curves obtained for the nominal composition of the alloy (see Figure 10) showed that the precipitation of  $\gamma''$  occurred earlier than that of  $\gamma'$ . A similar accelerated precipitation of  $\gamma'$  before that of  $\gamma''$  was reported previously<sup>[29]</sup> for Ni-Cr-Fe alloys with compositions approximating that of Alloy 718. This phenomenon is linked to high Ti + Al/Nb ratios<sup>[29]</sup> and in the present study, this ratio was around 1.03 and 2.35 for the nominal and interdendritic compositions, respectively, which could have accelerated the precipitation of  $\gamma'$  before that of  $\gamma''$  in the interdendritic region. However, no experimental research has been performed to confirm the results obtained in the present study.

## V. CONCLUSION

In this study, we investigated the microstructural evolution during EBM of Alloy 718 by microstructure modeling. Multiphase-field modeling and precipitation kinetics modeling using JMatPro were also conducted. We provided the following conclusions based on the results.

The as-built microstructure of the EBM Alloy 718 exhibited a microstructure gradient from the top to the bottom of the sample.

- The high bed temperature during production resulted in an “*in situ*” heat treatment, which had a homogenization effect on the solidified microstructure.
- Due to the smaller PDAS and relatively low Laves phase size, EBM Alloy 718 exhibited more rapid homogenization compared with the cast or wrought material, which may facilitate the design of specific heat treatment protocols for EBM printed Alloy 718.
- The segregation of the alloying elements into the interdendritic region (close to the Laves phase) changed the precipitation kinetics of the alloy and led to the formation of high amounts of  $\gamma'/\gamma''$  and  $\delta$  in this region compared with the dendritic core.
- This combined approach based on multiphase-field modeling using MICRESS and transformation kinetic modeling using JMatPro is a viable method for obtaining insights into microstructural formation during the additive manufacturing of nickel-based superalloys and subsequent heat treatments.

## ACKNOWLEDGMENTS

The authors would like to thank Dr. Bernd Böttger and Dr. Eiken, Janin at Access e.V., Aachen, Germany for valuable discussions and inputs regarding the modeling work using MICRESS. Funding from the European Regional Development Fund for project 3Dprint and from the KK Foundation (Stiftelsen för Kunskaps-och Kompetensutveckling) for project SUMAN-Next is also acknowledged.

## OPEN ACCESS

This article is distributed under the terms of the Creative Commons Attribution 4.0 International License (<http://creativecommons.org/licenses/by/4.0/>), which permits unrestricted use, distribution, and reproduction in any medium, provided you give appropriate credit to the original author(s) and the source, provide a link to the Creative Commons license, and indicate if changes were made.

## REFERENCES

1. W.J. Sames, F.A. List, S. Pannala, R.R. Dehoff, and S.S. Babu: *Int. Mater. Rev.*, 2016, vol. 6608, pp. 1–46.
2. M.M. Attallah, R. Jennings, X. Wang, and L.N. Carter: *MRS Bull.*, 2016, vol. 41, pp. 758–64.
3. C. Körner: *Int. Mater. Rev.*, 2016, vol. 61, pp. 361–77.
4. G.A. Knorovsky, M.J. Cieslak, T.J. Headley, A.D. Romig, and W.F. Hammett: *Metall. Trans. A*, 1989, vol. 20, pp. 2149–58.
5. W.J. Sames, K.A. Unocic, R.R. Dehoff, T. Lolla, and S.S. Babu: *J. Mater. Res.*, 2014, vol. 29, pp. 1920–30.
6. M.M. Kirka, K.A. Unocic, N. Raghavan, F. Medina, R.R. Dehoff, and S.S. Babu: *JOM*, 2016, vol. 68, pp. 1012–20.
7. I. Steinbach: *Model. Simul. Mater. Sci. Eng.*, 2009, vol. 17, pp. 73001–31.

8. J. Kundin, L. Mushongera, and H. Emmerich: *Acta Mater.*, 2015, vol. 95, pp. 343–56.
9. R. Acharya, J.A. Sharon, and A. Staroselsky: *Acta Mater.*, 2017, vol. 124, pp. 360–71.
10. J. Eiken, B. Böttger, and I. Steinbach: *Phys. Rev. E*, 2006, vol. 73, p. 066122.
11. J. Eiken: Shaker Verlag GmbH, Germany, 2010.
12. B. Böttger, J. Eiken, and M. Apel: *Comput. Mater. Sci.*, 2015, vol. 108, pp. 283–92.
13. Thermo-Calc Software, <http://www.thermocalc.com/>. Accessed 25 May 2018.
14. N. Warnken, D. Ma, A. Drevermann, R.C. Reed, S.G. Fries, and I. Steinbach: *Acta Mater.*, 2009, vol. 57, pp. 5862–75.
15. Micress Group: *MICRESS 6.4 - User Guide Volume II: Running MICRESS*, vol. 2.
16. J.K. Tien and T. Caulfield: *Superalloys, Supercomposites and Superceramics*, Academic Press, New York, 1989.
17. SAE: *AMS5383E-Nickel Alloy, Corrosion and Heat-Resistant, Investment Castings*, 2012.
18. JMatPro, <https://www.sentessoftware.co.uk/jmatpro>. Accessed 21 Octob 2018.
19. D. Deng, R.L. Peng, H. Söderberg, and J. Moverare: *Mater. Des.*, 2018, vol. 160, pp. 251–61.
20. N. Raghavan, R. Dehoff, S. Pannala, S. Simunovic, M. Kirka, J. Turner, N. Carlson, and S.S. Babu: *Acta Mater.*, 2016, vol. 112, pp. 303–14.
21. T. Antonsson and H. Fredriksson: *Metall. Mater. Trans. B*, 2005, vol. 36, pp. 85–96.
22. J.F. Radavich: *Superalloys 718 Metallurgy and Applications*, TMS, Pittsburgh, 1989, pp. 229–40.
23. P. Nie, O.A. Ojo, and Z. Li: *Acta Mater.*, 2014, vol. 77, pp. 85–95.
24. Y.S. Lee and W. Zhang: *Addit. Manuf.*, <https://doi.org/10.1016/j.addma.2016.05.003>.
25. G. Asala, A.K. Khan, J. Andersson, and O.A. Ojo: *Metall. Mater. Trans. A*, 2017, vol. 48, pp. 4211–28.
26. R.G. Carlson and J.F. Radavich: *Superalloys 718 Metall. Appl.*, 1989, pp. 79–95.
27. V. Beauvois, J. Huez, S. Coste, O. Brucelle, and J. Lacaze: *Mater. Sci. Technol.*, 2004, vol. 20, pp. 1019–26.
28. Y. Tian, D. McAllister, H. Colijn, M. Mills, D. Farson, M. Nordin, and S. Babu: *Metall. Mater. Trans. A*, 2014, vol. 45, pp. 4470–83.
29. R. Cozar and A.A. Pineau: *Metall. Trans.*, 1973, vol. 4, pp. 47–59.

**Publisher's Note** Springer Nature remains neutral with regard to jurisdictional claims in published maps and institutional affiliations.



## Paper D

# Modelling of anisotropic elastic properties in alloy 718 built by electron beam melting.

Chamara Kumara

Dunyong Deng

Johan Moverare

Per Nylén

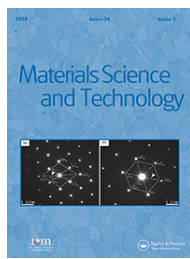
Published in *Materials Science and Technology*

vol. 34, no. 5, pp. 529–537, Mar. 2018

DOI: 10.1080/02670836.2018.1426258

Reprinted with CC BY-NC-ND 4.0





# Modelling of anisotropic elastic properties in alloy 718 built by electron beam melting

Chamara Kumara, Donyong Deng, Johan Moverare & Per Nylén

To cite this article: Chamara Kumara, Donyong Deng, Johan Moverare & Per Nylén (2018) Modelling of anisotropic elastic properties in alloy 718 built by electron beam melting, Materials Science and Technology, 34:5, 529-537, DOI: [10.1080/02670836.2018.1426258](https://doi.org/10.1080/02670836.2018.1426258)

To link to this article: <https://doi.org/10.1080/02670836.2018.1426258>



© 2018 The Author(s). Published by Informa UK Limited, trading as Taylor & Francis Group.



Published online: 28 Jan 2018.



Submit your article to this journal [↗](#)



Article views: 149



View Crossmark data [↗](#)



Citing articles: 1 View citing articles [↗](#)

## Modelling of anisotropic elastic properties in alloy 718 built by electron beam melting

Chamara Kumara<sup>a</sup>, Donyong Deng<sup>b</sup>, Johan Moverare<sup>a,b</sup> and Per Nylén<sup>a</sup>

<sup>a</sup>Division of abrasive and additive manufacturing processes, Department of Engineering Science, University West, Trollhättan, Sweden;

<sup>b</sup>Division of Engineering Materials, Department of Management and Engineering, Linköping University, Linköping, Sweden

### ABSTRACT

Owing to the inherent nature of the process, typically material produced via electron beam melting (EBM) has a columnar microstructure. As a result of that, the material will have anisotropic mechanical properties. In this work, anisotropic elastic properties of EBM built Alloy 718 samples at room temperature were investigated by using experiments and modelling work. Electron backscatter diffraction data from the sample microstructure was used to predict the Young's modulus. The results showed that the model developed in the finite element software OOF2 was able to capture the anisotropy in the Young's modulus. The samples showed transversely isotropic elastic properties having lowest Young's modulus along build direction. In addition to that, complete transversely isotropic stiffness tensor of the sample was also calculated.

### ARTICLE HISTORY

Received 3 August 2017

Revised 4 January 2018

Accepted 5 January 2018

### KEYWORDS

EBM; alloy 718; young's modulus; anisotropy; modelling; EBSD; elastic constants

*This paper is part of a thematic issue on Nuclear Materials.*

### Introduction



According to the ASTM standards, the term additive manufacturing (AM) is defined as a process of joining materials to make objects from 3D model data (from CAD model), usually layer upon layer, as opposed to subtractive manufacturing methodologies [1]. AM is also known as 3D printing, rapid manufacturing, rapid prototyping or freeform fabrication. In recent years, AM has gained high interest in the field of manufacturing engineering due to its attractive features compared to the conventional manufacturing methods such as casting, shaping and machining. Ability to produce complicated geometries, low cost of retooling and control of the microstructure are some of the advantages that have been reported [2].

Electron Beam Melting (EBM) is a type of powder bed AM technique, which was commercialised in 1997 by Arcam Corporation in Sweden [2]. In the EBM process, the powder material is selectively melted by using an electron beam in a layer-by-layer approach. Before melting, the powder material is sintered to overcome the problem with smoking effect caused by powder particle charging [3]. EBM has been shown to be capable of producing high-performance products such as biomedical implants and high-performance superalloy components used in gas turbine engine applications. Faster deposition rates due to high beam energy and speed, lower residual stresses, possibility of tailoring the microstructure [4] and reduced problems with oxida-

tion are some of the advantages of the EBM process when compared with laser powder bed processes [2].

Alloy 718 is a  $\gamma'$  precipitation hardened nickel-based superalloy, which is extensively used in gas turbine components due to its good mechanical properties at elevated temperatures, corrosion resistance and good weldability [5,6]. Nevertheless, manufacturing Alloy 718 components through traditional manufacturing methods are time consuming and expensive. For an example, machining of Alloy 718 to get the desired shape is difficult due to excessive tool wear and low material removal rate [7,8]. Therefore, the application of novel non-conventional processing methods, such as EBM, is a promising candidate for manufacturing near net shape complex components. In addition to that, EBM opens up a completely new manufacturing platform that enables design freedom for design engineers to come up with topologically optimised components that save material usage, time and money. EBM of Alloy 718 has, therefore, gained high interest within the AM community.

Typically, nickel-based superalloys exhibit anisotropic elastic behaviour at the crystal level depending upon the orientation of the crystal. Nevertheless, at the macroscopic level, the behaviour of these alloys tends to be isotropic due to the randomly oriented polycrystalline grains. When the alloy microstructure contain textured grains (such as in the AM components [2,9,10], directionally solidified alloys [11], cold rolled sheets [12]),

**CONTACT** Chamara Kumara  [chamara.kumara@hw.se](mailto:chamara.kumara@hw.se)  Division of abrasive and additive manufacturing processes, Department of Engineering Science, University West, 461 86 Trollhättan, Sweden

© 2018 The Author(s). Published by Informa UK Limited, trading as Taylor & Francis Group.

This is an Open Access article distributed under the terms of the Creative Commons Attribution-NonCommercial-NoDerivatives License (<http://creativecommons.org/licenses/by-nc-nd/4.0/>), which permits non-commercial re-use, distribution, and reproduction in any medium, provided the original work is properly cited, and is not altered, transformed, or built upon in any way.



the behaviour will become anisotropic. Then the elastic behaviour will change depend upon the direction of loading. Tayon et al. [10] showed that the Young's modulus of Electron Beam Freeform Fabricated Alloy 718 will change depend up on the angle with respect to the deposition direction. Recent studies [13–15] show that the typical microstructure resulting from the EBM process is columnar in nature with a strong fibre texture towards the build direction. Nevertheless, by changing process parameters and scanning strategies, this can be changed to a microstructure having equiaxed grains [4,9]. This strong texture in the EBM built alloy will cause the material to have anisotropic elastic properties. In the literature, few studies have been reported on evaluating these anisotropic elastic properties of the Alloy 718 produced via electron beam melting [2,9]. In these studies, Young's Modulus values were calculated using the tensile test data. However, these values are limited to the build direction and normal to the build direction. Both the studies [2,9] showed lower Young's modulus in the build direction compare to the normal to build direction. As to the authors' knowledge, no information has been reported on the complete anisotropic elastic property tensor of the EBM produced material. This elastic property tensor is a crucial parameter in finite element (FE) simulation of EBM build components. These FE simulations will help the design engineers to evaluate the performance (such as vibration, strength, stability) of their design before actual manufacturing and make necessary adjustments in advance. Obtaining this elastic tensor through experimental work is time consuming and tedious work.

In this study, a modelling approach was carried out to investigate the anisotropic elastic behaviour of the Alloy 718 produced via EBM. This modelling method, unlike experiments, does not require building relatively larger tensile specimens and thus can minimise time and cost associated with the experiments. It might, therefore, be a valuable technique to investigate the effect of microstructure on mechanical properties thus enabling tailoring the properties in AM.

## Experimental work

### Material and method

In the present study, the EBM sample was manufactured in an Arcam A2X EBM machine using plasma atomised powder (nominal size ranges from 25 to 106  $\mu\text{m}$ ) supplied by Arcam AB. The chemical composition of the powder is given in Table 1. The manufacturing process started after the powder bed was pre-heated to 1000°C. The Arcam standard setting for Alloy 718 was used in this batch. Each deposition cycle consisted of: (1) preheating of the current powder layer, (2) contour melting of the build geometry, (3) hatch melting of the interior of the build geometry, (4)

**Table 1.** Nominal chemical composition of the raw powder.

Element	Ni	Cr	Fe	Nb	Mo	Co	Ti	Al
wt-%	Bal.	19.1	18.5	5.04	2.95	0.07	0.91	0.58
Element	Mn	Si	Cu	C	P	S	N	O
wt-%	0.05	0.13	0.1	0.035	0.004	0.001	0.0128	0.0133

post-heating of the current layer and (5) lowering down the powder bed and raking the powders to form a uniform layer of approximately 75  $\mu\text{m}$  for next cycle. The as-manufactured sample was cuboid, with dimensions as shown in Figure 1.

### Tensile testing

It was shown in a previous study [15], by some of the co-authors of this article, that the hatch region of the built sample showed a strong  $\langle 001 \rangle$  fibre texture along the building direction. However, the overall microstructure of the contour region of the sample did not show any preferential crystallographic texture. They also found that the volume fraction of the contour region was very small compared to the hatch region. Therefore, the tensile test samples were machined out from the hatch region. In order to investigate the elastic properties, the tensile samples were machined out from the direction parallel and normal to the building direction. The geometry details are as shown in Figure 1. The tensile tests were performed with an Instron 5582 universal test machine in open air and at room temperature, the strain rate was set to 0.1%/s and due to the small sample size a digital image correlation (DIC) system, Image System AB, was utilised to measure the strains during the tensile tests. For each test condition, 3–4 tensile test was performed.

### Acquisition of electron backscatter diffraction images

In order to evaluate Young's Modulus of the sample (both parallel to the build direction and normal to the build direction), electron backscatter diffraction (EBSD) data was utilised. Therefore, to obtain the EBSD data, the as-built samples were cut parallel to the build direction and normal to the build direction as shown in Figure 2. The EBSD images were taken only from the hatch region of the sample.

The samples for EBSD analysis were mounted in Bakelite and mechanically ground from 500 Grit to 4000 Grit. Polishing started with diamond suspensions from 3 to  $\frac{1}{4}$   $\mu\text{m}$  and with OP-U colloidal silica suspension as the final step. Hitachi SU70 FEG scanning electron microscope, equipped with EBSD system from Oxford Instrument, was operated at 20 kV to do the EBSD mappings. The HKL Channel 5 program was used to plot the pole figures, inverse pole figures and the inverse pole figure colouring mapping.

The size of the EBSD images will have an impact on the results. Smaller size EBSD images containing fewer

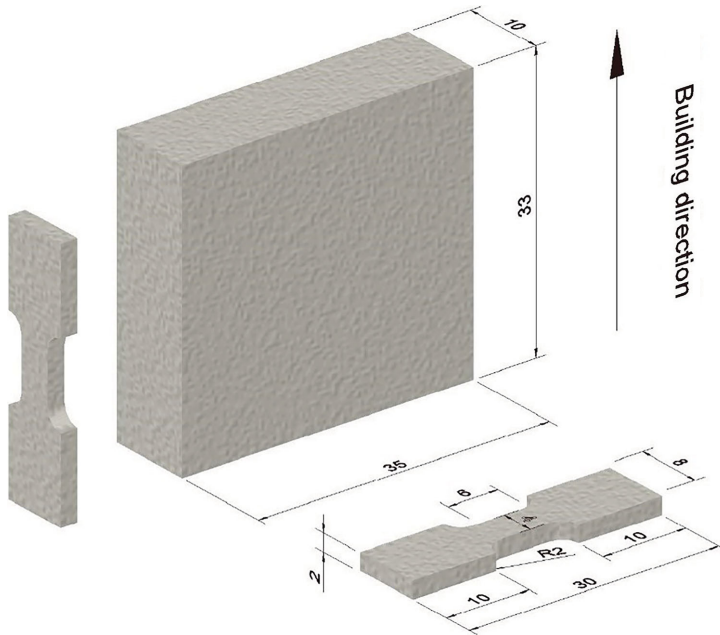


**Figure 1.** Schematic representation of the tensile test sample geometry (all dimensions are in mm). Both direction tensile specimens have the same dimensions.

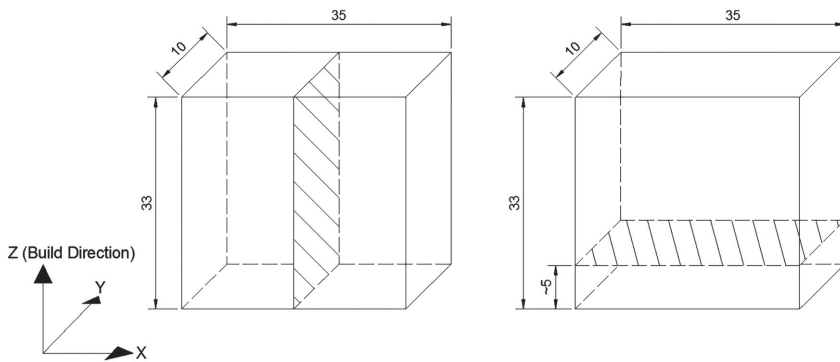


**Figure 2.** Schematic representation of the EBM samples. Hatch planes show the planes that were used to obtain EBSD data.

grains might not be a good representation of the grain orientation of the entire microstructure. Therefore, the size of an EBSD image was selected in such a way that a sufficient number of grains were captured. Details of the EBSD acquisition are shown in Table 2. To investigate the effect of build height on Young's Modulus EBSD, images were taken at different locations in the XZ plane.

### Modelling work

The EBSD image contains crystal orientations data of the microstructure. Therefore, it is possible to evaluate

the Young's Modulus of the sample based on these crystal orientations with the use of single-crystal elastic constant data [10,16]. FE analysis was then used to predict the Young's Modulus of the EBM build Alloy 718 sample. Additionally, a texture analysis method was utilised to visualise the Young's Modulus variation with respect to the build direction of the sample and to compute the anisotropic elastic material property tensor.

### Elastic constants of alloy 718

The generalised Hook's law for a material can be written as follows where  $\sigma_i$  is the stress vector,  $C_{ij}$  is the stiffness

**Table 2.** EBSD image acquisition details.

Image no.	Image acquisition plane	Rough location of the image in the plane	Dimensions (μm)			EBSD scan step size (μm)
			X	Y	Z	
1	YZ (parallel to BD)	~ 5 mm from bottom		2534	1434	1.5
2						
3		~ 12 mm from bottom		1740	2535	15
4						
5						
6	XY (normal to BD)	~ 3 mm from top		1739	708	1.5
7				1741	702	1
8				984	1944	1.5
9						
10		N/A	2535	1740		15
11			2535	1740		
12			2535	1740		
13			734	1739		1.5
14	YZ	~ 3 mm from top and 45° to BD	681	1738		1
				984	1994	1.5

**Table 3.** Single crystal elastic constants (units in GPa) of nickel-based superalloys and directional Young's Modulus values (units in GPa).

Material	C11	C12	C44	E < 001 >	E < 101 >	E < 111 >	Reference
Ni	<b>250.5</b>	<b>160.5</b>	<b>118.5</b>	125.1	220.0	294.4	[26]
ALLOY 718	<b>240.9</b>	<b>140.5</b>	<b>105.7</b>	137.4	214.5	263.8	[27]
ALLOY 718	<b>259.6</b>	<b>179.0</b>	<b>109.6</b>	113.5	204.6	279.0	[28]
ALLOY 718	<b>231.2</b>	<b>145.1</b>	<b>117.2</b>	119.3	212.4	287.1	[29]
Average	<b>243.9</b>	<b>154.9</b>	<b>110.8</b>	123.6	211.4	277.1	
IN600	<b>234.6</b>	<b>145.4</b>	<b>126.2</b>	123.3	223.0	305.3	[30]
IN625	<b>243.3</b>	<b>156.7</b>	<b>117.8</b>	120.5	215.3	291.7	[31]
IN738LC	<b>235.2</b>	<b>147.7</b>	<b>122.5</b>	121.2	218.6	298.6	[32]
IN792	<b>263.6</b>	<b>172.8</b>	<b>123.4</b>	126.7	226.8	307.8	[32]

matrix and the  $\varepsilon_j$  is the corresponding strain vector. Generally, with respect to an arbitrary coordinate system, the stiffness matrix has 21 independent components (elastic constants). However, with the presence of crystal symmetries, the number of independent elastic contents that is needed to define the stiffness matrix will be drastically reduced [17]. For instance, material having cubic, hexagonal and tetragonal crystal symmetries will have three, five and six elastic constants, respectively. In this study, it is assumed that the properties of Alloy 718 mainly originate from the matrix  $\gamma$  phase having the cubic crystal structure with three independent elastic constants.

Independent elastic constants are key parameters when it comes to computing material properties such as Young's Modulus, shear modulus and Elastic wave velocity  $= \sum C_{ij} \cdot \varepsilon_j$ , cities from microstructure data. Inputting reasonably right value for these constants make the prediction more reliable and accurate. Table 3 summarises the published data from the literature related to Alloy 718 elastic constants together with other nickel-based superalloys elastic constants (which has been used as Alloy 718 elastic constants in modelling works). For comparison purposes, elastic constants related to pure nickel are also presented. The directional Young's Modulus of the single crystal material presented in the Table 3 has been calculated by using the equation (1) found in the literature [17]. This helps to get a good picture of the effect of these elastic constants on the mechanical

behaviour, especially of a material having a strong texture.

$$\frac{1}{E_d} = S_{11} + \frac{(2S_{12} - 2S_{11} + S_{44})(k^2l^2 + l^2h^2 + h^2k^2)}{(h^2 + l^2 + k^2)}, \quad (1)$$

$$S_{11} = \frac{C_{11} + C_{12}}{C_{11}^2 + C_{11}C_{12} - 2C_{12}^2}, S_{12} = \frac{-C_{12}}{C_{11}^2 + C_{11}C_{12} - 2C_{12}^2}, S_{44} = \frac{1}{C_{44}}.$$

Here  $E_d$  is the directional Young's Modulus,  $S_{ij}$  are the compliance matrix constants,  $C_{ij}$  are the stiffness matrix constants and  $h$ ,  $k$ , and  $l$  are the direction indices.

As presented in the table, the reported elastic constants for the Alloy 718 gave different directional Young's Modulus values. In some cases, they were lower than the pure Nickel directional Young's Modulus value. The average values of the reported elastic constants were, therefore, used in this study.

### FE approach

To simulate the tensile test numerically, 2D FE modelling was carried out by using the open source software code, OOF2, developed at National Institute of Standards and Technology [18]. Information of about this software and its use can be found in [19].

First, the EBSD data were inputted to OOF2 through the orientation map function. Based on the orientation data, an EBSD image was constructed. The simple



**Figure 3.** Schematic representation of the boundary conditions used in OOF2 model.

meshing algorithm was used to generate an FE mesh. In this procedure, each pixel on the EBSD image was converted into two triangular elements. The diagonal dividing each pixel was alternated from pixel to pixel so that the orientations of the right-triangle elements were not all the same. Selected single crystal elastic constants were thereafter given as material property to the model. Plane stress condition was assigned and boundary conditions applied as shown in Figure 3. Finally, Young's Modulus values of the EBSD image were predicted by considering the applied displacement and the resulting force at the boundary.

### Texture analysis method

Based on the EBSD analysis data, the material exhibits a strong  $\langle 100 \rangle$  crystallographic orientation parallel to the build direction. Therefore, Young's Modulus of the material will vary in different directions. To visualise this variation, Young's Modulus of the sample was computed and plotted as a function of the angle with respect to the build direction. For this MTEX (version 4.5.0), a free texture analysis toolbox for Matlab [20] was used.

In order to calculate Young's Modulus using MTEX, Voight [21], Reuss [22] and Hill [23] average material stiffness tensors (6X6) have to be calculated. These tensors were, therefore, calculated based on the single crystal elastic constants and the crystal orientation data from EBSD analysis. The Voigt and Reuss solutions, respectively, provide the upper and lower bounds for the effective elastic stiffness for the material. When averaging the elastic stiffness of each crystal over the whole domain, Voight method assumes that the local strain is to be uniform in the material. Whereas in Reuss method, it assumes that the local stress of the material to be uniform. Measured elastic stiffness tensors of a polycrystalline material have been shown to usually lie between these upper and lower bound. Therefore, Hill [23] suggested an averaging criterion based on the upper and lower bound of the elastic field limits. Hill suggested that calculating the volume-weighted arithmetic mean of the Voight and Reuss solutions would give a better estimation of the elastic stiffness

value, which is close to the experimentally observed value. Using the computed Hill average material stiffness matrices, Young's Modulus values were computed with respect to the angle from the build direction.

### Results and discussion

When analysing the EBSD data, it was observed that the material has a columnar grain microstructure with strong crystallographic fibre texture along the build direction, as can be seen in Figure 4. In the building direction, the samples preferentially showed a strong  $\langle 001 \rangle$  crystallographic orientation. This could be due to the strong thermal gradient that results in the build direction while building the sample [9]. During the solidification process, materials having a f.c.c. crystal structure, like Alloy 718, has a tendency to orient the  $\langle 001 \rangle$  direction along the steepest thermal gradient direction [24]. In contrast, normal to the build direction, the material did not show any strong texture. Along both X and Y directions, grain orientations were more uniform with any random orientation between the  $\langle 001 \rangle$  and  $\langle 101 \rangle$  directions. This kind of columnar textured EBM Alloy 718 microstructures are in accordance with previously reported EBM Alloy 718 microstructures [4,9,25].

The Young's Modulus values predicted using the FE modelling work is given in Table 4. It can be seen that the selected image sizes were enough to predict Young's Modulus. In this study, deferent images with different resolutions were also evaluated. Higher resolution (images with  $1 \mu\text{m}$  step size) images give a more accurate representation of the grain orientations at a cost of higher EBSD image acquisition time. Whereas lower resolution (images with  $15 \mu\text{m}$  step size) will give less accurate information about the orientation distribution with faster EBSD accuation time. When looking at the results, a considerable amount of difference between the low- and high-resolution images was not observed. This indicates that low-resolution images were good enough to capture adequate information that is needed to represent the grain orientation of the microstructure. This also gives the additional advantage of decrease in computational time since the FE simulations based on high-resolution images are significantly more time consuming compared to analyses that use lower resolution images.

Figure 5, shows the average Young's Modulus values obtained from both the modelling work and the tensile testing in parallel to build direction and normal to the build direction. For comparison purposes, Young's Modulus values that are reported in the literature [2,9] for EBM Alloy 718 with a similar columnar microstructure are also shown. It can be seen that the Young's Modulus parallel to the build direction was lower than the value normal to the build direction indicating a strong anisotropy. This is as a result of the lowest Yong's

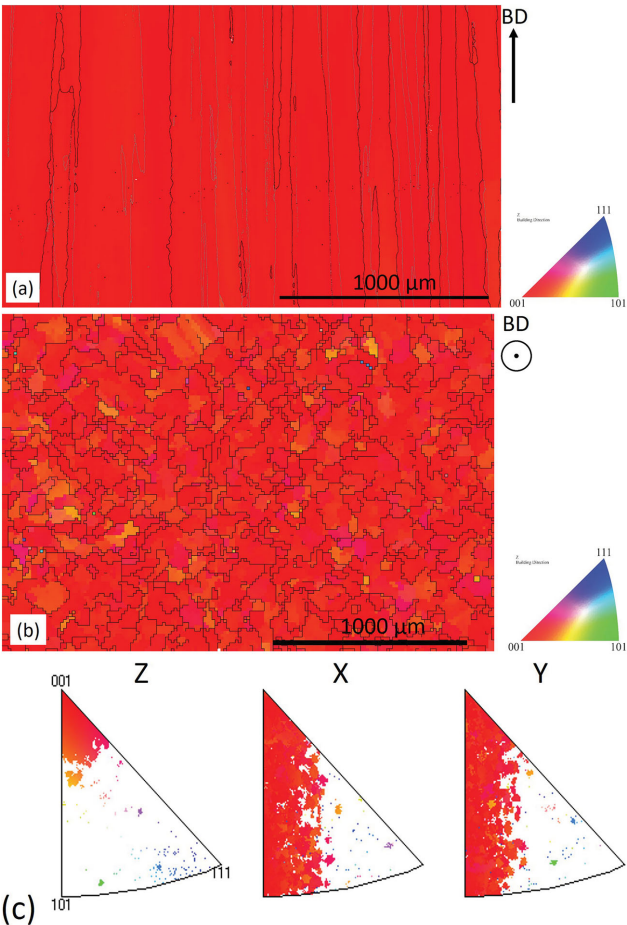


**Figure 4.** EBSD inverse pole figure colour maps from hatch region: (a) parallel to the build direction (BD), (b) normal to the build direction (BD), inverse pole figure maps for the EBSD image in (b).

**Table 4.** Predicted Young’s Modulus.

Image no.	Image acquisition plane	Dimensions (μm)			EBSD scan step size (μm)	Young’s Modulus (GPa)		
		X	Y	Z		X	Y	Z
1	YZ (parallel to BD)		2534	1434	1.5			126.3
2								124.3
3			1740	2535	15			126.5
4								127.2
5								127.2
6	XY (normal to BD)		1739	708	1.5			126.8
7			1741	702	1			126.5
8			984	1944	1.5			125.4
9		2535	1740		15	172.8	169.4	
10		2535	1740			167.5	167.8	
11	YZ	2535	1740			163.4	163.8	
12		734	1739		1.5	168.3	164.7	
13		681	1738		1	166.1	163.8	
14	YZ		984	1994	1.5	249.4	233.1	

modulus in the f.c.c. crystal is in the  $\langle 001 \rangle$  direction, Table 3. The average Young’s Modulus values in X and Y direction were very similar, Table 4. The values were

in between  $\langle 001 \rangle$  and  $\langle 101 \rangle$  directional Young’s Modulus values of the Alloy 718 single crystal. This is because of the observed random crystal orientation

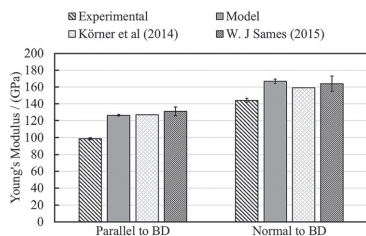


**Figure 5.** Average Young's Modulus from Experimental and Modelling work together with reported Young's Modulus values of EBM Alloy 718 with columnar microstructure.

**Table 5.** Overall elastic stiffness matrix.

$C_{ij}$ (GPa)	1	2	3	4	5	6
1	275.6	125.8	152.3			
2	125.8	274.5	153.4			
3	152.3	153.4	248.0			
4				107.6		
5					106.4	
6						68.0

distribution between  $\langle 001 \rangle$  and  $\langle 101 \rangle$  direction in the XY plane (refer inverse pole figures in Figure 4).

Both the predicted and the measured Young's Modulus data show that the material exhibits a transversely isotropic behaviour. This behaviour was also confirmed when analysing the overall Hill elastic matrix of the sample. The overall Hill elastic stiffness matrix that was calculated using the MTEX toolbox is shown in Table 5. The values that should appear in the blank cells in the table were actually not zero. However, compared with the larger values in the matrix, these were very small and, therefore, neglected (assumed to be zero). By looking at the values, it can be seen that  $C_{11} \approx C_{22}$ ,  $C_{13} \approx C_{23}$  and  $C_{44} \approx C_{55}$ . This indicates that the EBM Alloy 718 sample used in this study exhibits transversely isotropic elastic behaviour. This elastic tensor data will be valuable when conducting FE modelling work of EBM Alloy 718 components that exhibits transversely isotropic behaviour. In addition, it can be used to evaluate the Young's modulus and shear modulus

variation of the sample. Conducting experiments to get this tensor data would be complicated and tedious. Therefore, evaluating this matrix from EBSD data would be an easy alternative solution with reasonable accuracy.

The experimental Young's Modulus values obtained in this study were in general lower than the corresponding values predicted from the models. Moreover, they were lower than the values found in the published literature. Parallel to the build direction, the experimental Young's Modulus value was around 100 GPa which was lower than the lowest possible Young's Modulus value (in  $\langle 001 \rangle$  direction) for pure Nickel (refer Table 3). One can argue that this could be as a result of the observed porosity in the sample since the porosity was neglected in the modelling work. However, the observed porosity value (which were calculated by using Scanning Electron Microscopy Images) was approximately 1%. Therefore, the effect of porosity on Young's Modulus can be assumed negligible. A possible reason for the low experimental Young's Modulus could be due to the experimental method. As previously stated, the DIC method was utilised since the tensile samples were small. Therefore, the strain measurement of the experiments was not linked to the tensile testing while the test was performed. Strains were instead calculated separately using the obtained images from the DIC method. This might have caused an error when calculating the Young's Modulus from strains obtained from DIC measurements. The predicted Young's Modulus values were in good agreement with values found in the published literature for EBM Alloy 718 samples, which had a columnar microstructure. In addition to that, the method was able to capture the anisotropy of the build sample.

Figure 6 shows the Voigt, Ruess and Hill Young's Modulus variation with respect to the build direction. This variation is similar to Young's modulus variation that observed in the directionally solidified nickel-based superalloys [11]. From the graphs, it can be observed that Young's Modulus reached a higher value (even higher than normal to the build direction), at an angle of 50–60 degrees from the build direction.

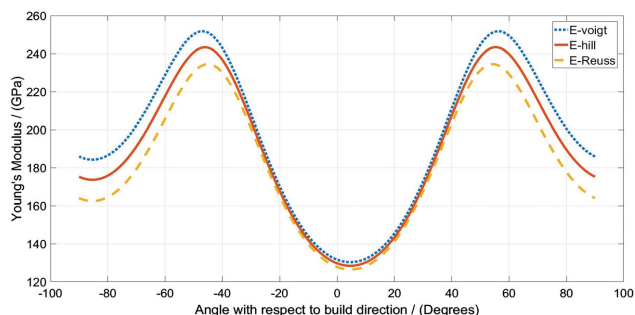


**Figure 6.** Young's Modulus variation with respect to the build direction.



The value is almost twice the value of the parallel to the build direction. This was also observed in the FE modelling work of Image 14, Table 4. This value is in between  $\langle 101 \rangle$  and  $\langle 111 \rangle$  directional Young's Modulus values of the ALLOY 718 single crystal. Therefore, the material will have a higher stiffness in this direction compared to other directions. This indicates that the stiffness that is needed in the loading direction of a physical component can be changed by changing the orientation of the build component in the build chamber.

## Conclusions

In this study, elastic properties of the Alloy 718 samples produced via EBM were studied. For this, both modelling and experimental methods were utilised. The following conclusions were made based on the observed results.

- The samples showed significant anisotropic elastic properties. Lowest Young's modulus was observed along the build direction. Normal to the build direction elastic properties were shown isotropic. Overall, elastic behaviour of the sample was similar to the transversely isotropic case.
- The modelling method used in this study was able to capture the anisotropic elastic properties with reasonable accuracy.
- Young's modulus of the sample varied with respect to the angle with the build direction. The highest Young's Modulus value was observed in between the build direction and normal to the build direction. This indicates that the stiffness of a component can be tailored by changing the component build orientation in the build chamber.
- These modelling results indicate that the proposed modelling method can be utilised in evaluating the elastic properties of functionally graded or tailored microstructures using EBM.

## Acknowledgements

The authors would like to thank Sandvik Machining Solutions AB in Sandviken, Sweden for providing EBM ALLOY 718 material for this research and Dr Stephen Langer at National Institute of Standards and Technology for the support in the modelling work with OOF2.

## Disclosure statement

No potential conflict of interest was reported by the authors.

## Funding

The funding from the European Regional Development Fund, project grant 3Dprint, and from KK Foundation (Stiftelsen för Kunskaps- och Kompetensutveckling), project grant SUMAN-Next is also acknowledged.

## ORCID

Chamara Kumara  <http://orcid.org/0000-0002-4087-6467>

Per Nylén  <http://orcid.org/0000-0001-7787-5444>

## References

- [1] Standard Terminology for Additive Manufacturing Technologies. F2792-12a A. West Conshohocken (PA): ASTM International; 2012. [www.astm.org](http://www.astm.org).
- [2] SAMES WJ. Additive manufacturing of Inconel 718 using electron beam melting: processing, post-processing, & mechanical properties, PhD Thesis. Texas A&M University, Texas. 2015.
- [3] Sames WJ, List FA, Pannala S, et al. The metallurgy and processing science of metal additive manufacturing. *Int Mater Rev*. 2016;6608:1–46.
- [4] Dehoff RR, Kirka MM, List FA, et al. Crystallographic texture engineering through novel melt strategies via electron beam melting: Inconel 718. *Mater Sci Technol*. 2015;31:939–944.
- [5] Attallah MM, Jennings R, Wang X, et al. Additive manufacturing of Ni-based superalloys: the outstanding issues. *MRS Bull*. 2016;41:758–764.
- [6] Wang Z, Guan K, Gao M, et al. The microstructure and mechanical properties of deposited-ALLOY 718 by selective laser melting. *J Alloys Compd*. 2012;513:518–523.
- [7] Costes JP, Guillet Y, Poulachon G, et al. Tool-life and wear mechanisms of CBN tools in machining of Inconel 718. *Int J Mach Tools Manuf*. 2007;47:1081–1087.
- [8] Attia H, Tavakoli S, Vargas R, et al. Laser-assisted high-speed finish turning of superalloy Inconel 718 under dry conditions. *CIRP Ann Manuf Technol*. 2010;59:83–88.
- [9] Körner C, Helmer H, Bauereiß A, et al. Tailoring the grain structure of ALLOY 718 during selective electron beam melting. *MATEC Web Conf*. 2014;14: doi:10.1051/mateconf/20141408001
- [10] Tayon Wa, Shenoy RN, Redding MR, et al. Correlation between microstructure and mechanical properties in an inconel 718 deposit produced via electron beam freeform fabrication. *J Manuf Sci Eng*. 2014;136:61005–061005–061007.
- [11] Hermann W, Sockel HGG, Han J, et al. Elastic properties and determination of elastic constants of nickel-base superalloys by a free-free beam technique. *Superalloys*. 1996: 229–238.
- [12] Hu HH. Elastic properties of cold-rolled and annealed sheets of phosphorus steel having high normal plastic anisotropy. *Texture Cryst Solids*. 1980;4:111–127.
- [13] Kirka MM, Unocic KA, Raghavan N, et al. Microstructure development in electron beam-melted Inconel 718 and associated tensile properties. *JOM*. 2016;68:1012–1020.
- [14] Helmer H, Bauereiß A, Singer RF, et al. Grain structure evolution in Inconel 718 during selective electron beam melting. *Mater Sci Eng A*. 2016;668:180–187.
- [15] Deng D, Moverare J, Peng RL, et al. Microstructure and anisotropic mechanical properties of EBM manufactured Inconel 718 and effects of post heat treatments. *Mater Sci Eng A*. 2017;693:151–163.
- [16] Den Toonder JM, Van Dommelen JAW, Baaijens FPT. The relation between single crystal elasticity and the effective elastic behaviour of polycrystalline materials: theory, measurement and computation. *Model Simul Mater Sci Eng*. 2000;7:909–928.

- [17] Hosford WF. The mechanics of crystals and textured polycrystals. Oxford: Oxford University Press; 1993.
- [18] OOF2. Available from: <https://www.ctcms.nist.gov/oof/oof2/>. 2017 May 13.
- [19] Langer SA, Fuller ER, Carter WC. OOF: an image-based finite-element analysis of material microstructures. *Comput Sci Eng*. 2001;3:15–23.
- [20] MTEX. Available from: <http://mtex-toolbox.github.io/>. 2017 May 13.
- [21] Voigt W. Lehrbuch der kristallphysik VW. mit ausschluß der kristalloptik. Sammlung von Lehrbüchern auf dem Gebiete der Math. Wissenschaften. Leipzig: B.G. Teubner; 1928.
- [22] Reuss A. Berechnung der Fließgrenze von Mischkristallen auf Grund der Plastizitätsbedingung für Einkristalle. *ZAMM. J Appl Math Mech/Zeitschrift für Angew Math und Mech*. 1929;9:49–58.
- [23] Hill R. The elastic behaviour of a crystalline aggregate. *Proc Phys Soc Sect A*. 1952;65:349–354.
- [24] Grong O. Metallurgical Modelling of Welding. Boca Raton (FL): CRC Press; 1997.
- [25] Strondl A, Palm M, Gnauk J, et al. Microstructure and mechanical properties of nickel based superalloy ALLOY 718 produced by rapid prototyping with electron beam melting (EBM). *Mater Sci Technol*. 2011;27:876–883.
- [26] Reed RC. The superalloys fundamentals and applications. Cambridge: Cambridge University Press; 2006.
- [27] Haldipur P, Margetan RBT FJ. Estimation of single-crystal elastic constants from ultrasonic measurements on polycrystalline specimens. *AIP Conf Proc AIP*. 2004;700(1):1061–1068.
- [28] Martin G, Ochoa N, Saï K, et al. A multiscale model for the elastoviscoplastic behavior of directionally solidified alloys: application to FE structural computations. *Int J Solids Struct*. 2014;51:1175–1187.
- [29] Jothi S, Merzlikin S V, Croft TN, et al. An investigation of micro-mechanisms in hydrogen induced cracking in nickel-based superalloy 718. *J Alloys Compd*. 2016;664:664–681.
- [30] Holden TM, Holt RA, Clarke AP. Intergranular strains in Inconel-600 and the impact on interpreting stress fields in bent steam-generator tubing. *Mater Sci Eng A*. 1998;246:180–198.
- [31] Wang Z, Stoica AD, Ma D, et al. Diffraction and single-crystal elastic constants of Inconel 625 at room and elevated temperatures determined by neutron diffraction. *Mater Sci Eng A*. 2016;674:406–412.
- [32] Han J, Bertram A, Olschewski J, et al. Identification of elastic constants of alloys with sheet and fibre textures based on resonance measurements and finite element analysis. *Mater Sci Eng A*. 1995;191:105–111.



## **Tidigare avhandlingar – Produktionsteknik**

PEIGANG LI Cold Lap Formation in Gas Metal Arc Welding of Steel An Experimental Study of Micro-lack of Fusion Defects, 2013:2.

NICHOLAS CURRY Design of Thermal Barrier Coatings, 2014:3.

JEROEN DE BACKER Feedback Control of Robotic Friction Stir Welding, 2014:4.

MOHIT KUMAR GUPTA Design of Thermal Barrier Coatings A modelling approach, 2014:5.

PER LINDSTRÖM Improved CWM Platform for Modelling Welding Procedures and their Effects on Structural Behavior, 2015:6.

ERIK ÅSTRAND A Framework for Optimised Welding of Fatigue Loaded Structures Applied to Gas Metal Arc Welding of Fillet Welds, 2016:7.

EMILE GLORIEUX Multi-Robot Motion Planning Optimisation for Handling Sheet Metal Parts, 2017:10.

EBRAHIM HARATI Improving fatigue properties of welded high strength steels, 2017:11.

ANDREAS SEGERSTARK Laser Metal Deposition using Alloy 718 Powder Influence of Process Parameters on Material Characteristics, 2017:12.

ANA ESTHER BONILLA HERNÁNDEZ On Cutting Tool Resource Management, 2018:16.

SATYAPAL MAHADE Functional Performance of Gadolinium Zirconate/YSZ Multi-layered Thermal Barrier Coatings, 2018:18.

ASHISH GANVIR Design of suspension plasma sprayed thermal barrier coatings, 2018:20.

AMIR PARSIAN Regenerative Chatter Vibrations in Indexable Drills: Modeling and Simulation, 2018:21.

ESMAEIL SADEGHIMERESHT High Temperature Corrosion of Ni-based Coatings, 2018:23.

VAHID HOSSEINI Super Duplex Stainless Steels. Microstructure and Properties of Physically Simulated Base and Weld Metal, 2018:24.

MORGAN NILSEN Monitoring and control of laser beam butt joint welding, 2019:27.

ARBAB REHAN Effect of heat treatment on microstructure and mechanical properties of a 5 wt.% Cr cold work tool steel, 2019:28.

KARL FAHLSTRÖM Laser welding of ultra-high strength steel and a cast magnesium alloy for light-weight design, 2019:29.

EDVARD SVENMAN An inductive gap measurement method for square butt joints, 2019:30.

NAGESWARAN TAMIL ALAGAN Enhanced heat transfer and tool wear in high-pressure coolant assisted turning of alloy 718, 2019:31.

ADNAN AGIC Edge Geometry Effects on Entry Phase by Forces and Vibrations, 2020:32.

ANA CATARINA FERREIRA MAGALHÃES Thermoelectric Measurements for Temperature Control of Robotic Friction Stir Welding, 2020:33.

ASHWIN DEVOTTA Improved finite element modeling for chip morphology prediction in machining of C45E steel, 2020:34.

TAHIRA RAZA Process Understanding and Weldability of Laser-Powder Bed Fusion Manufactured Alloy 718, 2020:35

PARIA KARIMI Electron Beam-Powder Bed Fusion of Alloy 718. Effect of Process Parameters on Microstructure Evolution [Forthcoming] 2020:37.

JONAS HOLMBERG High volumetric machining strategies of superalloy gas turbine components. Comparing conventional and non-conventional machining methods for efficient manufacturing [Forthcoming] 2020:40.

SNEHA GOEL Thermal post-treatment of Alloy 718 produced by electron beam melting [Forthcoming], 2020:41.

ARUN RAMANATHAN BALACHANDRAMURTHI  
[Forthcoming] 2020:42





# Microstructure Modelling of Additive Manufacturing of Alloy 718

When looking at the recent developments in metal AM, it is evident that metal AM has begun to revolutionise the manufacturing industry. It has provided new possibilities for engineers that did not exist with traditional manufacturing techniques. Nevertheless, to be able to fully employ its potential, research is needed that provides a solid understanding of the process–microstructure–property relationships with metal AM. To this end, the main research work presented in this thesis utilised a modelling approach to reveal the relationship between the thermal condition and microstructure formation in AM of Alloy 718. A multiphase–field modelling approach combined with transformation kinetics modelling was used. Two different AM processes, namely, laser metal powder directed energy deposition and electron beam powder bed fusion, were considered. The results revealed important relationships between the thermal conditions during the process (solidification conditions, thermal cycling, and global temperature of the build object during processing) and the phase transformation of Alloy 718. It was also revealed that the microsegregation of composition that occurred during the solidification changed the local equilibrium conditions and precipitation kinetics of Alloy 718. As a result, excess precipitation of  $\gamma'/\gamma''$  and  $\delta$  is observed in the interdendritic region compared with the dendrite core depending on the type of heat treatment that is used. In addition, the results revealed that, owing to the smaller dendrite spacing and relatively small Laves phase precipitate size, AM Alloy 718 exhibited more rapid homogenisation compared with the cast material.



## Chamara Sandun Sarath Kumara

Chamara comes from Kandy, Sri Lanka. He received his B.Sc. degree in Mechanical Engineering from the University of Peradeniya, Sri Lanka in 2013. He also won the best performance award for Mechanical Engineering undergraduate that year. After earning his bachelor's degree, he worked for two years as a temporary lecturer at the Mechanical Engineering Department, University of Peradeniya. In 2016, he received his

M.Sc. degree in Manufacturing Engineering from the University West. He also worked as a research assistant at University West during the summer of 2012 and during his master's programme. Immediately after he finished his master's, he started his PhD studies at University West. His research interests include additive manufacturing, thermal spraying, computational material science, and computation modelling and simulation of manufacturing processes.